Influence of snow properties on directional surface reflectance in Antarctica

Von der Fakultät für Physik und Geowissenschaften

der Universität Leipzig

genehmigte

DISSERTATION

zur Erlangung des akademischen Grades

Doktor der Naturwissenschaften

(Dr. rer. nat.)

vorgelegt

von M.Sc. Tim Carlsen

geboren am 16.10.1988 in 07381 Pößneck

Gutachter: Prof. Dr. Manfred Wendisch
Dr. Alexander Kokhanovsky

Tag der Verleihung: 09.07.2018

Bibliographische Beschreibung:

Carlsen, Tim
Influence of snow properties on directional surface reflectance in Antarctica
Universität Leipzig, Dissertation
170 S., 194 Lit., 60 Abb., 8 Tab.

Referat:

Die Bedeutung der Polarregionen für das Klima der Erde und die beobachtete, verstärkte Reaktion auf die Klimaveränderung, machen die Untersuchung der Reflexionseigenschaften von Schneeoberflächen und deren Einflussfaktoren notwendig. Deshalb wurden während des Südsommers 2013/14 über einen Zeitraum von 2 Monaten die spezifische Oberfläche (SSA, als ein Maß für die Schneekorngröße) und der hemisphärisch-direktionale Reflektanzfaktor (HDRF) von Schnee in der zentralen Antarktis (Forschungsstation Kohnen) gemessen.

Die SSA wurde anhand von bodengebundenen spektralen Albedomessungen des COmpact RAdiation measurement System (CORAS) und von flugzeuggetragenen Messungen des Spectral Modular Airborne Radiation measurement sysTem (SMART) berechnet. Im Zuge dessen wurde der snow grain size and pollution amount (SGSP) Algorithmus erweitert. Dieser wurde ursprünglich zur Analyse von satellitengetragenen Reflektanzmessungen mit dem MODerate Resolution Imaging Spectroradiometer (MODIS) entwickelt. Durch die Erweiterungen wurden der Einfluss des Sonnenstands auf die SSA-Ergebnisse reduziert und SSA-Werte auch unter bedeckten Bedingungen gewonnen. Spektrale Verhältnisse der Albedo bei 1280 nm und 1100 nm reduzieren die Messunsicherheit. Der Algorithmus wurde auf die bodengebundenen und flugzeuggetragenen Messungen angewandt und mit optischen in situ Beobachtungen der SSA (IceCube-Gerät) validiert. Die aus CORAS-Messungen berechnete SSA variierte zwischen 29 und 96 $\mathrm{m^2\,kg^{-1}}$. Auf durch Schneefälle verursachte relative Maxima in der SSA folgte ein allmähliches Absinken der SSA durch Metamorphismusprozesse im Schnee und den Transport von frischgefallenen Eiskristallen durch den Wind. Die Erweiterung auf bedeckte Messsituationen verbesserte die Datenabdeckung insbesondere in Zeiten von sich schnell ändernder SSA infolge von Schneefällen. Die SSA-Werte von CORAS und MODIS stimmen mit den in situ Messungen im Rahmen der Messungenauigkeiten überein. Allerdings unterschätzen die SMART-Werte die bodengebundenen Ergebnisse. Die räumliche Variabilität der SSA im Königin-Maud-Land ist in der selben Größenordnung wie die zeitliche Variabilität. Dabei traten Unterschiede zwischen Küstengebieten und Regionen im Innern der Antarktis auf. Die Validation bietet einen guten Test der SSA-Berechnung und kann zur Überprüfung von prognostischen Schneemodellen unter antarktischen Bedingungen verwendet werden.

Die HDRF von Schnee wurde aus flugzeuggetragenen Kameramessungen (Digitalkamera, Fischaugenobjektiv) für unterschiedliche Bedingungen (Rauigkeit, Schneekorngröße, Sonnenstand) berechnet. Die Kamera liefert Radianzmessungen unter Nutzung radiometrischer und geometrischer Kalibrierungen. Der Vergleich zwischen glatten und rauen Oberflächen (Sastrugi) zeigt deutliche Unterschiede in der HDRF. Diese werden vom Einfluss des Tagesgangs überlagert. Durch Inversion eines semi-empirischen, kernelbasierten Modells der bidirektionalen Reflektanzverteilungsfunktion (BRDF) wurde die HDRF bezüglich der Oberflächenrauigkeit, der Schneekorngröße und des Sonnenstands parametrisiert. Dies ermöglicht einen Vergleich der HDRF-Messungen mit BRDF-Resultaten der Satellitenfernerkundung.

Bibliographic Description:

Carlsen, Tim
Influence of snow properties on directional surface reflectance in Antarctica
Leipzig University, Dissertation
170 pp., 194 ref., 60 fig., 8 tab.

Abstract:

The significance of the polar regions for the Earth's climate system and their observed amplified response to climate change indicate the necessity for high temporal and spatial coverage for the monitoring of the reflective properties of snow surfaces and their influencing factors. Therefore, the specific surface area (SSA, as a proxy for snow grain size) and the hemispherical directional reflectance factor (HDRF) of snow were measured for a 2-month period in central Antarctica (Kohnen research station) during austral summer 2013/14.

The SSA data were retrieved on the basis of ground-based spectral surface albedo measurements collected by the COmpact RAdiation measurement System (CORAS) and airborne observations with the Spectral Modular Airborne Radiation measurement sysTem (SMART). The snow grain size and pollution amount (SGSP) algorithm, originally developed to analyze spaceborne reflectance measurements by the MODerate Resolution Imaging Spectroradiometer (MODIS), was modified in order to reduce the impact of the solar zenith angle on the retrieval results and to cover measurements in overcast conditions. Spectral ratios of surface albedo at 1280 and 1100 nm wavelength were used to reduce the retrieval uncertainty. The retrieval was applied to the ground-based and airborne observations and validated against optical in situ observations of SSA utilizing an IceCube device. The SSA retrieved from CORAS observations varied between 29 and $96\,\mathrm{m}^2\,\mathrm{kg}^{-1}$. Snowfall events caused distinct relative maxima of the SSA which were followed by a gradual decrease in SSA due to snow metamorphism and wind-induced transport of freshly fallen ice crystals. The ability of the modified algorithm to include measurements in overcast conditions improved the data coverage, in particular at times when precipitation events occurred and the SSA changed quickly. SSA retrieved from measurements with CORAS and MODIS agree with the in situ observations within the ranges given by the measurement uncertainties. However, SSA retrieved from the airborne SMART data underestimated the ground-based results. The spatial variability of SSA in Dronning Maud Land ranged in the same order of magnitude as the temporal variability revealing differences between coastal areas and regions in interior Antarctica. The validation presented in this study provided an unique test bed for retrievals of SSA under Antarctic conditions where in situ data are scarce and can be used for testing prognostic snowpack models in Antarctic conditions.

The HDRF of snow was derived from airborne measurements of a digital 180° fish-eye camera for a variety of conditions with different surface roughness, snow grain size, and solar zenith angle. The camera provides radiance measurements with high angular resolution utilizing detailed radiometric and geometric calibrations. The comparison between smooth and rough surfaces (sastrugi) showed significant differences in the HDRF of snow, which are superimposed on the diurnal cycle. By inverting a semi-empirical kernel-driven model for the bidirectional reflectance distribution function (BRDF), the snow HDRF was parameterized with respect to surface roughness, snow grain size, and solar zenith angle. This allows a direct comparison of the HDRF measurements with BRDF products from satellite remote sensing.

Contents

1 The cryosphere in the global climate system

Water can exist in solid, liquid, and gaseous thermodynamic phases within the Earth's atmosphere. That is because the triple point of water at 273.16 K (0.01 °C) and 611.2 Pa is well within the range of atmospheric temperatures and water vapor pressures. The cryosphere comprises all components of the Earth's climate system where water exists in its solid thermodynamic phase: snow, ice shelves and ice sheets, sea ice, lake and river ice, glaciers, and frozen ground. The term cryosphere comes from the Greek words *kryos* (cold) and *sphaira* (ball, globe); it was introduced by Antoni Boleslaw Dobrowolski in 1923 (Barry et al., 2011).

Figure 1.1 shows the averaged global distribution of the components of the cryosphere.

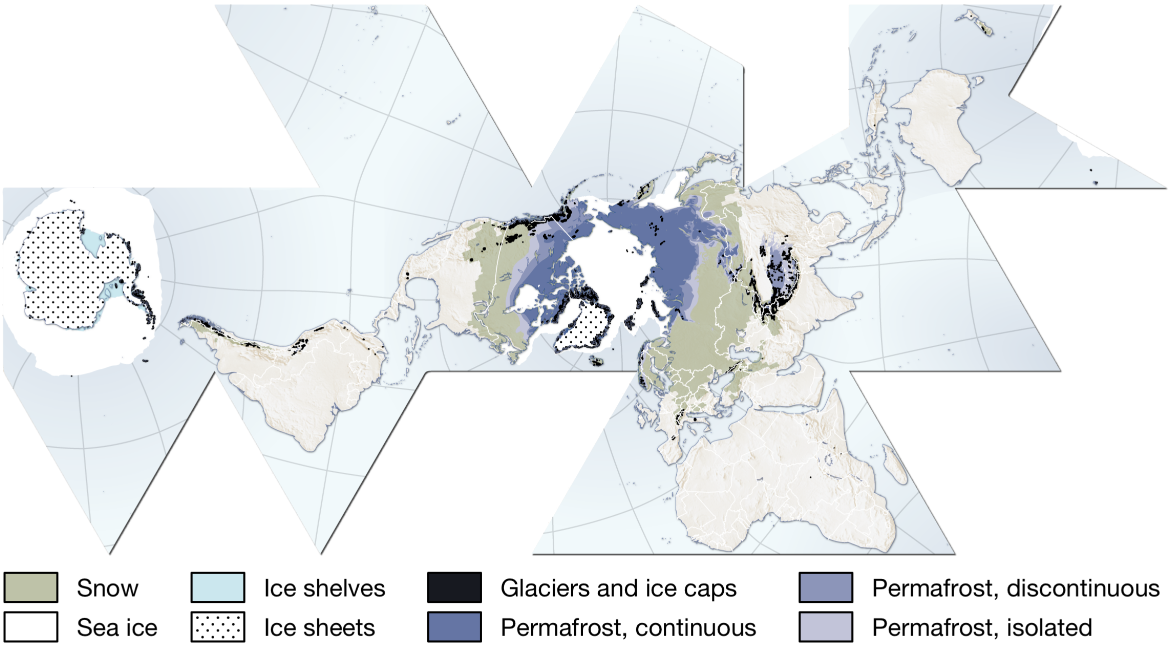

Figure 1.1: Global distribution of cryospheric components (modified from Eamer et al., 2007). Snow cover extent for Northern Hemisphere (NH) is represented by the 1966-2005 February average, for Southern Hemisphere (SH) by the 1987-2003 August average. Sea ice extent for NH: 1979-2003 March average, for SH: 1979-2002 September average.

More than half of the global land surface area ($A_\mathrm{L} = 148 \times 10^6\,\mathrm{km}^2$) is permanently or seasonally frozen or covered with snow and ice (Vaughan et al., 2013). In terms of land surface area, seasonally frozen ground (33 % of A_L), the highly variable seasonal snow cover (1.3-30.6 %), and terrestrial permafrost (9-12 %) dominate. The Antarctic and Greenland ice sheets add 9.5 %. The remaining land area is covered by lake and river ice (1.1 %) and glaciers (0.5 %). Furthermore, the Antarctic ice shelves and sea ice cover up to 5.7 % of the global ocean area ($A_\mathrm{O} = 363 \times 10^6\,\mathrm{km}^2$) during austral spring, whereas Arctic sea ice covers a maximum of about 3.9 % (of A_O) in boreal winter (Vaughan et al., 2013). The seasonal variations in snow and ice cover are considerably more pronounced on the Northern Hemisphere (NH, factor of 6 between winter and summer) than on the Southern Hemisphere (SH, factor of 2, Eamer et al., 2007).

The cryosphere supplies up to 80 % of the Earth's fresh water; up to 2 billion people directly depend on glacier-fed rivers. Beside their manifold socio-economic and ecological effects (e.g., Eamer et al., 2007; Bokhorst et al., 2016), the individual components of the cryosphere influence the global climate system on different timescales. Firstly, they play a fundamental role in determining the Earth's surface radiative energy budget, as snow and sea ice exhibit the highest surface albedo on Earth. Secondly, snow acts as an insulator due to its low thermal conductivity and, thereby, influences surface-atmosphere and ocean-atmosphere energy fluxes. The vast ice sheets of Antarctica and Greenland have influenced the Earth's climate over thousands to millions of years, but may have more rapid effects on the sea level. Their combined sea level equivalent is estimated to be in the range of 65 m (Vaughan et al., 2013). The large ice sheets imply global interactions and feedback mechanisms of snow and sea ice with the Earth's climate system, while glaciers as well as river and lake ice primarily impact ecosystems on a local scale. Similarly, permafrost influences the local soil water content and vegetation.

The climate system is invariably undergoing natural changes due to variations in: (a) the solar irradiance incident at the top of the atmosphere (TOA) caused by the variability of the Sun itself or by long-term changes of the Earth's orbit, (b) the planetary albedo due to, for example, volcanic eruptions, (c) the Earth's thermal emission in the terrestrial spectral range, and (d) internal climate variability and feedback mechanisms. However, since the beginning of the industrialization, the global climate has been unequivocally influenced by anthropogenic causes (Myhre et al., 2013), mainly due to increased emissions of greenhouse gases through fossil fuel combustion and land use change. Greenhouse gases, e.g., water vapor ($\mathrm{H_2O}$), carbon dioxide ($\mathrm{CO_2}$), and methane ($\mathrm{CH_4}$), absorb and re-emit terrestrial radiation originally emitted by the Earth's surface, thereby warming the atmosphere. This natural greenhouse effect (Arrhenius, 1896) is enhanced due to human activity. In 1750, the globally averaged abundance of CO_2 was 278 ppm based on ice core and firn measurements (Etheridge et al., 1996). It reached 403 ppm in 2016. On 23 May 2016, the last station on Earth (South Pole, Antarctica) measured a CO_2 concentration exceeding 400 ppm. As a result, the globally averaged combined land and ocean surface temperature increased by 0.85 K between 1880 and 2012 (Hartmann et al., 2013). This warming is spatially heterogeneous. For the Arctic, Overland et al. (2016) reported a temperature increase of 3 K for land stations north of 60° N since the beginning of the 20th century. In general, the Arctic has experienced an unprecedented, rapid warming in particular in the last 25 to 30 years; the near-surface air temperature exceeds the global warming by a factor of two to three (Wendisch et al., 2017) – a phenomenon which is referred to as Arctic Amplification. An amplified climate sensitivity of the Arctic region is a distinctive aspect of the Earth's climate system. It is evident in paleoclimatic records: temperature changes in the Arctic were three to four times stronger than for the NH for four intervals over the last three million years (both warmer and colder; Miller et al., 2010). Also, Arctic Amplification is consistently identified in coupled climate model simulations forced with increased greenhouse gas concentrations (e.g., Holland and Bitz, 2003).

The amplified Arctic warming could be the consequence of different feedback processes that are especially effective in the Arctic. Firstly, an initial warming would result in the melting of the highly reflective snow and sea ice, thereby exposing darker ocean and land surfaces. The corresponding increase in absorption of solar radiation leads to a warming of the land surface or the oceanic mixing layer, eventually increasing energy fluxes from the surface to the atmosphere and enhancing the initial warming (e.g., Hall, 2004; Winton, 2006; Serreze and Barry, 2011; Wendisch et al., 2017). Secondly, beside this surface albedo feedback, a decline or thinning of the thermally insulating sea-ice cover enhances the vertical heat fluxes between the Arctic ocean and the atmosphere (Screen and Simmonds, 2010). Thirdly, as a result of an ice-free and warmer oceanic mixing layer, more water vapor is evaporated which is then available for cloud development (Graversen and Wang, 2009). Clouds in the Arctic mainly warm the underlying surface due to the increase in downward terrestrial radiation (e.g., Francis and Hunter, 2006; Screen and Simmonds, 2010; Wendisch et al., 2013). According to Vavrus (2004), approximately 40 % of Arctic warming might result from increased cloudiness. Lastly, as discussed by Hansen and Nazarenko (2004), higher concentrations of soot particles on snow surfaces due to fossil burning and meridional transport can influence snow surface albedo. The higher abundance of black carbon and decreasing concentrations of sulphate aerosol particles in the atmosphere might additionally have contributed to the rapid warming in the Arctic (Shindell and Faluvegi, 2009). However, the dominant mechanisms behind Arctic Amplification still remain elusive and inconclusive. A more thorough understanding of the processes is required to disentangle the individual feedback mechanisms from the general warming signal.

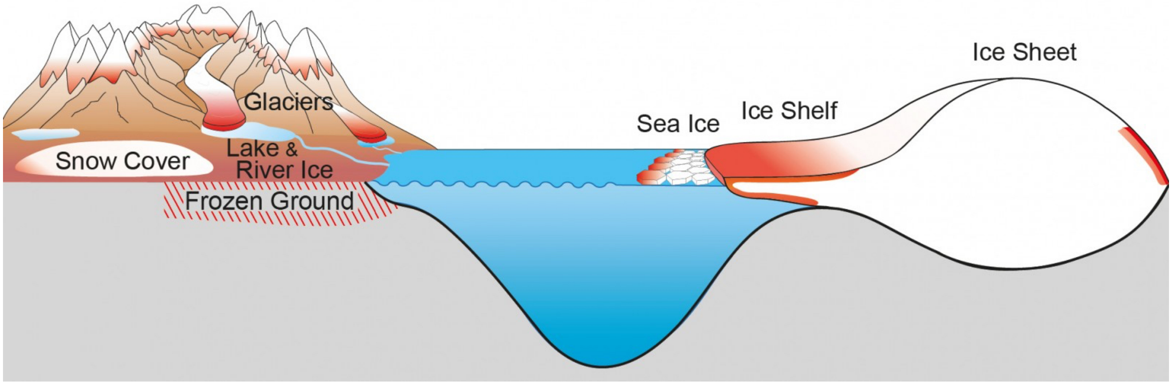

Figure 1.2: Components of the cryosphere and their observed response to climate change (Vaughan et al., 2013). Red colors illustrate melting or a decrease in extent.

Whilst influencing the climate on different spatial and temporal scales, the cryosphere is also a passive indicator of climate change, as snow and sea ice are inherently sensitive to changes in the near-surface air temperature as well as the amount and type of precipitation. Figure 1.2 illustrates the currently observed changes of the components of the cryosphere: frozen ground decreased in thickness by 32 cm since the 1930s; permafrost temperatures increased by up to 2 K within the same period; winter lake and river ice duration reduced on the NH, ice mass loss increased from glaciers outside Greenland and Antarctica ($0.76\,\mathrm{mm\,yr^{-1}}$ of sea-level equivalent between 1993 and 2009); and ice shelves and ice sheets in Greenland and Antarctica thinned and collapsed (e.g., Vaughan et al., 2013). The most cited proxy of cryospheric response to climate change is the decline in Arctic sea ice. The September 2016 minimum extent of Arctic sea ice ($4.14 \times 10^6\,\mathrm{km^2}$) was 33 % lower than the average minimum sea ice extent between 1981 and 2010 (Overland et al., 2016). At the same time, Kwok and Rothrock (2009) recorded substantial losses of the average Arctic sea ice thickness in winter from 3.6 m to 1.9 m. Lindsay and Schweiger (2015) reported a reduction in sea ice thickness of up to 65 % between 1975 and 2012. Notz and Stroeve (2016) could link the September sea-ice area to the cumulative CO_2 emissions since 1850. Beside enhanced melting due to increasing temperatures, also changing wind patterns can explain about one third of the downward linear trend of Arctic sea ice cover over the past 31 years (Ogi et al., 2010).

The response of snow cover to the changing climate parameters is complex. According to simulations with global climate models, on the colder side of the -20 °C isotherm in late 20th century November-March mean near-surface air temperature, snow cover is likely to increase due to enhanced precipitation (Räisänen, 2008). However, on the warmer side, the more efficient snow melt dominates and reduces snow cover. Brown et al. (2010) estimated a decrease in Arctic snow covered area of 46 % in June and 14 % in May based on microwave satellite observations and reconstructed snow cover estimates. The National Oceanic and Atmospheric Administration (NOAA) historical satellite record shows an anomalous annual increase in snow cover over Eurasia in October. This could be a result of the persistent decrease in winter surface air temperature in central Eurasia over the last 25 years, but Brown and Derksen (2013) and Mudryk et al. (2017) found the NOAA dataset to be subject to internal mapping trends and, thus, concluded that the observed snow cover increase is not significant.

It has been suggested that the cooling over central Eurasia was related to sea-ice loss in the Barents-Kara Sea. However, McCusker et al. (2016) assessed this relation to be unlikely and explained the cooling with sea-ice independent, internally generated circulation patterns over the Barents-Kara Sea. This is one example of possible teleconnections between Arctic warming and mid-latitude weather. Arctic Amplification probably influences NH mid-latitude weather by changing storm tracks, the polar jet stream, and planetary wave activity (directly or indirectly through stratospheric linkages, Cohen et al., 2014). However, to disentangle the influence of Arctic Amplification from natural variability and climate change outside the Arctic is a complex and ongoing challenge (e.g., Overland et al., 2016).

The amplification mechanisms are not restricted to the Arctic but observed and projected warming are considerably weaker in Antarctica (Salzmann, 2017). Coupled climate models from the Coupled Model Intercomparison Project phase 5 (CMIP5) estimated surface air temperature anomalies of 4.2 ± 1.6 K in the Arctic and 1.5 ± 0.7 K in Antarctica for the years of 2081-2100 relative to the 1986-2005 baseline time period in the RCP4.5 scenario (Collins et al., 2013). A weaker Antarctic surface albedo feedback (Manabe and Stouffer, 1980), more efficient ocean heat uptake in the Southern Ocean together with Antarctic ozone depletion (Masson-Delmotte et al., 2013), and different responses of this heat uptake to ozone and greenhouse gas forcing in the Arctic and Antarctica (Marshall et al., 2014) seem to contribute to this polar amplification asymmetry. Furthermore, the high elevation of the Antarctic ice sheet (on average above 2 km a.s.l.) plays a major role: Salzmann (2017) performed CO_2-doubling ex-

periments with a coupled climate model and found the polar amplification to become considerably more symmetric when assuming Antarctica to be a low-level plateau.
Accordingly, Antarctica experienced less warming compared to the Arctic except for the Antarctic Peninsula (3.7 ± 1.6 K per century, Vaughan et al., 2003) and the West Antarctic ice sheet (0.1 K per decade over last 50 years, Steig et al., 2009). On the contrary, recent findings suggest that the Antarctic Peninsula is not warming that much. Turner et al. (2016) found a cooling of -0.5 K per decade since the late 1990s over the Peninsula, however these authors state that both the observed warming and cooling are consistent with natural variability. The interior of the Antarctic continent is suspected to have cooled slightly. Due to the low temperatures, nearly no surface melting takes place except from parts of the Peninsula and on the coast. Between August 2006 and April 2011, the mean snowfall rate on the Antarctic ice sheet (north of 82° S) was about 171 mm water equivalent per year (Palerme et al., 2014). Antarctic snowfall is predicted to increase in a warmer climate (Church et al., 2013).
In contrast to the Arctic, the Antarctic sea-ice extent increased slightly (Parkinson and DiGirolamo, 2016). Strong katabatic wind patterns, more precipitation over the Antarctic ice zone, higher salinity of the surface water in the Southern Ocean, and the influence of westerlies on the sea ice, which extends well into 55° S, are possible explanations for the differences in sea ice trends between the northern and southern hemispheres (Simmonds, 2015). No link between increasing Antarctic sea ice extent and stratospheric ozone depletion in the SH was found by Sigmond and Fyfe (2010). However, in 2016 an unprecedented decline in Antarctic sea ice extent was observed. Turner et al. (2017) attributed this special event to surface pressure anomalies.

2 Physical background and definitions

Ice crystals in the atmosphere that grow sufficiently large to fall are deposited on the ground as snow. Snow is a porous medium and consists of different components: ice, air, impurities, and liquid water if the snow is wet. In the first part of this chapter, microphysical and macroscopic properties of a snow layer are described. Subsequently, the optical properties of a snow layer are characterized. Microstructural parameters are defined following the notation in Fierz et al. (2009). For the definition of reflectance quantities and optical properties used within this study, it is referred to Schaepman-Strub et al. (2006) and Wendisch and Yang (2012).

2.1 Microphysical and macroscopic properties of a snow layer

2.1.1 Formation of solid precipitation

One liter of cloudy air typically contains 10^6 cloud droplets with diameters in the order of 10 µm, whereas the same volume contains just one raindrop with a diameter of around 1 mm (Wallace and Hobbs, 2006). Warm rain formation through collision, coalescence, and condensation growth can occur in the tropics. However, around 80 % of the global precipitation is formed at temperatures below 0 °C involving the ice phase. The specific type of precipitation is then defined by the vertical temperature profile of the atmosphere below the cloud. Due to the energy barrier characterizing the phase transition of freezing, liquid water droplets can still exist below 0 °C and the process of freezing always requires nucleation. Homogeneous nucleation of a supercooled droplet describes a stochastic process in the pure liquid water phase in the absence of a foreign substance at temperatures below around -38 °C and, thus, is relevant mainly in the upper troposphere. Below this temperature limit, freezing is initiated via the catalysis by a foreign body (e.g., Cantrell and Heymsfield, 2005), which acts as an ice nucleating particle (INP). Examples for suitable INPs are mineral dust, metal oxides, organics, and soot (Kanji et al., 2017). This heterogeneous freezing occurs through different

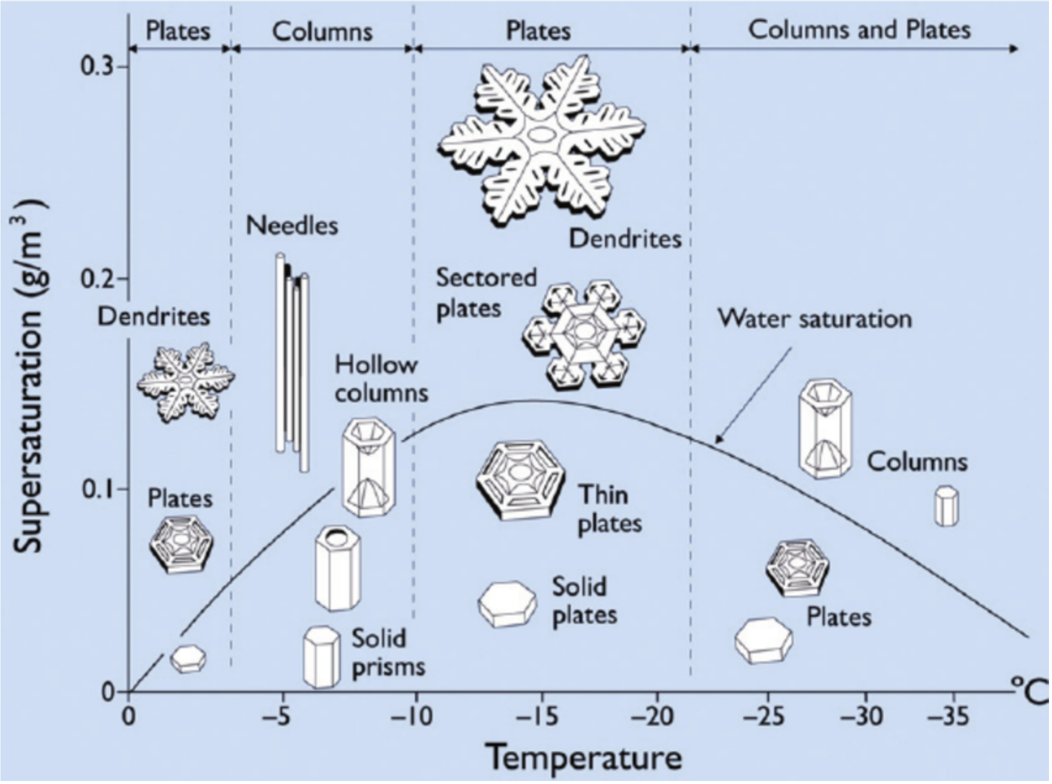

Figure 2.1: Morphology diagram showing the growth of snow crystals at atmospheric pressure as a function of temperature and water vapor supersaturation relative to the equilibrium water vapor pressure over ice (morphology diagram, Libbrecht, 2005).

modes such as condensation freezing, immersion freezing or contact freezing.

The resulting ice crystal habit is mainly influenced by the ambient temperature and the water vapor supersaturation relative to the equilibrium water vapor pressure over ice. Figure 2.1 shows the corresponding snow crystal morphology diagram based on laboratory studies (Nakaya, 1954).

With decreasing temperature, the crystal habit transforms from plates to columns (at around -3 °C) to plates (at -10 °C) to predominantly columns ($T < -30$ °C). The complexity of the structure is mainly determined by the amount of supersaturation (Libbrecht, 2005). During freezing, water molecules arrange in a crystal lattice with fixed positions for the oxygen atoms and the hydrogen atoms providing the bonds. The resulting lattice exhibits a hexagonal symmetry in the basal plane (LaChapelle, 1969).

2.1.2 Metamorphism in deposited snow

The snow crystals deposited on the surface experience constant evolution through the sublimation and subsequent redeposition of water molecules. From the viewpoint of material science and under terrestrial conditions, snow is a hot medium due to its high temperatures close to the melting point of water. Consequently, the high homologous temperature and high vapor pressure give rise to sintering and recrystallization processes that are called snow metamorphism (e.g., Colbeck, 1997; Kaempfer and Schneebeli, 2007). Thus, as snow ages, the grains become larger and more spherical (Colbeck, 1983; Kaempfer and Schneebeli, 2007). From a thermodynamic point of view, freshly fallen snow crystals have unstable shapes (LaChapelle, 1969). The often dendritic structure results in a large ratio of surface area to volume and, thus, large surface free energy. According to the second law of thermodynamics, the snow crystals change in order to minimize the surface free energy with the ideal shape being a sphere. Note that snow metamorphism is also effective below the freezing temperature. It mainly depends on snow microstructure, snow temperature, and its vertical gradient within the snowpack.

If no local, mainly vertical temperature gradient exists in the snowpack below the freezing level, the reduction of the surface free energy by mass redistribution is the dominant process and the metamorphism is described as isothermal (Kaempfer and Schneebeli, 2007). The destructive nature of isothermal metamorphism is illustrated in Fig. 2.2.

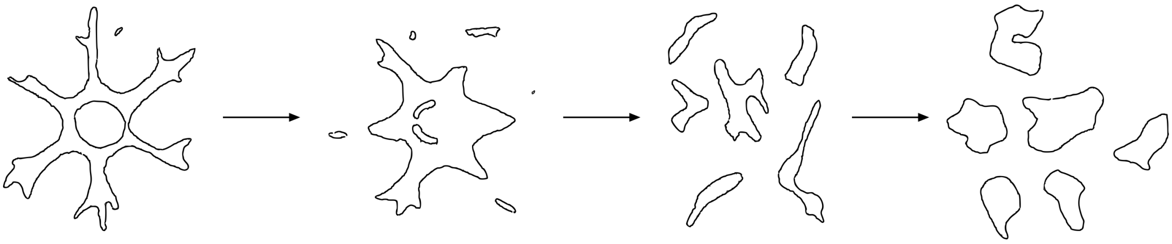

Figure 2.2: Sketch of isothermal metamorphism (adapted from LaChapelle, 1969). The original, dendritic ice crystal fragments and forms rounded ice grains.

The branches of the dendritic crystal break leading to several ice grains that become rounded particles of ice. Whereas grain size diminishes in the early stages of fragmentation, it increases during the growth of the rounded ice grains. In nature, only the center of the polar ice shields provide conditions for long-term isothermal metamorphism (Arnaud et al., 1998).

The temperature-gradient metamorphism prevails when the local temperature gradients exceed about 0.1 $\mathrm{K\,cm^{-1}}$ (LaChapelle, 1969) and is characterized by the sublimation of the warmest parts of the snow grains and its deposition on the coldest parts through water vapor transport across the interstitial air pores (e.g., Yosida et al., 1955; Colbeck, 1983; Flin and Brzoska, 2008; Calonne et al., 2014). Local temperature gradients develop through the difference in atmospheric temperature close to the snow surface and the ground temperature beneath the snowpack which is fairly constant at around 0 °C. This would result into matter transport from the bottom to the top of the snowpack. However, the temperature gradient and its direction can change within the snowpack. Calonne et al. (2014) observed grain growth as well as the faceting of the bottom parts and rounding of the upper parts of the crystals as a result of temperature-gradient metamorphism using 3-dimensional X-ray tomography of snow samples in the laboratory.

2.1.3 Snow layer microstructure

It is known from visual observation that the size of snow crystals and grains may vary from 0.05 up to at least 10 mm. The physical size of a snow grain E is traditionally defined by the length of the largest extension of a snow grain (Fierz et al., 2009; Leppänen et al., 2015), which causes ambiguities due to the complex shapes of snow grains. Figure 2.3 a shows a photograph of snow crystals under a magnifying glass taken in Sodankylä, Finland. The large variability of the snow grain sizes and shapes likely causes an observer-related bias in the estimation of E (Leppänen et al., 2015). Therefore, the snow grain size is introduced via the optical-equivalent grain size defined as the radius R_{opt} of a collection of spheres with the same total volume and surface area compared to the actual nonspherical snow grain of volume V and surface area A (Grenfell and Warren, 1999; Neshyba et al., 2003). The volume-to-surface ratio of these spheres is equal to that of the nonspherical particle. For a sphere, the ratio V/A is equal to one third of its radius. Thus, the optical-equivalent grain size is defined as

$$R_{\text{opt}} = 3\,\frac{V}{A} = 3\,\frac{m}{\rho_{\text{ice}} \cdot A}\,, \tag{2.1}$$

with the mass of the nonspherical snow grain m and the density of ice ρ_{ice} (917 kg m^{-3}). Figure 2.3 illustrates the concept of the optical-equivalent grain size in contrast to the traditional grain size.

Note that in order to conserve the mass, a collection of equivalent spheres which radii follow Eq. (2.1) is needed to represent a single nonspherical particle. Similar to the concept of the effective droplet radius of a cloud, optical measurements assign a single value $R_{\text{opt,eff}}$ representative for the polydisperse size distribution of snow grains of a snow layer with total volume V_{tot} and surface area A_{tot}:

$$R_{\text{opt,eff}} = 3\,\frac{V_{\text{tot}}}{A_{\text{tot}}}\,. \tag{2.2}$$

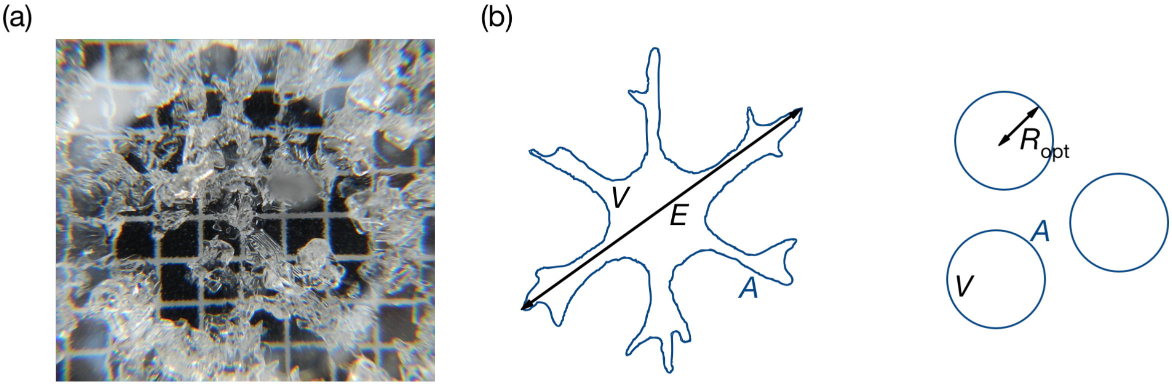

Figure 2.3: (a) Photograph of ensemble of snow grains under a magnifying glass against a 1 mm reference grid. The snow grains were collected at Sodankylä, Finland, on 13 February 2017. **(b)** Definition and concept of traditional and optical-equivalent snow grain size (partly adapted from LaChapelle, 1969).

Strictly speaking, all values R_{opt} that stem from optical measurements within this work are effective quantities of a snow layer based on Eq. (2.2). For reasons of lucidity, the notion of effective is omitted in the remainder of this thesis.

From Eq. 2.1, the specific surface area (surface area of ice–air interface per unit mass, A/m) is related to the optical radius of the snow grains and the density of ice by

$$\mathrm{SSA} = \frac{3}{\rho_{\mathrm{ice}} \cdot R_{\mathrm{opt}}}. \tag{2.3}$$

SSA (in units of $\mathrm{m}^2\,\mathrm{kg}^{-1}$) is measured with techniques such as methane adsorption (e.g., Domine et al., 2001; Legagneux et al., 2002), stereology (e.g., Matzl and Schneebeli, 2010), and X-ray microtomography (e.g., Flin et al., 2005; Kaempfer and Schneebeli, 2007). These methods are difficult to employ in the field. Therefore, optical measurements that utilize the spectral absorption of snow grains are applied in field studies (e.g., Gallet et al., 2009) for the in situ measurement of SSA. However, they are restricted to single observation sites. Consequently, longer time series of SSA are scarce in remote Arctic and Antarctic areas.

2.1.4 Macroscopic surface roughness

The interplay of wind and moving snow particles leads to the formation of surface features of variable shapes and dimensions. These aeolian features are the result of both snow deposition and erosion. The transport of snow particles is governed mainly by saltation and creep (Filhol and Sturm, 2015). If the turbulent shear stress exerted by the wind surpasses the gravitational and interparticular forces, snow particles are

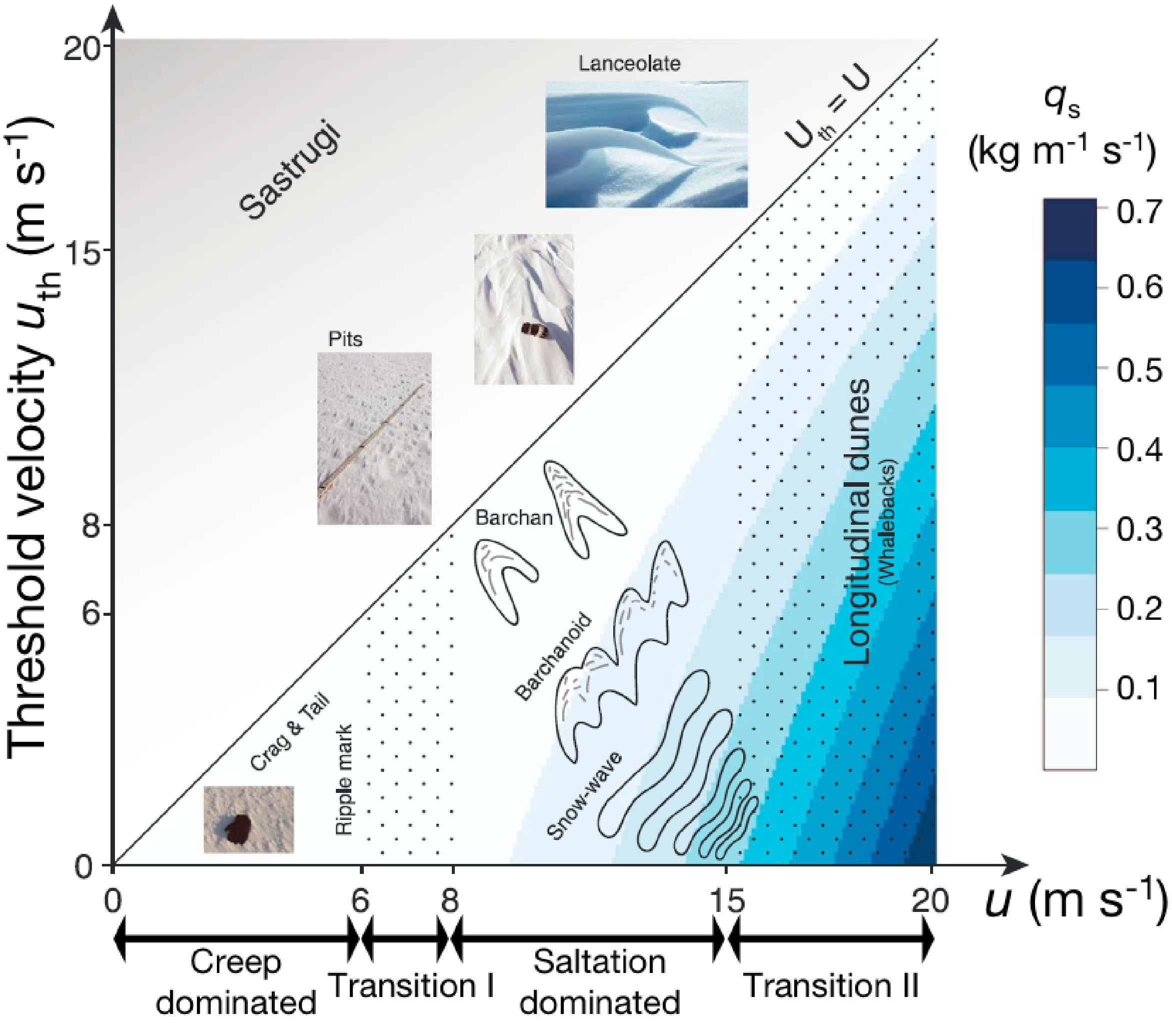

Figure 2.4: Classification of snow bedforms with respect to the average horizontal wind speed u, the average threshold horizontal wind velocity u_{th}, and the flux of saltating snow q_{s} in shades of blue (modified, Filhol and Sturm, 2015).

lifted from the ground. The mode of saltation describes the downwind motion of airborne particles that fall and repeatedly bounce off the ground. Thereby, other particles become airborne and add to the saltating flux. At wind speeds of around $10\,\mathrm{m\,s^{-1}}$, 80-90 % of the moving snow is saltating (Kobayashi, 1972). The second mode of transport, creep, describes the rolling or sliding of particles at the surface due to wind or the impact of other grains entrained by the wind.

Figure 2.4 classifies snow bedforms with respect to the average horizontal wind speed u, the average threshold horizontal wind velocity u_{th} (both in $\mathrm{m\,s^{-1}}$), and the saltation flux q_{s} (in $\mathrm{kg\,m^{-1}\,s^{-1}}$). If the average horizontal wind speed outweighs the threshold wind speed ($u > u_{\mathrm{th}}$), a saturated saltation flux is maintained and aeolian features of depositional type such as ripples (creep dominated), snow dunes like barchans and snow waves (saltation dominated) or longitudinal dunes form depending on the flux q_s. Conversely, for $u < u_\mathrm{th}$, erosional features like sastrugi prevail (Filhol and Sturm, 2015).

There are apparent similarities between snow bedforms and those made of sand. However, whereas both develop through analogous transport mechanisms, the key difference is the ability of snow to sinter, i.e., the snow particles can form bonds with each other. Sintering can harden and seal the snow surface within hours. Thus, snow dune growth is limited and snow dunes (height rarely above 1 m) are generally much smaller compared to sand dunes that may reach heights of 100 m as a result of continuous growth over centuries. Snow sintering immobilizes the bedform which is then subject to erosion. Therefore, the most common snow bedform are erosional features such as sastrugi.

The macroscopic roughness as a result of snow bedforms influences the radiative properties of snow surfaces by casting shadows and changing the effective incidence angle of the solar radiation. In addition, roughness structures modify the exchange of air between the atmosphere and the firn thereby affecting the paleoclimatologic interpretation of ice cores (Birnbaum et al., 2010).

2.2 Definition of basic radiative and angular reflectance quantities

The spectral radiant energy flux $\mathit{\Phi}_\lambda$ (units of $\mathrm{W\,nm^{-1}}$) is defined as the radiant energy E_rad passing through the infinitesimal area element d^2A within the wavelength range $\lambda + \mathrm{d}\lambda$ and time interval $t + \mathrm{d}t$ at time t and location $\vec{\boldsymbol{r}}$:

$$\mathit{\Phi}_\lambda\left(\vec{\boldsymbol{r}}, t\right) = \frac{\mathrm{d}^2 E_\mathrm{rad}}{\mathrm{d}t\,\mathrm{d}\lambda}. \tag{2.4}$$

The normalization with respect to the area element d^2A yields the spectral radiant energy flux density

$$F_\lambda\left(\vec{\boldsymbol{r}}, t\right) = \frac{\mathrm{d}^2\mathit{\Phi}_\lambda}{\mathrm{d}^2A} = \frac{\mathrm{d}^4 E_\mathrm{rad}}{\mathrm{d}t\,\mathrm{d}\lambda\,\mathrm{d}^2A}. \tag{2.5}$$

F_λ is also called spectral irradiance and has the units $\mathrm{W\,m^{-2}\,nm^{-1}}$. It quantifies the spectral radiant energy flux from the entire hemisphere through a unit area.

The corresponding spectral radiance I_λ (units of $\mathrm{W\,m^{-2}\,nm^{-1}\,sr^{-1}}$) is defined as the radiant energy that is confined within a solid angle element $\mathrm{d}^2\mathit{\Omega}$ and pointing along the direction $\hat{\boldsymbol{s}}$. The geometry for the definition of the spectral radiance is shown in

Fig. 2.5. The spectral radiance is defined by

$$I_\lambda(\vec{\boldsymbol{r}}, \hat{\boldsymbol{s}}, t) = \frac{\mathrm{d}^4\varPhi_\lambda}{\mathrm{d}^2 A_\perp \, \mathrm{d}^2\varOmega} = \frac{\mathrm{d}^6 E_\mathrm{rad}}{\cos\theta \, \mathrm{d}t \, \mathrm{d}\lambda \, \mathrm{d}^2 A \, \mathrm{d}^2\varOmega}. \tag{2.6}$$

θ represents the angle between the normal unit vector $\hat{\boldsymbol{n}}$ of the area element $\mathrm{d}^2 A$ and the direction of propagation $\hat{\boldsymbol{s}}$ of the radiation, whereas $\mathrm{d}^2 A_\perp$ denotes the projection of the area element onto a plane perpendicular to $\hat{\boldsymbol{s}}$ (see Fig. 2.5). Note that within a nonabsorptive medium the radiance is invariant along the propagation of radiant energy, whereas the corresponding irradiance is inversely proportional to the square of the distance to the source.

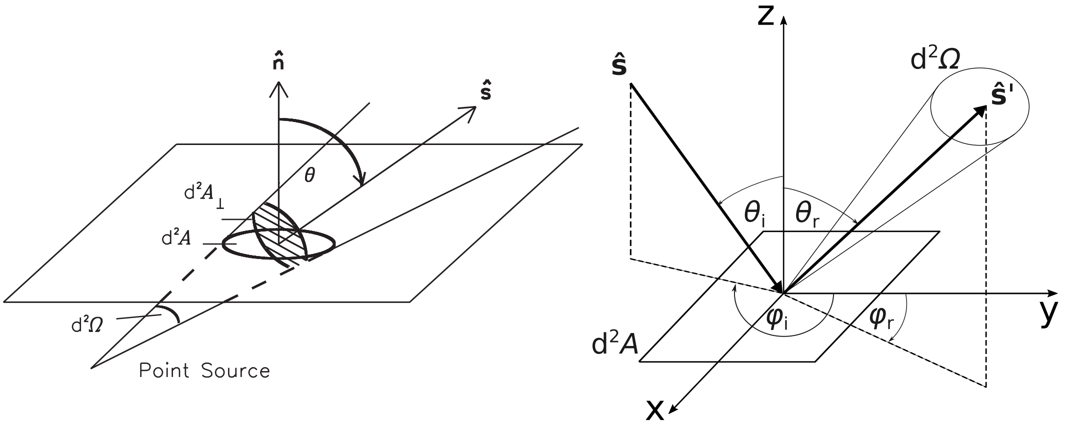

Figure 2.5: Left: Geometry for the definition of radiance (Wendisch and Yang, 2012). Right: Illustration of incident $(\hat{\boldsymbol{s}}, \theta_\mathrm{i}, \varphi_\mathrm{i})$ and reflection $(\hat{\boldsymbol{s}}', \theta_\mathrm{r}, \varphi_\mathrm{r})$ geometry.

From the integration of the spectral radiance over the upper or the lower hemisphere, the downward irradiance $F_\lambda^\downarrow$ or, respectively, the upward irradiance $F_\lambda^\uparrow$ are obtained by

$$F_\lambda^\downarrow(\vec{\boldsymbol{r}}, t) = -\int_0^{2\pi}\int_{\pi/2}^{\pi} I_\lambda(\vec{\boldsymbol{r}}, \theta, \varphi, t) \cdot \cos\theta \cdot \sin\theta \, \mathrm{d}\theta \, \mathrm{d}\varphi \,, \tag{2.7}$$

$$F_\lambda^\uparrow(\vec{\boldsymbol{r}}, t) = \int_0^{2\pi}\int_0^{\pi/2} I_\lambda(\vec{\boldsymbol{r}}, \theta, \varphi, t) \cdot \cos\theta \cdot \sin\theta \, \mathrm{d}\theta \, \mathrm{d}\varphi. \tag{2.8}$$

Equations 2.7 and 2.8 assume a unit area on a horizontal reference plane. The irradiance comprises a direct (radiation that is not scattered) and a diffuse component scattered within the atmosphere due to gases, aerosol particles, and clouds.

In the following, reflectance quantities are defined based on the geometry illustrated in Fig. 2.5. The incident beam, impinging on the surface in the direction $\hat{\boldsymbol{s}}$ with the

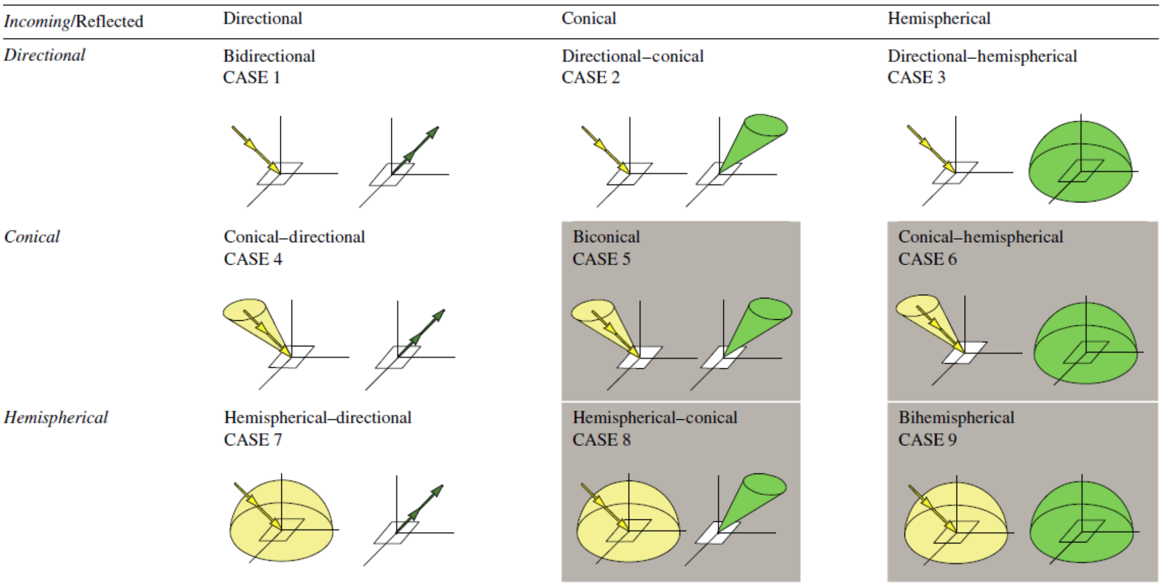

Figure 2.6: Reflectance quantities and relation of incoming and reflected radiance terminology (Schaepman-Strub et al., 2006).

zenith angle θ_i and azimuth angle φ_i is reflected into direction $\hat{\boldsymbol{s}}'$ with zenith and azimuth angles θ_r and φ_r.

The dimensionless reflectance is defined as:

$$\rho\left(\theta_\mathrm{i}, \varphi_\mathrm{i}; \theta_\mathrm{r}, \varphi_\mathrm{r}; \lambda\right) = \frac{\mathrm{d}\Phi_\mathrm{r}\left(\theta_\mathrm{i}, \varphi_\mathrm{i}; \theta_\mathrm{r}, \varphi_\mathrm{r}; \lambda\right)}{\mathrm{d}\Phi_\mathrm{i}\left(\theta_\mathrm{i}, \varphi_\mathrm{i}; \theta_\mathrm{r}, \varphi_\mathrm{r}; \lambda\right)} \tag{2.9}$$

The intrinsic reflectance properties of a surface are given by its bidirectional reflectance distribution function (BRDF). It quantifies the reflection of the incident radiation at the surface and its scattering from one direction into another direction of the hemisphere. Figure 2.6 shows the terminology used for describing different reflectance quantities. It illustrates that integration of the BRDF (case 1 in Fig. 2.6) over the respective range of solid angles gives the conical or hemispherical quantities (cases 2 to 9).

The spectral BRDF, denoted using the symbol f_BRDF, gives for each illumination geometry of incident direct irradiance $F_\mathrm{i}\left(\theta_\mathrm{i}, \varphi_\mathrm{i}; \lambda\right)$ the reflected radiance for all reflection angles $I_\mathrm{r}\left(\theta_\mathrm{i}, \varphi_\mathrm{i}; \theta_\mathrm{r}, \varphi_\mathrm{r}; \lambda\right)$ by

$$f_\mathrm{BRDF} = \frac{\mathrm{d}I_\mathrm{r}\left(\theta_\mathrm{i}, \varphi_\mathrm{i}; \theta_\mathrm{r}, \varphi_\mathrm{r}; \lambda\right)}{\mathrm{d}F_\mathrm{i}\left(\theta_\mathrm{i}, \varphi_\mathrm{i}; \lambda\right)} \tag{2.10}$$

The BRDF is dimensionless, non-negative, and fulfills the Helmholtz reciprocity. However, as a ratio of infinitesimal quantities, it is purely conceptual and cannot be measured.

A reflectance factor is obtained when the radiant flux reflected by a sample surface is divided by the radiant flux reflected by an ideal (lossless) and diffuse (Lambertian) standard surface into the identical beam geometry when illuminated under the same conditions. This way, the bidirectional reflectance factor (BRF) and the hemispherical-directional reflectance factor (HDRF, case 7 in Fig. 2.6) can be defined. The BRF is given by

$$f_{\mathrm{BRF}} = \frac{\mathrm{d}\Phi_{\mathrm{r}}\left(\theta_{\mathrm{i}},\varphi_{\mathrm{i}};\theta_{\mathrm{r}},\varphi_{\mathrm{r}}\right)}{\mathrm{d}\Phi_{\mathrm{r}}^{\mathrm{ideal}}\left(\theta_{\mathrm{i}},\varphi_{\mathrm{i}}\right)} = \frac{\mathrm{d}I_{\mathrm{r}}\left(\theta_{\mathrm{i}},\varphi_{\mathrm{i}};\theta_{\mathrm{r}},\varphi_{\mathrm{r}}\right)}{\mathrm{d}F_{\mathrm{i}}\left(\theta_{\mathrm{i}},\varphi_{\mathrm{i}}\right)} \cdot \frac{\mathrm{d}F_{\mathrm{i}}\left(\theta_{\mathrm{i}},\varphi_{\mathrm{i}}\right)}{\mathrm{d}I_{\mathrm{r}}^{\mathrm{ideal}}\left(\theta_{\mathrm{i}},\varphi_{\mathrm{i}}\right)} = \pi \cdot f_{\mathrm{BRDF}}. \tag{2.11}$$

In Eq. 2.11 and in the remainder of this section, the spectral dependance is omitted for reasons of simplicity. However, note that all definitions describe spectral quantities.
The definition of the HDRF is analogous to the BRF but includes irradiance from the entire hemisphere:

$$\begin{aligned} f_{\mathrm{HDRF}} &= \frac{\mathrm{d}\Phi_{\mathrm{r}}\left(\theta_{\mathrm{i}},\varphi_{\mathrm{i}},2\pi;\theta_{\mathrm{r}},\varphi_{\mathrm{r}}\right)}{\mathrm{d}\Phi_{\mathrm{r}}^{\mathrm{ideal}}\left(\theta_{\mathrm{i}},\varphi_{\mathrm{i}},2\pi\right)} = \frac{\mathrm{d}I_{\mathrm{r}}\left(\theta_{\mathrm{i}},\varphi_{\mathrm{i}},2\pi;\theta_{\mathrm{r}},\varphi_{\mathrm{r}}\right)}{\mathrm{d}I_{\mathrm{r}}^{\mathrm{ideal}}\left(\theta_{\mathrm{i}},\varphi_{\mathrm{i}},2\pi\right)} \\ &= f_{\mathrm{BRF}}(\theta_0,\varphi_0;\theta_{\mathrm{r}},\varphi_{\mathrm{r}}) \cdot f_{\mathrm{dir}} + f_{\mathrm{BRF}}(2\pi;\theta_{\mathrm{r}},\varphi_{\mathrm{r}}) \cdot \left(1 - f_{\mathrm{dir}}\right). \end{aligned} \tag{2.12}$$

f_{dir} denotes the fraction of direct radiant flux (i.e. $f_{\mathrm{dir}} \in [0,1]$).
The additional integration over all reflection angles leads to the bihemispherical reflectance (BHR), generally called albedo α:

$$\begin{aligned} \alpha = f_{\mathrm{BHR}} = \rho\left(\theta_{\mathrm{i}},\varphi_{\mathrm{i}},2\pi;2\pi\right) &= \frac{\mathrm{d}\Phi_{\mathrm{r}}\left(\theta_{\mathrm{i}},\varphi_{\mathrm{i}},2\pi;2\pi\right)}{\mathrm{d}\Phi_{\mathrm{i}}\left(\theta_{\mathrm{i}},\varphi_{\mathrm{i}},2\pi\right)} \\ &= \rho\left(\theta_0,\varphi_0;2\pi\right) \cdot f_{\mathrm{dir}} + \rho\left(2\pi;2\pi\right) \cdot \left(1 - f_{\mathrm{dir}}\right). \end{aligned} \tag{2.13}$$

As each instrument measures the incoming radiation related to a certain field of view (FOV), the only measurable quantities illustrated in Fig. 2.6 are cases 5, 6, 8, and 9 (shaded gray) with conical or hemispherical viewing geometry. However, if the HDRF is constant over the full cone angle of the instrument's FOV, then the hemispherical-conical reflectance factor (HCRF) equals the HDRF.

2.3 Optical properties of a snow layer

Electromagnetic (EM) radiation impinging on a particle is scattered, absorbed and re-emitted. The emission is closely related to the process of absorption, especially in the infrared part of the EM spectrum. The interaction of EM radiation with an individual particle is determined by its inherent optical properties: the complex index of reflection

$\tilde{n}$, the extinction cross section C_{ext}, the single-scattering albedo $\tilde{\omega}$, the phase function $\mathcal{P}$, and the asymmetry parameter g. Averaging the individual optical properties over the particle size distribution of a small volume element yields the volumetric (bulk) optical properties. The apparent optical properties of a snow layer, e.g. its spectral surface albedo and HDRF, depend both on the inherent optical properties and the geometry of the incident and viewing directions.

2.3.1 Single-scattering properties

Complex index of refraction

The scattering of an electromagnetic (EM) wave at an ice crystal is determined, among others, by the complex index of refraction $\tilde{n}$ of ice that is defined as

$$\tilde{n} = \tilde{n}_{\mathrm{re}} + \tilde{n}_{\mathrm{im}} \cdot \mathrm{i} \tag{2.14}$$

where $\mathrm{i} = \sqrt{-1}$. The real part $\tilde{n}_{\mathrm{re}}$ gives the ratio of the phase speed of the EM wave within the enclosing medium to the phase speed within the ice particle. The rate of absorption of the EM wave within the ice crystal is determined by the imaginary part $\tilde{n}_{\mathrm{im}}$.

Figure 2.7 shows the EM wavelength spectrum of the imaginary part $\tilde{n}_{\mathrm{im}}$ between 300 and 2500 nm wavelength based on the data from Warren and Brandt (2008). From the visible (VIS, 370-750 nm) to the near infrared (NIR, 750-2000 nm) part of the spectrum, $\tilde{n}_{\mathrm{im}}$ increases over several orders of magnitude. Thus, ice absorption is small in the VIS and becomes increasingly dominant in the NIR.

Optical cross sections

Optical cross sections (in units m^2)describe the efficiency of the interaction (extinction, absorption, scattering) of an individual particle with EM radiation. They are defined as the ratio of radiant energy flux $\varPhi$ that is subject to extinction, absorption, or scattering to the incident irradiance F_{inc}:

$$C_{\mathrm{ext}} = \frac{\varPhi_{\mathrm{ext}}}{F_{\mathrm{inc}}}\,, \tag{2.15}$$

$$C_{\mathrm{abs}} = \frac{\varPhi_{\mathrm{abs}}}{F_{\mathrm{inc}}}\,, \tag{2.16}$$

$$C_{\mathrm{sca}} = \frac{\varPhi_{\mathrm{sca}}}{F_{\mathrm{inc}}}\,. \tag{2.17}$$

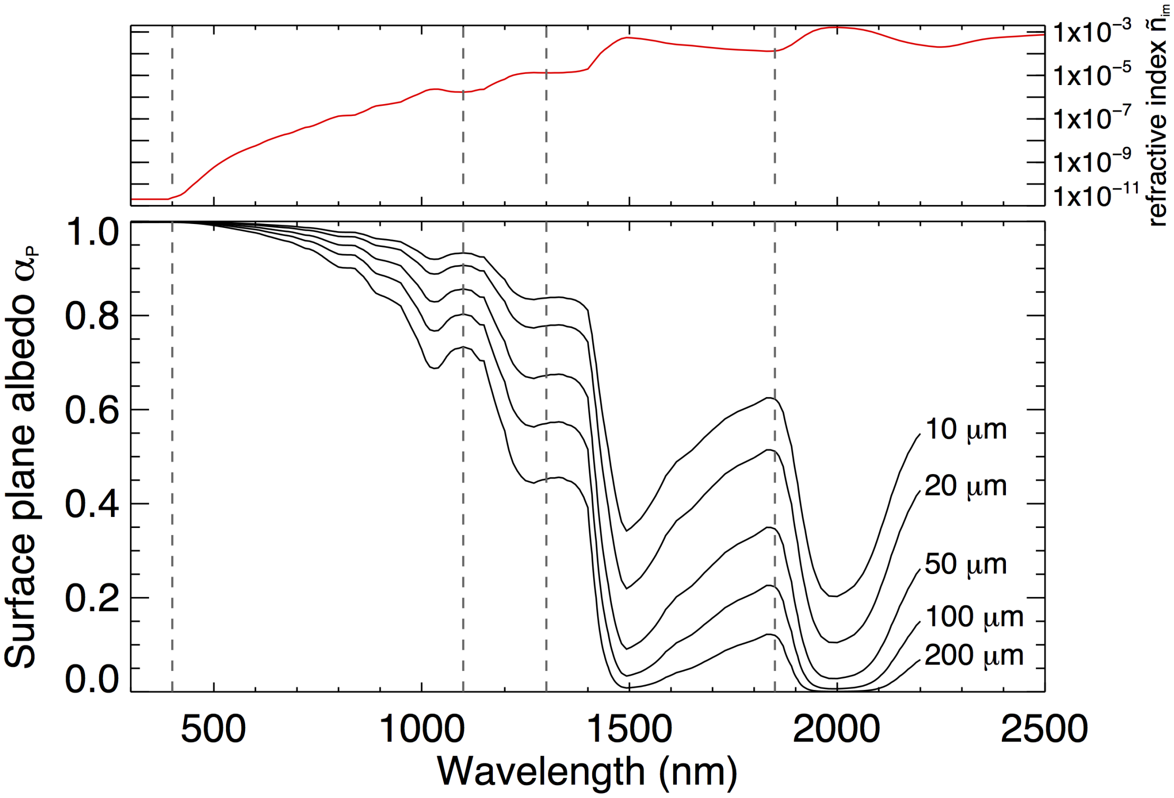

Figure 2.7: Top: Spectrum of the imaginary part $\tilde{n}_{\text{im}}$ of the complex refractive index of ice $\tilde{n}$ based on data by Warren and Brandt (2008). **Bottom:** Surface plane albedo for optical snow grain sizes between 10 and 200 µm; solar zenith angle $\theta_0 = 60°$. Vertical dashed lines at 400, 1100, 1300, and 1850 nm wavelength.

As extinction combines absorption and scattering, the corresponding extinction cross section C_{ext} is given by,

$$C_{\text{ext}} = C_{\text{abs}} + C_{\text{sca}} \tag{2.18}$$

Single-scattering albedo

The dimensionless single-scattering albedo $\tilde{\omega}$ quantifies the relative contribution of scattering or absorption to the total extinction:

$$\tilde{\omega} = \frac{C_{\text{sca}}}{C_{\text{ext}}} = \frac{C_{\text{sca}}}{C_{\text{abs}} + C_{\text{sca}}} \tag{2.19}$$

$\tilde{\omega}$ is confined within the limits of non-scattering ($\tilde{\omega} = 0$) and non-absorbing particles ($\tilde{\omega} = 1$).

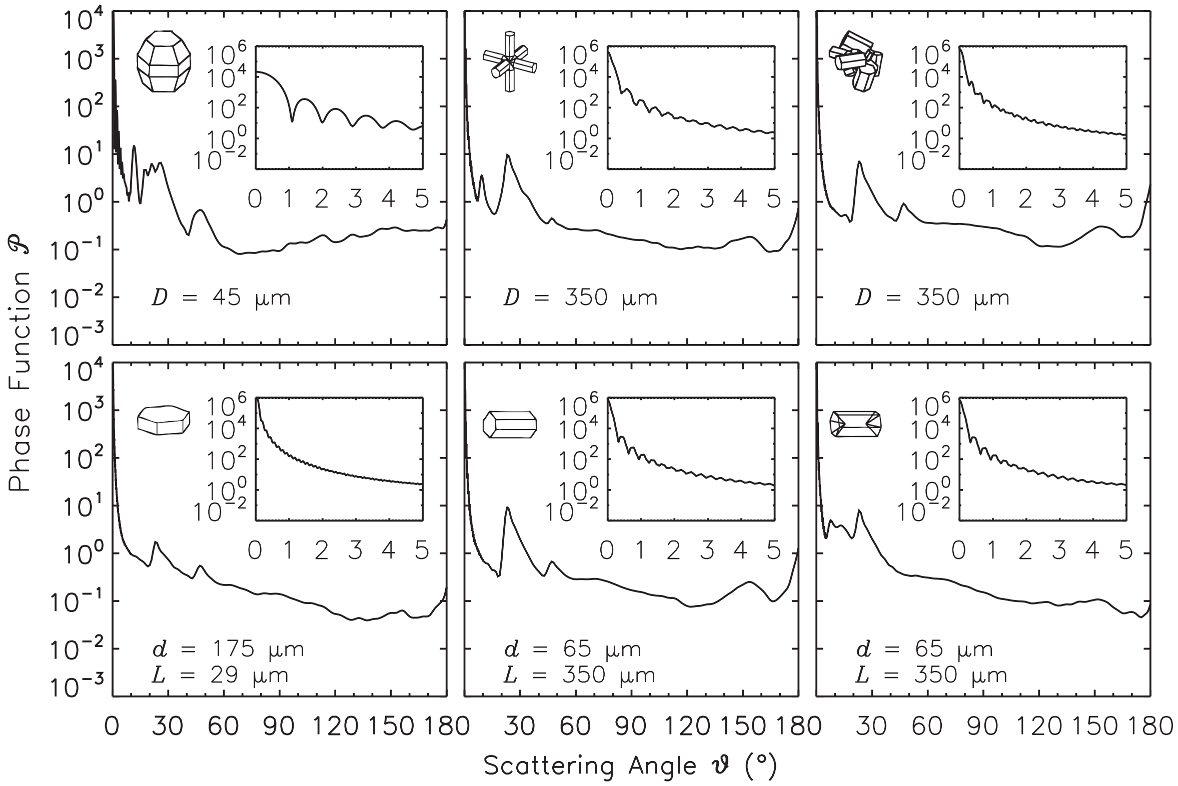

Figure 2.8: Computed phase functions for various ice crystal shapes at 0.65 μm wavelength (Wendisch and Yang, 2012). **Top:** Droxtals, bullet rosettes, and aggregates with maximum dimension D. **Bottom:** Hexagonal plates, columns, and hollow columns of height L and cross-sectional semiwidth d.

Phase function

The dimensionless phase function $\mathcal{P}$ gives the relative angular distribution of the scattered EM radiation:

$$\mathcal{P}(\theta) = 4\pi \cdot \frac{f(\theta)}{k^2 \cdot C_{\mathrm{sca}}} \,. \tag{2.20}$$

It depends on the scattering angle θ, the scalar scattering function f(θ) describing the angular distribution of the scattered EM radiation, the scattering cross section C_{sca}, and the modified wavenumber k ($k = 2\pi/\lambda$). It is a measure for the probability of scattering radiation from the incident direction (θ_{i}, φ_{i}) into the direction (θ, φ) and is normalized such that:

$$\iint_{4\pi} \mathcal{P}\left[(\theta_{\mathrm{i}}, \varphi_{\mathrm{i}}) \rightarrow (\theta, \varphi)\right] \, \mathrm{d}^2\Omega = 4\pi \,. \tag{2.21}$$

The phase function $\mathcal{P}$ varies considerably for different ice crystal shapes. Figure 2.8 (from Wendisch and Yang, 2012) shows computations of $\mathcal{P}$ for various ice crystal shapes using an improved geometric-optics method (Yang and Liou, 1996). The enhanced forward scattering as visible at small scattering angles is typical for all ice crystals independent of their shape. For scattering angles lower than 5°, the values of $\mathcal{P}$ increases over several orders of magnitude. Furthermore, enhanced scattering at 22° and 46° corresponding to the halo peaks is found for the hexagonal crystals.

Asymmetry parameter

The asymmetry parameter g serves as a rough estimate for the angular distribution of scattered radiation by the individual particle. Assuming that $\mathcal{P}$ is independent of the scattering azimuthal angle, g is defined as:

$$g = \frac{1}{2} \int_{-1}^{1} \cos\theta \cdot \mathcal{P}(\cos\theta)\, \mathrm{d}\cos\theta \,. \tag{2.22}$$

g can take values between -1 (for pure backward scattering) and 1 (for pure forward scattering); g is zero in the case of isotropic scattering. The strong forward scattering characteristic for ice crystals as deduced from the phase functions in Fig. 2.8 is also found in the values for the asymmetry parameter. Dang et al. (2016) calculated g of nonspherical ice crystals with different aspect ratios (diameter/length) for 0.5 µm wavelength. They found g to vary between 0.74 and 0.86 for aspect ratios between 0.1 and 10. The asymmetry parameter of a spherical ice crystal is 0.89 at this wavelength.

2.3.2 Volumetric optical properties

To derive the volumetric optical properties of an ensemble of particles confined within a volume element, the single-scattering properties of the individual particles are averaged with respect to the number size distribution $\mathrm{d}N/\mathrm{d}\log D$ of the particles. The number size distribution gives the number $\mathrm{d}N$ of particles (in m^{-3}) within the size interval $[D - \Delta D, D + \Delta D]$, whereas D denotes the particle diameter (in µm).

Hence, the volumetric extinction coefficient b_{ext} (in units of m^{-1}) is obtained from the extinction cross section C_{ext}:

$$b_{\mathrm{ext}}(\lambda) = \int_{0}^{\mathrm{inf}} C_{\mathrm{ext}}(\lambda, D') \cdot \frac{\mathrm{d}N}{\mathrm{d}\log D}(D')\, \mathrm{d}\log D' \,. \tag{2.23}$$

Similarly, the volumetric absorption coefficient b_{abs} (in m^{-1}) is calculated by:

$$b_{\mathrm{abs}}(\lambda) = \int_{0}^{\inf} C_{\mathrm{abs}}(\lambda, D') \cdot \frac{\mathrm{d}N}{\mathrm{d}\log D}(D')\,\mathrm{d}\log D' \,. \tag{2.24}$$

Correspondingly, the volumetric single-scattering albedo, the volumetric asymmetry factor, and the volumetric phase function are derived.

2.3.3 Spectral surface albedo

The surface albedo depends on the absorption properties of the ice crystals of the snow layer, which is why its spectral behavior mimics that of $\tilde{n}_{\mathrm{im}}$ but is inverted. Fig. 2.7 shows the simulated spectral surface plane albedo α_{p} of a snow layer consisting of snow grains of size R_{opt}. The simulations are based on the asymptotic solution of the radiative transfer equation (Eqs. 5.4 and 5.10 in Sect. 5.2.2). R_{opt} ranges from 10-200 µm. In the VIS, where ice absorption is low, α_{p} is close to one and varies only slightly with wavelength. This is why snow is seen by the human eye as a bright and white surface. However, for longer wavelengths, α_{p} significantly decreases. Note the local maxima of α_{p} at approximately 400, 1100, 1300, and 1850 nm wavelength which correspond to local minima in $\tilde{n}_{\mathrm{im}}$.

The larger the snow grains are, the longer the photon path length through the individual ice crystals is, and the higher the probability of photon absorption is leading to a lower surface albedo (Wiscombe and Warren, 1980). This effect is most pronounced at wavelengths larger than 1000 nm where the imaginary part of the complex refractive index of ice increases.

2.3.4 Hemispherical-directional reflectance

The snow HDRF depends on the angular distribution of the radiation scattered by a snow layer. Hence, similarities between the HDRF and the phase function $\mathcal{P}$ as the corresponding, inherent optical property are expected. Figure 2.9 shows an exemplary measurement of the snow HDRF in Antarctica on 2 January 2014. The polar plot of the HDRF is rotated such that the Sun is on the left. Again, the high values of the HDRF around one demonstrate the high reflectivity of a snow layer. Enhanced HDRF values are visible in the forward scattering direction. This is in accordance with the increase in $\mathcal{P}$ at small scattering angles. However, as the HDRF is representative for a snow layer

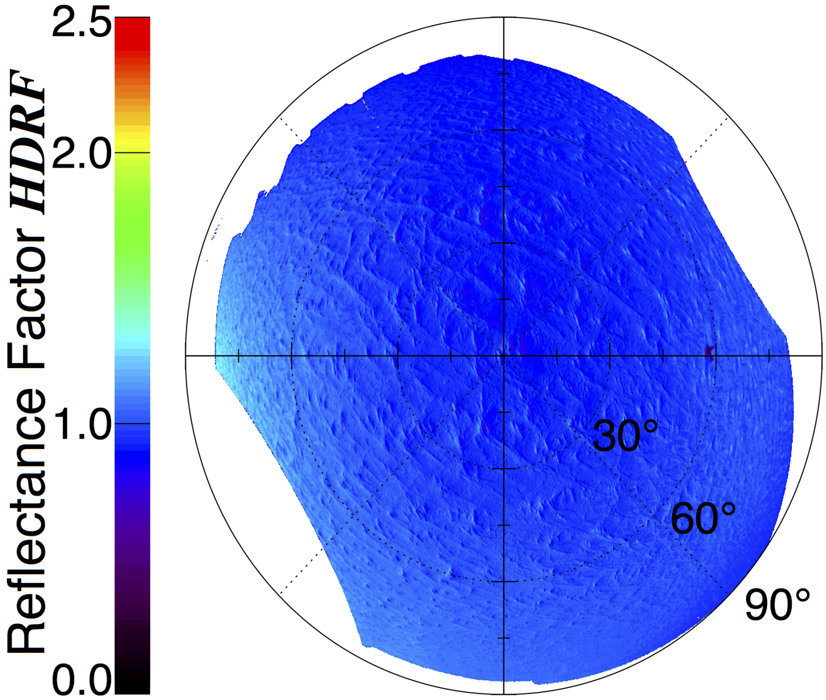

Figure 2.9: Exemplary measurement of snow HDRF in Antarctica on 2 January 2014.

consisting of a large number of ice crystals with varying sizes and shapes, this feature is less pronounced than for the single-scattering property $\mathcal{P}$. Note that the HDRF is further influenced by macroscopic properties of the snow layer. The rippled structure of the surface roughness is still noticeable in terms of the small-scale variability in the HDRF values. These surface structures cast shadows and reduce the effective incident angle of the solar radiation thereby influencing the angular distribution of the reflected radiation.

3 Motivation and objectives

3.1 Sensitivity of snow surface albedo

Solar radiation reaches the surface either directly or after multiple scattering events within the atmosphere. The reflection at the snow surface is anisotropic and determined by its BRDF under the current illumination conditions. As illustrated in Fig. 3.1, roughness structures of the snow surface such as wind-driven sastrugi cause shadows and, therefore, increase the anisotropy of the snow BRDF.

The surface albedo of a snow layer depends on different factors such as the snow grain

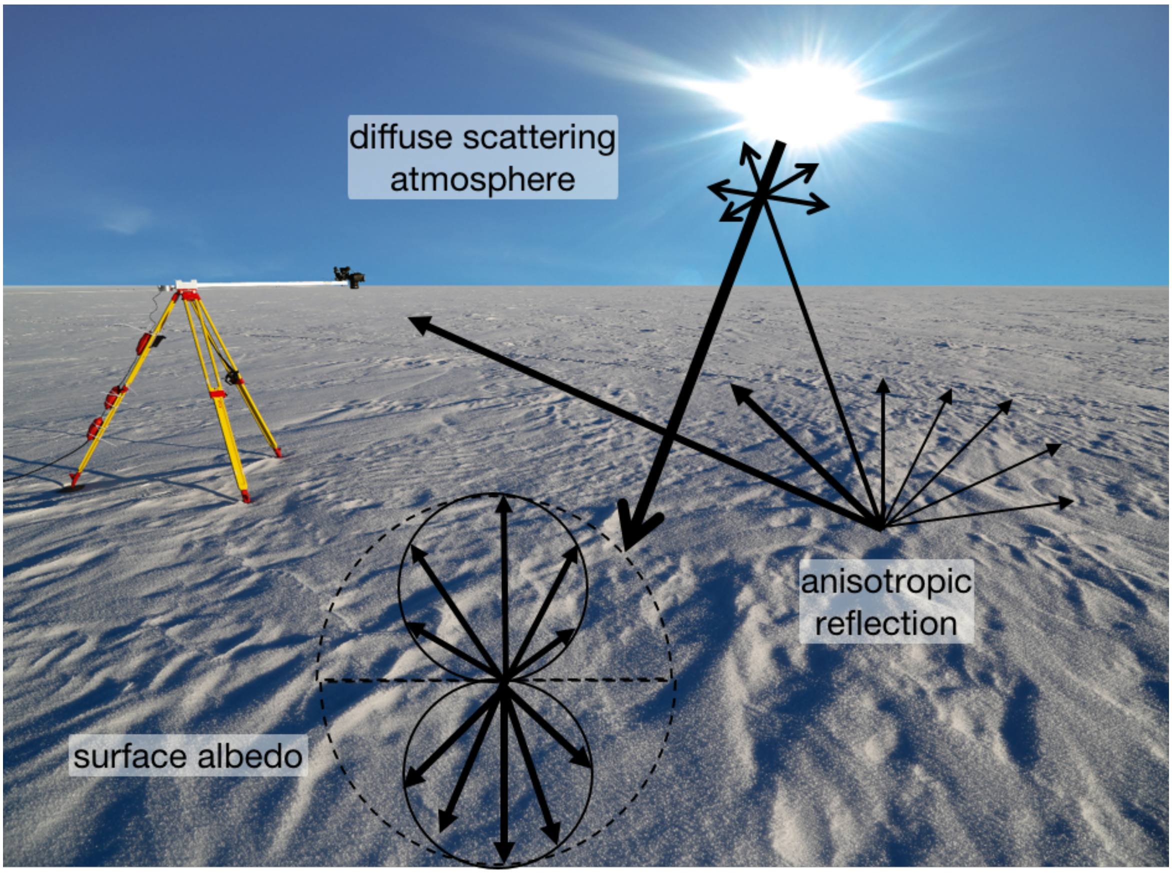

Figure 3.1: Illustration of the scattering of solar radiation in the atmosphere and at the snow surface. Photograph: G. Birnbaum.

size, the wavelength, the Sun position, atmospheric conditions (e.g., cloud cover), the snow impurity content, and macroscopic surface roughness. From these, the snow grain size exerts the dominant effect on the snow albedo. The dependence of the simulated spectral plane albedo on the optical snow grain size is shown in Fig. 2.7. However, with respect to the radiative energy budget, the broadband albedo describes the total amount of solar radiative energy reflected by the surface. The broadband albedo α_{BB} integrated over the wavelength range between $\lambda_1 = 300\,\mathrm{nm}$ and $\lambda_2 = 2200\,\mathrm{nm}$ is calculated by integrating the spectral albedo weighted by the spectral downward irradiance,

$$\alpha_{\mathrm{BB}} = \frac{\int\limits_{\lambda_1}^{\lambda_2} \alpha_{\mathrm{p}}(\lambda) \cdot F^{\downarrow}(\lambda)\,\mathrm{d}\lambda}{\int\limits_{\lambda_1}^{\lambda_2} F^{\downarrow}(\lambda)\,\mathrm{d}\lambda}\,. \tag{3.1}$$

For this sensitivity study, the global spectral irradiance $F^{\downarrow}(\lambda)$ is simulated with the library for radiative transfer libRadtran (Mayer and Kylling, 2005) using the discrete ordinate radiative transfer solver DISORT by Stamnes et al. (1988) for a solar zenith angle of $\theta_0 = 52°$ and the geographical coordinates of Kohnen research station (75°0′ S, 0°4′ E; 2892 m above sea level).

Figure 3.2 shows the sensitivity of the broadband albedo with respect to the optical snow grain size ($R_{\mathrm{opt}} = 10 - 200\,\mu\mathrm{m}$). For a typical optical grain size of 100 µm, α_{BB} is 0.83. Larger snow grains exhibit stronger absorption and, thus, lead to a lower α_{BB}, while for smaller grain sizes the broadband albedo increases up to 0.92 for $R_{\mathrm{opt}} = 10\,\mu\mathrm{m}$.

To quantify the amount of solar radiation that is absorbed by the surface and, therefore, leads to a warming of the surface, the net irradiance F_{net} which is equal to the difference between $F^{\downarrow}$ and $F^{\uparrow}$ is calculated by:

$$F_{\mathrm{net}} = F^{\downarrow} - F^{\uparrow} = F^{\downarrow} \cdot (1 - \alpha_{\mathrm{BB}})\,. \tag{3.2}$$

During the measurements analyzed within this study, the optical snow grain size gradually increased due to snow metamorphism by approximately 5 µm per day between 18 and 30 December 2013. The optical snow grain size on 18 December 2013 was approximately 45 µm, the net irradiance 104.2 W m^{-2}. On 19 December 2013, the optical snow grain size increased to 50 µm, the net irradiance increased to 107.3 W m^{-2}. Thus, an increase in optical snow grain size of 5 µm already lead to an increase in the amount of absorbed solar radiation by about 3 W m^{-2}. This demonstrates the large influence of the snow microstructure on the local surface radiative energy budget.

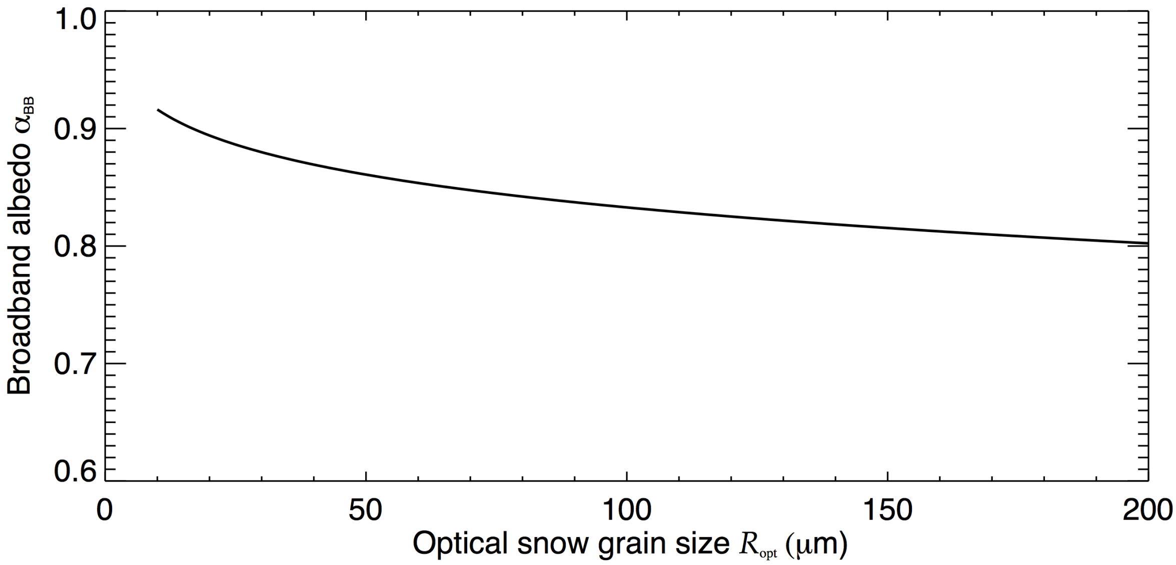

Figure 3.2: Sensitivity of simulated broadband albedo ($\lambda = 300 - 2200\,\mathrm{nm}$) with respect to optical snow grain size ($R_{\mathrm{opt}} = 10 - 200\,\mu\mathrm{m}$).

3.2 Challenges in remote sensing of snow properties

The significance of the polar regions for the Earth's climate system and their observed amplified response to climate change (see Ch. 1) indicate the need for high temporal and spatial coverage for the monitoring of the reflective properties of snow surfaces. However, the snow surface albedo is highly variable both on a temporal and spatial scale which causes problems in determining the surface solar radiative energy budget in these areas. Furthermore, they are difficult to reach as a consequence of the remote and harsh environment. This implies the necessity for remote sensing of the reflective properties of snow surfaces and their influencing parameters. In the following, past observational and modeling efforts concerning the surface albedo and the BRDF of snow are discussed. Subsequently, some of the current challenges in the remote sensing of snow properties are identified.

3.2.1 Snow surface albedo and solar radiative energy budget

The surface albedo comprises a major boundary condition for radiative transfer in the atmosphere. Firstly, it governs multiple scattering and absorption processes in the solar spectral range. Secondly, it determines the conversion of radiation energy from the solar to the terrestrial wavelength range. Consequently, the surface albedo is a constraining factor for the radiative energy budgets of the surface and the atmosphere (Wendisch et al., 2004). The high surface albedo of snow and sea ice amplifies their impact, in particular in cloudy conditions. Picard et al. (2016) estimated that a hypothetical change in global surface albedo of one percent would offset a difference in reflected solar radiative energy comparable to the globally averaged radiative forcing of $1.82\,\mathrm{W\,m^{-2}}$ caused by the increase in CO_2 concentration since the preindustrial time period (Myhre et al., 2013). This change in global surface albedo could be caused either by a variation in snow and sea ice cover or by changes of snow and sea ice properties and related snow albedo changes. During boreal winter, snow and sea ice cover up to 15 % of the Earth's surface (Vaughan et al., 2013). Although these areas are mainly in polar regions with partly low values of incoming solar radiation, the high snow and sea ice albedo may facilitate substantial changes in the local surface energy budget mostly during polar day. In Antarctica, more than 99.8 % of the continent and most of the sea ice are covered with snow all year round (Burton-Johnson et al., 2016). However, the snow surface albedo varies both on temporal and spatial scales. For example, Munneke et al. (2008) found variations of the broadband albedo of snow in a range between 0.77 and 0.88 at five locations in Dronning Maud Land.

Changes of broadband and spectral snow albedo are caused by different parameters such as snow grain size (and shape), surface roughness (e.g., Warren et al., 1998), soot content (e.g., Bond et al., 2013), and cloudiness. It further depends on wavelength (e.g., Hudson et al., 2006; Warren and Brandt, 2008) as well as solar position (e.g., Wiscombe and Warren, 1980; Dumont et al., 2010) and varies with snow depth (e.g., Wiscombe and Warren, 1980) and liquid water content (e.g., Wiscombe and Warren, 1980; Gallet et al., 2014a).

From these parameters, the snow grain size exerts the dominant effect on snow albedo (e.g., Dang et al., 2015). Simulations by Wiscombe and Warren (1980) showed that the spectral albedo in the near-infrared part of the EM spectrum may drop by a factor of two or more when the snow grain size increases from 50 to 1000 µm. Dang et al. (2015) showed that the transition from freshly fallen snow with a typical snow grain size of 100 µm to aged snow (1000 µm) leads to a decrease in snow albedo (spectrally integrated over 0.3–4.0 µm) from 0.83 to 0.72. This relation has been identified in ground-based measurements by Domine et al. (2006) analyzing snow samples taken at Svalbard in 2001. These authors measured a decrease in reflectance at 1310 nm wavelength by 45 % with increasing grain size from 290 to 1175 µm. Libois et al. (2015) and Picard et al. (2016) retrieved a 3-year time series of SSA from spectral albedo measurements at Dome C (75° 6′ S, 123° 0′ E), Antarctica, which emphasized the dynamical evolution of near-surface SSA by displaying a 3-fold decrease every summer in response to the increase of near-surface air temperature. A detailed comparison of this dataset with snow model simulations and a geophysical interpretation are presented by Libois et al. (2015). Similar seasonal, but little year-to-year variation, were found by Jin et al. (2008), who retrieved snow grain sizes from measurements with the MODerate Resolution Imaging Spectroradiometer (MODIS) at 1.64 and 0.64 µm wavelength over the Antarctic continent for 4 days each year between 2000 and 2005. Therefore, as a positive feedback mechanism, increasing snow temperatures are followed by an accelerated snow metamorphism and a decrease of the snow albedo, which leads to higher absorption and heating of the snow. However, the expected snow albedo decrease due to temperature-induced metamorphism (0.3 % for a warming of 3 K) can be overcompensated by an increase in snow albedo by 0.4 % owing to a projected increase in precipitation during the 21st century in interior Antarctica (Picard et al., 2012).

3.2.2 Observation and modeling of the bidirectional reflectance of snow

The high spatial and temporal variability of the snow surface albedo raises the need for continuous observations with global coverage, which are provided by satellite instruments. Satellites monitor the reflectance at the TOA. However, they are restricted in terms of discrete observation angles and a limited number of spectral bands. According to a review by Qu et al. (2015), the processing of satellite measurements for monitoring of surface albedo typically requires three steps: atmospheric correction, angular modeling of the reflectance, and narrow-to-broadband conversion. During the first step, the TOA reflectance is converted into a surface reflectance by means of an atmospheric correction (e.g., Vermote and Kotchenova, 2008). For the calculation of the narrowband surface albedo, an accurate knowledge of the BRDF of the surface is required due to the limited number of observation angles. Finally, in using a linear combination of the discrete spectral band measurements with specific weighting, the broadband surface albedo is calculated (e.g., Brest and Goward, 1987; Klein and Stroeve, 2002; Liang et al., 2003). The largest uncertainty in this three-step process is introduced by the angular modeling of the surface BRDF, especially when the reflection of the underlying surface is highly anisotropic.

Due to its high surface albedo, most of the solar radiation that is impinging on a snow surface is reflected back to the atmosphere, at least in cloudless conditions. This reflection depends strongly on the BRDF of the snow surface and, thus, on the illumination and viewing geometry. In general, most of the photons are scattered into the forward scattering direction. Yet, the BRDF varies with snow grain morphology, the solar zenith and azimuth angles, the liquid water content (LWC) of the snowpack, the snow impurity concentration, the dimension and orientation of surface roughness structures, and the wavelength.

The anisotropic reflection at snow surfaces was already demonstrated by Li (1982) with simulations of the snow BRDF using Mie theory and the doubling and adding method (e.g., Wendisch and Yang, 2012). Applying Mie theory and the discrete ordinate method (e.g., Wendisch and Yang, 2012), Han (1996) retrieved the surface albedo from satellite measurements in the Arctic. Leroux and Fily (1998) developed a snow BRDF model including the effect of sastrugi by means of regularly spaced, identical, and rectangular protrusions. Leroux et al. (1998) and Leroux et al. (1999) employed the doubling and adding method, Mie theory, and ray tracing to develop a polarized BRDF model. Comparing the simulated values with observations in the principal plane, they found that the BRDF in the NIR is strongly affected by the snow grain shape and that simulations with hexagonal particles yield a better agreement with the observations compared to assuming spheres. Accordingly, Aoki et al. (2000) stressed the importance of the shape of the scattering phase function used in their BRDF model when comparing to observations at 0.52 to 2.21 µm wavelength in Hokkaido, Japan. The comparison of in situ measured BRDF with simulations is essential in terms of model validation. However, as an infinitesimal quantity, the BRDF of a surface cannot be measured under natural illumination conditions. From a rigorous physical point of view, most satellites, airborne and ground-based instruments measure the HCRF, or, if it is constant over the full cone angle of the instrument's FOV, the HDRF (Schaepman-Strub et al., 2006). The HDRF can only be converted into the BRDF if the atmospheric influence is well characterized.

Several studies observed a less anisotropic snow BRDF than estimated from model simulations (Warren et al., 1998; Painter and Dozier, 2004a; Hudson et al., 2006; Hudson and Warren, 2007). In the solar principal plane, the models mainly overestimate the forward scattering and underestimate the backward scattering. Implementing nonspherical grains in the BRDF models (e.g., Mishchenko et al., 1999; Xie et al., 2006; Jin et al., 2008) improves the comparison with observations. The nonspherical model of Jin et al. (2008) agrees within ± 10 % for viewing zenith angles less than 60° with observations in Antarctica performed by Hudson et al. (2006). However, the asymmetry between forward and backward scattering still remains. This highlights the need to further incorporate macroscopic effects in the models (Leroux et al., 1998; Hudson and Warren, 2007).

Observations of the BRDF or HDRF are conducted using a variety of different measurement concepts. For ground-based applications, manual or automated gonio-spectrometer systems are employed (e.g., Painter et al., 2003; Pegrum et al., 2006; Bourgeois et al., 2006a). Kuhn (1985) observed a peak in reflectance in the azimuthal directions up to 60° to both sides of the solar azimuth that becomes more prominent with increasing solar zenith angle and snow grain size. Marks et al. (2015) characterized the HDRF of snow between 400 and 1600 nm wavelength with the Gonio Radiometric Spectrometer System (GRASS, Pegrum et al., 2006) for the inter-calibration of satellite optical data at Dome C, Antarctica. Their observations also showed prominent forward scattering. In addition, they observed a larger anisotropy of the surface reflection at longer wavelengths. Employing the gonio-spectrometer developed at the Institute for Atmospheric and Climate Science (IAC) of the Swiss Federal Institute of Technology (ETH) in Zürich (Bourgeois et al., 2006a), Bourgeois et al. (2006b) observed strong variations of the HDRF between 0.6 and 13 (in the wavelength range 350-1050 nm) depending on the solar zenith angle and the surface roughness at Summit, Greenland. Measurements with the Automated Spectro-Goniometer (ASG, Painter et al., 2003) showed a decrease of snow HDRF at all wavelengths between 400 to 2500 nm when the snow grain size increased from 80 to 280 µm (Painter and Dozier, 2004b). Further comparisons with a forward discrete ordinates radiative transfer model (Stamnes et al., 1988) showed larger deviations between the simulations and observations for more complex, faceted crystals. The importance of the crystal habit for the anisotropy of reflection at snow surfaces was further shown by Dumont et al. (2010) and Stanton et al. (2016). The latter measured increasing anisotropy during the growth of surface hoar in the laboratory.

Ground-based instruments observe the directional reflectance of a characteristic, homogenous surface, whereas airborne observations average over a larger measurement area. Thus, airborne measurements are more suitable for (a) the comparison with the large pixel size of satellite observations, and (b) studying the influence of macroscopic surface roughness on the surface BRDF. Gatebe and King (2016) provided an extensive database of airborne spectral BRDFs for various surface types, e.g., ocean, vegetation, snow, desert, and clouds. The BRDFs were acquired by the Cloud Absorption Radiometer (CAR, Gatebe et al., 2005) of the National Aeronautics and Space Administration (NASA) over a 30-year period between 1984 and 2014. The CAR is a scanning radiometer covering 14 spectral channels between 480 and 2324 nm. The effect of surface roughness on the BRDF was studied by Lyapustin et al. (2010) with CAR measurements during the ARCTAS Spring campaign. Their results showed a good agreement between the Ross-Thick Li-sparse model (RTLS, Lucht et al., 2000) used in the operational MODIS BRDF/albedo product (Schaaf et al., 2002) and the CAR measurements to within ±0.05. The RTLS model performed better in the forward scattering direction, whereas the Modified Rahman-Pinty-Verstraete model (MRPV, Martonchik et al., 1998) used for the processing of data from the multi-angle imaging spectroradiometer (MISR) achieved better in the backscattering direction. Nolin et al. (2002) employed multiangular measurements with MISR for the characterization of surface roughness over Greenland and Antarctica. Measurements with the clouds and the Earth's radiant energy system (CERES) showed monthly regional biases between -12 and 7.5 $\mathrm{W\,m^{-2}}$ in the clear-sky TOA solar flux density. This biases were attributed to the effect of sastrugi, which introduce a solar azimuth dependence: Kuchiki et al. (2011) observed a diurnal cycle in MODIS reflectances over the South Pole. In general, sastrugi decrease the forward scattering by casting shadows, increase the backward scattering due to a lower effective incident angle caused by the sastrugi slope, and the snow BRDF loses its azimuthal symmetry (Warren et al., 1998). Zhuravleva and Kokhanovsky (2011) observed a larger effect for a higher density of the sastrugi field.

The instantaneous measurement of multiple viewing angles facilitates aerial BRDF measurements with digital cameras. Cox and Munk (1954) analyzed radiance calibrated photographs for the parameterization of the ocean BRDF. Nowadays, digital cameras are increasingly applied in vegetation and soil monitoring (Lebourgeois et al., 2008). Ehrlich et al. (2012) used a commercial digital camera equipped with a wide-angle lens with FOV of 100° for measurements of the HDRF of snow-covered sea ice, ocean, and clouds (viewing zenith angle up to around 60°).

The modeling of the snow reflectance is also of relevance to the retrieval of cloud properties and aerosol particles over snow (Lyapustin et al., 2010). Ehrlich et al. (2017) quantified the effect of the snow grain size on the retrieved optical properties of Arctic liquid water clouds. They found the largest impact of up to 83 % on the retrieved cloud optical thickness and 62 % on the cloud droplet effective radius in case of small snow grain sizes and optically thin clouds.

The dimensionless aerosol optical depth (AOD) is defined as the integral over the extinction coefficient over the entire vertical column and, thus, is a measure for the amount of scattering and absorbing aerosol particles within the column. However, the retrieval of the AOD over highly reflecting surfaces is complicated as it is hard to separate the surface and aerosol contributions to the measured radiance at the TOA (Tomasi et al., 2015). This holds true especially for the large solar zenith angles, the bright snow surfaces, and the comparably low aerosol particle load in the polar regions (Mei et al., 2013). To overcome this problems, an accurate model of the snow BRDF is needed. Yang et al. (2014) compared MODIS measurements of AOD at 550 nm over Eastern China with ground-based data from the Aerosol Robotic Network (AERONET). Using a Lambertian forward model, 53.6 % of the regression points fell within the expected error envelope around the 1:1 line. This is improved to 68.7 % applying a non-Lambertian model accounting for anisotropic reflection at the land surface.

Furthermore, the snow surface of the Antarctic ice sheet is used for the validation and cross-calibration of polar orbiting satellites (Jaross and Warner, 2008).

3.2.3 Current challenges

From the above discussion, some urgent issues concerning the remote sensing of snow properties are deduced:

(a) **Validation of remote sensing products:** The remoteness of the polar regions leads to a scarcity of in situ data as well as ground-based and airborne remote sensing observations. Furthermore, the satellite coverage at high latitudes is limited.

(b) **Conversion of bi-conical reflectance into albedo:** This is a core step in the processing of satellite products, which is not straightforward especially for the anisotropic reflection at snow surfaces.

(c) **Validation of modeling:** This comprises both the angular modeling involved in the processing of satellite measurements as well as prognostic snowpack models. The latter are mainly developed for avalanche forcasting in Alpine regions. Their applicability to the specific conditions of polar regions needs to be tested.

3.3 Objectives

The main goal of this thesis is to study the variations in snow surface albedo and HDRF as caused by changes in snow properties in order to investigate and improve the current knowledge on radiative properties of snow. An extensive observational effort forms an integral part of this analysis. So far, simultaneous measurements of the broadband and spectral surface albedo, the HDRF, atmospheric properties, and the microphysical properties of the snow layer have never been conducted covering an entire austral summer season. Therefore, it was a unique chance to embed comprehensive

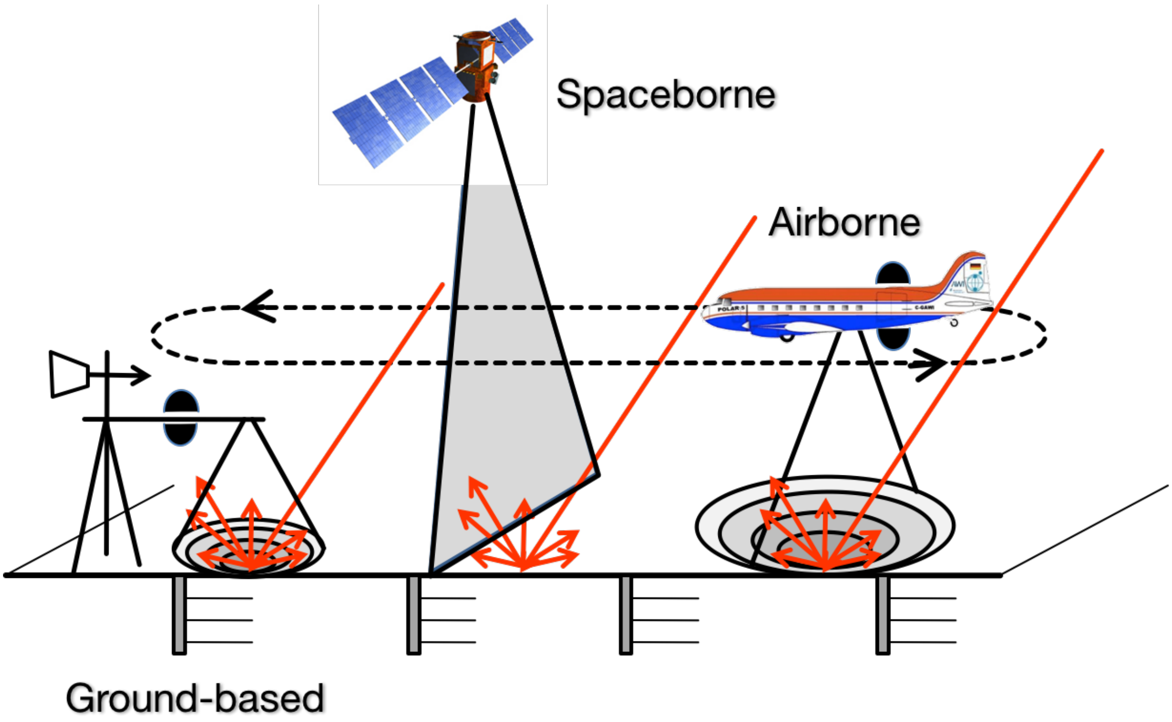

Figure 3.3: Illustration of the measurement strategy utilizing a combination of ground-based and airborne observations (modified, courtesy of A. Ehrlich).

radiation measurements in the glaciological project Coldest Firn (CoFi) performed on the East Antarctic Plateau in the austral summer season 2013/14. In order to cover the variability of microphysical and reflective properties both on a temporal and spatial scale, ground-based measurements at Kohnen research station (75°0′ S, 0°4′ E; 2892 m above sea level) were coupled with airborne observations using the Polar 6 research aircraft. Both Kohnen research station and the Polar 6 research aircraft are operated by the Alfred Wegener Institute, Helmholtz Centre for Polar and Marine Research (AWI). The combined approach of the measurement strategy is illustrated in Fig. 3.3.

Both ground-based and airborne observations include spectral surface albedo measurements. The two datasets can be linked due to an identical radiometric calibration of both instruments. They can be utilized to quantify how the surface albedo and consequently the energy budget of the Antarctic ice sheet is altered by macroscopic (e.g., surface roughness) and microphysical (e.g., snow grain size) snow properties. The scarcity of observational data in Antarctica (Challenge a in Sect. 3.2.3) highlights the relevance of this comprehensive measurement effort. The campaign, instrumentation, post-processing of the data as well as the measurement uncertainties are discussed in Chapter 4.

From the spectral surface albedo measurements, the temporal evolution of the snow SSA (and respective R_{opt}) is derived from ground-based and airborne observations and compared to in situ measurements at Kohnen research station. Kohnen research station is an ideal place to investigate the development of dry and clean snow. At the same time, the airborne observations relate the local measurements to the variability observed in Dronning Maud Land. Thus, the temporal and spatial variability of the SSA provides a useful dataset for the validation of satellite products (Challenge a), namely the snow grain size and pollution amount (SGSP) algorithm. Chapter 5 describes the methodology of the SSA retrieval in more detail. In addition, the application of the SGSP algorithm to spectral surface albedo measurements and its extension to overcast conditions is explained. The validation study is shown in Chapter 6. The comparison of different methods to retrieve the SSA at Kohnen station has been published by Carlsen et al. (2017a). This thesis includes substantial parts of this article. The SSA datasets of the ground-based, airborne, and spaceborne retrievals was made available by Carlsen et al. (2017b) in the Publishing Network for Geoscientific & Environmental Data (PANGAEA). This could be used to validate prognostic snowpack models for Antarctic conditions in future studies (Challenge c).

An analysis of the dependence of the snow HDRF with respect to the solar zenith angle, the macroscopic surface roughness, and the SSA targets Challenge b in Sect. 3.2.3. The parameterization involves the inversion of a semi-empirical kernel-driven BRDF model as described in Chapter 5. Chapter 7 includes the parameterization of the HDRF measurements with respect to the solar zenith angle, and the surface roughness as obtained from two case studies.

In the concluding Chapter 8, the findings of this work are summarized and perspectives for future studies are given.

4 Measurements and instrumentation

4.1 Observations at Kohnen station and in Dronning Maud Land

The measurements were conducted at and in the vicinity of the Kohnen research station operated by the Alfred Wegener Institute, Helmholtz Centre for Polar and Marine Research (AWI). Kohnen station is located at the outer part of the East Antarctic plateau (75°0′ S, 0°4′ E; 2892 m above sea level) as illustrated in Fig. 4.1, approximately 500 km from the coastline, where the local weather is mostly determined by weak catabatic winds.

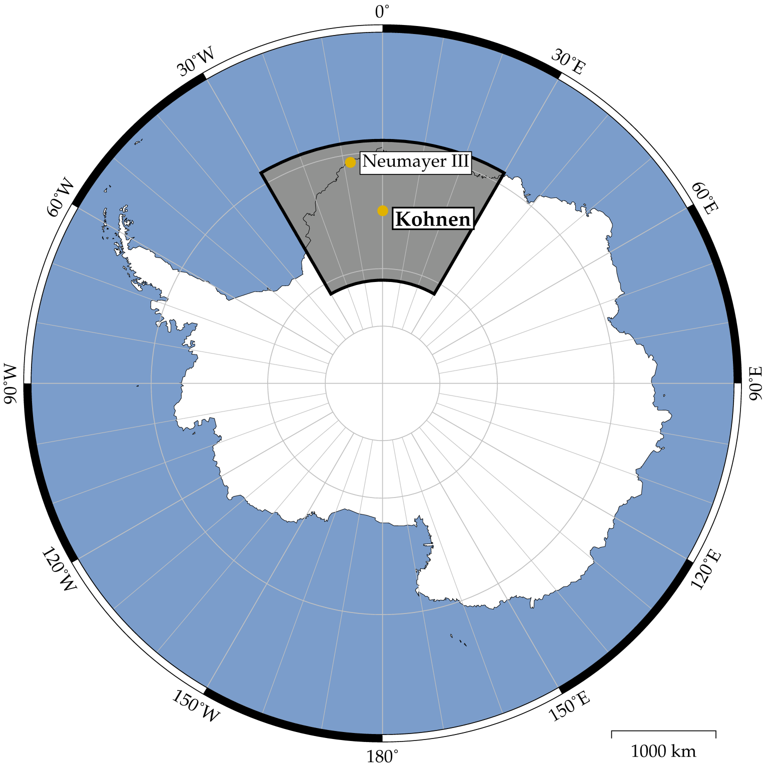

Figure 4.1: Location of the German research stations Kohnen and Neumayer III that are operated on the Antarctic continent. The area of observation (shaded gray) covers large parts of Dronning Maud Land.

The annual snow accumulation is 62 mm liquid water equivalent (Oerter et al., 2000) with moderate snowfall (1 mm to more than 5 mm water equivalent) occurring only a few times per year (Birnbaum et al., 2006). The atmosphere is clean, with an AOD at Kohnen station of 0.015 (at 500 nm, measured 2001–2006, Tomasi et al., 2007). Furthermore, the atmosphere is dry as is demonstrated by a mean integrated atmospheric water vapor of 1.1 kg m^{-2} between December 2013 and January 2014. The black carbon (BC) concentration in the snowpack on the Antarctic plateau is low; for the South Pole, Hansen and Nazarenko (2004) reported a mean BC concentration of 0.2 ppbw (parts per billion by weight).

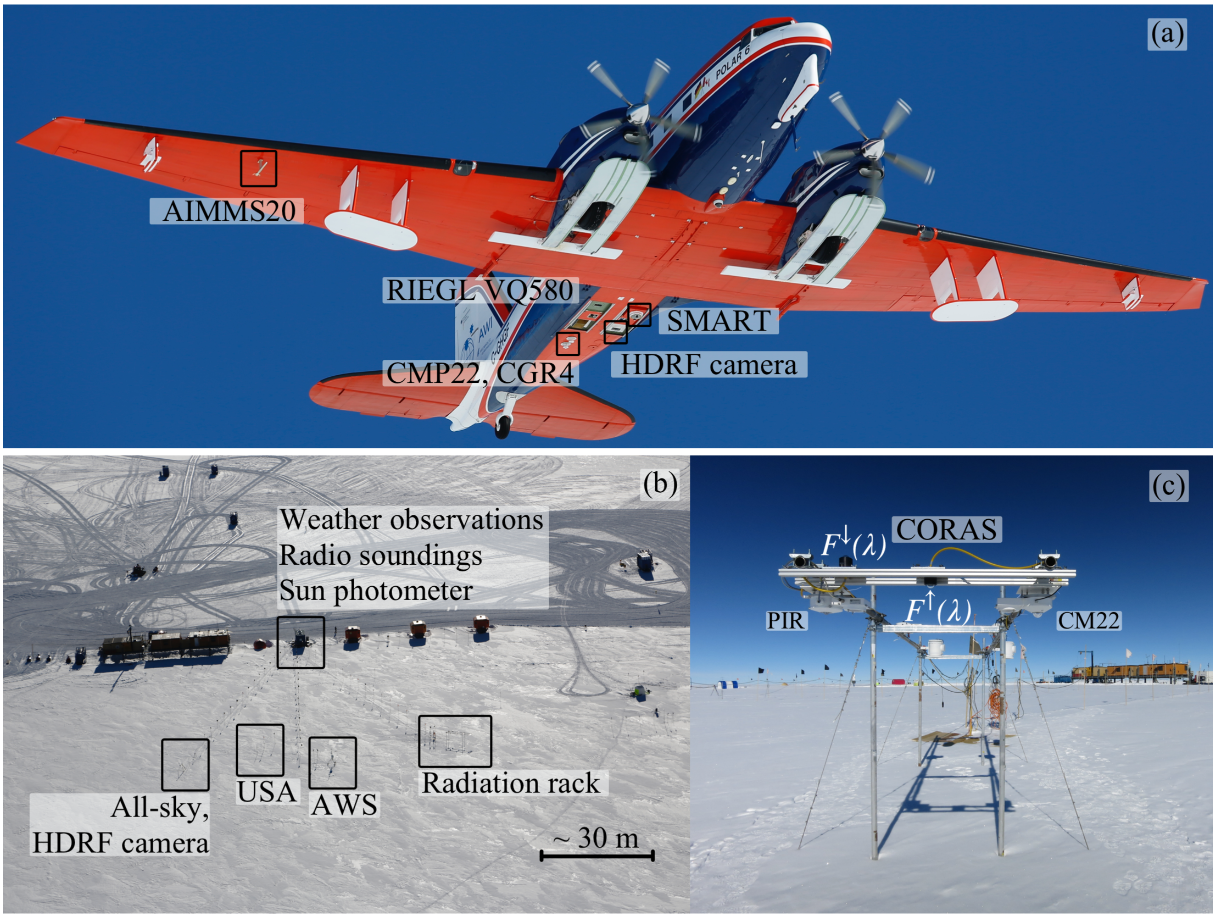

Figure 4.2: (a) Photograph of Polar 6 research aircraft. The positions of the airborne instruments are marked with black rectangles. **(b)** Aerial photograph of Kohnen station. The positions of different ground-based instruments are marked with black rectangles. USA: ultrasonic anemometer. AWS: automatic weather station. **(c)** Instrument setup at the ground-based radiation rack: optical inlets of the CORAS instrument and the broadband radiation instruments CM22 and PIR. Photographs: G. Birnbaum.

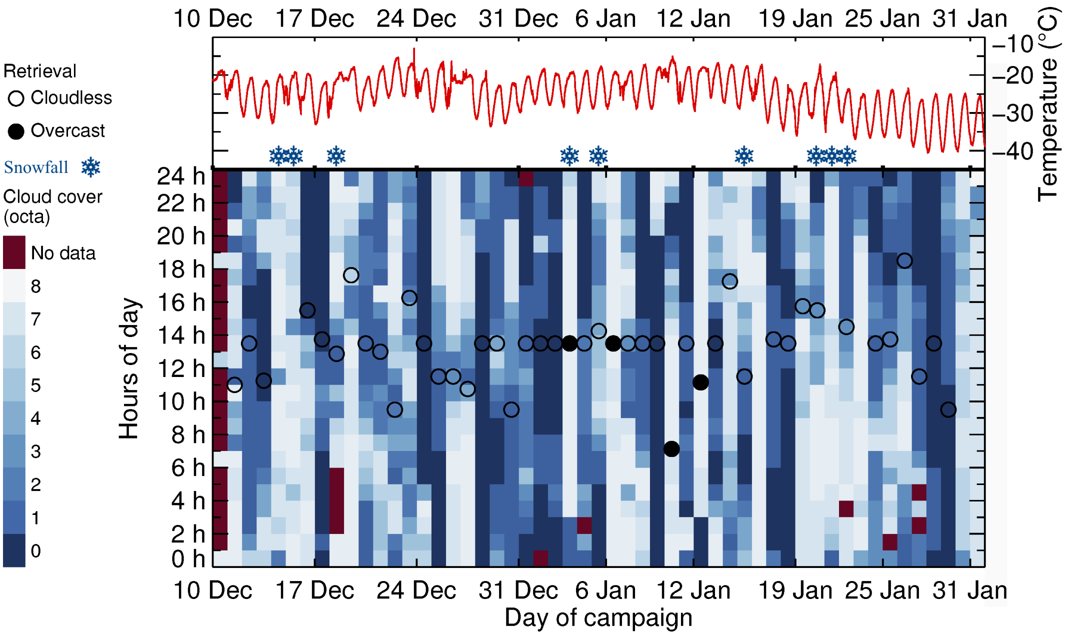

Figure 4.3: Time series of 2 m air temperature (red line) and hourly cloud cover (blueish squares) at Kohnen station between 10 December 2013 and 31 January 2014. Snowflake symbols denote days with snowfall. Black circles show times when SSA was retrieved from CORAS measurements (Fig. 6.1) and denote retrievals for cloudless (open circles) and overcast (filled circles) conditions.

4.1.1 Ground-based observations

The ground-based measurements were embedded in the Coldest Firn (CoFi) project by AWI, which investigates the microstructure as well as physical and chemical composition of snow and firn (compacted snow that has survived at least one summer) on the Antarctic plateau. The location and mounting of the ground-based instrumentation are illustrated in Fig. 4.2.

Solar broadband and spectral radiation measurements of snow surface albedo combined with meteorological observations (air temperature, humidity, wind velocity and direction, radio sounding, and synoptic observations) were conducted. In addition, optical snow grain size and density of snow samples were measured on a daily basis at Kohnen station, accompanied by measurements of vertical snow temperature profiles. Snow samples from in situ measurements were extracted daily (except on 5 December, 12, 17, 18, and 19 January) along a 100 m transect.

Two downward-looking digital cameras were employed for ground-based photogrammetric measurements of surface roughness structures. Another digital camera was used to resolve the HDRF of the snow surface following a method introduced by Ehrlich et al. (2012). Furthermore, an all-sky camera was used for cloud observations. The

Table 4.1: List of instruments operated on ground and on Polar 6 aircraft.

	Instrument	**Measured quantity**	**Specifications**
Ground-based	Kipp & Zonen CM22	$F^{\downarrow}$, $F^{\uparrow}$ ($\mathrm{W\,m^{-2}}$)	Broadband, 0.2-3.6 µm
(Kohnen)	Eppley Precision Infrared Radiometer	$F^{\downarrow}$, $F^{\uparrow}$ ($\mathrm{W\,m^{-2}}$)	Broadband, 3.5-50 µm
	CORAS	$F^{\downarrow}(\lambda)$, $F^{\uparrow}(\lambda)$ ($\mathrm{W\,m^{-2}\,nm^{-1}}$)	Spectral, 0.3-2.2 µm
	CANON EOS 6D	$I^{\uparrow}$ ($\mathrm{W\,m^{-2}\,nm^{-1}\,sr^{-1}}$)	180° fish-eye lens
	CANON EOS 600D	All-sky images	
	CANON EOS 600D (2x)	Photogrammetric images	Image overlap: 50 %
	Sun photometer SP1A31	AOD	10 channels: 368.5 to 1019.4 nm
	Automatic weather station	p, T, RH, $F^{\uparrow}$, $F^{\downarrow}$, $\overrightarrow{v}$, snow accumulation	1 min averages
	Ultrasonic anemometer	$\overrightarrow{v}$	
	Radio sounding	p, T, RH, $\overrightarrow{v}$	
	Synoptic observations	Cloud cover, precipitation	Visual observation
	IceCube by A2 Photonic Sensors	SSA ($\mathrm{m^2\,kg^{-1}}$), ρ_{snow} ($\mathrm{kg\,m^{-3}}$)	Wavelength: 1310 nm
	Pt-100	Snow temperature profile	
Airborne	Kipp & Zonen CMP22	$F^{\downarrow}$, $F^{\uparrow}$ ($\mathrm{W\,m^{-2}}$)	Broadband, 0.2-3.6 µm
(Polar 6)	Kipp & Zonen CGR4	$F^{\downarrow}$, $F^{\uparrow}$ ($\mathrm{W\,m^{-2}}$)	Broadband, 4.5-42 µm
	SMART	$F^{\downarrow}(\lambda)$, $F^{\uparrow}(\lambda)$ ($\mathrm{W\,m^{-2}\,nm^{-1}}$)	Spectral, 0.3-2.2 µm
		$I^{\downarrow}(\lambda)$, $I^{\uparrow}(\lambda)$ ($\mathrm{W\,m^{-2}\,nm^{-1}\,sr^{-1}}$)	Spectral, 0.3-2.2 µm
	CANON EOS 1D Mark III	$I^{\uparrow}$ ($\mathrm{W\,m^{-2}\,nm^{-1}\,sr^{-1}}$)	180° fish-eye lens
	RIEGL VQ580	Surface topography	Airborne laser scanner
	AIMMS20	$\overrightarrow{v}$, p	Meteorological measurements
	KT19	T_{surf}	Radiation thermometer

$F^{\downarrow}$: downward irradiance, $F^{\uparrow}$: upward irradiance, λ: wavelength (indicates spectral quantity), $I^{\uparrow}$: reflected radiance, AOD: aerosol optical depth, p: pressure, T: temperature, RH: relative humidity, $\overrightarrow{v}$: wind vector, SSA: specific surface area, ρ_{snow}: snow density, T_{surf}: surface temperature

mean AOD at 500 nm as determined by a sun photometer was 0.016 during the observation period (Andreas Herber, AWI Bremerhaven, personal communication, August 2017).

The ground-based measurements were carried out during austral summer between 4 December 2013 and 31 January 2014. Within this period, nine snowfall events occurred (recorded by visual observation), the surface temperature ranged from −40 to −15 °C. The time series of the measured 2-m air temperature and the hourly cloud fraction are presented in Fig. 4.3. The temperature indicates a typical diurnal cycle on most days. Only on days with high cloud cover, the 2-m air temperatures remained almost constant. Towards the end of the measurement period, the air temperature decreased due to lower Sun elevations. The mean total cloud amount over the entire period was less than 4 octa. Only five completely overcast days were reported. The total cloud cover was highly variable and mainly determined by cirrus clouds.

The spectral snow albedo $\alpha(\lambda)$ was measured from ground-based and airborne instruments. At Kohnen station, the COmpact RAdiation measurement System (CORAS) measured upward and downward spectral irradiance $[F^{\uparrow}(\lambda), F^{\downarrow}(\lambda)]$ within 0.3 to 2.2 µm

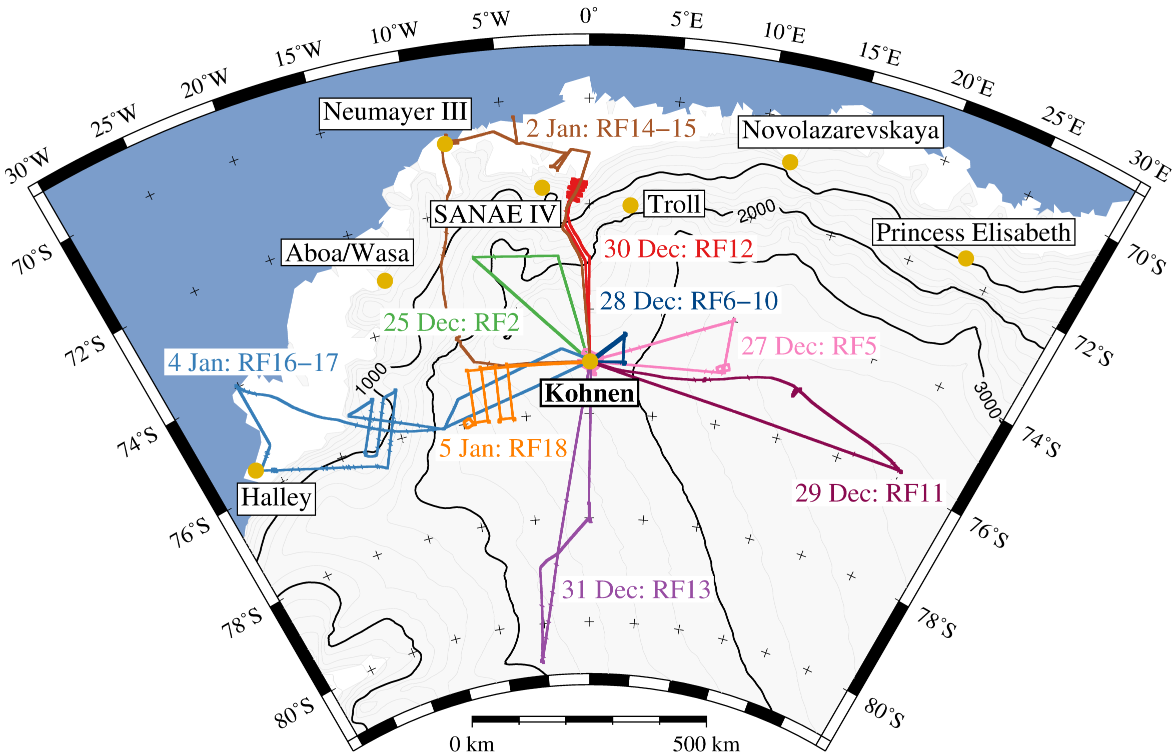

Figure 4.4: Map of flight patterns with the Polar 6 research aircraft during the campaign. Each color corresponds to a different flight.

wavelength. Table 4.1 lists the ground-based and airborne instruments relevant for this thesis.

4.1.2 Airborne observations

To characterize the representativeness of the local ground-based measurements, an intensive observation phase including airborne surveys using the Polar 6 research aircraft from AWI was conducted between 24 December 2013 and 5 January 2014. The aircraft flew 60 h to characterize the spatial variability of snow properties above Dronning Maud Land. A map of the tracks of the 18 research flights is shown in Fig. 4.4. During each flight, an overpass over Kohnen station was realized to compare airborne and ground-based measurements. The airborne observations covered a wide variety of surface roughness structures as well as precipitation patterns. Beside solar broadband and spectral radiation measurements, the airborne observations included measurements of snow HDRF by means of a digital camera and surface roughness measurements using a laser scanner (see Fig. 4.2). Meteorological measurements were provided by the Aircraft-Integrated Meteorological Measurement System (AIMMS20). The aircraft instrumentation additionally included geophysical observations within the CoFi project (snow and ice thickness). On Polar 6, irradiance measurements similar to the ground-based observations were conducted using the Spectral Modular Airborne Radiation measurement sysTem (SMART).

4.2 Spectral albedo measurements

Wendisch et al. (2001) introduced the modular design of a spectroradiometer to measure spectral radiometric quantities from airborne platforms. Initially, the albedometer SMART measured upward and downward irradiance in the wavelength range between 400 and 1000 nm (Wendisch et al., 2001; Wendisch and Mayer, 2003; Wendisch et al., 2004). Subsequently, it was applied for measurements of actinic flux densities (Jäkel et al., 2005) and spectral radiance (Ehrlich et al., 2008) and Bierwirth (2008) extended the wavelength range to 2200 nm. CORAS is the ground-based version of the airborne spectroradiometer and has been used for measuring solar transmissivity on the Polarstern research vessel (Brückner et al., 2014). During the measurements in Antarctica, CORAS was mounted to the radiation rack at Kohnen station, whereas SMART was installed on the Polar 6 research aircraft (see Fig. 4.2).

4.2.1 Ground-based and airborne spectroradiometers

The setups of the ground-based and airborne spectroradiometers are shown in Fig. 4.5. CORAS consists of three main components: optical inlets for irradiance, optical fibers, and spectrometers. Figure 4.6 shows a sketch of an irradiance optical inlet which follows the design of Crowther (1997). After passing through a quartz dome, incident photons are collected in an integrating sphere coated with Spectralon® that acts as a diffuser. This way, the collection of the photons coming from the entire hemisphere is weighted with the cosine of the incidence angle. The collected photons are transferred to the spectrometers by bifurcated optical fibers. A conical aperture prevents direct incidence to the optical fibers. The spectrometer box includes a multi channel spectrometer (MCS) covering the visible to near-infrared spectral wavelength region (VNIR, 0.3-1.0 µm) and a plane grating spectrometer (PGS) covering the shortwave-infrared wavelength region (SWIR, 0.9-2.2 µm). The photons reaching the spectrometers are dispersed by a grating and directed on a single-line photodiode array (PDA). The PDAs of the VNIR and the SWIR spectrometers consist of silicon (Si, 1024 photodiodes) and indium-gallium-arsenide (InGaAs, 256 photodiodes), respectively. The setup with two optical inlets and one spectrometer for each wavelength region requires consecutive measurements with a full spectrum measured every 15 s. The spectral

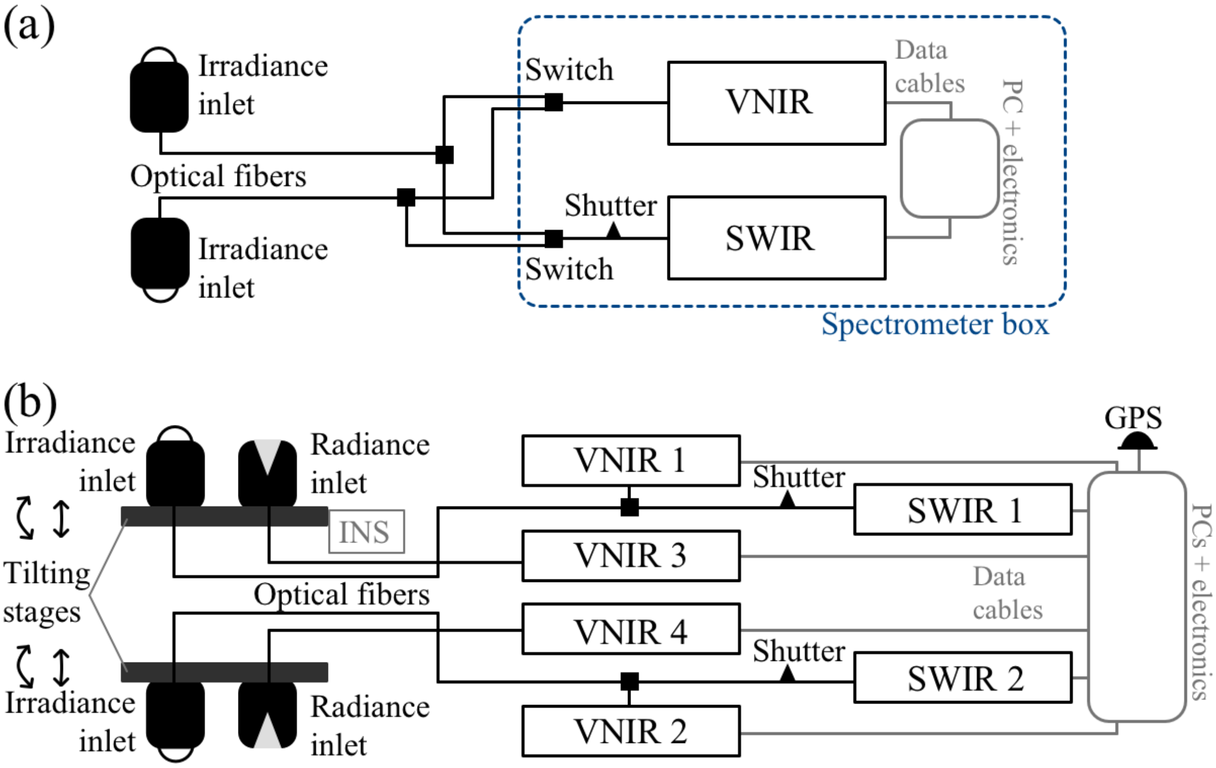

Figure 4.5: **(a)** Scheme of the CORAS setup measuring up- and downward spectral irradiance at the radiation rack. **(b)** Scheme of the SMART setup measuring up- and downward spectral irradiance and radiance on Polar 6.

resolution (specified in terms of the FWHM) is 2 to 3 nm between 0.3 and 1.0 µm and 15 nm up to 2.2 µm wavelength. The temperature dependence of the thermally induced dark signal in the SWIR spectrometer requires real-time sampling of the dark spectrum (sum of dark current and electronic offset). This is realized with an optical shutter that blocks the optical path. The difference of consecutive measurements with open and closed optical shutter gives the net signal. $F^{\uparrow}(\lambda)$ and $F^{\downarrow}(\lambda)$ were measured with an integration time of 3 s (VNIR) and 0.5 s (SWIR). SMART additionally comprises two optical inlets for measuring radiance. They contain a borosilicate crown (BK) 7 collimator lens with a focal length of 31.6 mm (Ehrlich, 2009) and collect photons within an opening angle of 2°. To correct for aircraft movement, SMART applies an active horizontal stabilization including an accurate aircraft roll and pitch angle measurement unit and an active horizontal adjustment system (Wendisch et al., 2001; Ehrlich et al., 2008). The internal navigation system (INS) consists of three linear servo-acceleration sensors and three fiber optical gyros measuring the aircraft velocity, position, and angular rates with respect to an inertial earth-fixed coordinate system. In combination with a global positioning system (GPS), the aircraft position and attitude (roll, pitch, and yaw angles) are measured. Two separate two-dimensional tilting

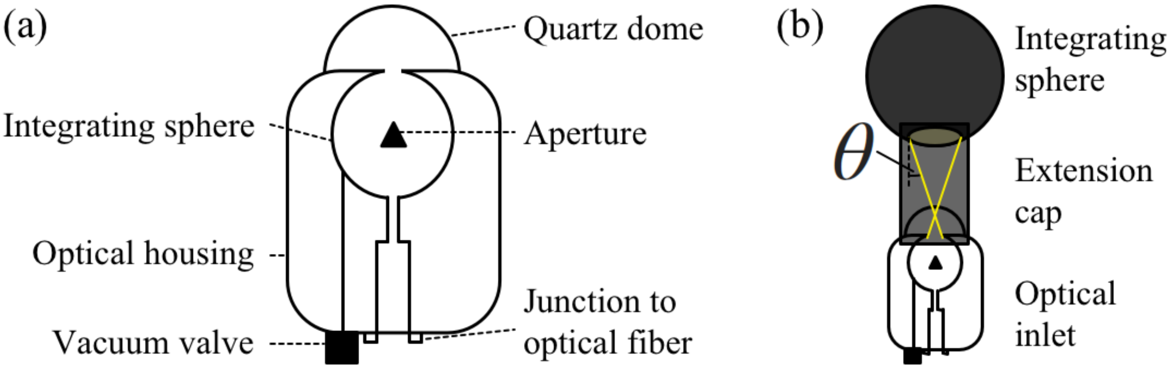

Figure 4.6: (a) Sketch of optical inlet for measuring irradiance. **(b)** Setup for cross-calibration. Extension cap is inserted between integrating sphere and optical inlet.

stages driven by servo motors horizontally adjust the attitude of the optical inlets in a range of ±6° to allow for horizontal leveling in the earth-fixed coordinate system. This is critical as a misalignment of 1° already yields an uncertainty in the measured irradiance of about 30 % at a solar zenith angle of 70° (Wendisch et al., 2001). SMART measured $F^{\uparrow}(\lambda)$ and $F^{\downarrow}(\lambda)$ with an integration time of 0.5 s (both VNIR and SWIR); the temporal resolution is in the order of 1 s.

4.2.2 Radiometric calibration

The calculation of the surface albedo α from the measured raw spectra $s(\lambda)$ involves three main steps: (a) the correction for dark and stray light, (b) the correction for the non-ideal angular response of the sensor–spectrometer system, and (c) the cross-calibration of the up- and downward looking optical inlets.

In case no photons are incident on the optical inlets, the spectrometers still register a non-zero signal due to a thermally induced dark current and stray light. This dark signal strongly depends on the temperature and integration time. However, the latter was kept constant throughout the entire observation period and can be neglected. For the SWIR spectrometer, $s_{\text{dark}}(\lambda)$ is sampled on-site. The dark signal at the wavelengths covered by the VNIR spectrometer is lower and calculated in the post-processing. For this, a dark measurement conducted in the laboratory is scaled to each measured spectrum based on the average signal between 200 and 270 nm wavelength where the transmissivity of the optical fibers and the sensitivity of the spectrometer are low. This scaled dark spectrum is regarded as $s_{\text{dark}}(\lambda)$. The signal $s_{\text{dc+sl}}$ is the raw signal corrected for dark current and stray light and is obtained by

$$s_{\text{dc+sl}}(\lambda) = s(\lambda) - s_{\text{dark}}(\lambda)\,. \tag{4.1}$$

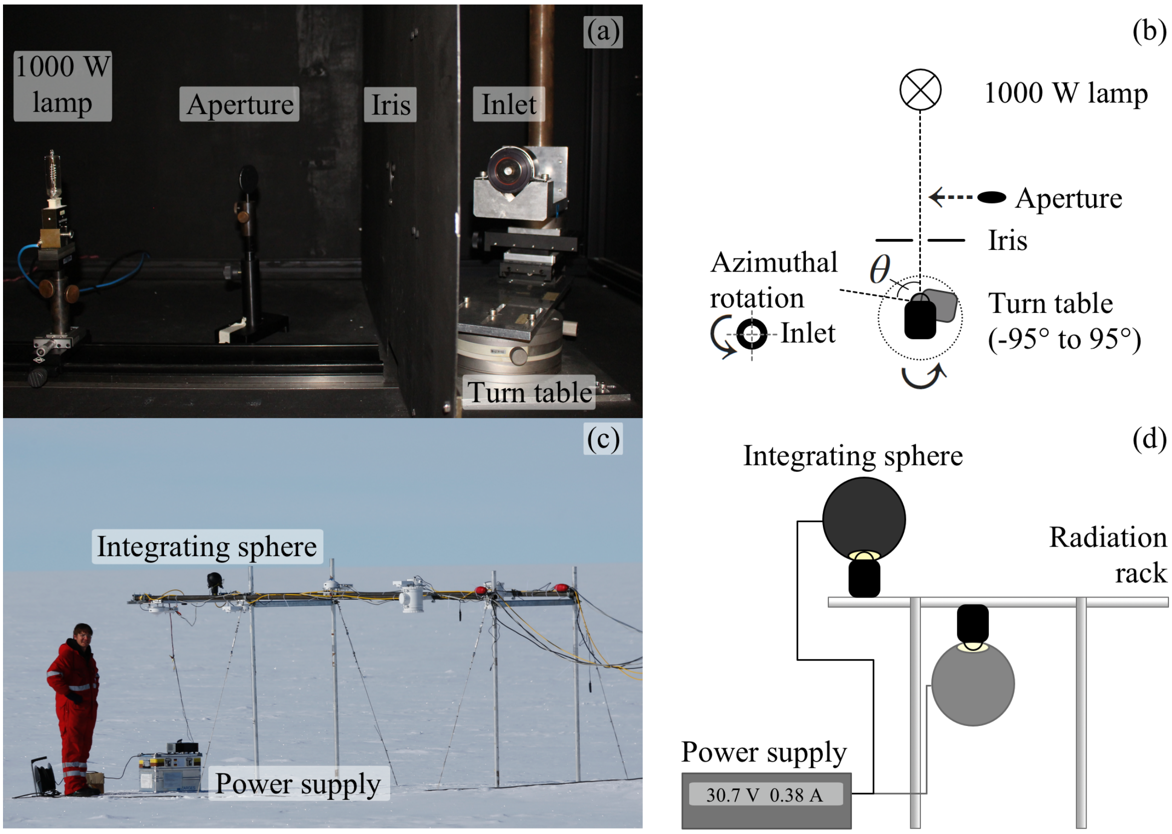

Figure 4.7: (a) Characterizing the angular response of the irradiance inlets in the laboratory. **(b)** Schematic setup for the characterization of the angular response. **(c)** Cross-calibration of the CORAS optical inlets at Kohnen station on 20 January 2014. Photograph: G. Birnbaum. **(d)** Schematic setup of the cross-calibration.

Ideally, the optical inlets collect incoming photons weighted by the cosine of the angle of incidence θ following the definition of irradiance. However, the actual angular response deviates from the ideal cosine law (e.g., Dirmhirn and Eaton, 1975; Grenfell et al., 1994; Wendisch, 2002; Bierwirth, 2008). To correct for the difference, cosine correction factors $C_{\mathrm{cos,dir}}$ and $C_{\mathrm{cos,diff}}$ (applying to the direct and diffuse component of the measured signal) are introduced as

$$C_{\mathrm{cos,dir}}(\theta,\lambda) = \frac{s_{\mathrm{dc+sl}}(\theta=0^\circ,\lambda)\cdot\cos\theta}{s_{\mathrm{dc+sl}}(\theta,\lambda)}\,, \tag{4.2}$$

and

$$C_{\mathrm{cos,diff}}(\lambda) = 2\cdot\int\limits_{0}^{90} C_{\mathrm{cos,dir}}(\theta,\lambda)\cdot\cos\theta\cdot\sin\theta\,\mathrm{d}\theta\,. \tag{4.3}$$

To derive the correction factors $C_{\mathrm{cos,dir}}$ and $C_{\mathrm{cos,diff}}$, the angular response of the irradiance optical inlets was characterized by laboratory measurements (see Fig. 4.7). The optical inlets were mounted on a turn table and the lamp signal under different angles of incidence (-95° to +95° in steps of 5°) was recorded. At each angular position, an additional measurement was performed with an aperture inserted in the optical path to correct for stray light in the setup. This procedure was repeated for four different relative azimuth angles between lamp and optical inlet. Figure 4.8 shows the measured signal $s_{\mathrm{dc+sl}}$ for different zenith angles θ normalized to $s_{\mathrm{dc+sl}}(\theta = 0°)$ for 600 nm wavelength. The comparison with the ideal cosine response (red line in Fig. 4.8) shows that the integrating sphere (see Fig. 4.6) prefers photons incident under zenith angles between 10° and 30°. On the contrary, the sensitivity of the sensor for large zenith angles around 75° is too low. The differences between the four different relative azimuth angles were low. In addition, Fig. 4.8 shows the computed correction factors $C_{\mathrm{cos,dir}}(\theta_0)$ and $C_{\mathrm{cos,diff}}(\lambda)$ for the up- and downward-looking optical inlets. For each wavelength, the results for $C_{\mathrm{cos,dir}}$ are fitted to a polynomial of order 9 with respect to the solar zenith angle (10th-order for SWIR wavelengths). The correction factors show a similar behavior for both optical inlets. For θ_0 up to around 70°, $C_{\mathrm{cos,dir}}$ is close to one but strongly increases for higher zenith angles. The error bars illustrate the variability of $C_{\mathrm{cos,dir}}$ computed for the four different relative azimuth angles. Differences are only visible at $\theta_0 = 85°$; the azimuthal stability is about 3.5 %. $C_{\mathrm{cos,dir}}$ is shown exemplarily for two different wavelengths (600 nm and 1200 nm); however, the dependence on the wavelength is weak. The correction by the 6th-order polynomial fit of $C_{\mathrm{cos,diff}}$ is in the order of ±5 % and varies only slightly with wavelength. The discontinuity in $C_{\mathrm{cos,diff}}$ at the transition from VNIR to SWIR is due to the two separate spectrometers with different sensitivities. Below 350 nm and above 1700 nm wavelength, the low signal at grazing incident angles leads to high noise. However, this is an artifact and $C_{\mathrm{cos,diff}}$ is assumed to be constant at these wavelengths.

The signal $s_{\mathrm{dc+sl+cos}}$ accounting for the angular response of the optical inlet is calculated using the azimuthally averaged correction factors $C_{\mathrm{cos,dir}}(\theta_0)$ and $C_{\mathrm{cos,diff}}(\lambda)$, the solar zenith angle at the time of measurement, the wavelength, and the direct fraction of the global irradiance f_{dir}:

$$s_{\mathrm{dc+sl+cos}}(\lambda) = f_{\mathrm{dir}} \cdot C_{\mathrm{cos,dir}}(\theta_0, \lambda) \cdot s_{\mathrm{dc+sl}}(\lambda) + (1 - f_{\mathrm{dir}}) \cdot C_{\mathrm{cos,diff}}(\lambda) \cdot s_{\mathrm{dc+sl}} \, . \tag{4.4}$$

The correction for the non-ideal angular response is critical for the upward looking sensor, which is subject to direct illumination. f_{dir} was simulated with the library for radiative transfer libRadtran by Mayer and Kylling (2005) using the discrete ordinate radiative transfer solver DISORT by Stamnes et al. (1988). The radiosondes released up to four times a day were used as meteorological input (profiles of air temperature,

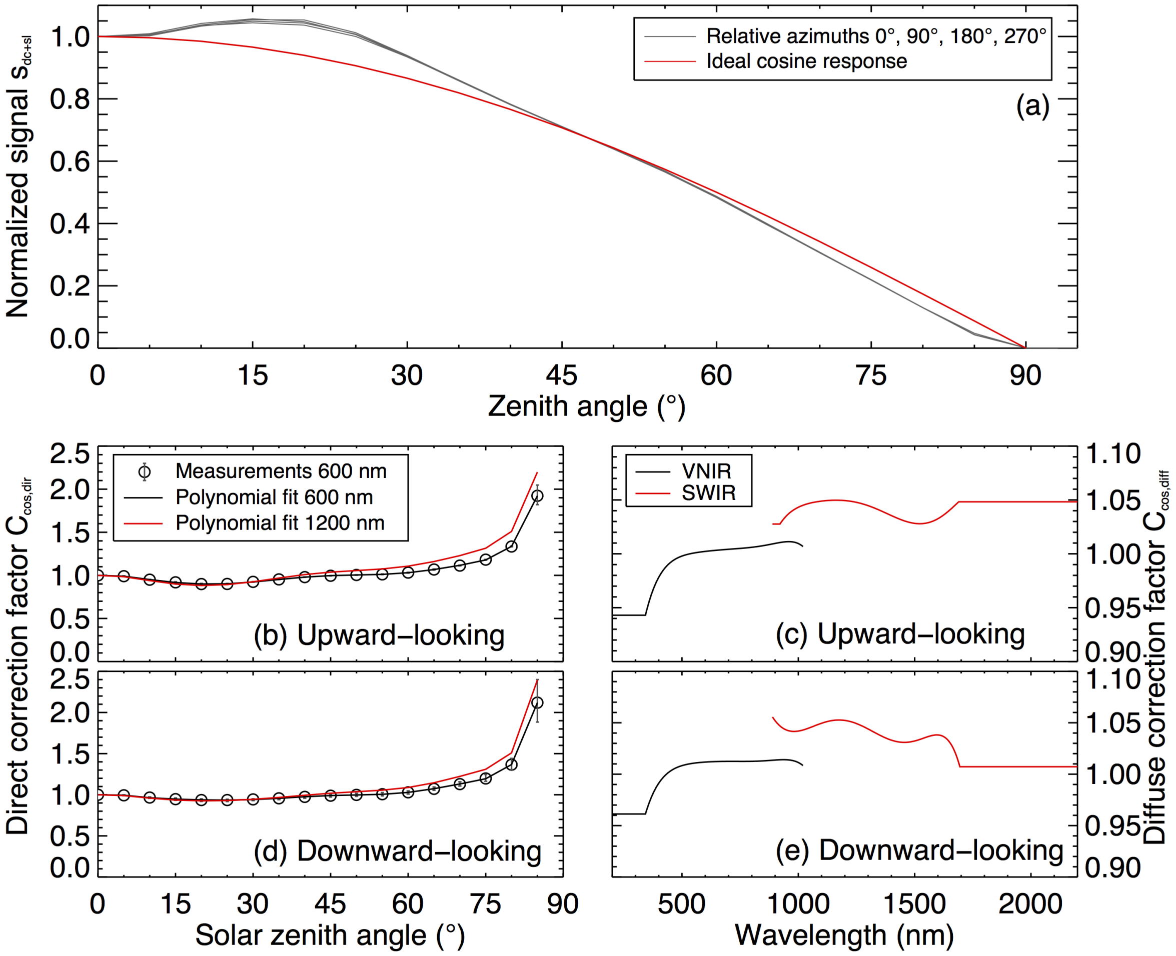

Figure 4.8: (a) Laboratory measurement of $s_{\mathrm{dc+sl}}$ normalized to $s_{\mathrm{dc+sl}}(\theta = 0°)$ in dependence of the zenith angle for four different relative azimuth angles (gray). Red line: ideal cosine response. **(b)** Polynomial fit of $C_{\mathrm{cos,dir}}(\theta_0)$ for upward-looking sensor for 600 nm (black) and 1200 nm (red) wavelength. Black circles: individual measurements. Error bars: azimuthal variability. **(c)** Polynomial fit of $C_{\mathrm{cos,diff}}(\lambda)$ for upward-looking sensor for VNIR (black) and SWIR (red). **(d), (e)** Same as in (b) and (c), but for downward-looking sensor.

relative humidity, and static air pressure). The signal of the downward looking sensor is corrected following Eq. (4.6) but assuming diffuse illumination ($f_{\mathrm{dir}} = 0$).

For albedo measurements, an absolute calibration converting the digital numbers registered by the spectrometers into units of irradiance is not required. However, the different sensitivities of the sensor–spectrometer systems need to be accounted for by means of a cross-calibration. As shown in Fig. 4.7, this was performed in the field during the observations and comprised successive measurements of the signals of the up- and downward-looking sensors [$s^{\uparrow}_{\mathrm{cc}}(\lambda)$ and $s^{\downarrow}_{\mathrm{cc}}(\lambda)$] under the same illumination with an integrating sphere. The downward-looking sensor measuring the reflected radiation is

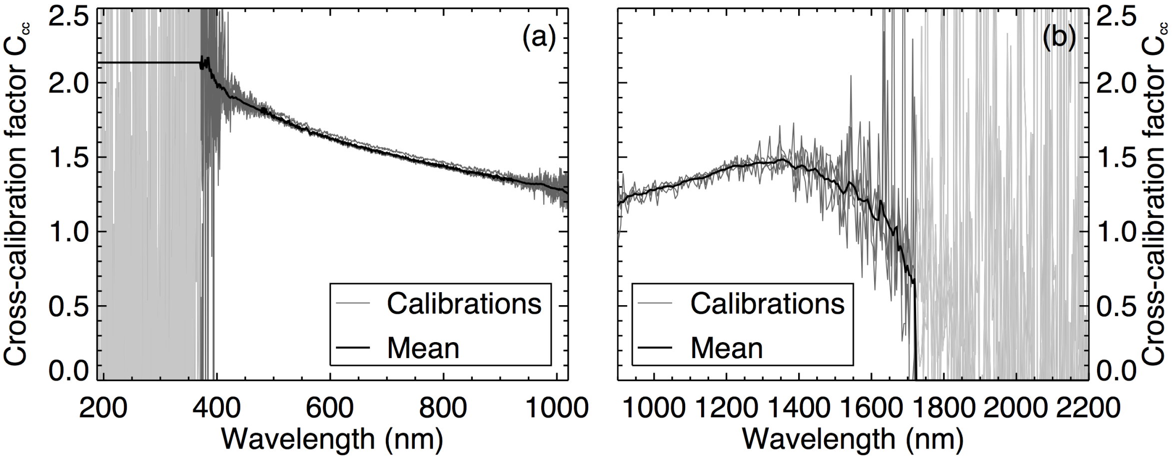

Figure 4.9: (a) Temporal stability of $C_{\text{cc}}(\lambda)$ for the VNIR spectrometer: the separate cross-calibrations (light gray) and the mean C_{cc} in dependence of the wavelength. **(b)** Same as in (a), but for the SWIR spectrometer.

then corrected by

$$C_{\text{cc}}(\lambda) = \frac{s^{\downarrow}_{\text{cc}}(\lambda)}{s^{\uparrow}_{\text{cc}}(\lambda)}\,, \tag{4.5}$$

where C_{cc} denotes the spectral cross-calibration factor, which was determined at six cross-calibrations performed obetween 16 December 2013 and 1 February 2014. The temporal stability of C_{cc} is shown in Fig. 4.9.

Within Fig. 4.9, the separate cross-calibrations throughout the observation period are shown together with the temporal mean of $C_{\text{cc}}(\lambda)$ for both the VNIR and the SWIR spectrometer. Over almost the entire wavelength range, the upward-looking sensor and respective optical fiber have a higher transmissivity than its downward-looking counterpart. At the edges of the wavelength ranges, the noise drastically increases. Below 400 nm, this is mainly due to the low radiation output of the integrating sphere. Above 1700 nm, the high noise stems from the low signal transmitted by the optical fibers, which were originally designed for the VNIR wavelength range but were erroneously connected to the SWIR spectrometer (see 4.2.3 for details). The cross-calibration on 16 December 2013 used a different power supply for the integrating sphere and during the first cross-calibration on 26 December 2013 icing occured on the quartz domes of the optical inlets. Thus, they were excluded from the calculation of the mean $C_{\text{cc}}(\lambda)$ and are not shown in Fig. 4.9. The remaining four cross-calibrations (second on 26 December 2013, as well as 5, 20 January, and 1 February 2014) show a high temporal stability, which is estimated with 1.0-4.5 % depending on wavelength. Thus, the mean $C_{\text{cc}}(\lambda)$ value is used for the correction of the reflected radiation following Eq. (4.5).

Until now, the cross-calibration process does not account for the different angular responses of the two sensors. As can be seen from Fig. 4.6, an cylindrical extension cap (length: 5.8 cm, diameter: 5 cm) was used to attach the integrating sphere to the optical inlets. The openings of the integrating sphere and the optical inlet are 4.9 cm and 0.85 cm, respectively. Hence, the maximum possible angle of incidence of photons during the cross-calibration is 27° (θ in Fig. 4.6). For both optical inlets, another diffuse correction factor $C_{\mathrm{cos,diff},0-30}$ is calculated following Eq. (4.3) but performing the integration only from 0° to 30°. The signal $s^{\uparrow}_{\mathrm{dc+sl+cos+cc}}$ after applying the cross-calibration is then obtained by

$$s^{\uparrow}_{\mathrm{dc+sl+cos+cc}}(\lambda) = s^{\uparrow}_{\mathrm{dc+sl+cos}}(\lambda) \cdot C_{\mathrm{cc}}(\lambda) \cdot \frac{C^{\downarrow}_{\mathrm{cos,diff},0-30}}{C^{\uparrow}_{\mathrm{cos,diff},0-30}} \,. \tag{4.6}$$

The high values of the snow surface albedo close to one (especially in the visible part of the EM spectrum) require detailed and accurate calibration procedures. The calibrations described in this section were analogously executed for the two irradiance inlets, two VNIR, and two SWIR spectrometers of SMART. The results are similar to CORAS and therefore not shown for reasons of clarity.

4.2.3 Data quality and post-processing

In the following, instrument failures and post-processing steps are described concerning (a) the interchanged optical fibers for CORAS, (b) the impossible calibration of the SMART radiance data, (c) the correction for the SMART attitude offset between INS and sensor plate, (d) the reconstruction of SWIR data for CORAS. Subsequently, the separate steps in the calculation of the surface albedo are illustrated and the filtering of the data is described.

CORAS: interchange of VNIR and SWIR optical fibers

During the CORAS measurements at Kohnen station, the optical fibers for the VNIR and SWIR were interchanged. The fibers designed for SWIR wavelengths feature larger core diameters for higher transmission at longer wavelengths. For the VNIR part of the radiation, the effect of the interchange is negligible. However, photons of the SWIR part of the EM spectrum could not pass the VNIR fiber. Therefore, the raw signal is very low due to this attenuation for wavelengths longer than 1600 nm.

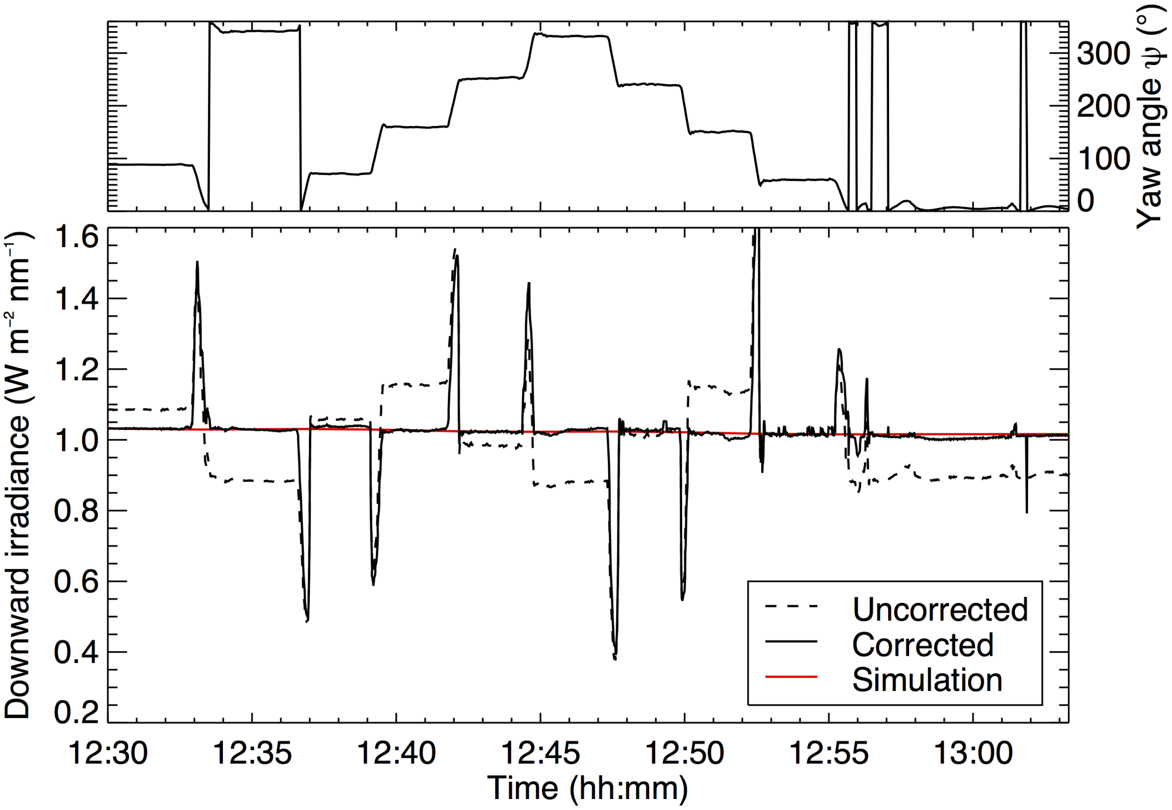

Figure 4.10: Top: Aircraft heading (yaw angle ψ) during square flight pattern. **Bottom:** Measured (scaled) and simulated downward irradiance for 600 nm wavelength during square flight pattern on 27 December 2013. Black dashed line: $F^{\downarrow}_{\mathrm{dc+sl+cos+abs}}$ (uncorrected), Black solid line: $F^{\downarrow}_{\mathrm{dc+sl+cos+abs+att}}$ (corrected for offset angles $\Delta\Phi = -0.8°$ and $\Delta\Theta = -6.4°$), Red solid line: simulated $F^{\downarrow}$.

SMART: calibration of radiance data

Due to a broken optical fiber, the downward spectral radiance $I^{\downarrow}(\lambda)$ was not measured during the campaign. Normally, the cross-calibration is used to transfer the absolute calibration as measured in the laboratory to the field to account for changes in the transmissivity of the sensor–fiber–spectrometer system. For this, comparable measurements with the same integrating sphere both in the laboratory and in the field are needed. Unfortunately, the power supply of the integrating sphere for calibrating SMART was set differently in the field (30.7 V, 0.38 A) compared to the laboratory calibration before the campaign (28.3 V, 0.38 A). After returning from Antarctica, the integrating sphere used in the field was directly sent to Inuvik, Canada, for the Radiation-Aerosol-Cloud Experiment in the Arctic Circle (RACEPAC) in April and May 2014. As the integrating sphere got destroyed at a cross-calibration during RACEPAC, it could not be used later for an additional laboratory calibration of

SMART with regard to the Antarctic measurements. Therefore, a radiometric calibration of $I^{\uparrow}(\lambda)$ was not possible which is why the radiance data could not be used for data analysis.

SMART: correction for attitude offset

The INS of the horizontal stabilization is fixed to the aircraft and not to the sensors. This allows active horizontal stabilization for both the zenith and nadir viewing sensors with only one INS. However, since the INS not directly measures the attitude of the sensor, the offset angles between aircraft and sensor plate introduced during the sensor installation need to be determined. For this purpose, square patterns were flown in cloudless conditions and the measured and simulated $F^{\downarrow}(\lambda)$ were compared.

The measured $F^{\downarrow}_{\mathrm{dc+sl+cos+abs}}(\lambda)$ (in units of $\mathrm{W\,m^{-2}\,nm^{-1}}$) is calculated from the signal $s^{\downarrow}_{\mathrm{dc+sl+cos}}(\lambda)$ applying an absolute calibration factor $C_{\mathrm{abs}}(\lambda)$:

$$F^{\downarrow}_{\mathrm{dc+sl+cos+abs}}(\lambda) = C_{\mathrm{abs}}(\lambda) \cdot s^{\downarrow}_{\mathrm{dc+sl+cos}}(\lambda) \tag{4.7}$$

The absolute calibration was carried out in the laboratory before and after the campaign using a 1000 W quartz-halogen lamp traceable to the National Institute of Standards and Technology (NIST) standard. Similar to f_{dir}, $F^{\downarrow}(\lambda)$ was simulated with libRadtran using DISORT and meteorological input from the radiosondes. Note that, as explained above, the absolute calibration could not be applied to SMART due to the failed transfer calibration. Therefore, an offset is visible between measured and simulated $F^{\downarrow}(\lambda)$. However, on a cloudless day the simulations should agree well with the measurements due to the low AOD and the low relative humidity. Hence, the measurements were scaled to the simulations on cloudless days for realistic irradiance values.

Fig. 4.10 shows the comparison of the scaled measured $F^{\downarrow}_{\mathrm{dc+sl+cos+abs}}(\lambda)$ (black dashed line) and simulated $F^{\downarrow}(\lambda)$ (red solid line) for 600 nm wavelength together with the aircraft heading (top panel) for a square flight pattern on 27 December 2013. The time series of measured $F^{\downarrow}_{\mathrm{dc+sl+cos+abs}}(\lambda)$ shows discontinuities related to changes in the aircraft heading. This illustrates a horizontal misalignment as a result of the offset angles between aircraft and sensor plate. Bannehr and Schwiesow (1993) introduced the correction factor k:

$$k = \frac{\sin h_0}{\cos h_0 \sin \varPhi \sin(\varphi_0 - \psi) + \cos h_0 \sin \Theta \cos \varPhi \cos(\varphi_0 - \psi) + \sin h_0 \cos \Theta \cos \varPhi} . \tag{4.8}$$

k depends on the solar altitude angle h_0 ($h_0 = 90° - \theta_0$), the solar azimuth angle φ_0, and the attitude angles $\varPhi$ (roll, positive for left wing up), Θ (pitch, positive for nose down), and ψ (yaw, mathematical negative system with North = 0°). The roll $\varPhi$ and pitch Θ comprise of the aircraft attitude angles and the respective offset to the sensor plate:

$$\varPhi = \varPhi_{\mathrm{aircraft}} + \Delta\varPhi\,, \tag{4.9}$$

$$\Theta = \Theta_{\mathrm{aircraft}} + \Delta\Theta\,. \tag{4.10}$$

The correction factor k is applied to the measured $F^{\downarrow}_{\mathrm{dc+sl+cos+abs}}(\lambda)$ depending on the direct fraction of the global irradiance f_{dir}:

$$F^{\downarrow}_{\mathrm{dc+sl+cos+abs+att}}(\lambda) = f_{\mathrm{dir}} \cdot F^{\downarrow}_{\mathrm{dc+sl+cos+abs}}(\lambda) \cdot k + (1 - f_{\mathrm{dir}}) \cdot F^{\downarrow}_{\mathrm{dc+sl+cos+abs}}(\lambda) \tag{4.11}$$

Equations (4.8) and (4.11) are applied to the measured $F^{\downarrow}_{\mathrm{dc+sl+cos+abs}}(\lambda)$ iteratively with slightly adjusted offset angles until the discontinuities in the time series are compensated for. The best result was obtained for the offset angles $\Delta\varPhi = -0.8°$ and $\Delta\Theta = -6.4°$. The corrected time series (black solid line in Fig. 4.10) shows no dependence on the aircraft heading anymore and agrees well with the temporal evolution of the simulation. The absolute values of corrected measurements and simulations cannot be compared due to the scaling applied to the measurements. Note that only the direct fraction of the global irradiance can be corrected in this manner.

CORAS: reconstruction of SWIR data

To correct for the thermally induced dark signal, real-time sampling of $s_{\mathrm{dark}}(\lambda)$ is performed for the SWIR spectrometer of CORAS by means of an optical shutter (see Fig. 4.5). However, between 13 and 16 December 2013 and for most of January 2014, the optical shutters of CORAS did not close properly. In the following, the recovery of the original raw spectra is described.

In addition to the net signal (bright minus dark) $s_{\mathrm{dc+sl}}$, the dark signal from the measurement with closed optical shutter s_{dark} is stored by CORAS. In case the shutter did not close, the dark signal is equal to the bright signal, resulting in a net signal of around zero. The idea behind the reconstruction of the SWIR data is to get a real dark measurement from another timestep when the shutter was working. Therefore, at first, a library is created with all dark measurements $s_{\mathrm{dark,lib}_i}$ of timesteps when the shutter did work. For the timesteps of these days, the dark measurements are stored consecutively in the library file. This way, dark measurements at different near-surface

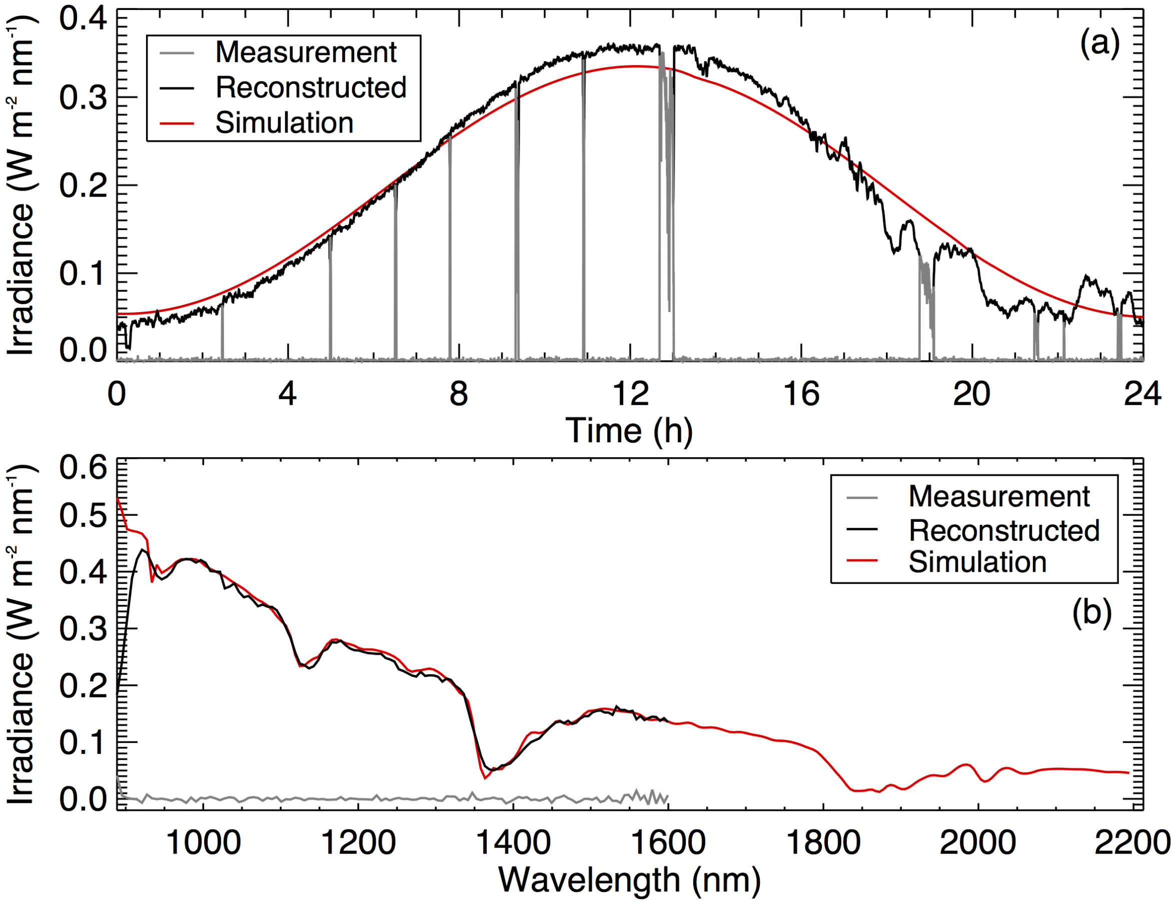

Figure 4.11: (a) Time series of downward irradiance $F^{\downarrow}_{\mathrm{dc+sl+cos+abs}}$ at 1100 nm wavelength on 15 January 2014. Grey: Calibrated, uncorrected time series. Black: Reconstructed time series. Red: Simulation. **(b)** Spectrum of downward irradiance $F^{\downarrow}_{\mathrm{dc+sl+cos+abs}}$ over SWIR wavelength range on 15 January 2014 at 10 UTC. Grey: Calibrated, uncorrected spectrum. Black: Reconstructed spectrum. Red: Simulation.

air temperatures from 13 days between 17 December 2013 and 26 January 2014 were used.

Afterwards, the SWIR data for timesteps with shutter failures is reconstructed using this library. Each measurement with a net signal lower than 50 DN at 1100 nm wavelength is regarded as a measurement with shutter failure. For these timesteps, the stored dark signal (with erroneously open shutter) actually describes a bright measurement $s^{\mathrm{failed}}_{\mathrm{dark}}$. The dark spectrum $s_{\mathrm{dark,lib}_i}$ from the library file, which is closest to the failed dark measurement $s^{\mathrm{failed}}_{\mathrm{dark}}$ is chosen. For the comparison, the water vapor absorption band at 1875 nm wavelength is chosen as the measured signal is low despite the open shutter.

If the difference between the spectrum from the library file and the failed dark measurement is lower than 10 DN, the reconstructed signal is calculated by

$$s_{\mathrm{dc+sl}} = s_{\mathrm{dark}}^{\mathrm{failed}} - s_{\mathrm{dark,lib}_i} \, . \tag{4.12}$$

In case the difference is larger than 10 DN, this offset is additionally subtracted from $s_{\mathrm{dark}}^{\mathrm{failed}}$ in Eq. (4.12). This way, $s_{\mathrm{dc+sl}}$ is reconstructed for timesteps with a shutter failure.

Figure 4.11 shows the time series at 1100 nm on 15 January 2014 and a spectrum at 10 UTC on that day for a measurement with failures of the optical shutter and for the reconstructed measurement. In order to test the applied method, the calibrated and reconstructed irradiances $F^{\downarrow}_{\mathrm{dc+sl+cos+abs}}(\lambda)$ calculated by Eq. 4.7 are compared to simulations of $F^{\downarrow}$ with libRadtran.

The time series of the original measurement (gray) reveals shutter failures for almost the entire day. The reconstructed time series (black) complements the few time steps with working optical shutter. In addition, the reconstructed irradiance agrees well with the simulations, especially until noon. As can be deduced from Fig. 4.3, the cloud cover increased from cloudless to overcast over the course of the afternoon mainly due to cirrus clouds. This could explain short periods of enhanced downward irradiance due to increased scattering in the atmosphere in early afternoon as well as irradiances lower than the simulated value after around 17 UTC. The reconstructed spectrum in Fig. 4.11 agrees well with the simulations until 1600 nm wavelength. Higher wavelengths are not considered due to the low transmission of the optical fibers. The spectrum is smoothed as one drawback of the reconstruction is increased noise. However, the good agreement between reconstructed measurement and the simulations justifies the applied method.

Illustration of post-processing for albedo calculation

The spectral snow surface albedo from the ground-based CORAS measurements is obtained by

$$\alpha(\lambda) = \frac{s^{\uparrow}_{\mathrm{dc+sl+cos+cc}}(\lambda)}{s^{\downarrow}_{\mathrm{dc+sl+cos}}(\lambda)} \, . \tag{4.13}$$

The airborne SMART measurements are additionally corrected for the attitude offset; α is calculated by

$$\alpha(\lambda) = \frac{s^{\uparrow}_{\mathrm{dc+sl+cos+cc+att}}(\lambda)}{s^{\downarrow}_{\mathrm{dc+sl+cos}}(\lambda)} \, . \tag{4.14}$$

The influence of the different calibrations and post-processing steps is illustrated in Fig. 4.12. It shows a CORAS measurement of the zenith-viewing optical inlet on 24

December 2013 (cloudless) averaged between 17:00 and 17:10 UTC. The corresponding solar zenith angle is around 64°. The measurement on late afternoon was chosen to increase the visible effect of the cosine correction due to the higher θ_0 while at the same time allowing for a sufficiently high signal. The top panel shows the effect of the dark and stray light correction. To increase lucidity, the raw measurement at the SWIR wavelength range is not shown due to its large dark current. In the VNIR, the dark correction removes an offset that is almost constant with wavelength. The remaining offset at around 300 nm wavelength (low spectrometer sensitivity) and at wavelengths larger than 1800 nm is close to zero.

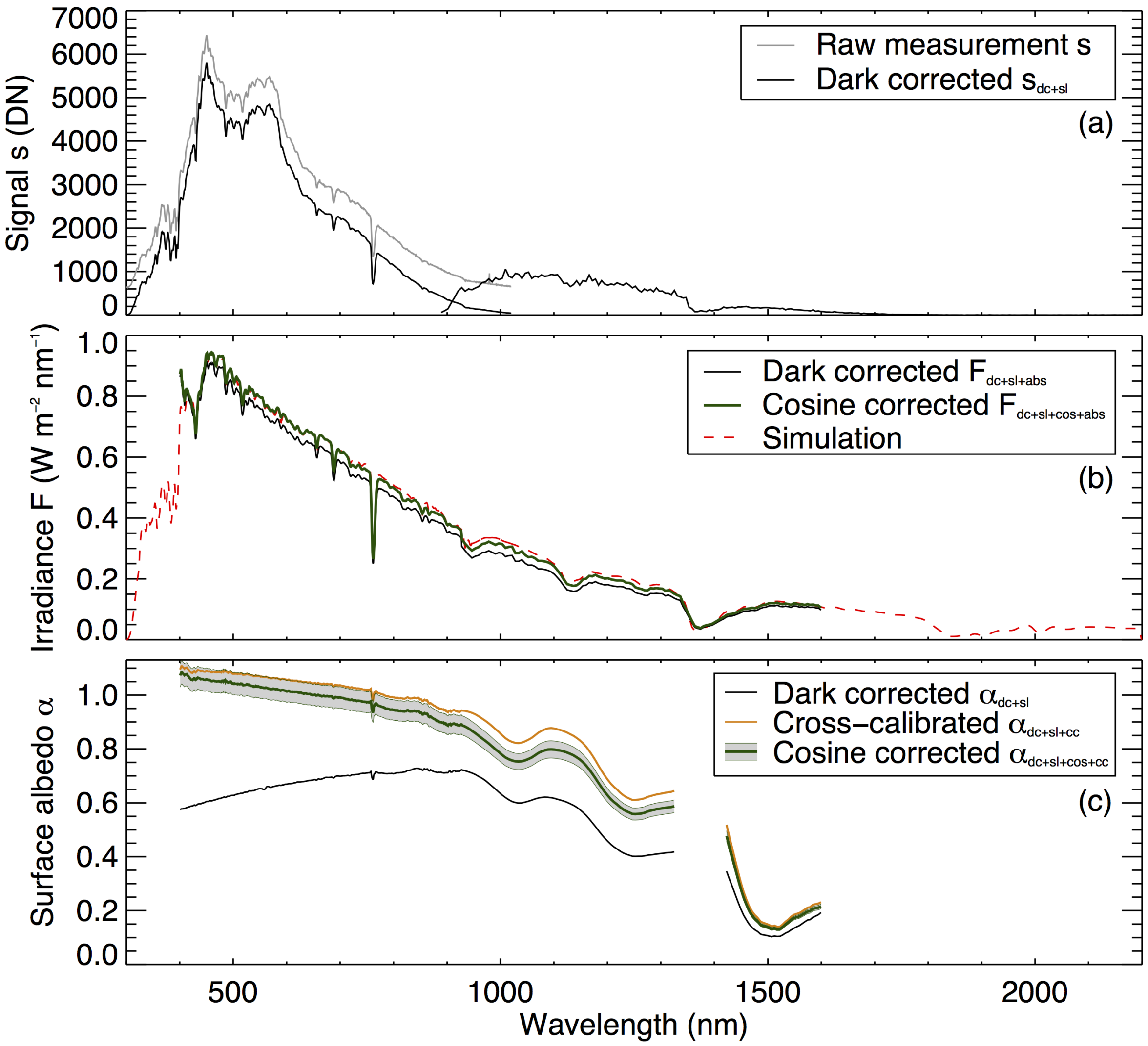

Figure 4.12: Illustration of post-processing for CORAS measurement (24 December 2013, 17:00-17:10 UTC-average, $\theta_0 = 64°$). **(a)** Gray: Raw signal s. Black: $s_{\mathrm{dc+sl}}$ for VNIR and SWIR. **(b)** Black: $F_{\mathrm{dc+sl+abs}}$. Green: $F_{\mathrm{dc+sl+cos+abs}}$. Red: Simulation. **(c)** Black: $\alpha_{\mathrm{dc+sl}}$. Orange: $\alpha_{\mathrm{dc+sl+cc}}$. Green: $\alpha_{\mathrm{dc+sl+cos+cc}}$. Shaded gray: uncertainty.

The absolute calibration step (middle panel in Fig. 4.12) strongly influences the shape of the spectrum, accounting for the lower spectrometer sensitivities at the edges of its wavelength range. The measurements are shown from 400 nm; shorter wavelengths are excluded due to the large noise in C_{abs} as a result of the low signal during the absolute calibration in the laboratory at these wavelengths. The comparison of the dark corrected measurement (black) with simulations by libRadtran using DISORT (red dashed line) for the downward irradiance reveals deviations that are compensated for by the application of the cosine correction (green solid line). Hence, the calibrated irradiance measured by CORAS agrees well with the simulations. This indicates an adequate calibration process.

For the calculation of the surface albedo (bottom panel in Fig. 4.12), the absolute calibration has no influence. The largest effect on the shape of the surface albedo is exercised by the cross-calibration step. Especially in the VNIR, the slope of the surface albedo is strongly affected which is expected from the spectral behavior of the cross-calibration factor C_{cc} (compare Fig. 4.9). The temporal stability of C_{cc} is a prerequisite for robust albedo measurements. At wavelengths below 750 nm, the surface albedo exceeds one. This is an unphysical result but stems from the measurement uncertainties especially at larger solar zenith angles and the fact that the true albedo values of snow surfaces are already close to one in that spectral range. This artifact has been reported in other studies (e.g., Wuttke et al., 2006; Carmagnola et al., 2013; Libois et al., 2015; Pedersen et al., 2015). However, the range of measurement uncertainties (shaded gray in Fig. 4.12) extends to values below one. No further screening of the data for albedo values above one is done as this work focuses on the SWIR part of the EM spectrum.

Data filtering

In 45 % of the CORAS measurements, the optical shutter failed and the SWIR spectrum was reconstructed. No additional filtering due to instrument failures was applied. The data filtering applied to the SMART measurements is exemplarily shown in Fig. 4.13 for the research flight on 27 December 2013. The triangular flight pattern covered an area north-east of Kohnen station. The different colors denote the times and corresponding locations of excluded data due to instrument failures (green) and the aircraft attitude (purple). Instrument failures include the SWIR spectrometer; data is excluded when the SWIR spectrometer was not working or during takeoff and landing of the aircraft. Failures of the horizontal stabilization system dominated the instrument failures during that flight (no active stabilization between 11:45-12:20 UTC).

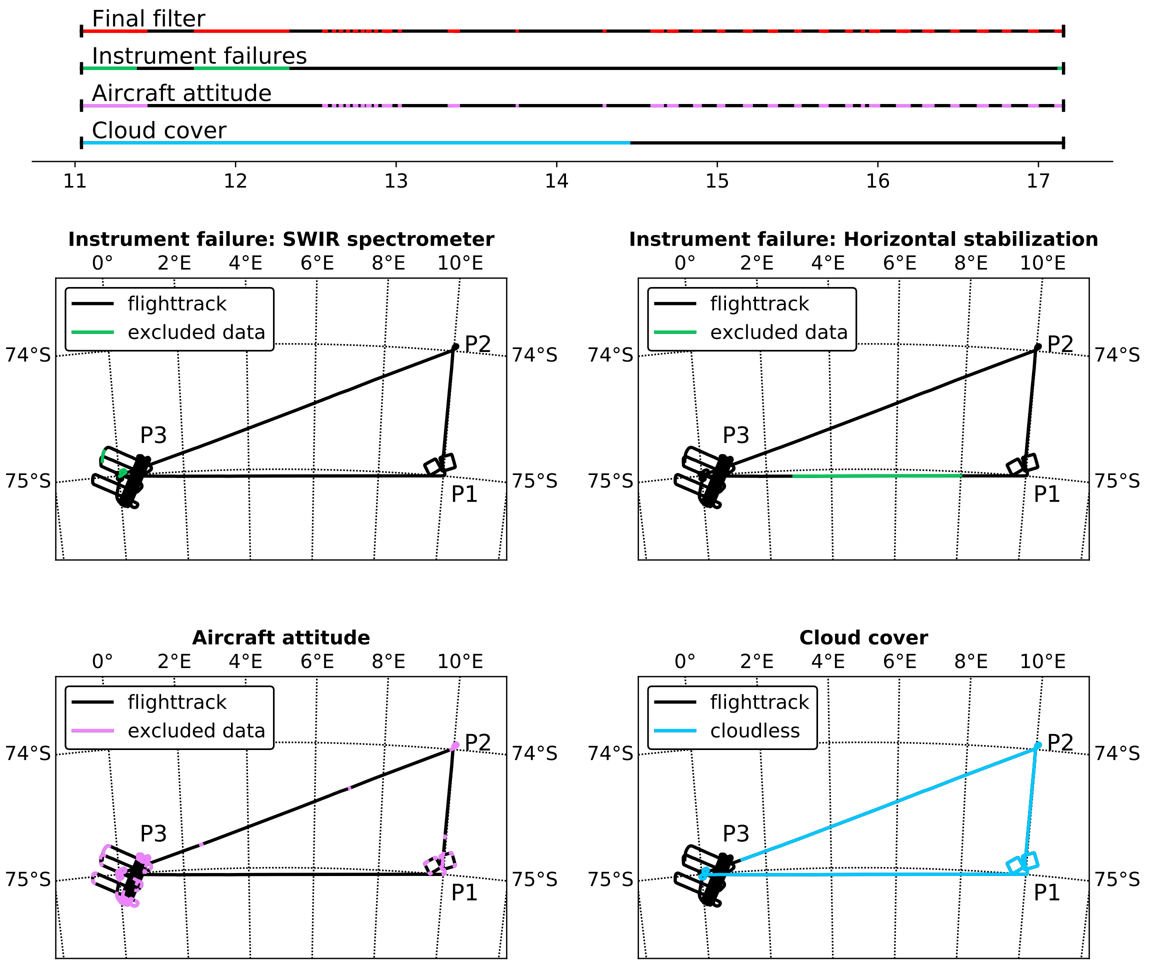

Figure 4.13: Illustration of the data filter (red) applied to the airborne SMART measurements depending on the status of the SWIR spectrometer and the horizontal stabilization (both green) as well as the aircraft attitude (purple). In addition, cloudless periods are are flagged in blue.

Furthermore, the active stabilization is only assumed valid for roll and pitch angles below ±5°. This mainly excludes the turns and periods of fast ascent or descent. In addition, cloudless periods are shown in blue. Note the square flight pattern in the vicinity of way point P1. The two squares were used for the correction of the attitude offset (compare Fig. 4.10). As can be seen from Fig. 4.13, the requirements for this flight pattern, namely a working horizontal stabilization and no cloud cover above the aircraft, were met. The final data filter (red) combines instrument failures and the aircraft attitude filter.

The stabilization failed for the entire flights on 24 and 25 December 2013 (three flights). On 26 December, the flight was aborted due to bad weather after 15 minutes. This left 14 research flights for the analysis between 27 December and 5 January 2014.

During this time, the SWIR spectrometers were not working for 9 % of the airborne measurements. The horizontal stabilization failed in 15 % of the time; similarly, 15 % of the measurements were excluded due to the aircraft attitude. In total, 27 % of the data were excluded and not used for the data analysis. From the remaining data, 58 % of the spectra were collected in cloudless conditions.

4.2.4 Measurement uncertainties

The uncertainties of surface albedo measurements with CORAS range between 4 to 8 % depending on wavelength and combining different sources of instrumental errors, namely (a) the signal-to-noise ratio, (b) the accuracy of the dark correction, (c) the wavelength calibration, (d) the accuracy of the cross-calibration, and (d) the non-ideal cosine response of the optical inlets.

The signal-to-noise ratio (χ_{snr}) is estimated using the mean noise between 1950-2213 nm wavelength (± 20 DN) where the transmissivity of the optical fibers and the sensitivity of the spectrometer is low and the signal during noon on 24 December 2013 (around 1000 DN). It accounts for 1.3-3.0 % uncertainty between 900 and 1330 nm and strongly increases towards longer wavelengths due to the low signals at these wavelengths.

Dark spectra were recorded constantly throughout the measurements resulting in a reliable correction for dark current and stray light within the spectrometer. After dark correction, the mean net signal at wavelengths without incoming radiation (1950-2213 nm) is 1.4 ± 7.7 DN. The residual dark signal of around 1 DN compared to around 1000 DN maximum signal (noon on 24 December 2013) results in an estimated uncertainty due to the dark current and stray light correction of 0.1 % (χ_{dcsl}).

The wavelength calibration of the spectrometer was done using emission lines of spectral lamps. The corresponding uncertainty (χ_{wl}) was determined from the FWHM of the spectrometers and is 1.0 %.

For albedo measurements, the two optical inlets were cross-calibrated with an identical radiation source at four times during the observation period. The temporal stability of this cross-calibration (χ_{cc}) is estimated with 1.0-4.5 % depending on wavelength.

The azimuthal stability of the correction factors of 3.5 % was used to estimate the instrumental errors attributed to the non-ideal cosine response of the optical inlets (χ_{cos}).

All instrumental errors are assumed to be uncorrelated and random. From the Gaussian equation for normally-distributed errors, the uncertainty of the signal s due to

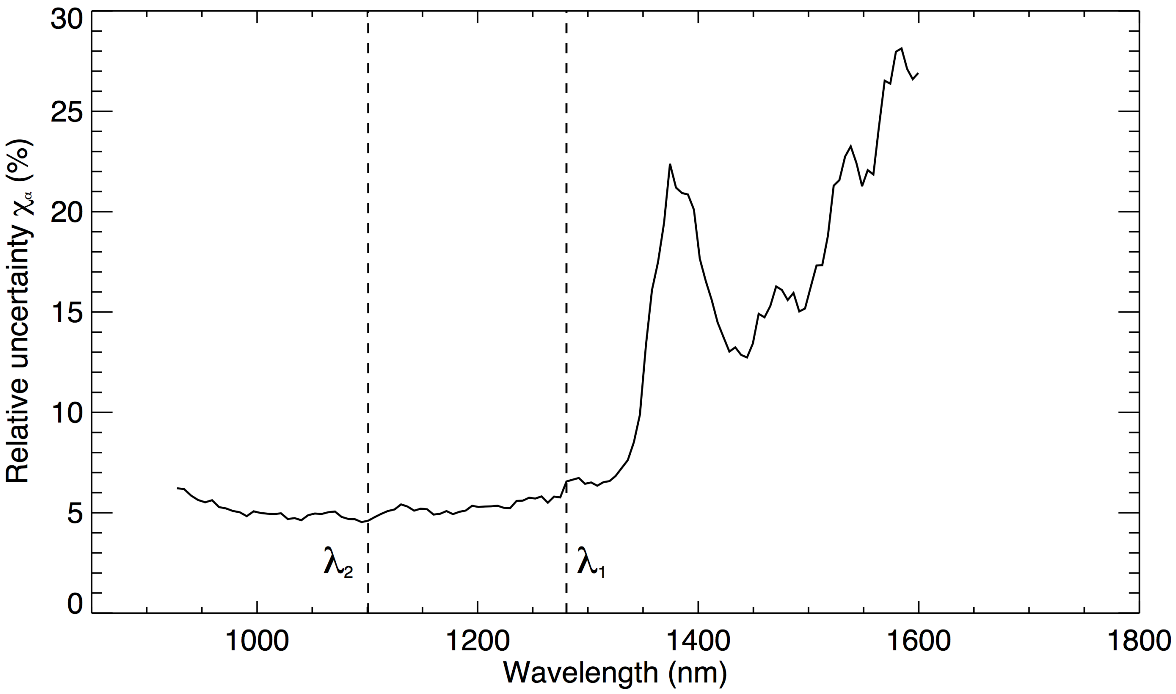

Figure 4.14: Relative uncertainties of the CORAS measurements in dependence of the wavelength.

spectrometer errors is:

$$\chi_{\mathrm{spec}} = \sqrt{(\chi_{\mathrm{snr}})^2 + (\chi_{\mathrm{dcsl}})^2 + (\chi_{\mathrm{wl}})^2} \tag{4.15}$$

One albedo measurement combines the signal uncertainties of two measurements (zenith- and nadir-viewing), the uncertainty due to the cross-calibration and the cosine error (already includes both optical inlets):

$$\chi_\alpha = \sqrt{2 \cdot (\chi_{\mathrm{spec}})^2 + (\chi_{\mathrm{cc}})^2 + (\chi_{\mathrm{cos}})^2} \tag{4.16}$$

The overall relative uncertainties of the albedo measurements with CORAS are shown in Fig. 4.14. They range between 4.0 and 8.0 % below 1350 nm wavelength. It strongly increases for longer wavelengths due to the low signal-to-noise ratio. The analyzed measurement times were carefully selected to avoid errors due to frost formation and shadow effects which were typically observed during early morning.

The albedo measurements with SMART have an estimated uncertainty between 4.1 to 8.1 % also taking into consideration uncertainties due to the active horizontal stabilization of 1.0 %.

4.3 Directional reflectance measurements using a digital camera

The digital camera Canon EOS-1D Mark III was used for the airborne HDRF measurements of the snow surface. Its installation on the bottom frame of the Polar 6 research aircraft is shown in Fig. 4.2.

The EOS-1D Mark III is a digital single-lens reflex camera with a complementary metal oxide semiconductor (CMOS) image sensor. The CMOS sensor covers 3908×2600 picture elements (pixels) on a sensor area of $28.1 \times 18.7\,\mathrm{mm}$ (Advanced Photo System APS-H format). During the observations, the camera was configured with the 8 mm F3.5 EX DG Circular Fisheye lens by Sigma.

The fisheye lens with a FOV of 180° enables the camera to collect solar radiation from the entire lower hemisphere. To relate each sensor pixel to a camera viewing zenith and azimuth angle (θ_v, φ_v), a geometric calibration of the camera-lens system was applied. The measured signal was converted into the physical quantity of radiance (unit of $\mathrm{W\,m^{-2}\,sr^{-1}}$) by means of a radiometric calibration in the laboratory. As the camera is fixed to the aircraft frame, a correction for the aircraft attitude was implemented. In the following, the characteristics of the camera (linearity, dark current, electronic noise, relative spectral response, footprint) as well as the different steps of calibration (geometric and radiometric) are discussed.

4.3.1 Characterization of camera properties

The schematic of the camera measurements is shown in Fig. 4.15. The fisheye lens consists of 11 lenses ordered in 6 groups and directs the incident solar radiation onto the CMOS sensor. The larger the angle of incidence, the longer the distance of the receiving pixel to the image center (yellow and red beam paths in Fig. 4.15). The CMOS sensor consists of an array of pixels that each include a photodiode, electrodes, and an amplifier. Within the photodiodes made of silicon, charges are generated based on the internal photoelectric effect. The energy of a photon is proportional to its frequency. If the photon energy is higher than the band gap (energy difference between top of valence band and bottom of conduction band in semiconductors) for silicon (1.11 eV at 300 K), electrons are lifted from the valence to the conduction band. Thereby, vacant positions are left in the valence band and, thus, electron-hole pairs are generated. By applying an external voltage, electrons and holes move in opposite directions and charge carriers are stored within the potential well caused by

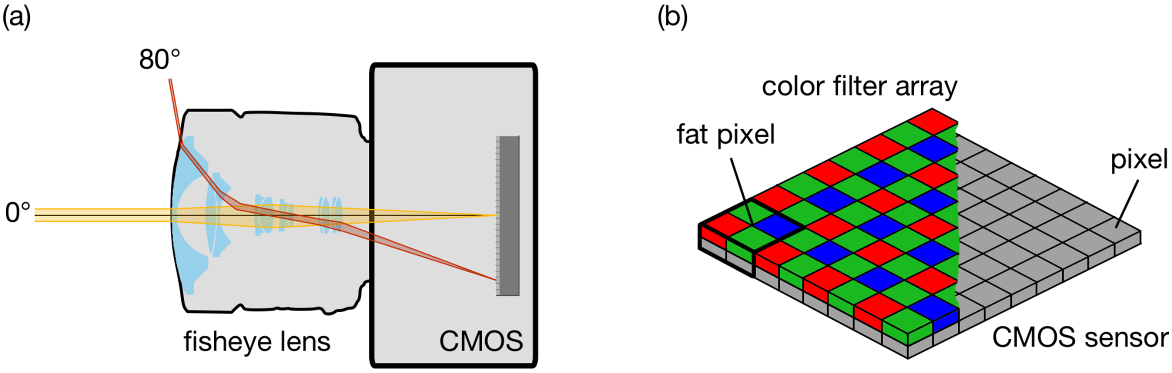

Figure 4.15: Schematic of the measurement principle of the digital camera.

the voltage of the electrodes. In contrast to traditional charge coupled device (CCD) sensors, CMOS sensors utilize an active pixel sensor where an amplifier is part of each pixel. After exposure, the amplifier converts the charges into a voltage signal which is digitized by an analog-to-digital converter. The main advantage of CMOS compared to CCD sensors is its fast readout and small power consumption. In addition, CMOS sensors are characterized by low noise and dark current (Kaufmann, 2010).

Color information is obtained by means of a color filter array (CFA) in front of the CMOS sensor (see Fig. 4.15). The CFA consists of red (R), green (G), and blue (B) color filters which determine the spectral response of the underlying pixel. The repetitive pattern (the so-called Bayer pattern) of the filter arrangement relates each block of 2×2 photodetectors to one R filter, two G filters, and one B filter. A complex demosaicing algorithm attributes R, G, and B values to each single pixel using surrounding photodetector outputs.

Image format

The measured signal s (in digital numbers, DN) is saved essentially verbatim in the proprietary Raw format CR2 (Canon Raw version 2). This ensures highest flexibility in the data analysis as no interpolation or white balance color correction is applied to the raw[1] data. Full control over the post-processing steps is a prerequisite for radiometric measurements. The Raw photos are decoded utilizing the open source tool DCRAW (Coffin, 2017). The CR2 images are converted into portable pixmap format (ppm) files by the command

```
dcraw -c -v -t 0 -o 0 -r 1 1 1 1 -k 0 -S 16383 -4 image.CR2 > image.ppm
```

---

[1] Within this thesis, 'raw' denotes the raw sensor data. However, the proprietary output format 'Raw' is capitalized.

The darkness level was set to 0 DN (see below) and the saturation level to 16383 DN as the camera captures images with color depth of 14 bit. In between, the raw data is linearly interpolated. The multipliers for all channels are set to one meaning no white balance color correction is applied. The dynamic range of the output file is 16 bit (saturation at 65536 DN).

Unfortunately, during the airborne measurements, the camera was set to produce sRaw output format (small raw). The image saved in sRaw format has approximately one-fourth of the number of pixels compared to the Raw image (1944 × 1296). Originally, this smaller files should provide an alternative to the larger Raw files while still providing the benefits of raw sensor data. Note that as both Raw and sRaw are proprietary image formats, the manufacturer does not provide detailed information about the internal processing of these formats. Kerr (2015) provide an extensive insight into Raw and sRaw based on reverse engineering. A detailed description is beyond the scope of this thesis. In short, a CFA cluster of four photodetectors is considered to correspond to one pixel of the sRaw format (a so-called fat pixel, see Fig. 4.15. In contrast to the Raw format, at some point chrominance subsampling is performed. This process is irreversible (Kerr, 2015). Therefore, it is impossible to reconstruct the raw sensor data from an sRaw image.

Thus, in using sRaw as output format during the measurements, the data from 75 % of the sensor pixels were lost and the image resolution was decreased. In addition, the internal chrominance subsampling applied by the camera might undermine the advantages of raw data output (e.g. a known and reproducible correlation between incident radiation and generated electron-hole pairs in the photodiodes). This highlights the need for a thorough investigation and characterization of the camera properties.

Linearity of the sensor

An advantage of CMOS sensors is their linear correlation between the intensity of the incident radiation and the generated electron-hole pairs within the photodiode. Only if saturation is reached, no more charge carriers can be stored in the potential well and deviations from the linear response occur.

To characterize the linearity of the sensor, photos from the radiation emitted by an integrating sphere were taken with the camera. An integrating sphere is coated with a diffusely reflecting material (Polytetrafluoroethylene). A 100 W halogen lamp with adjustable aperture emits radiation which is reflected multiple times within the sphere before leaving it through its aperture. The emitted radiation from the integrating

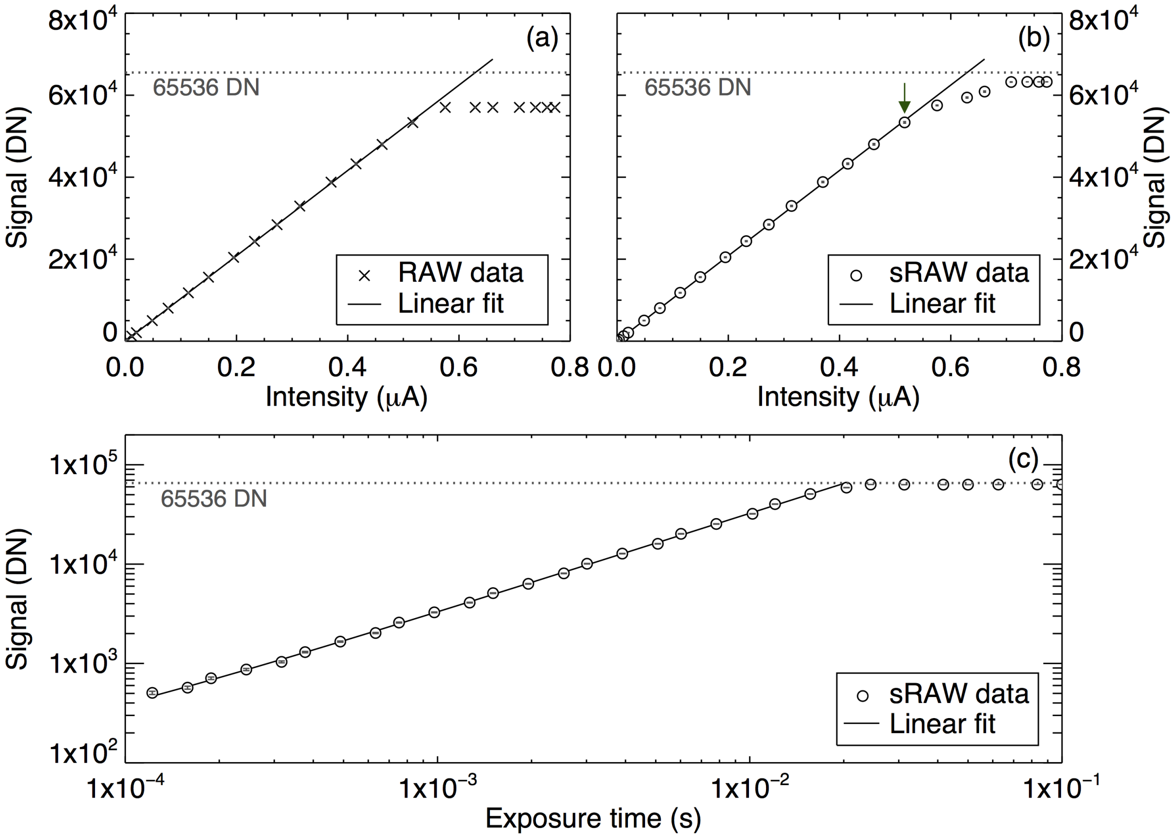

Figure 4.16: (a) Measured signal in dependence of intensity of incident radiation for optometer currents at integrating sphere between 0.7725 µA and 0 µA at constant exposure time of 1/40 s. Averaged over pixels at sensor centre. File format: Raw. **(b)** Same as (a) but for sRaw format. Green arrow marks the upper limit for linearity at 53363 DN. **(c)** Measured signal s_{sRaw} in dependence of exposure time for times between 1/8000 and 1/10 s.

sphere is unpolarized and uniform. The intensity of the lamp is measured with an optometer. The photos were taken for different intensities of the incident radiation and for different exposure times of the camera. The f-number was set to f/8, the ISO number to 125, and measurements were analyzed for the channel G. If not stated differently, this configuration holds true for all measurements presented in this thesis. Figure 4.16 shows the measured signal s in dependence of the incident radiation for optometer currents at the integrating sphere $\mathcal{I}_{\mathrm{sphere}}$[2] between 0.7725 µA down to 0 µA at constant exposure time of 1/40 s. At each measurement, the camera simultaneously saved the photo as Raw and sRaw for comparison.

For both file formats, the measured raw data linearly depends on the intensity of the incident radiation until saturation is reached. For Raw, the saturation level was at 57023 DN which is slightly lower than the theoretical dynamic range of 16 bit

---

[2] To avoid confusion with the radiance I, the electric current within this thesis is denoted with the calligraphic $\mathcal{I}$

(65535 DN). For sRaw, the saturation level was 63343 DN. However, starting from 53363 DN (marked with green arrow in Fig. 4.16) and approaching the saturation level, the relationship between s and the intensity gets less linear. This could be a consequence of the internal processing for the sRaw output as described above. However, below 53363 DN, the coefficient of correlation (R^2) equals that of the Raw measurements and was exceptionally high with 0.99998. The equation for the linear regression is given by

$$s_{\mathrm{sRaw}} = 104133.8\,\mathrm{DN}\,\mu\mathrm{A}^{-1} \cdot \mathcal{I}_{\mathrm{sphere}} + 1.7\,\mathrm{DN}. \tag{4.17}$$

For the determination of Eq. 4.17, the measurements above the green arrow (53363 DN) were omitted. The dependence of the measured signal s_{sRaw} with respect to varying exposure times (1/8000 to 1/10 s) at constant $\mathcal{I}_{\mathrm{sphere}}$ of 0.7724 µA shows a similar linear behavior ($R^2 = 0.99912$). Although still present, the logarithmic scaling of the axes masks the deviation from linearity at high signal values.

To make full use of the large FOV of the lens, a similar linear response of the measured signal with respect to the incident intensity is needed at the edge of the camera-lens system. In this regard, the camera was rotated such that the illuminated area was at the edge of the image sensor. Similar results were found as compared to the central illumination.

In summary, a distinct linear relationship between s and the incident intensity of the radiation was found. For the sRaw format it is limited to measured signals below approximately 53000 DN. However, during all research flights, this upper limit was rarely measured. From a total of 42,373 photos, just 189 (0.4 %) contained pixels with signals higher than 53000 DN. Those photographs were excluded from the analysis.

Dark current and electronic noise

At temperatures above 0 K, electrons can be lifted to the conduction band even without incident EM radiation due to their thermal movement. The signal s_{dc} measured in the absence of incident radiation is called dark current and depends on the temperature of the sensor, the exposure time, and the pixel position. The exposure time mainly used throughout the measurements was 1/1000 s. At this configuration, 100 dark photos were taken with the cap on the camera at a temperature of around 20 °C. The mean value over all pixels and photos was 5.0 DN with a standard deviation of 5.3 DN. Compared to the dynamic range, the dark current is negligible. The measurements were taken at considerably lower temperatures than the dark measurements in the laboratory (see Fig. 4.3). Thus, the dark current during the flights was, if at all, even lower.

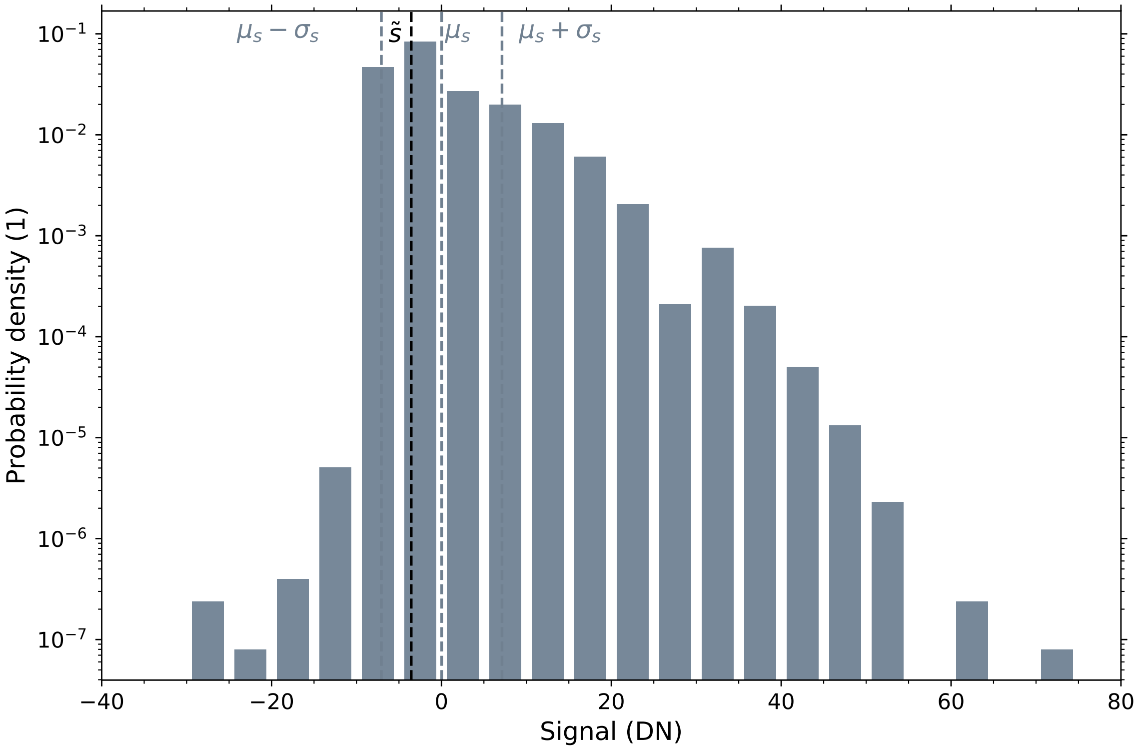

Figure 4.17: Histogram of probability densities for signals of the noise image. Exposure time: 1/1000 s.

Fast readout of the pixels can lead to a loss of electrons, whereas slow readout can lead to errors due to the non-ideal isolation of the single pixels. This read-out noise s_{noise} is independent from the exposure time or the measured signal. To determine the electronic noise, the 100 dark photos were averaged and subtracted from a single dark photograph. The resulting noise image had a median value $\tilde{s}$ of -3.6 DN and a mean value (μ_{s}) and standard deviation (σ_{s}) of 0.03 ± 7.10 DN. The probability densities of the signals of the noise image are shown in Fig. 4.17. The histogram shows a unimodal, asymmetric distribution that is skewed to the right with outliers up to 71.2 DN and -29.2 DN. The standard deviation σ_{s} of 7.10 DN describes the read-out noise.

Relative spectral response

Information on the spectral response of the camera is needed for the radiometric calibration. It determines the extent to which radiation of a certain wavelength passes the fisheye-lens as well as the CFA and is registered by the photodiodes. In this regard, the relative spectral response (RSR) function in units nm^{-1} of the three camera channels

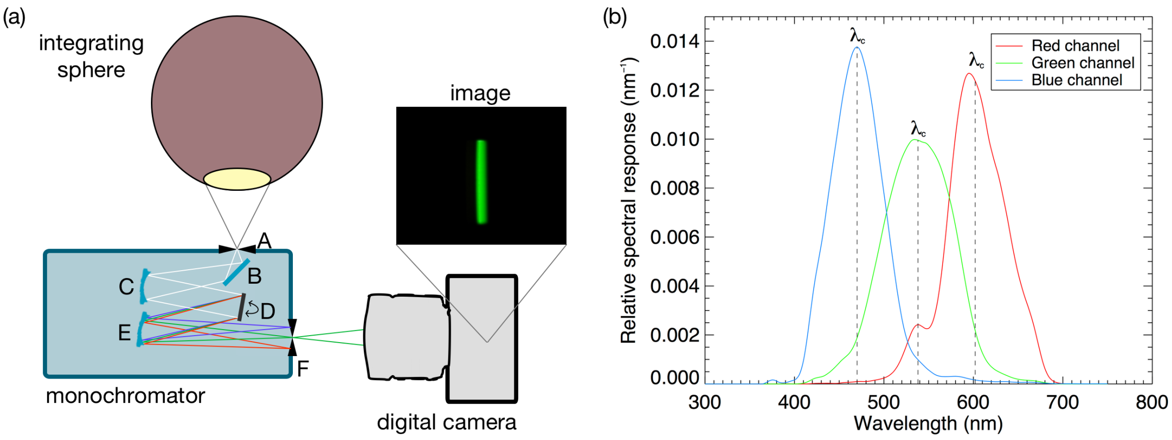

Figure 4.18: Relative spectral response function.

is defined as

$$\mathrm{RSR}(\lambda) = \frac{T_\mathrm{c}(\lambda)}{\int\limits_0^\infty T_\mathrm{c}(\lambda)\,\mathrm{d}\lambda}. \tag{4.18}$$

$T_\mathrm{c}(\lambda)$ with $\mathrm{c} = \mathrm{R}, \mathrm{G}, \mathrm{B}$ denotes the dimensionless spectral transmission coefficients. The RSR function is normalized such that

$$\int\limits_0^\infty \mathrm{RSR}(\lambda)\,\mathrm{d}\lambda = 1. \tag{4.19}$$

The setup for the measurement of the RSR functions of the camera in the laboratory is illustrated in Fig. 4.18. The spectral radiance $I_\mathrm{sphere}(\lambda)$ emitted from an integrating sphere falls through the entrance slit (A) of a monochromator (Zolix Omni-λ305) and is reflected on a mirror (B) and a concave mirror (C) onto a dispersing element (grating, D). The angle of reflection at the rotatable grating depends on the wavelength. In adjusting the position of the grating, the wavelength of the radiation leaving the monochromator via a second concave mirror (E) through the exit slit (F) is tunable. This way, the wavelength of the outgoing radiation was varied between 300 and 750 nm in increments of 5 nm wavelength. For each separate wavelength, the camera measured the signal $s_\mathrm{c}(\lambda)$ as the average over the pixels that received radiation from the exit slit. The spectral transmission coefficient T_c is then calculated as the smoothed ratio between s_c and I_sphere:

$$T_\mathrm{c}(\lambda) = \frac{s_\mathrm{c}(\lambda)}{I_\mathrm{sphere}(\lambda)}. \tag{4.20}$$

Thus, the RSR functions are calculated using Eqs. 4.18 and 4.20 by

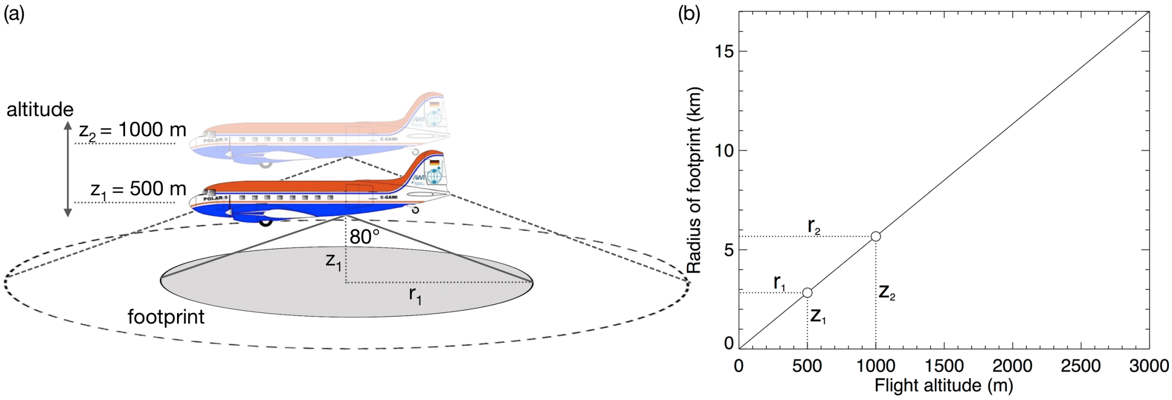

Figure 4.19: Footprint of HDRF measurements in dependence of the flight altitude.

$$\mathrm{RSR}(\lambda) = \frac{\frac{s_\mathrm{c}(\lambda)}{I_\mathrm{sphere}(\lambda)}}{\int\limits_0^\infty \frac{s_\mathrm{c}(\lambda)}{I_\mathrm{sphere}(\lambda)}\,\mathrm{d}\lambda}, \tag{4.21}$$

and are shown in Fig. 4.18. The central wavelengths λ_c of the non-Gaussian RSR functions are 602 nm (R), 538 nm (G), and 470 nm (B). Their full width at half maximum (FWHM) varies between 68 nm for the blue channel and 95 nm for the green channel. Table 4.2 lists the characteristic values for the RSR functions.

Table 4.2: Central wavelengths λ_c and FWHM for the RSR functions of the red, green, and blue camera channels.

Channel	Central wavelength λ_c (nm)	FWHM (nm)
Red	602	70
Green	538	95
Blue	470	68

Field of view and camera footprint

The FOV of the camera is 180° due to the optics of the fisheye lens. However, the camera is installed slightly above the lower aircraft body so that the camera is protected especially during takeoff and landing. Therefore, parts of the aircraft frame are constantly in the FOV of the camera, which is why the effective FOV is reduced to approximately 160°.

From trigonometric considerations, the footprint of the camera (twice the radius r of the disc on the ground pictured by the camera) depends on the flight altitude z and the FOV:

$$r = z \cdot \tan 80^\circ. \tag{4.22}$$

The geometry for the footprint calculation and the dependence of the r on the flight altitude is illustrated in Fig. 4.19. At an altitude of 100 m, the radius is 570 m and the footprint approximately 1 km. The footprint grows with increasing altitude to 5.7 km ($z_1 = 500$ m) and 11.3 km ($z_2 = 1000$ m).

4.3.2 Geometric calibration

The geometric calibration of the camera-lens system relates each sensor pixel to a viewing zenith and azimuth angle (θ_v, φ_v). Often, the process of geometric calibration of a camera involves calibration equipment or the use of planar targets such as check patterns (e.g., Tsai, 1987; Urquhart et al., 2016). Within this work, a stellar calibration method is applied (e.g., Schmid, 1974; Klaus et al., 2004; Mori et al., 2013; Urquhart et al., 2016) utilizing the high precision to which the positions of stellar objects are known.

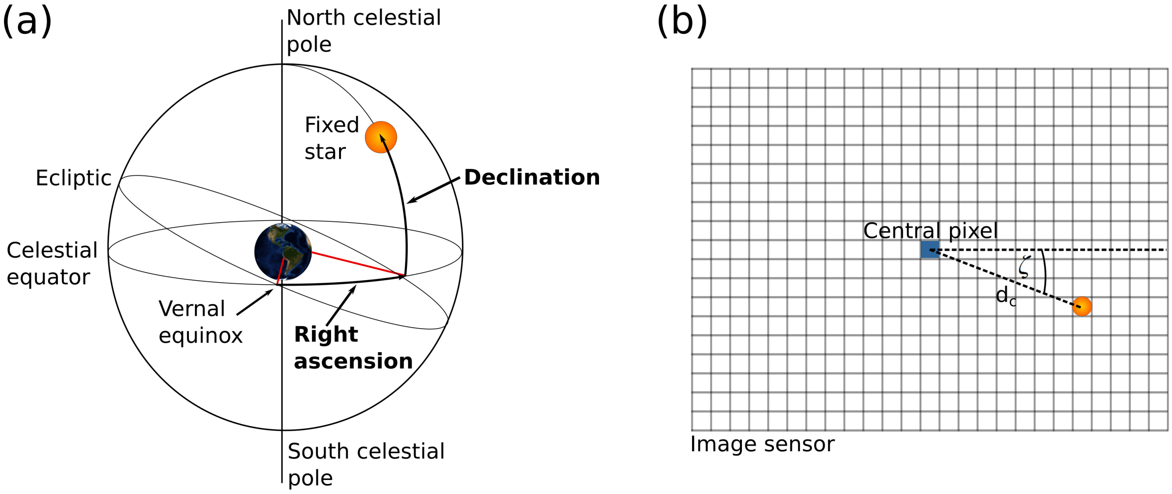

Figure 4.20: Concept of the geometric calibration. **(a)** Definition of the equatorial coordinate system. **(b)** Image of the fixed star on the sensor. d_c denotes the distance of the exposed to the central pixel. The angle to the image horizontal is given as ζ.

Figure 4.20 illustrates the definition of the equatorial coordinate system. The fixed star is positioned on the celestial sphere, an imaginary sphere with the Earth in its centre. Projected onto this sphere are the Earth's equator and orbit plane (ecliptic). The

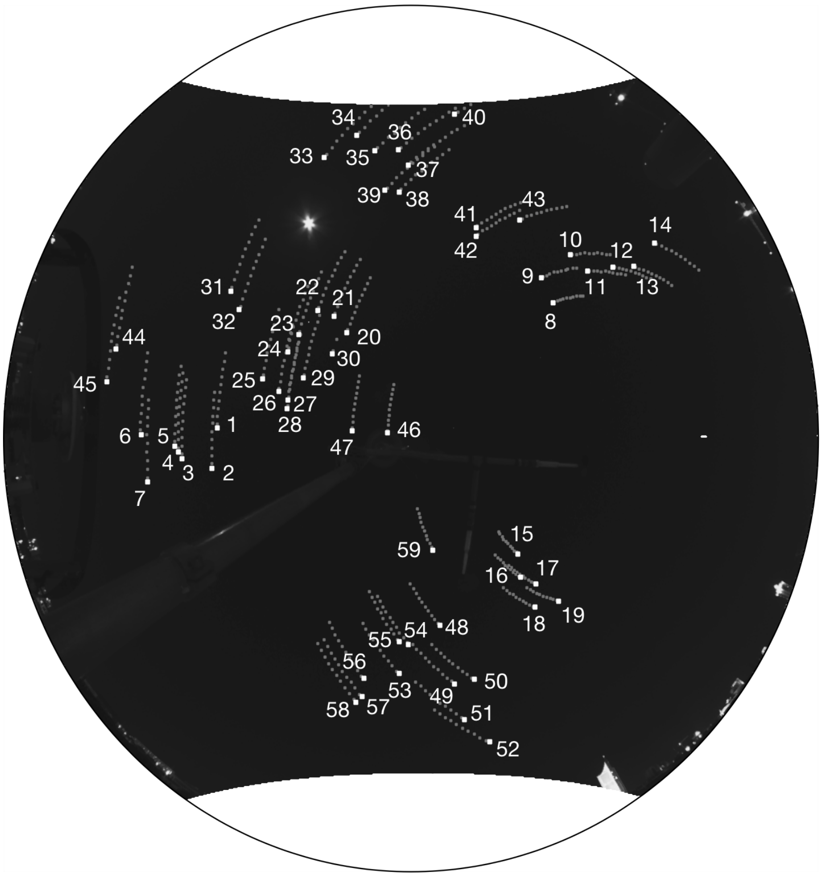

Figure 4.21: Image taken during geometric calibration at LIM on 12 February 2014. Up to 59 fixed stars were manually identified in each calibration picture (white dots). Composite of stellar positions for the twelve images used in the calibration process (gray dots). The names, RA and δ for the numbered fixed stars are tabulated in Appendix A.

angle between celestial equator and ecliptic is 23.5°. The vernal equinox denotes the intersection between the planes of the celestial equator and the ecliptic on 21 March. The celestial coordinates include the right ascension (RA) and the declination (δ). They are analogous to the longitude and latitude on Earth. The RA of a fixed star gives its distance along the celestial equator from the vernal equinox. The declination δ is measured north or south of the celestial equator. The RA and δ of fixed star change slowly over time due to the precession of the Earth's axis of rotation. Hence, star catalogues give the celestial coordinates of a fixed star to a reference epoch. Currently, the standard epoch J2000 is used equivalent to approximately noon on 1 January 2000 UTC.

On 12 February 2014, pictures of the night sky were taken on the roof of the Leipzig Institute for Meteorology (LIM). The exposure time was set to 20 s. The horizontal alignment of the camera frame was checked with the miniature attitude heading reference system 3DM-GX3® by MicroStrain and was better than 0.2° in both roll and

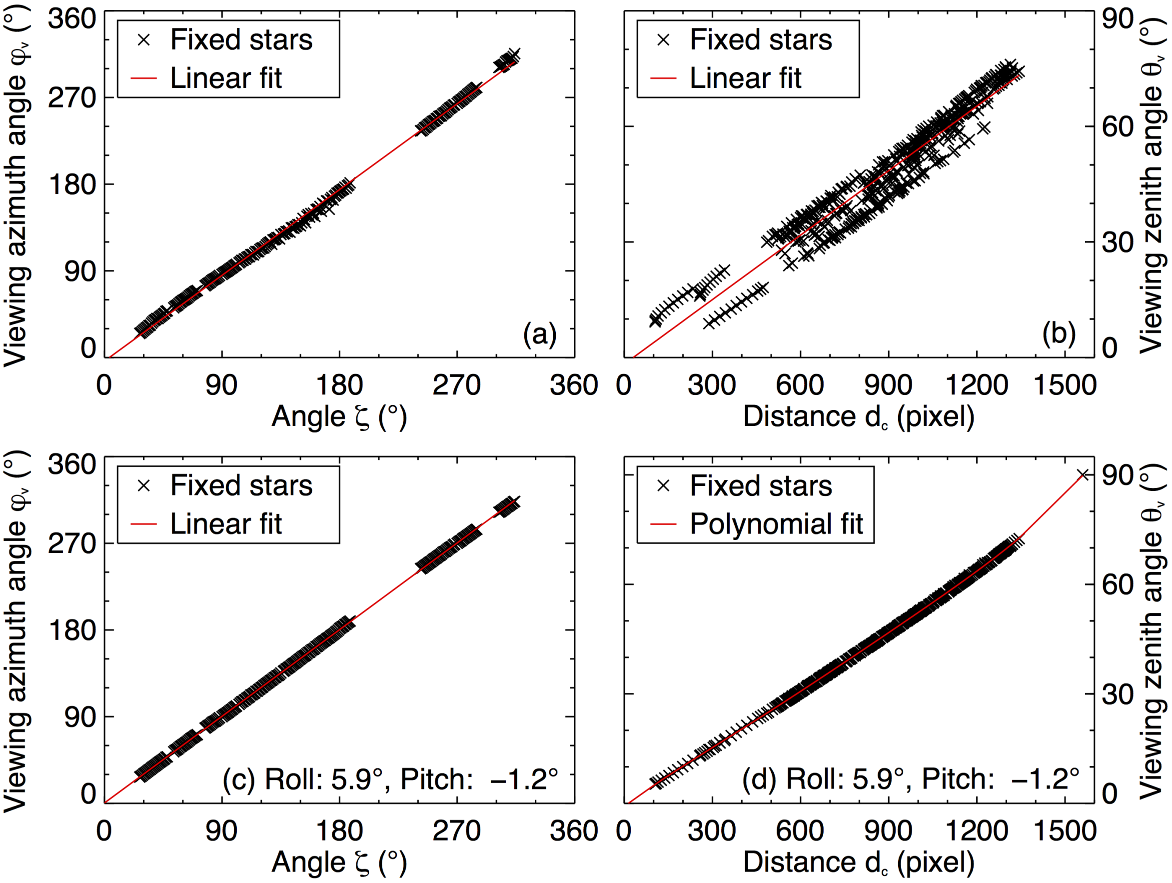

Figure 4.22: **(a)** Viewing azimuth angle φ_v with respect to angle to the image horizontal ζ for all stellar positions. Red: Linear fit. **(b)** Viewing zenith angle θ_v with respect to distance to image center d_c for all stellar positions. Red: Linear fit. **(c)** Same as in (a), but corrected for camera attitude. **(d)** Same as in (b), but corrected for camera attitude.

pitch direction. An exemplary picture of the night sky is shown in Fig. 4.21. In each photograph, up to 66 fixed stars were manually identified using star constellations and the apparent magnitude (brightness) of the stars. Using subsequent images over the course of the night, 684 different star positions could be utilized for the geometric calibration (see Fig. 4.21). The RA and δ data for the identified stars were taken from the Yale Bright Star Catalogue and are tabulated in Appendix A.

The corresponding camera viewing zenith and azimuth angles θ_v and φ_v are calculated by

$$\sin(90^\circ - \theta_v) = \sin\delta \cdot \sin\varphi + \cos\delta \cdot \cos\varphi \cdot \cos \mathrm{LHA}\,, \tag{4.23}$$

and

$$\cos\varphi_\mathrm{v} = \frac{\sin\delta - \sin(90^\circ - \theta_\mathrm{v}) \cdot \sin\varphi}{\cos(90^\circ - \theta_\mathrm{v}) \cdot \cos\varphi}\,. \tag{4.24}$$

The local hour angle (LHA) depends on the local siderial time (LST) and the RA,

$$\mathrm{LHA} = \mathrm{LST} - \mathrm{RA}\,, \tag{4.25}$$

whereas the LST is calculated by

$$\mathrm{LST} = 100.46 + 0.985647 \cdot d_{\mathrm{J2000}} + 15.0 \cdot t_{\mathrm{UTC}} + \Lambda\,. \tag{4.26}$$

The latitude (φ) and longitude (Λ) of the LIM in Leipzig are 51.3° and 12.4°, respectively. The number of days since the standard epoch J2000 is denoted with d_{J2000}; t_{UTC} gives the time of measurement (in UTC). The true direction of the incident radiation deviates from the apparent direction due to refraction in the Earth's atmosphere. This was corrected for the time of measurement (air pressure: 993 hPa, near-surface air temperature: 4.1 °C). For example, the calculation of θ_{v} and φ_{v} for the fixed star Rigel ($\delta = -8.2°$, RA $= 78.6°$, No. 7 in Fig. 4.21) yields 60.4° and 257.1°, respectively.

Figure 4.22 shows the viewing angles θ_{v} as calculated for the 684 different stars with respect to the distance to the image center (d_{c}) and φ_{v} with respect to the angle to the image horizontal (ζ). The definitions for d_{c} and ζ are shown in Fig. 4.20. In both cases, a nearly linear relationship is found. However, the deviations especially for θ_{v} could be significantly reduced by applying a correction for the camera attitude (roll angle: 5.9°, pitch angle: -1.2°). The correction for the camera attitude is further described in Sect. 4.3.4. Hence, there is an obvious discrepancy between the alignment of the camera frame (which has been tested) and the alignment of the sensor–lens system. The corrected viewing angles θ_{v} and φ_{v} are also shown in Fig. 4.22 yielding linear correlation coefficients close to one. Eventually, the respective polynomial fits for $\theta_{\mathrm{v}}(d_{\mathrm{c}})$ (degree: 5) and $\varphi_{\mathrm{v}}(\zeta)$ (degree: 1) are used to calculate the viewing angles for each sensor pixel of the camera:

$$\theta_{\mathrm{v}} = \sum_{i=0}^{5} c_i \cdot (2 \cdot d_{\mathrm{c}})^i \tag{4.27}$$

with the coefficients c_i

$$c_0 = -0.81\,, \tag{4.28}$$

$$c_1 = 0.06\,, \tag{4.29}$$

$$c_2 = -3.92 \cdot 10^{-5}\,, \tag{4.30}$$

$$c_3 = 6.95 \cdot 10^{-8}\,, \tag{4.31}$$

$$c_4 = -5.32 \cdot 10^{-11}\,, \tag{4.32}$$

$$c_5 = 1.54 \cdot 10^{-14}\,, \tag{4.33}$$

and

$$\varphi_\mathrm{v} = 0.9998 \cdot \zeta + 0.4475\,. \tag{4.34}$$

The factor 2 in Eq. 4.27 stems from the reduced image format sRaw (one-fourth of pixels compared to Raw) during the measurements as the geometric calibration was performed using Raw images.

4.3.3 Radiometric calibration

The quantum efficiency relates the registered electrons and the incident photons to each other and is therefore a measure for the pixel sensitivity. In case of an ideal CMOS sensor with constant sensitivity throughout all pixels, an uniformly illuminated object would produce at each pixel the same signal s. However, the pixel respond differently to an uniform illumination due to manufacturing tolerances (e.g., irregularities in the used silicon), contamination with dust particles, and optical effects at the edges of the lenses. These deviations lead to the photo response non-uniformity (PRNU) and need to be corrected. The setup for the radiometric calibration is shown in Fig. 4.24. The camera is positioned in front of an integrating sphere. Due to the large FOV and the small aperture of the integrating sphere, the camera needs to be rotated in all directions while constantly taking photos. In the end, 259 photos were stitched

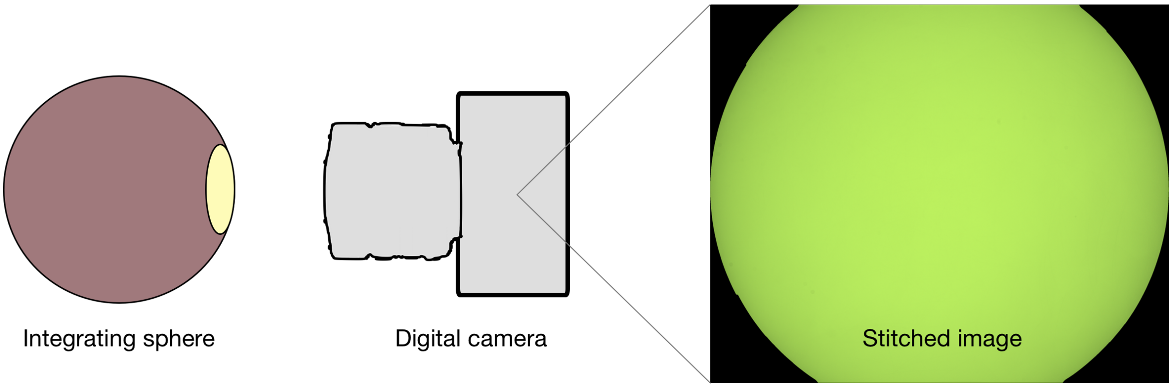

Figure 4.23: Setup of radiometric calibration. Successive photos are taken while the camera is rotated. During post-processing, the composite image is generated combining 259 single photos.

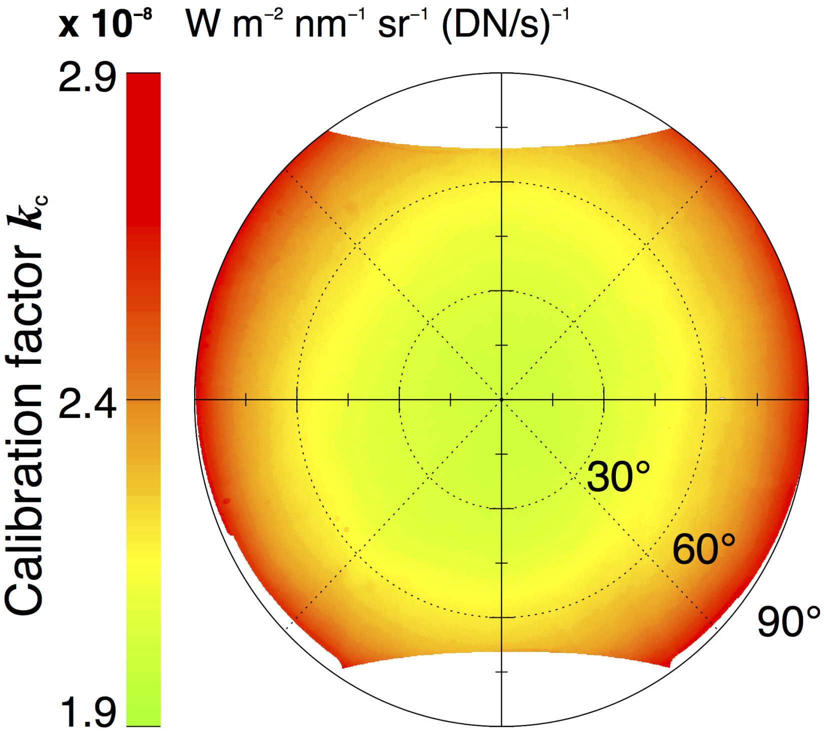

Figure 4.24: Absolute calibration factor $k_\mathrm{c}(x, y)$ in units $\mathrm{W\,m^{-2}\,nm^{-1}\,sr^{-1}\,(DN/s)^{-1}}$.

together to one image so that all pixels were illuminated at least once. In case a pixel was illuminated multiple times due to overlap between the photos, the mean of the measured signals was calculated. The stitched image is shown in Fig. 4.24. Instead of an uniform area, a distinct decrease in brightness is visible from the centre to the edges of the sensor. This vignetting effect is typical for digital cameras (e.g., Lebourgeois et al., 2008).

From the data sheet, the spectral radiance $I_\mathrm{ref}(\lambda)$ that the camera emits at an optometer current of 0.5936 µA is known. From this, the spectral radiance $I_\mathrm{ref,int}(\lambda)$ that passes through the CFA and reaches the CMOS sensor can be calculated by

$$I_\mathrm{ref,int}(\lambda) = \int_0^\infty I_\mathrm{ref}(\lambda) \cdot \mathrm{RSR}(\lambda)\,\mathrm{d}\lambda. \tag{4.35}$$

The output $I_\mathrm{sphere}(\lambda)$ of the integrating sphere is assumed to be linear with respect to the optometer current $\mathcal{I}$ in the range of operation during the calibration:

$$I_\mathrm{sphere}(\lambda) = \frac{\mathcal{I}}{0.5936\,\mathrm{\mu A}} \cdot I_\mathrm{ref,int}(\lambda). \tag{4.36}$$

To correct for the PRNU, the calibration factor $k_\mathrm{c}(i, j)$ is defined at each pixel location (x, y) as

$$k_\mathrm{c}(x,y) = \frac{I_\mathrm{sphere}(\lambda)}{s(x,y)} \cdot t_\mathrm{exp} = \frac{1.3 \cdot I_\mathrm{ref,int}(\lambda)}{s(x,y)} \cdot t_\mathrm{exp}. \tag{4.37}$$

The second step in Eq. (4.37) makes use of Eq. (4.36). The mean optometer current during the time of calibration was $\mathcal{I} = 0.7717\,\mu\mathrm{A}$; the exposure time t_exp was set to $1/1000\,\mathrm{s}$. The calibration factor has the units $\mathrm{W\,m^{-2}\,nm^{-1}\,sr^{-1}\,(DN/s)^{-1}}$ and is shown in Fig. 4.24. Not only does k_c correct for the PRNU, it simultaneously performs the absolute calibration transforming the measured digital signal into the physical quantity of radiance with units $\mathrm{W\,m^{-2}\,nm^{-1}\,sr^{-1}}$. A small factor corresponds to a large sensitivity (central part), whereas larger values imply lower sensitivity (at the edge of the sensor).

4.3.4 Aircraft attitude correction

Beside the geometric calibration, the viewing angles θ_v and φ_v of the camera are determined by the attitude angles of the aircraft. The definition of the roll $\varPhi$ (positive for left wing up), pitch Θ (positive for nose down), and yaw ψ (mathematical negative system with North $= 0°$) is shown together with an illustration of the airborne-fixed and Earth-fixed coordinate systems in Fig. 4.25. The direction of the reflected radiation in Earth-fixed coordinates is given by the zenith and azimuth angles θ_r and φ_r (compare Fig. 2.5). It depends on the position of the Sun (θ_0, φ_0) and the scattering angle θ. The viewing and reflection angles only coincide for zero pitch and roll angles. Hence, the movement of the aircraft needs to be corrected to obtain the reflection angles θ_r and φ_r. In this regard, Euler rotations of θ_v and φ_v are applied using the rotation matrices $\mathbf{R_{roll}}$, $\mathbf{R_{pitch}}$, and $\mathbf{R_{yaw}}$:

$$\mathbf{R_{roll}} = \begin{pmatrix} 1 & 0 & 0 \\ 0 & \cos\varPhi & \sin\varPhi \\ 0 & -\sin\varPhi & \cos\varPhi \end{pmatrix}, \tag{4.38}$$

$$\mathbf{R_{pitch}} = \begin{pmatrix} \cos\Theta & 0 & -\sin\Theta \\ 0 & 1 & 0 \\ \sin\Theta & 0 & \cos\Theta \end{pmatrix}, \tag{4.39}$$

$$\mathbf{R_{yaw}} = \begin{pmatrix} \cos(360° - \psi) & \sin(360° - \psi) & 0 \\ -\sin(360° - \psi) & \cos(360° - \psi) & 0 \\ 0 & 0 & 1 \end{pmatrix}. \tag{4.40}$$

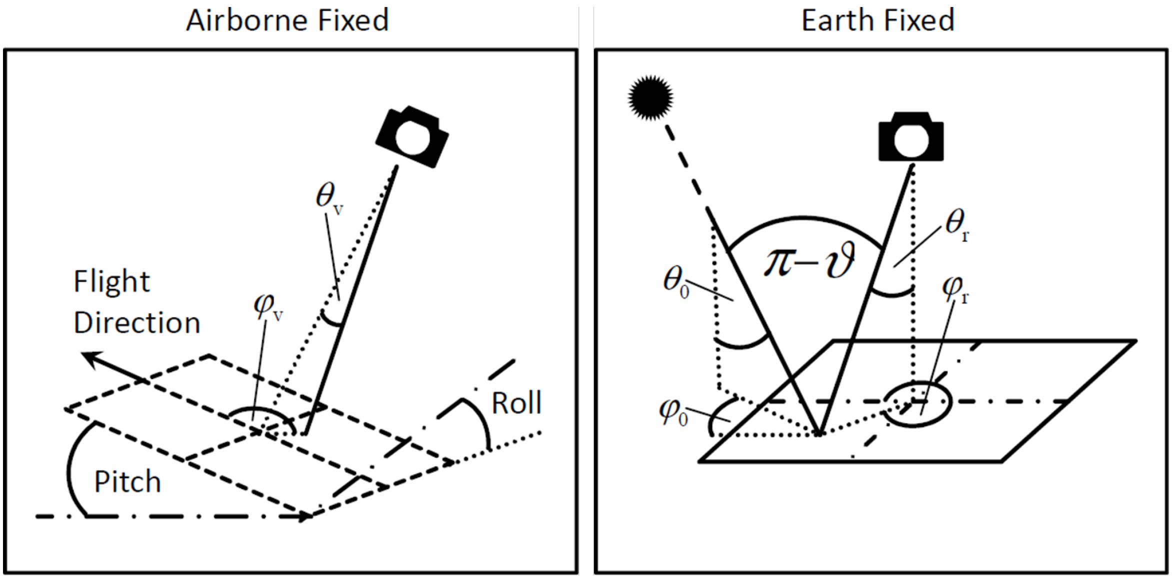

Figure 4.25: Definition of coordinate systems (Ehrlich et al., 2012).

As the camera and the aircraft were aligned in the same direction, the respective yaw angle is zero. The rotation matrices are applied to the viewing angles (transformed to cartesian coordinates) by,

$$\begin{pmatrix} x' \\ y' \\ z' \end{pmatrix} = \mathbf{R}_{\mathbf{roll}} \cdot \mathbf{R}_{\mathbf{pitch}} \cdot \mathbf{R}_{\mathbf{yaw}} \cdot \begin{pmatrix} \sin\theta_\mathrm{v} \cdot \cos(360^\circ - \varphi_\mathrm{v}) \\ \sin\theta_\mathrm{v} \cdot \sin(360^\circ - \varphi_\mathrm{v}) \\ \cos\theta_\mathrm{v} \end{pmatrix} , \tag{4.41}$$

leading to the cartesian coordinates in the Earth-fixed coordinate system $(x', y', z')^T$. The transformation to spherical coordinates yields the required reflection angles:

$$\theta_\mathrm{r} = \arccos \frac{z'}{\sqrt{x'^2 + y'^2 + z'^2}} , \tag{4.42}$$

and

$$\varphi_\mathrm{r} = \arctan \frac{y'}{x'} . \tag{4.43}$$

4.3.5 Data quality and post-processing

The camera took pictures with a temporal resolution of about 8 s. Exemplarily, Fig. 4.26 a shows a raw image taken by the camera on 2 January 2014 (8:16 UTC). The post-processing of each raw image involves (a) the radiometric calibration, (b) the geometric calibration, (c) the aircraft attitude correction, and (d) the calculation

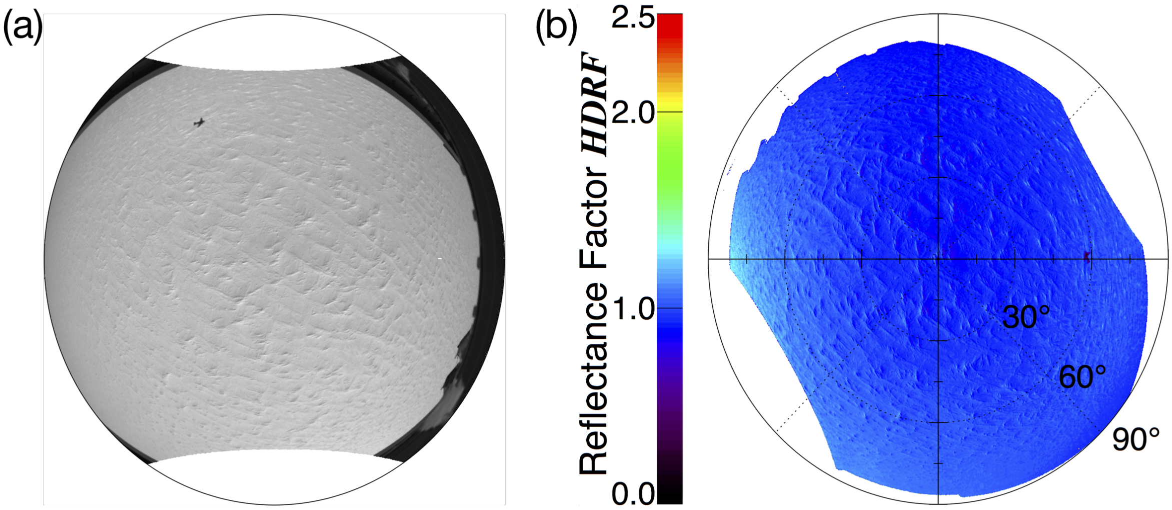

Figure 4.26: (a) Raw image taken on 2 January 2014 at 8:16 UTC. **(b)** Polar plot of snow HDRF calculated from raw image.

of the HDRF.

Firstly, the pixels receiving radiation from the direction of the aircraft frame are excluded. For each pixel location $(x,\, y)$, the radiance $I(x, y)$ (in units $\mathrm{W\,m^{-2}\,nm^{-1}\,sr^{-1}}$) is calculated from the measured signal s using the absolute calibration factor k_c and the exposure time t_exp:

$$I(x,y) = \frac{s(x,y)}{t_\mathrm{exp}} \cdot k_\mathrm{c}(x,y) \tag{4.44}$$

The camera viewing angles are calculated from the geometric calibration for each pixel. Utilizing the data from the INS and the GPS on Polar 6, the viewing angles are corrected depending on the roll, and pitch angles of the aircraft at the time of measurement. Based on the resulting reflection angles, a polar plot of measured radiances is created. To achieve comparability, each image is rotated into the azimuthal direction of the Sun.

Finally, the HDRF is calculated by:

$$f_\mathrm{HDRF}(\theta_\mathrm{r}, \varphi_\mathrm{r}) = \frac{\pi \cdot I(\theta_\mathrm{r}, \varphi_\mathrm{r})}{F^{\downarrow}}\,. \tag{4.45}$$

Note that the downward irradiance measurements from SMART could not be used for the calculation of the HDRF due to the failed transfer calibration (see Sect. 4.2.3). Instead, the global irradiance was simulated along the flight track with libRadtran using DISORT. The simulated irradiance was integrated over the wavelength range of each camera channel and weighted with the RSR function of the camera. The use of simulations limits the validity of absolute values of the measured HDRF to cloudless conditions. However, within this work mainly the shape of the HDRF is analyzed which is independent from the absolute value of $F^{\downarrow}$. Together with the raw image, the corresponding HDRF polar plot is shown for the camera channel G in Fig. 4.26 b. The HDRF is close to one over almost the entire hemisphere and shows a prominent maximum in the forward scattering direction. Note, that the Sun is always positioned in the left of the image. The inhomogeneities of the snow surface directly affect the measured HDRF. A representative HDRF for the prevailing conditions is obtained from averaging over successive HDRF measurements.

To assess the quality and accuracy of the camera measurements, they can be compared to SMART observations. Ideally, the radiance measured by the nadir-looking pixel of the camera could be compared with the upward radiance measured by SMART. Ehrlich et al. (2012) found differences in the mean radiance values between the camera and SMART to range within the measurement uncertainties of both instruments (1 to 4 % depending on camera channel). This demonstrates the potential of the camera to measure reflected radiances. However, in contrast to the study of Ehrlich et al. (2012), the camera was equipped with a fish-eye lens instead of a wide-angle lens.

As no calibrated radiance measurements were available during the measurements presented in this work, the measured upward irradiances had to be compared. This gives rise to uncertainties related to (a) the uncertainty in the absolute calibration of the SMART irradiance due to the failed transfer calibration, and (b) the incomplete coverage of the reflection hemisphere by the digital camera (compare Fig. 4.26 b). Hence, instead of integrating the measured radiance from zero to $\pi/2$ in Eq. (2.8), the integration is performed from zero to the upper limit of $\theta_{\mathrm{obs}} = 70°$. Assuming an isotropic radiation field, this would yield 88.3 % of the actual irradiance. Note that due to the anisotropy of the surface reflection at snow surfaces, this value is likely lower for the presented measurements. Therefore, the integrated radiance (from zero to 70°) multiplied with 1.13 serves as a lower boundary for irradiance measured with the camera. For the comparison, the spectral irradiance measured with SMART is weighted with respect to the RSR function of the camera.

The comparison between the camera and SMART is shown in Fig. 4.27 for a cloudless flight leg on 2 January 2014 between 10:00-11:12 UTC. Indeed, independent of the camera channel, the upward irradiances derived by the camera underestimate the irradiances measured by SMART (see Figs. 4.27 a-c). However, for the red and green channel, F_{camera} is within or close to the range given by the measurement uncertainties of F_{SMART}. The offset for the blue camera channel is larger. As expected, the camera values mark a lower boundary for the actual irradiance. Figure 4.27 d shows the cor-

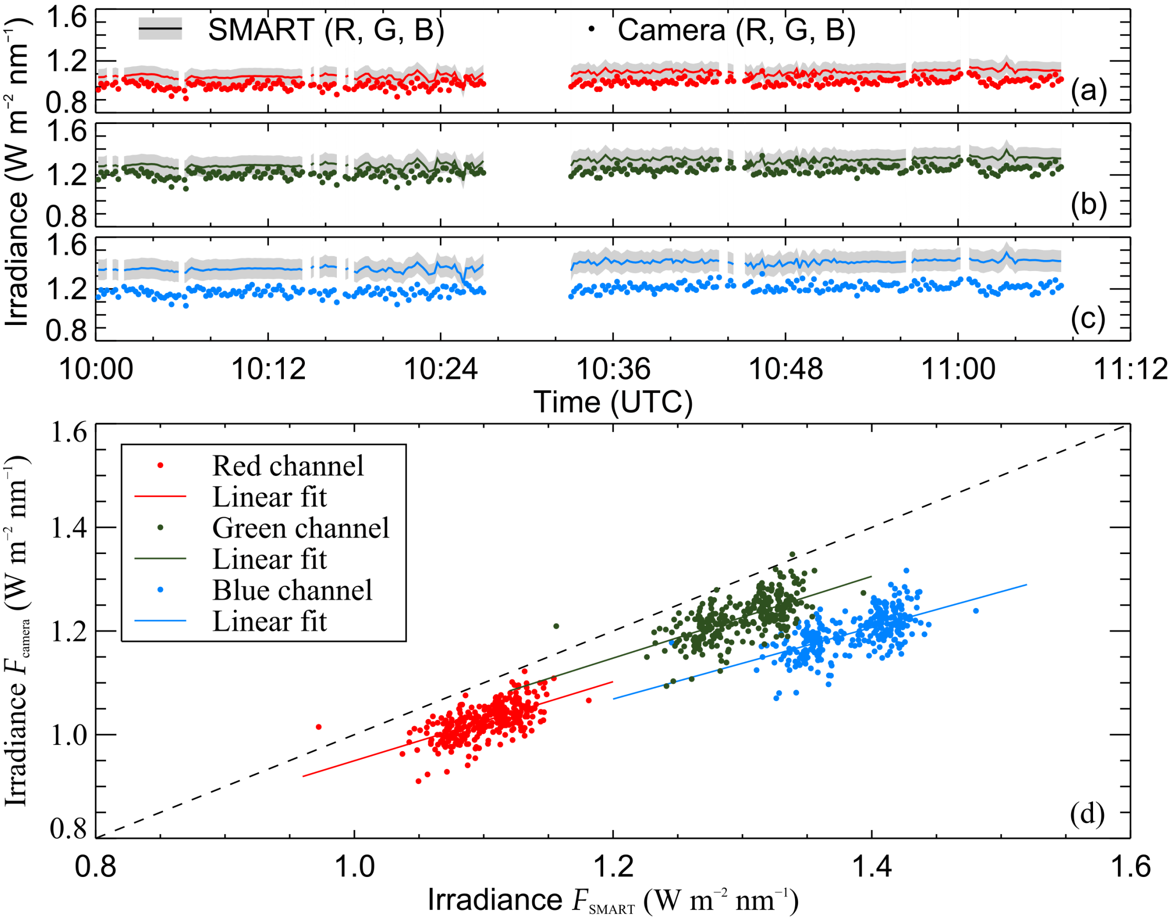

Figure 4.27: Comparison between upward irradiances measured by SMART and the digital camera between 10:00–11:12 UTC on 2 January 2014. **(a)** Timeseries of SMART (solid line) and the camera (dotted) for the red camera channel. Shaded gray: measurement uncertainty of SMART. **(b)** Same as in (a), but for green camera channel. **(c)** Same as in (a), but for blue camera channel. **(d)** Regression plot between F_{SMART} and F_{camera} for all three camera channels. Dots: measurements corresponding to individual images. Solid lines: linear fits. Dashed line: 1:1-line.

responding regression plot for the three camera channels. The slopes of the linear fits are 0.79 (G), 0.76 (R), and 0.69 (B). The linear correlation coefficients are 0.63 (G), 0.61 (R), and 0.62 (B), respectively. In order to decrease the influence of $\theta_{\text{obs}} \leq 70°$, a cloudless flight leg close to noon with lower anisotropy was chosen. Apart from the explicable offset between F_{SMART} and F_{camera}, the potential of the camera measurements is demonstrated. Due to the highest correlation coefficient, the green camera channel is used in the analysis of this thesis. Moreover, the resolution of the raw data of the green camera channel is better resulting from the RGGB design of the CFA (Bayer pattern).

4.3.6 Measurement uncertainties

The uncertainties in the HDRF measurements with the digital camera stem from (a) sensor characteristics (signal-to-noise ratio, dark current, linearity, read-out noise, chrominance subsampling), (b) the radiometric calibration, and (c) the geometric calibration and correction for the aircraft attitude.

The main source of uncertainty is related to the uncertainty in the certified output of the integrating sphere (χ_{radio}). For the wavelength range of the three camera channels, it amounts to about 4 %.

The uncertainties attributed to the sensor characteristics (χ_{sensor}) combine different sources of uncertainty. The linearity of the sensor is exceptionally high; the dark current and the read-out noise are negligible compared to the dynamical range of the sensor. The sRaw output format introduces an additional error source due to chrominance subsampling. Nevertheless, the characterization of the sensor characteristics showed that their contribution to the overall uncertainty is small. Thus, it is estimated with 0.5 %.

It is difficult to estimate the uncertainty related to the geometric calibration and the subsequent correction for the aircraft attitude ($\chi_{\mathrm{geometric}}$). However, the aircraft shadow on the snow surface in Fig. 4.26 a can serve as an indication. The relative azimuth angle with respect to the Sun should be 180°. Thus, in the polar plot of the HDRF, the aircraft shadow should appear on the right part of the horizontal axis (Sun is on the left). As can be seen from Fig. 4.26 b, this holds true: the aircraft shadow is small but still distinguishable at a reflection zenith angle of about 59°, which coincides with the solar zenith angle at the time of measurement. Hence, the geometric calibration and the correction for the aircraft attitude seem accurate; their uncertainty is estimated with 1 %. Note that the uncertainty might increase for larger viewing zenith and aircraft attitude angles.

All instrumental errors are assumed to be uncorrelated and random. The overall uncertainty is estimated from the Gaussian equation for normally-distributed errors by:

$$\chi_{\mathrm{HDRF}} = \sqrt{(\chi_{\mathrm{sensor}})^2 + (\chi_{\mathrm{radio}})^2 + (\chi_{\mathrm{geometric}})^2} \tag{4.46}$$

Thus, the overall relative uncertainty of the HDRF measurements with the digital camera range in the order of 4.5 %. The error in the absolute value of f_{HDRF} might be higher depending on the atmospheric conditions due to the usage of simulated values for the global irradiance $F^{\downarrow}$ in Eq. (4.45).

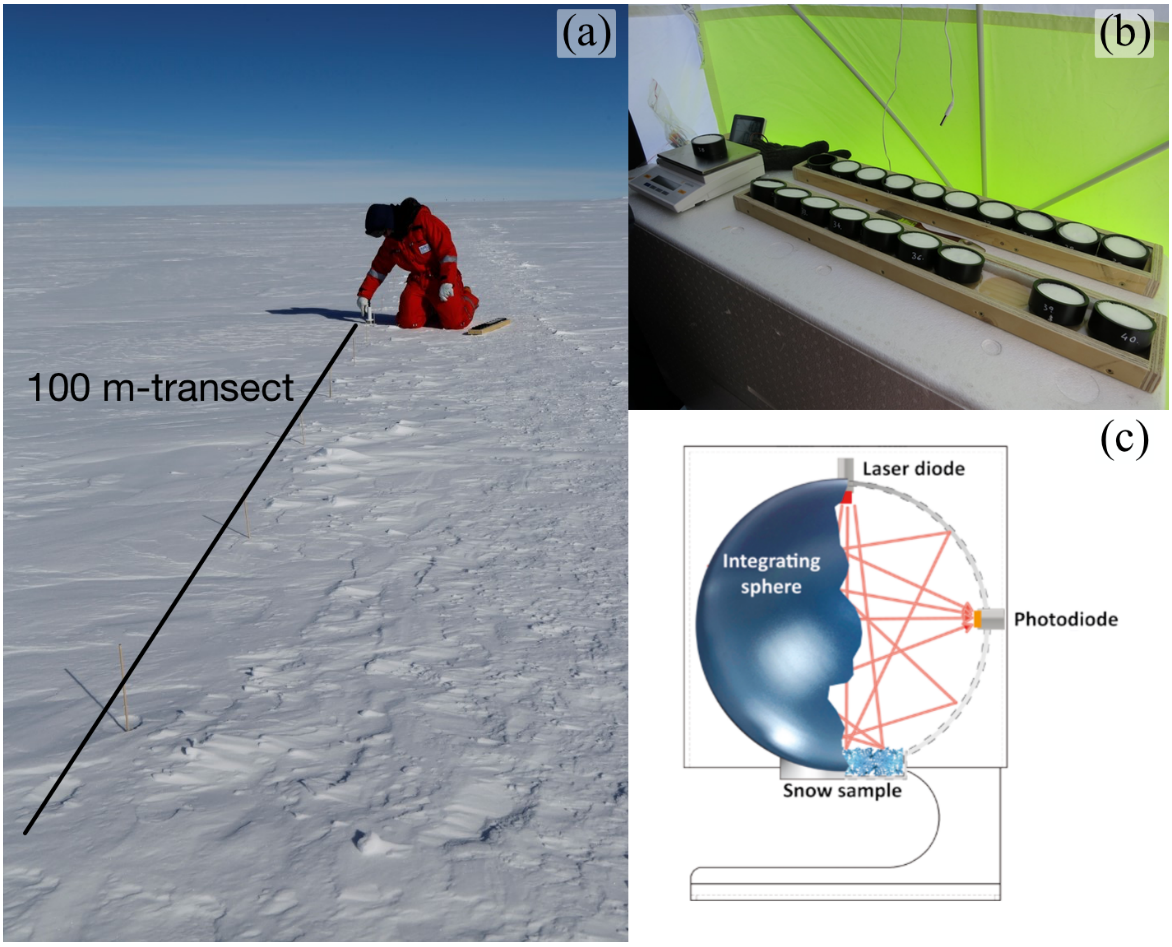

Figure 4.28: In situ measurements of snow SSA at Kohnen station. Photographs: G. Birnbaum. **(a)** Snow sampling along the transect. **(b)** Storage of snow samples in measurement tent. **(c)** Schematic of the measurement principle of the IceCube device (taken from `www.a2photonicsensors.com`, 2 February 2018).

4.4 Snow specific surface area measurements using an IceCube device

Snow samples from in situ measurements were extracted daily (except 5 December, 12, 17, 18, and 19 January) along a 100 m-transect between 15 and 18 UTC. The transect was divided into $1 \times 1\,\mathrm{m}^2$-squares from which cylindric snow samples (height: 25 mm, diameter: 60 mm) were extracted randomly with a piston. After extraction, the measurements of SSA were conducted with an IceCube device by A2 Photonic Sensors in a measurement tent to protect the samples from wind, drifting snow and direct radiation. As described by Gallet et al. (2009), the IceCube uses a laser diode at 1310 nm to illuminate the snow sample underneath an integrating sphere. The waves

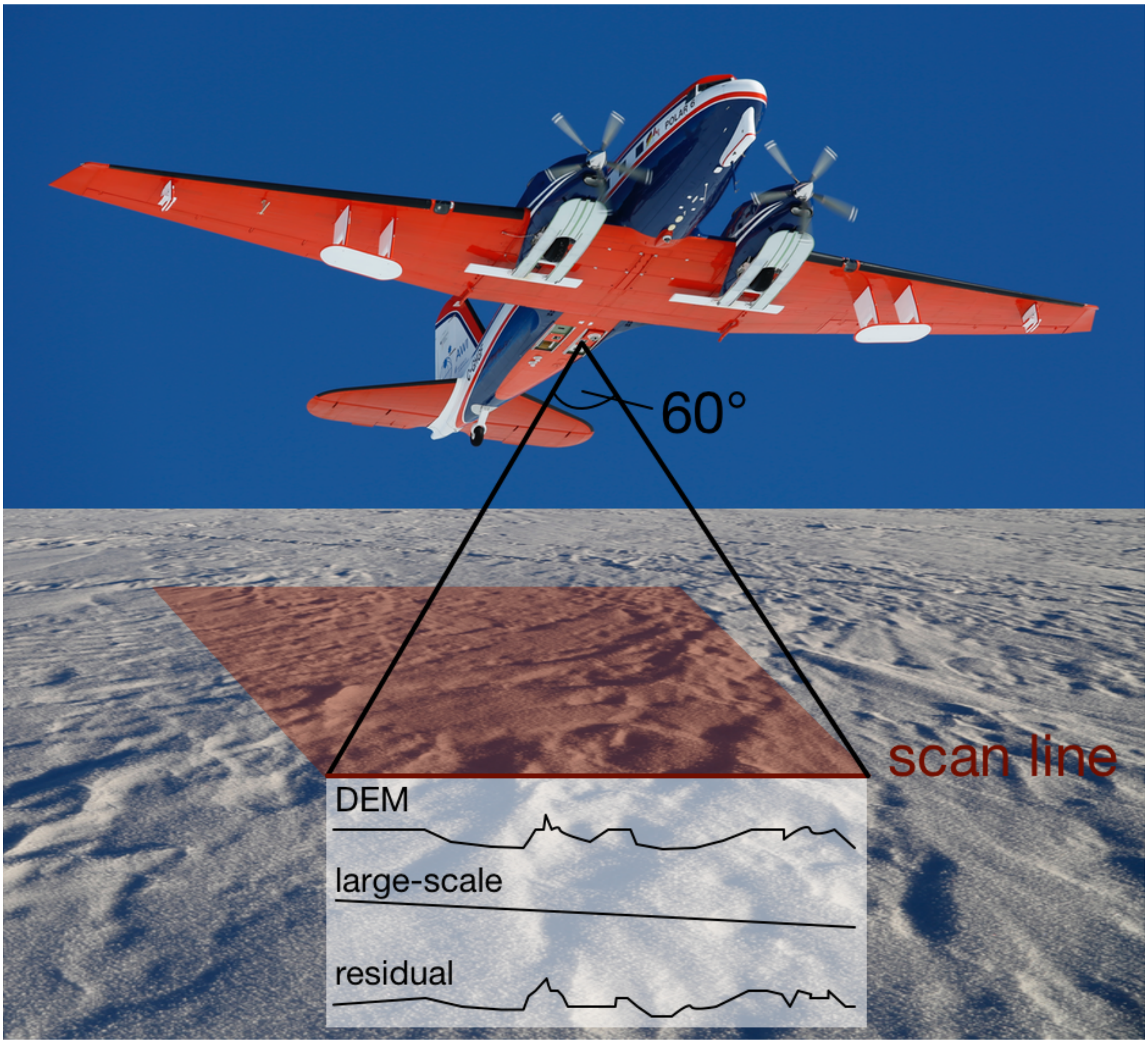

Figure 4.29: Schematic of the measurement principle. The scan line is determined by the FOV of 60° and the flight altitude. Photographs: G. Birnbaum.

penetrate 1 cm into a snow body with density of 200 kg m^{-3} and the reflected signal is detected by a photodiode. By means of a certified standard, the hemispherical infrared reflectance is derived, which is used to calculate SSA and R_{opt}, applying a radiative transfer model (Gallet et al., 2009). Figure 4.28 illustrates the measurement strategy and principle.

For the derived SSA values between 5 and 130 m^2 kg^{-1}, the measurement uncertainty is in the range of 10 %. SSA values above 60 m^2 kg^{-1} require caution as the insufficient optical depth of the snow sample may cause artifacts as reported by Gallet et al. (2009). However, the densities of the snow samples for which Gallet et al. (2009) reported this limitation were below 100 kg m^{-3}, whereas the observed snow densities within this study were all well above this value (around 60 % of the samples with densities between

280 and 350 $\mathrm{kg\,m^{-3}}$). The higher optical depth of the samples might indicate a higher limit for the SSA measurements. However, SSA values above 60 $\mathrm{m^2\,kg^{-1}}$ occurred only in 10 % of the cases.

4.5 Surface roughness measurements using a laser scanner

The snow surface topography was measured using the airborne laser scanner RIEGL VQ580. The basic measurement principle is illustrated in Fig. 4.29.
In time-of-flight laser ranging, a near-infrared laser beam (1064 nm wavelength) is emitted downward and subsequently reflected upward by the snow surface before the echo is acquired by the sensor. From the time lag between emission and detection, the distance to the ground can be calculated with a range precision of about 25 mm depending on flight altitude. A fast-rotating polygonal mirror with a FOV of 60° and 10 to 150 scans per second allows for fully linear, unidirectional and parallel scan lines. After a correction for the aircraft attitude, a $1{\times}1\,\mathrm{km^2}$ digital elevation model (DEM) is generated from the geotagged laser point cloud with a resolution of 1 m. Subtracting the large scale topography (smoothed DEM), the residual field contains the roughness information. The standard deviation of the residual field is interpreted as the surface roughness at the centre coordinate of the DEM. Thus, roughness data is given for one data point per 1 km along the flight track of the aircraft. The uncertainty of the absolute height measurements (used for DEM generation) is less than 0.1 m. The relative analysis applied to the measurements yields an even higher accuracy (Veit Helm, AWI Bremerhaven, personal communication, December 2017).

5 Methodology

5.1 Approximations for surface reflectivity and bidirectional reflectance

5.1.1 Asymptotic radiative transfer

Absorption of solar radiation by ice becomes crucial in the near-infrared part of the solar EM wavelength spectrum (Warren and Brandt, 2008). As the effective photon path is longer within larger snow grains, the magnitude of absorption is determined by the size of the snow grains. Hence, snow surface albedo in the near-infrared mainly depends on the optical snow grain size.

To retrieve SSA and R_{opt}, measurements of reflected solar radiation are required (e.g., Bohren and Barkstrom, 1974; Wiscombe and Warren, 1980; Grenfell et al., 1994). The retrievals are based on the spectral variability of the snow albedo as a function of the optical snow grain size. Snow albedo models are employed to calculate the spectral surface albedo and to invert the measurements to retrieve the optical snow grain size (e.g., Wiscombe and Warren, 1980). These albedo models mostly assume spherical grains, the inherent scattering properties can then be calculated using Mie theory (Mie, 1908) with high accuracy. However, this gives rise to typical scattering features (e.g., rainbow, glory) which are not observed in snow. To avoid this, the Henyey-Greenstein scattering function is widely used concerning the radiative transfer in snow (e.g., Grenfell and Warren, 1999; Aoki et al., 2000). Still, assuming spheres is unrealistic because the grain shape is usually far from being spherical (e.g., Kokhanovsky and Zege, 2004; Libois et al., 2013; Leppänen et al., 2015; Krol and Löwe, 2016). Picard et al. (2009) estimated an uncertainty of ±20 % when determining SSA from albedo measurements in case of an unknown snow grain shape. A common approach to account for the nonspherical shape of snow grains is to represent them by a population of spherical grains with the same area-to-mass ratio in the spectral albedo model. However, as shown by Dang et al. (2016), this approximation can lead to an underestimation of the retrieved optical snow grain size by a factor of more than two.

Within this work, the framework of the asymptotic radiative transfer theory (ARTT) is applied, which accounts for the non-sphericity of the snow grains and provides analytical formulas. In the following, the equations from ARTT that are essential for this study are briefly discussed. However, a derivation of the main equations of the ARTT is beyond the scope of this work. For a detailed description it is referred to Kokhanovsky (2006).

The Beer-Lambert-Bouguer law describes the extinction of radiance I along a slant path of length s through a non-scattering medium:

$$\mathrm{d}I = -b_{\mathrm{ext}} \cdot I \,\mathrm{d}s\,, \tag{5.1}$$

with the volumetric extinction coefficient b_{ext}. Accounting for light scattering from all other directions $\varOmega'$ to a given direction $\varOmega$ yields the radiative transfer equation:

$$\frac{\mathrm{d}I(\varOmega)}{\mathrm{d}s} = -b_{\mathrm{ext}} I(\varOmega) + \int\limits_{4\pi} b_{\mathrm{sca}}(\varOmega, \varOmega') I(\varOmega')\,\mathrm{d}\varOmega'\,. \tag{5.2}$$

$b_{\mathrm{sca}}(\varOmega, \varOmega')$ denotes the differential scattering coefficient describing the local scattering law. In the following, a plane-parallel, vertically and horizontally homogeneous scattering layer as illustrated in Fig. 5.1 is assumed. Furthermore, I is separated into a diffuse and direct component ($I = I_{\mathrm{dir}} + I_{\mathrm{diff}}$). Thus, Eq. (5.2) simplifies to:

$$\begin{aligned}\cos\theta \frac{\mathrm{d}I_{\mathrm{diff}}(\theta,\varphi)}{\mathrm{d}\tau} = -I_{\mathrm{diff}}(\theta,\varphi) &+ \frac{\tilde{\omega}}{4\pi} \int\limits_0^{2\pi} \int\limits_0^{\pi} I_{\mathrm{diff}}(\theta',\varphi') \cdot \mathcal{P}\left[(\theta',\varphi') \rightarrow (\theta,\varphi)\right]\,\mathrm{d}\theta'\,\mathrm{d}\varphi' \\ &+ \frac{\tilde{\omega}}{4\pi} \cdot F_{\mathrm{inc}} \cdot \mathcal{P}\left[(\theta_0,\varphi_0) \rightarrow (\theta,\varphi)\right] \cdot \exp\left\{-\frac{\tau}{\cos\theta_0}\right\}.\end{aligned} \tag{5.3}$$

The vertical coordinate is introduced as $\mathrm{d}\tau = b_{\mathrm{ext}}\,\mathrm{d}z$; $\tilde{\omega}$ denotes the single-scattering albedo, $\mathcal{P}$ the phase function, and F_{inc} the irradiance at the top of the scattering layer. The incident direction is described by (θ_0, φ_0), the viewing direction is defined by (θ, φ). From this, asymptotic equations for the reflection and transmission functions of optically thick layers were first derived by Germogenova (1961) and independently by Sobolev (1975) and van de Hulst (1968). Rozenberg (1962) developed exponential approximations of these asymptotic equations. They are valid for semi-infinite, weakly-absorbing ($\tilde{\omega} \rightarrow 1$), optically thick ($z_0 \gg b_{\mathrm{ext}}^{-1}$) turbid media. These assumptions generally hold true for Antarctic snow layers due to (a) the weak ice absorption ($\tilde{n}_{\mathrm{im}} < 1.5 \cdot 10^{-5}$ for $\lambda < 1370\,\mathrm{nm}$), and (b) their large vertical extent. Kokhanovsky et al.

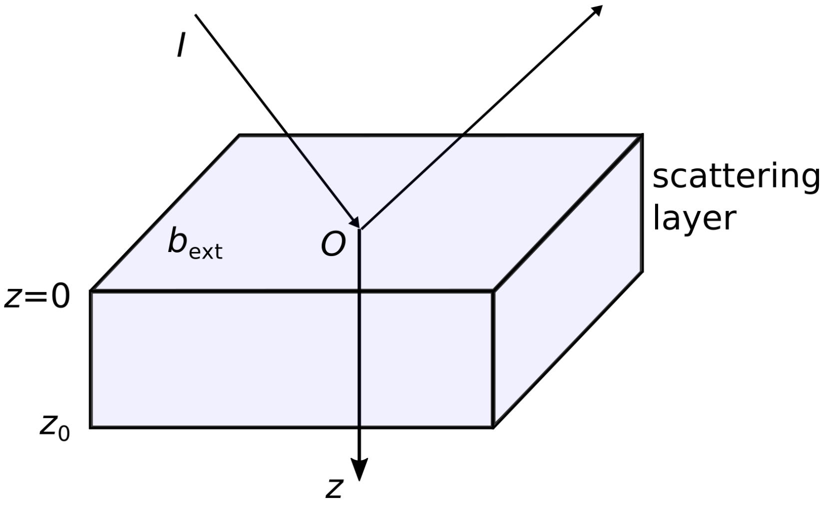

Figure 5.1: Illustration of the geometry of the plane-parallel, homogeneous scattering layer.

(2005) validated the applicability of ARTT to snow with in situ measurements of snow reflectance between 545-2210 nm wavelength and verified a high accuracy.

Zege et al. (1991) showed that the plane albedo $\alpha_\mathrm{p}(\theta_0)$ as a function of solar zenith angle θ_0 can be parameterized using ARTT ($\tilde{\omega} \to 1$) by

$$\alpha_\mathrm{p}(\theta_0) = \exp\left[-y \cdot K_0(\mu_0)\right] \, , \tag{5.4}$$

with

$$K_0(\mu_0) = \frac{3}{7}\,(1 + 2\,\mu_0) \, . \tag{5.5}$$

The escape function $K_0(\mu_0)$ (dimensionless, $\mu_0 = \cos\theta_0$) describes the angular distribution of the number of photons escaping from a non-absorbing, semi-infinite medium. From energy conservation, it follows that $K_0(\mu_0)$ is normalized via (van de Hulst, 1980)

$$2\int\limits_0^1 K_0(\mu_0) \cdot \mu_0 \, \mathrm{d}\mu_0 = 1 \, . \tag{5.6}$$

The uncertainty of α_p introduced by the approximation of $K_0(\mu_0)$ given in Eq. (5.5) is below 2 % for $\theta_0 < 78°$ (Kokhanovsky and Zege, 2004). Following Kokhanovsky and Zege (2004), the parameter y depends on the volumetric extinction and absorption coefficients of snow, b_ext and b_abs (both in m^{-1}), and the dimensionless asymmetry parameter (average cosine over the phase function) $g(\xi)$ of the snow grain, which shape is represented by the parameter ξ:

$$y = 4\sqrt{\frac{b_{\mathrm{abs}}}{3\,b_{\mathrm{ext}} \cdot \big[1 - g(\xi)\big]}}\,. \tag{5.7}$$

Assuming pure snow and applying the principles of geometrical optics, the volumetric extinction and absorption coefficients of snow are derived by (Kokhanovsky and Zege, 2004)

$$b_{\mathrm{ext}} = \frac{1.5\,C_{\mathrm{v}}}{R_{\mathrm{opt}}}\,, \tag{5.8}$$

$$b_{\mathrm{abs}} = B(\xi) \cdot b_{\mathrm{abs,ice}} \cdot C_{\mathrm{v}} = B(\xi) \cdot \frac{4\pi\,\tilde{n}_{\mathrm{im}}}{\lambda} \cdot C_{\mathrm{v}}\,. \tag{5.9}$$

Calculating the optical properties using geometrical optics is justified as the size of snow grains (0.05-10 mm) is much larger than the wavelength in the VIS and NIR part of the EM spectrum. b_{ext} and b_{abs} depend on the volumetric concentration of snow grains C_{v} (dimensionless, $\rho_{\mathrm{snow}}/\rho_{\mathrm{ice}}$), the optical snow grain size R_{opt}, the absorption enhancement parameter $B(\xi)$ (dimensionless), and the absorption coefficient of pure ice, $b_{\mathrm{abs,ice}}$ (m^{-1}), which is determined by the imaginary part of the complex refractive index of ice $\tilde{n}_{\mathrm{im}}$ at wavelength λ. Consequently, Eq. (5.7) reduces to

$$y = A \cdot \sqrt{\frac{4\pi\,\tilde{n}_{\mathrm{im}}}{\lambda} \cdot R_{\mathrm{opt}}}\,, \tag{5.10}$$

with

$$A = \frac{4}{3}\sqrt{\frac{2\,B(\xi)}{1 - g(\xi)}}\,. \tag{5.11}$$

The form factor A accounts for the snow grain shape by merging $B(\xi)$ and $g(\xi)$ into a single parameter. Equation (5.10) forms the basis of the snow grain size and pollution amount (SGSP) retrieval algorithm by Zege et al. (2011), who applied the $\tilde{n}_{\mathrm{im}}$ database by Warren and Brandt (2008) and assumed a form factor of $A = 5.8$. In general, the factor A varies between 5.1 (Kokhanovsky and Macke, 1997) for fractals and 6.5 for spheres.

5.1.2 Modeling of the bidirectional reflectance

A BRDF model can be either physical, empirical, or semi-empirical. Physical BRDF models accurately simulate the scattering of an EM wave at a surface by applying physical laws. The high accuracy comes at the cost of very complex computations. Empirical BRDF models mimic the surface reflection by means of a simple, non-physical formulation. However, the drawback of the rather simple computations is their restricted accuracy. Semi-empirical models use simple, direct parameterizations of a more complex physical BRDF with a limited number of independent parameters. The shape of the BRDF is described by a weighted sum of trigonometric functions, generally referred to as kernels for volumetric scattering (K_{vol}), geometric scattering (K_{geo}), and isotropic scattering (K_{iso}).

The kernel-driven semi-empirical Ross-Li model (Lucht et al., 2000), which forms the basis of the MODIS 16-day BRDF/albedo product (Schaaf et al., 2002), is applied within this thesis. The BRDF is given as a linear combination of the kernels with corresponding non-negative weighting functions f_{iso}, f_{vol}, and f_{geo}:

$$f_{\mathrm{BRDF}}\left(\theta_{\mathrm{r}},\theta_0,\Delta\varphi,\lambda\right)=f_{\mathrm{iso}}(\lambda)\cdot K_{\mathrm{iso}}+f_{\mathrm{vol}}(\lambda)\cdot K_{\mathrm{vol}}\left(\theta_{\mathrm{r}},\theta_0,\Delta\varphi\right)+f_{\mathrm{geo}}(\lambda)\cdot K_{\mathrm{geo}}\left(\theta_{\mathrm{r}},\theta_0,\Delta\varphi\right), \tag{5.12}$$

with the viewing zenith angle θ_{r}, solar zenith angle θ_0, relative viewing azimuth angle $\Delta\varphi$, and wavelength λ. The kernels,

$$K_{\mathrm{iso}}=1, \tag{5.13}$$

$$K_{\mathrm{vol}}=\frac{\left(\frac{\pi}{2}-\theta\right)\cos\theta+\sin\theta}{\cos\theta_0+\cos\theta_{\mathrm{r}}}-\frac{\pi}{4}, \tag{5.14}$$

$$K_{\mathrm{geo}}=\mathcal{O}\left(\theta_{\mathrm{r}},\theta_0,\Delta\Phi\right)-\sec\theta_0-\sec\theta_{\mathrm{r}}+\frac{1}{2}\left(1+\cos\theta\right)\cdot\sec\theta_0\cdot\sec\theta_r, \tag{5.15}$$

depend on the scattering angle θ and the function $\mathcal{O}$:

$$\cos\theta=\cos\theta_0\cdot\cos\theta_{\mathrm{r}}+\sin\theta_0\cdot\sin\theta_{\mathrm{r}}\cdot\cos\Delta\Phi, \tag{5.16}$$

$$\mathcal{O}\left(\theta_{\mathrm{r}},\theta_0,\Delta\Phi\right)=\frac{1}{\pi}\left(\mathcal{C}-\sin\mathcal{C}\cdot\cos\mathcal{C}\right)\cdot\left(\sec\theta_0+\sec\theta_{\mathrm{r}}\right). \tag{5.17}$$

The functions $\mathcal{C}$ and $\mathcal{D}$ depend solely on the viewing and illumination geometry:

$$\cos\mathcal{C}=\frac{2\cdot\sqrt{\mathcal{D}^2+\left(\tan\theta_{\mathrm{r}}\cdot\tan\theta_0\cdot\sin\Delta\Phi\right)^2}}{\sec\theta_0+\sec\theta_{\mathrm{r}}}, \tag{5.18}$$

$$\mathcal{D}=\sqrt{\tan^2\theta_{\mathrm{r}}+\tan^2\theta_0-2\tan\theta_{\mathrm{r}}\cdot\tan\theta_0\cdot\cos\Delta\Phi}. \tag{5.19}$$

Originally, the concept of the model was developed studying typical features in observations of the bidirectional reflectance of various surface types (Roujean et al., 1992).

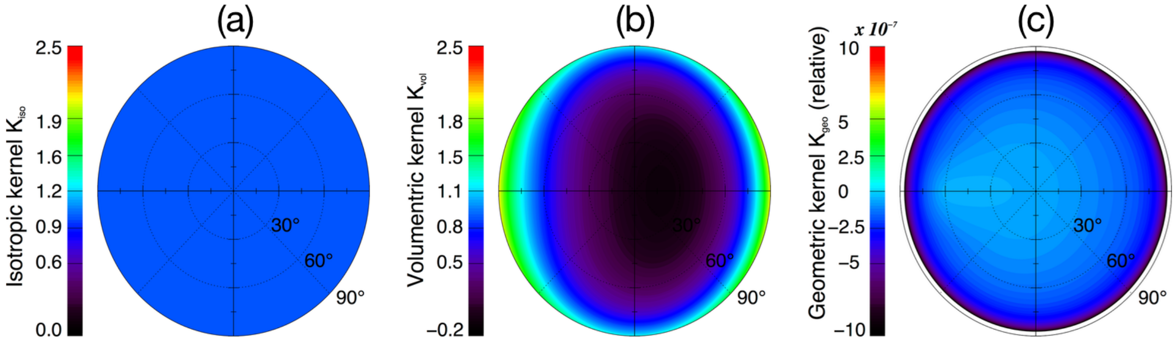

Figure 5.2: Shape of the three kernels for $\theta_0 = 60°$ and $\varphi_0 = 0°$. **(a)** Isotropic kernel K_{iso}. **(b)** Volumetric kernel K_{vol}. **(c)** Geometric kernel K_{geo}. For reasons of clarity, K_{geo} is shown normalized to the minimum value of K_{geo}. The color bar ranges from $-10 \cdot 10^{-7}$ to $10 \cdot 10^{-7}$.

Firstly, bare soil surfaces exhibited strong backscattering characteristics and showed the effect of geometrical structures on the surface. Secondly, dense leaf canopies typically featured a minimum reflectance close to the nadir-direction that increased off-nadir for all azimuthal directions. In their approach, Roujean et al. (1992) represented the BRDF model as a linear combination of these two observational characteristics; the former being accounted for by K_{geo}, the latter by K_{vol}. The volumetric kernel K_{vol} stems from volume scattering radiative transfer models (Ross, 1981). Thereby, randomly located facets that absorb and scatter incident radiation are modeled under the single-scattering approximation. The formula given in Eq. 5.14 corresponds to the Ross–Thick kernel for a dense leaf canopy. The geometric kernel K_{geo} is derived from surface scattering and geometric shadow casting theory (Li and Strahler, 1992) and expresses effects caused by intercrown gaps within vegetation. It represents randomly orientated vertical protrusions on a flat and horizontal surface that isotropically reflect radiation. Eq. (5.15) gives the Li–Sparse geometric kernel describing the casting of shadows by a sparse ensemble of surface objects.

The three kernels K_{iso}, K_{vol}, and K_{geo} are shown in Fig. 5.2 for direct illumination under the zenith angle of 60° and azimuth angle of 0°. The isotropic kernel has the value one, is equal for all viewing angles and accounts for isotropic BRDF effects. K_{vol} is characterized by strong forward and backward scattering, with a minimum around the nadir direction. This is in agreement with the observed BRDF pattern for dense leaf canopies. K_{geo} is shown in Fig. 5.2 normalized to its minimum value for reasons of clarity. It decreases over several orders of magnitude at large viewing zenith angles (white area in Fig. 5.2). Note that K_{vol}, and K_{geo} are zero for $\theta_0 = \theta_r = 0°$. Hence, the model parameter f_{iso} is equal to the nadir reflectance in case the Sun is at zenith.

Hu et al. (1997) validated kernel-based BRDF models with 27 multi-angular data sets from various land cover types. The accuracy of the model was high. The correlation coefficient between model and observations was above 0.7 for all and above 0.9 for more than half of the data sets. Although originally calculated for surfaces covered with vegetation, the Ross–Thick and Li–Sparse kernels are also applied for snow surfaces for the MODIS BRDF/albedo product. Stroeve et al. (2005) and Stroeve et al. (2013) assessed the accuracy of the 16-day albedo product of eleven years of measurements at 17 AWS on the Greenland ice sheet. They retrieved physically realistic ice sheet albedo values with an overall mean bias between MODIS and the in situ measurements of 0.022.

5.2 Retrieval of snow microstructure

Several algorithms have been developed that consider snow grains of irregular shape (e.g., Kokhanovsky and Zege, 2004; Lyapustin et al., 2009). The SGSP retrieval algorithm by Zege et al. (2011) to analyze satellite observations by MODIS was validated against ground-based in situ measurements from the Arctic, the Antarctic, Greenland, and Japan, revealing a correlation coefficient of 0.86 (Wiebe et al., 2013). Up to now, grain size products of polar orbiting satellites do not provide a sufficiently high temporal resolution that may resolve snow precipitation and metamorphism that typically can advance in a matter of hours. In this work, ground-based measurements with high temporal resolution were utilized to study the evolution of optical snow grain size in central Antarctica. In this regard, the SGSP algorithm was advanced and adapted to ground-based and airborne spectral albedo measurements.

5.2.1 Retrieval algorithm using satellite data

Within the SGSP algorithm, a value of 5.8 is used for the form factor A as an average value over a mixture of randomly oriented hexagonal plates and columns with $B(\xi) \approx 1.5$ and $g(\xi) \approx 0.84$. This is in accordance with Libois et al. (2014), who recommend a value for $B(\xi)$ within 1.6 ± 0.2 based on measurements in Antarctica and the French Alps. Any inaccuracy in the form factor A will affect the snow grain size retrieval in addition to instrumental errors. According to Zege et al. (2011), the retrieval inaccuracy, which may result from an inaccurate assumption of A, is less than 25 %. For the retrieval of optical snow grain size from satellite data, snow–atmosphere radiative interactions have to be taken into account by employing a model such as described by Zege et al. (2011). The effect of the atmosphere has been removed by employing a radiative transfer model (Tynes et al., 2001) using the subarctic winter atmospheric model (Kneizys et al., 1996) and the Arctic background aerosol model (Tomasi et al., 2007). The pollution level in Antarctica is low. Tomasi et al. (2007) measured an AOD of 0.015 at 500 nm wavelength at Kohnen station. During the observation period (December 2013–January 2014), the mean AOD (at 500 nm) as determined by a sun photometer was 0.016 (Andreas Herber, AWI Bremerhaven, personal communication, August 2017). Therefore, the effect of the low pollution level in Antarctica onto the retrieval results can be neglected (Zege et al., 2011).

Radiance data from MODIS (Level 1B Collection 5) on board the Aqua and Terra satellites were used to retrieve optical snow grain sizes in the area covered by the campaign. The SGSP algorithm was applied for cloudless areas. After a preliminary separation of snow pixels, the optical snow grain size of each pixel is retrieved from radiance measurements of MODIS channels 3 (469 nm wavelength), 2 (858 nm), and 5 (1240 nm). Assuming a spectrally constant BRDF of snow and using the combination of three spectral channels, the angular dependency of the measured radiance is excluded.

The optical snow grain sizes are provided in 2-D maps with a spatial resolution of 1 km. For the local optical snow grain size at Kohnen station, the spatial average of the 50×50 pixel of MODIS surrounding the geographic coordinates of Kohnen was calculated. Daily averages combine up to four MODIS overpasses per day under cloudless conditions. For the solar zenith angle range between 60° and 80°, the relative error of the retrieval is below 10 % for optical snow grain sizes between 30 and 300 µm. It grows with increasing solar zenith angle and gets as high as 20 % for $\theta_0 = 85°$ and even higher for lower Sun elevations. Therefore, the retrieval is generally not applied for cases with $\theta_0 > 85°$. The large uncertainty of the SGSP retrieval for high solar zenith angles is related to the assumptions on the particle form factor A and the approximation of the escape function $K_0(\mu_0)$, which is less accurate for oblique illumination angles. In combination with the strong forward scattering characteristic for snow grains, small errors in the assumed values of A and $K_0(\mu_0)$ can significantly distort the albedo. Similarly, the spectral behavior of the BRDF of snow depends on the illumination angle (Zege et al., 2011). Consequently, within this work the satellite retrieval is limited to $\theta_0 \leq 75°$. Furthermore, an additional uncertainty of 2 % originates from the atmospheric model.

5.2.2 Retrieval from spectral albedo measurements

For the ground-based and airborne spectral albedo measurements the atmospheric influence can be neglected because of the high surface elevation which causes a dry and aerosol-free atmosphere (Wendisch et al., 2004). To test this assumption, the direct fraction of global irradiance was simulated with the library for radiative transfer libRadtran by Mayer and Kylling (2005) using the discrete ordinate radiative transfer solver DISORT by Stamnes et al. (1988). The radiosondes released up to four times a day were used as meteorological input (profiles of air temperature, relative humidity, and static air pressure). The contribution of direct solar radiation to the global irradiance measured at the surface was estimated to vary between 94.6 and 99.8 % at the wavelengths used in the retrieval algorithm. Therefore, the simulated diffuse part hardly exceeded 5 % of the total incident irradiance. Hence, after careful selection of cloudless periods, the optical snow grain size can be calculated directly by inverting Eqs. (5.4) and (5.10):

$$R_{\mathrm{opt}} = \left[\frac{\ln \alpha_{\mathrm{p}}}{A \cdot K_0(\mu_0) \cdot \sqrt{\frac{4\pi\,\tilde{n}_{\mathrm{im}}}{\lambda}}}\right]^2 . \tag{5.20}$$

The uncertainty of the retrieved R_{opt} is related to the measured albedo and the assumed particle shape. Especially surface albedo values close to unity are uncertain due to the small differences between upward and downward irradiance. To minimize uncertainties, the retrieval algorithm was adapted to spectral ratio measurements as introduced by Werner et al. (2013) and Brückner et al. (2014). Using ratios of measured snow albedo at different wavelengths decreases the retrieval error as the impact of measurement uncertainties is reduced. For the ground-based CORAS and airborne SMART measurements, the ratio $\mathcal{R}$ of albedo measurements at 1280 nm normalized by the albedo at a weakly absorbing wavelength of 1100 nm was used:

$$\mathcal{R} = \frac{\alpha(\lambda_1 = 1280\,\mathrm{nm})}{\alpha(\lambda_2 = 1100\,\mathrm{nm})} . \tag{5.21}$$

Equation (5.20) thus transforms to

$$R_{\mathrm{opt}} = \left\{\frac{\ln \mathcal{R}}{A \cdot K_0(\mu_0) \cdot \left[\sqrt{\frac{4\pi\,\tilde{n}_{\mathrm{im}}(\lambda_2)}{\lambda_2}} - \sqrt{\frac{4\pi\,\tilde{n}_{\mathrm{im}}(\lambda_1)}{\lambda_1}}\right]}\right\}^2 , \tag{5.22}$$

with $\lambda_1 = 1280\,\mathrm{nm}$ and $\lambda_2 = 1100\,\mathrm{nm}$.

Figure 5.3a shows simulated snow surface plane albedo plots based on Eqs. (5.4) and (5.10) for the wavelength range between 300 and 2200 nm for different optical snow grain sizes (10 to 200 µm) at 54° solar zenith angle ($A = 5.8$, $\tilde{n}_{\mathrm{im}}$ data from

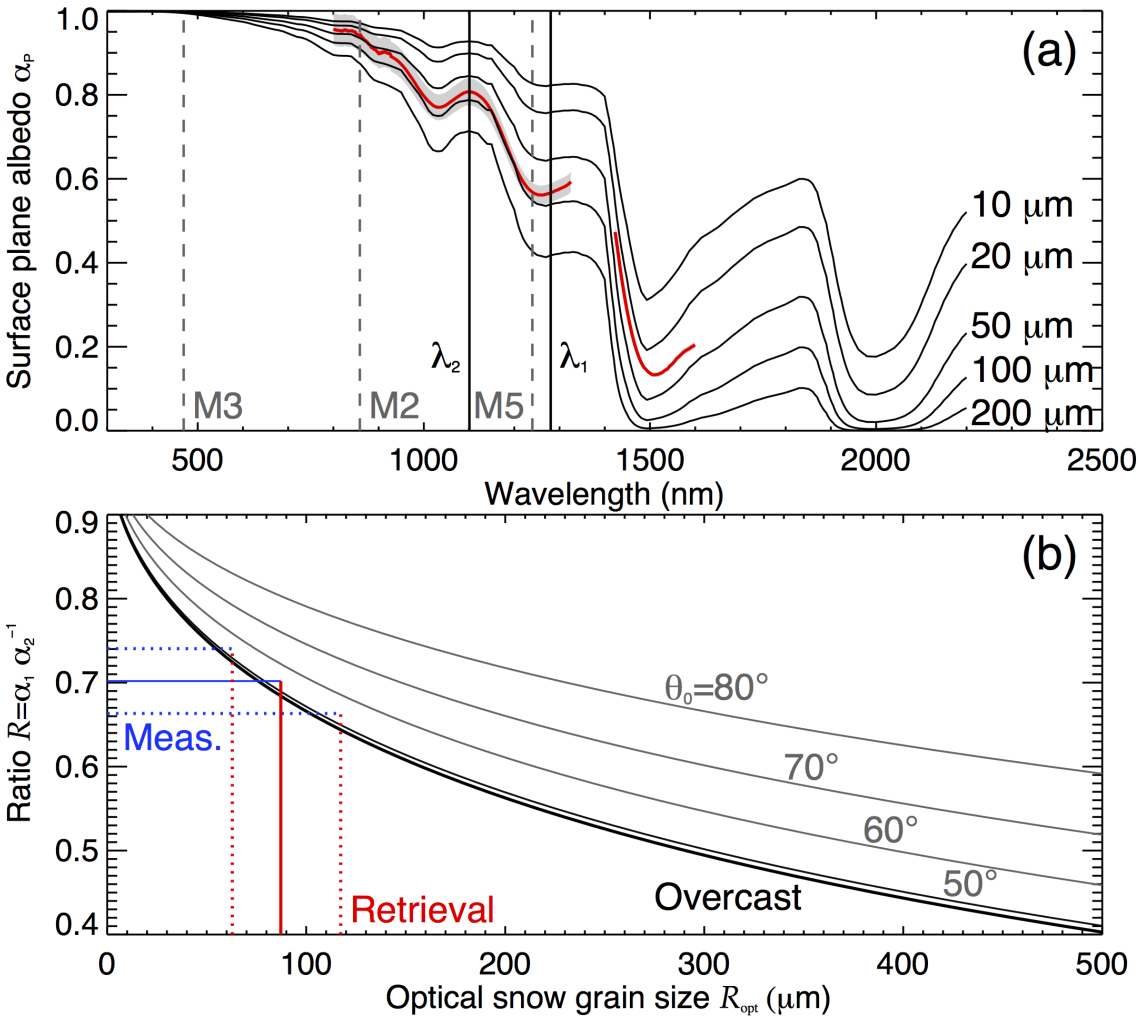

Figure 5.3: **(a)** α_p for $R_\mathrm{opt} = 10 - 200\,\mu\mathrm{m}$; $\theta_0 = 54°$. M3, M2, M5: MODIS bands used within SGSP algorithm. λ_1, λ_2: wavelengths used within CORAS and SMART retrieval. Red solid line and shaded gray: α measured by CORAS on 24 December 2013 (14:00 UTC). **(b)** Illustration of retrieval principle: $\mathcal{R}$ with respect to R_opt for $\theta_0 = 50 - 80°$ and for overcast conditions; retrieval of R_opt (red) from a measured $\mathcal{R} = 0.70 \pm 0.04$ (blue).

Warren and Brandt, 2008). In addition, it shows the MODIS channels used within the SGSP algorithm (M3, M2, and M5) and the spectral albedos α_p at wavelengths λ_1 and λ_2 used for calculating the albedo ratio $\mathcal{R}$. The spectra of α_p are related to the wavelength dependence of the imaginary part of the complex refractive index of ice. Band M5 and λ_1 are situated within a spectral albedo region which is more sensitive to optical snow grain size due to stronger absorption by ice. Furthermore, a spectral albedo between 700 and 1600 nm wavelength measured by CORAS on 24 December 2013 (14:00 UTC) is shown. The data gap between 1300 and 1400 nm wavelength is due to low signal-to-noise ratios at these wavelengths. The retrieval principle is illustrated in Fig. 5.3b. For four different solar zenith angles ($\theta_0 = 50$–$80°$), it shows the dependence of the measured albedo ratio $\mathcal{R}$ with respect to the optical snow grain size utilizing Eq. (5.22) ($A = 5.8$, $\tilde{n}_{\mathrm{im}}$ data from Warren and Brandt, 2008). Photons entering the snowpack under grazing angles have a higher probability of escaping the snowpack due to the pronounced forward scattering of ice crystals. This increases the spectral albedo mostly in the spectral range with strong ice absorption. Therefore, $\mathcal{R}$ increases with lower Sun position. The overcast line in Fig. 5.3b corresponds to a solar zenith angle of around 50° in cloudless conditions, which is in accordance with Wiscombe and Warren (1980). The measurement uncertainty of albedo measurements at 1280 nm wavelength was estimated with 6.8 % (compare Fig. 4.14). Using $\mathcal{R}$, the uncertainty is reduced to 5.5 %.

In addition to the instrumental errors, the surface slope at the footprint scale may influence the retrieval results. Using data from Picard et al. (2016), Dumont et al. (2017) found variations of the surface slope caused by wind drift at Dome C of ±2°. They estimated a resulting uncertainty of 10 % in retrieved SSA due to these variations of the surface slope. Assuming a similar variability of the slope of the surface at Kohnen, an additional uncertainty of 10 % is assumed for the retrieval of SSA. Applying Eq. (5.22) to the spectral albedo measured by CORAS on 24 December 2013 (Fig. 5.3a), the measured ratio $\mathcal{R}$ of 0.702 ± 0.039 leads to an estimated optical snow grain size of about $87 \pm 30\,\mu\mathrm{m}$ at $\theta_0 = 54°$ (blue and red lines in Fig. 5.3b). This corresponds to an estimated SSA of $38 \pm 14\,\mathrm{m^2\,kg^{-1}}$. However, the relative uncertainty of the retrieval varies with solar position and optical snow grain size. In general, it is higher for smaller snow grains. Overall, the retrieval uncertainty ranges between 25 and 37 % for the SSA throughout the measurement period.

Application in cloudless conditions

The retrieval algorithm was tested for specific measurements collected on a day with prevailing cloudless conditions. During this day, changes in optical snow grain size are expected to be small as the last snowfall took place six days earlier. Figure 5.4 shows the results retrieved from ground-based measurements with CORAS (SSA and optical snow grain size) on 24 December 2013 between 06:00 and 18:00 UTC. During this time, the solar zenith angle varied between 52° and 67°. Optical snow grain sizes were calculated according to Eq. (5.22) using the escape function $K_0(\mu_0)$ given by Eq. (5.5) (black line). The retrieved SSA shows a pronounced diurnal cycle and varies between 28 and $38\,\mathrm{m^2\,kg^{-1}}$ ($R_{\mathrm{opt}} = 86$–$117\,\mu\mathrm{m}$). As no snowfall occurred on that day, the diurnal cycle is very likely an artefact originating from the change in solar zenith angle and the assumed escape function $K_0(\mu_0)$. The approximation for the

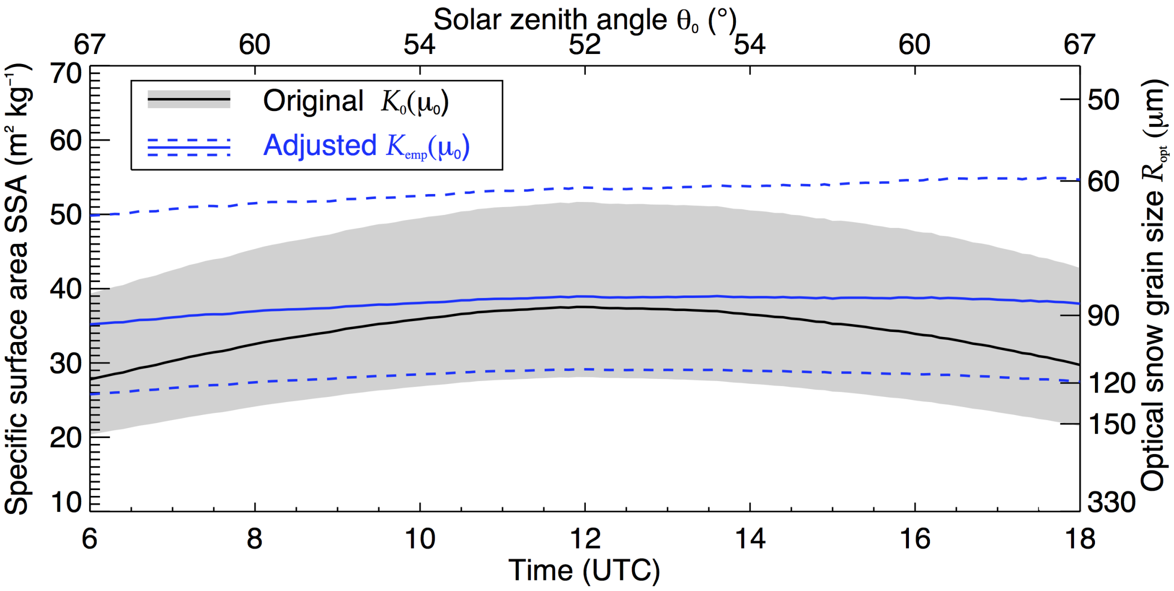

Figure 5.4: Diurnal cycle of SSA retrieved from CORAS measurements and optical snow grain size at Kohnen station on 24 December 2013. Black: SSA retrieved with original escape function $K_0(\mu_0)$ (solid line) with retrieval uncertainty (shaded gray); blue: SSA retrieved with empirically adjusted escape function $K_{\mathrm{emp}}(\mu_0)$ (solid line) and retrieval uncertainty (dashed lines).

escape function (Eq. 5.5) might be incorrect for snow at oblique incidence due to its elongated phase function. At the same time, a representative form factor A is required to account for the nonspherical snow grain shape. In order to eliminate the unrealistic diurnal cycle in the retrieved time series, the escape function was empirically adjusted to

$$K_{\mathrm{emp}}(\mu_0) = \frac{3}{7}\,(1.53 + 1.2\,\mu_0). \tag{5.23}$$

Note that $K_{\mathrm{emp}}(\mu_0)$ complies with the normalization condition in Eq. (5.6). Applying K_{emp}, the diurnal cycle in the retrieved SSA was significantly reduced (blue line in Fig. 5.4). The SSA ranges only between 35 and 39 $\mathrm{m^2\,kg^{-1}}$ (84–93 µm). The analysis of measurements during other cloudless days showed similar features: the diurnal variability was reduced from 32–39 to 40–41 $\mathrm{m^2\,kg^{-1}}$ (on 28 December 2013), from 24–32 to 31–34 $\mathrm{m^2\,kg^{-1}}$ (2 January 2014), and from 23–29 to 32–33 $\mathrm{m^2\,kg^{-1}}$ (28 January 2014), respectively. Therefore, K_{emp} was applied for the entire period of measurements. However, it should be noted that the escape function K_{emp} from Eq. (5.23) is an empirical approximation for the cases investigated here. To derive a more general description of the escape function, more cases and explicit BRDF measurements are needed, which is beyond the scope of this study.

Furthermore, Gallet et al. (2014b) observed SSA variations on a sub-daily scale using the DUFISSS instrument (DUal Frequency Integrating Sphere for Snow SSA measurements; Gallet et al., 2009) at Dome C in January 2009. They measured a decrease in SSA around noon from 40 to 33 $\mathrm{m^2\,kg^{-1}}$ before the SSA increased again to 41 $\mathrm{m^2\,kg^{-1}}$ at midnight. These temporal changes were attributed to the growth of sublimation crystals during daytime and nighttime formation of surface hoar. The SSA variations observed by CORAS on 24 December 2013 are of the same order of magnitude. However, the variations observed by Gallet et al. (2014b) are not symmetric to noon and their sign changes on a day-to-day basis due to the strong dependence on meteorological conditions. Even though an influence of crystal growth processes cannot be ruled out for the measurements presented here, the evident dependence on the solar zenith angle and the constant symmetry to noon of the diurnal cycle observed in the SSA retrieved from CORAS measurements strongly indicate a dominating influence of the solar zenith angle.

To minimize the impact of solar zenith angle even further, measurements between 13:00 and 14:00 UTC were preferably analyzed to represent the typical daily value of SSA and R_{opt}. Using these times of day additionally ensures higher upward and downward irradiances and, therefore, a reduced measurement uncertainty by enhanced signal-to-noise ratios. The retrieval time period is also close to the probing of in situ SSA between 15:00 and 18:00 UTC, which is favorable for the comparison. For each day, the times when SSA was retrieved from measurements with CORAS are added to Fig. 4.3 as black open circles. It should be noted that the cloud cover was estimated from visual observation every full hour, whereas CORAS measurements were partly analyzed for times in between the visual inspections, thus the manually observed cloud cover might not be perfectly representative for the actual CORAS measurement (e.g., 5 octa on 27 December 2013). Therefore, the CORAS measurements were carefully screened for any cloud contamination by analyzing the downward solar irradiance to guarantee homogeneous cloudless or overcast conditions.

Extension to overcast conditions

Even though new approaches to retrieve optical snow grain size below liquid clouds from airborne remote sensing are available and potentially applicable to spaceborne observations (Ehrlich et al., 2017), the SGSP algorithm is restricted to cloudless atmospheric conditions. However, in case of ground-based measurements, the analysis can be extended to cloudy conditions by using the spherical albedo and assuming isotropic illumination by the clouds. In this case, the spherical albedo α_{s} can be expressed by using $K_0(\mu_0) = 1$ (isotropic) in Eq. (5.4) (Kokhanovsky and Zege, 2004):

$$\alpha_\mathrm{s} = \exp(-y). \tag{5.24}$$

Using the albedo ratio $\mathcal{R}$ in Eq. (5.22), the retrieved optical snow grain size is obtained in overcast conditions:

$$R_\mathrm{opt}^\mathrm{cld} = \left\{ \frac{\ln \mathcal{R}}{A \cdot \left[\sqrt{\frac{4\pi\, \tilde{n}_\mathrm{im}(\lambda_2)}{\lambda_2}} - \sqrt{\frac{4\pi\, \tilde{n}_\mathrm{im}(\lambda_1)}{\lambda_1}} \right]} \right\}^2 . \tag{5.25}$$

Equation (5.25) is illustrated within Fig. 5.3b for comparison (overcast line). Retrievals in overcast conditions were applied on four days and are denoted as black filled circles in Fig. 4.3.

Retrieval using airborne measurements

For the airborne observations, SSA and R_opt were retrieved in a similar way as described above for ground-based data but using measurements of SMART. For comparison with the ground-based observations, any flight leg over the 5×5 pixel of MODIS surrounding Kohnen station ($5 \times 5\,\mathrm{km}^2$) is regarded as an overflight. The retrieval was not applied to each single measurement point but to the mean albedo measured within this box. The uncertainties of the retrieval were estimated similarly to the ground-based CORAS measurements, with the exception that the uncertainty of irradiance measurements is assumed to be slightly higher due to the additional uncertainty in the horizontal leveling of the airborne sensors by the horizontal stabilization of SMART (6.9 % at 1280 nm wavelength). As a result, the estimated uncertainty of the measured albedo ratio $\mathcal{R}$ is about 5.6 %.

5.2.3 Influence of wavelength choice

The in situ measurements and all retrievals (in the original and adapted SGSP algorithm) use different wavelengths. Therefore, each instrument retrieves the optical snow grain size from a different depth within the snowpack. All retrievals considered in this study were performed neglecting snow layer stratification. Vertical differences in snow grain size may impose systematic differences in the retrieved values between the various instruments. To quantify the impact of the choice of wavelength, the *e*-folding penetration depth $\epsilon(\lambda)$ was calculated, which is defined as the vertical distance in the

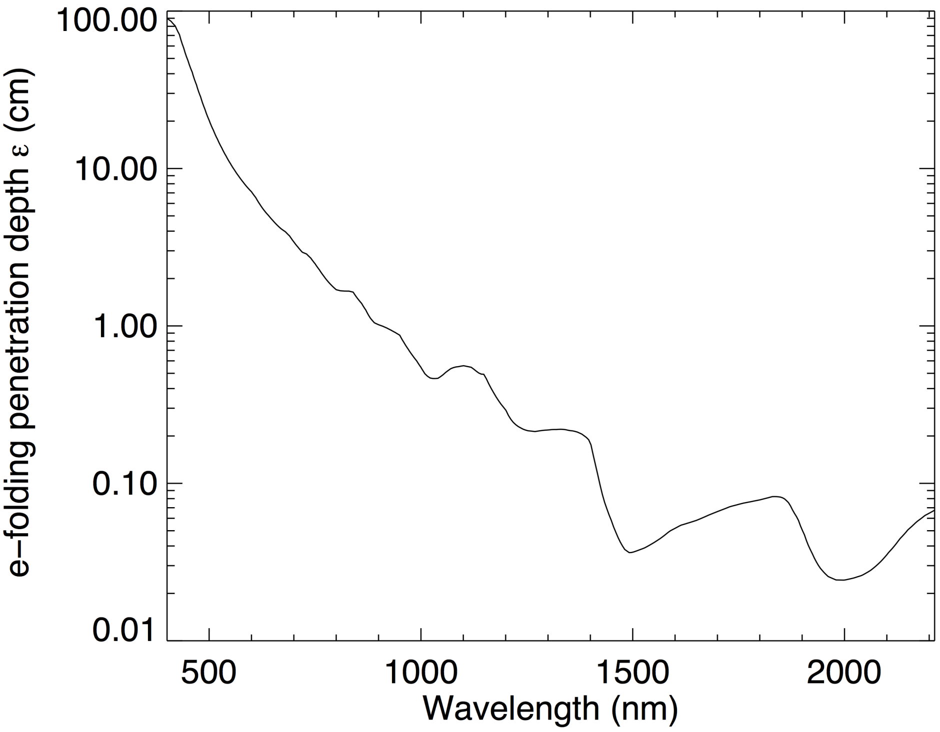

Figure 5.5: The e-folding penetration depth $\epsilon(\lambda)$ as a function of wavelength. The calculation assumed R_{opt} of 85 µm, ρ_{snow} of 330 kg m^{-3}, and a mixture of hexagonal plates and columns.

snow layer over which the irradiance reduces to $1/e$ or 37 % of the incident value. Following Zege et al. (1991), it is calculated by

$$\epsilon(\lambda) = \left\{ 3\,\frac{\rho_{\mathrm{snow}}}{\rho_{\mathrm{ice}}} \cdot \sqrt{2\pi \cdot \frac{\tilde{n}_{\mathrm{im}}}{\lambda\, R_{\mathrm{opt}}} \cdot B(\xi) \cdot \big[1 - g(\xi)\big]} \right\}^{-1} . \tag{5.26}$$

The calculation assumed a mixture of hexagonal plates and columns ($\rho_{\mathrm{ice}} = 916.7\,\mathrm{kg\,m^{-3}}$, $B(\xi) = 1.5$, $g(\xi) = 0.84$). The $\tilde{n}_{\mathrm{im}}$ data are taken from Warren and Brandt (2008). Moreover, ϵ depends on the wavelength λ, the optical grain size R_{opt}, and the density of snow ρ_{snow}. To allow for calculations representative for the measurements at Kohnen station, the in situ measurements of R_{opt} and ρ_{snow} are analyzed. During the two months of measurements, the optical grain size varied between 46 and 118 µm and the snow density changed between 281 and 359 kg m^{-3}. Figure 5.5 shows the spectral variation of ϵ at the mean values of $R_{\mathrm{opt}} = 85$ µm and $\rho_{\mathrm{snow}} = 330\,\mathrm{kg\,m^{-3}}$. The penetration depth is smaller at wavelengths with stronger ice absorption.

The ranges of R_{opt} and ρ_{snow} as measured throughout the observation period are used to calculate the range of variation of ϵ for the specific instrument wavelengths. The

IceCube system penetrates 0.14–0.31 cm into the snowpack at 1310 nm (at snow densities between 280 and 360 $\mathrm{kg\,m^{-3}}$ and optical grain sizes between 40 and 120 µm). At the wavelengths more sensitive to ice absorption, CORAS (SMART) mainly measures photons reflected in a depth up to 0.30 cm (at 1280 nm) and MODIS channel 5 (1240 nm) receives reflected radiation from a depth similar to the IceCube system. Hence, the penetration depth is almost identical for all measurement devices, which allows a comparison of the different SSA retrievals.

5.3 Characterization of hemispherical-directional reflectance of snow

Two approaches to characterize the snow HDRF measurements are described. Firstly, an anisotropy index AI is defined which follows the framework of an empirical BRDF model. However, this simple formulation is used as a diagnostic tool providing a measure for the anisotropy of the HDRF. Secondly, the weighting functions f_{iso}, f_{vol}, and f_{geo} are retrieved from the HDRF measurement by means of an inversion of the Ross–Thick-Li–Sparse semi-empirical BRDF model described in Sect. 5.1.2.

5.3.1 Anisotropy index

The anisotropy index AI is calculated from the values at three characteristic points P_1, P_2, and P_3 in the two-dimensional angular space of the HDRF. The viewing zenith angle (θ_{v}) and the relative viewing azimuth angle ($\Delta\Phi$) for each point are listed in Table 5.1.

Table 5.1: Viewing zenith angle θ_{v} and relative viewing azimuth angle $\Delta\Phi$ for the three points P_1, P_2, and P_3 that are used for the calculation of the anisotropy index AI.

Point	θ_{v} (°)	$\Delta\Phi$ (°)	f_{HDRF} **in Fig. 5.6**
P_1	60	0	1.381
P_2	0	0	0.895
P_3	60	45	1.250

The illustration of the point positions is shown in Fig. 5.6. The exemplary snow HDRF measured on 28 December 2013 exhibits a strong maximum in the forward scattering direction. The anisotropy index AI is defined as

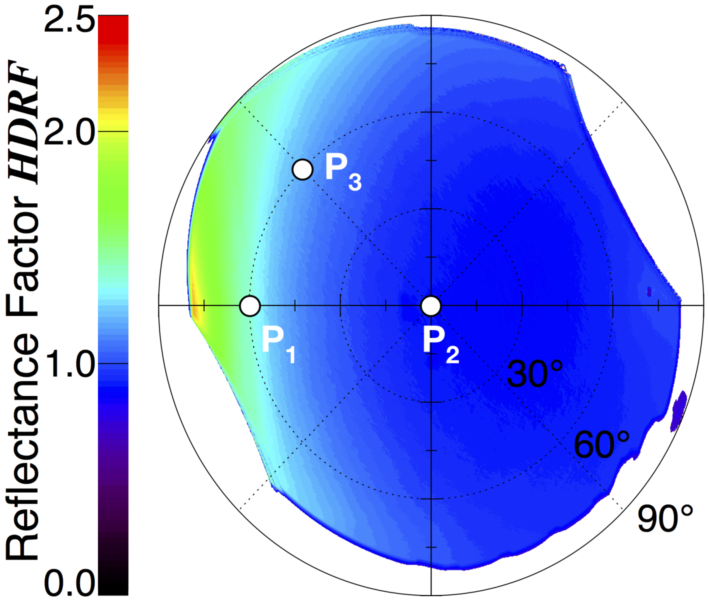

Figure 5.6: Exemplary snow HDRF measurement from 28 December 2013. In addition, the three points P_1, P_2, and P_3 use for the derivation of the anisotropy index AI are marked with white circles.

$$AI = \left[f_{\mathrm{HDRF}}\left(P_1\right) - f_{\mathrm{HDRF}}\left(P_2\right) \right] + \left[f_{\mathrm{HDRF}}\left(P_3\right) - f_{\mathrm{HDRF}}\left(P_2\right) \right] . \tag{5.27}$$

AI quantifies the maximum of the HDRF in the forward scattering direction. Preferably, P_1 would be shiftet to higher θ_{v}. However, P_1 could then be hidden by the aircraft frame depending on the flight direction with respect to the Sun. Thus, P_1 at $\theta_{\mathrm{v}} = 60°$ ensures a valid calculation of AI for all measurements. From the values f_{HDRF} of the points (see Table 5.1), an anisotropy index of 0.84 is derived.

5.3.2 Inversion of semi-empirical, kernel-driven model

The main benefit of retrieving the weighting functions f_{iso}, f_{vol}, and f_{geo} from the HDRF measurements is the comprehension of all radiance observations from the image. The retrieval is done inverting the RossThick-LiSparse BRDF model. Compared to the three points used for the calculation of the anisotropy index, about 500,000 observations and, thus, information about the complete two-dimensional shape of the HDRF are employed.

The modeled $f_{\mathrm{BRDF}}\left(\theta_{\mathrm{r}}, \theta_0, \Delta\Phi, \lambda\right)$ from Eq. 5.12 can be written in form of a sum

$$f_{\mathrm{BRDF},l} = \sum_{k=1}^{3} f_k \cdot K_{kl} . \tag{5.28}$$

The spectral dependence is omitted; the index l denotes a particular viewing and illumination geometry $(\theta_\mathrm{r}, \theta_0, \Delta\Phi)_l$. Considering an observation with N directional measurements ρ_l $(l = 1, \ldots, N)$, the error function $\mathcal{E}^2$ is defined as the difference between the observed and the modeled reflectances such that

$$\mathcal{E}^2 = \frac{1}{d} \sum_{l=1}^{N} \frac{\left(\rho_l - f_{\mathrm{BRDF},l}\right)^2}{w_l}. \tag{5.29}$$

The degree of freedom d is $(N - 3)$ and w_l denotes weights which are assigned to the respective observations. In general, w_l could take the values 1, ρ_l, or ρ_l^2. The goal of the inversion is the determination of the model weighting functions f_k such that $\mathcal{E}^2$ gets minimal. Hence, the inversion depends on the choice of the error function $\mathcal{E}^2$ and, thus, on the choice of the weights w_l. Weights equal to unity would yield minimization of the absolute error leading to smaller errors in angular domains with a large reflectance but causing larger deviations in domains with a small reflectance. Vice versa, relative error minimization (e.g., $w_l = \rho_l, \rho_l^2$) performs better in angular regions with lower reflectance. Different choices for w_l were tested for the retrievals performed in this work. Eventually, $w_l = \rho_l^2$ was applied as it yields lower retrieval errors for a larger angular domain.

Mathematically, the minimization equates to:

$$\frac{\partial \mathcal{E}^2}{\partial f_j} = \frac{1}{d} \sum_{l=1}^{N} \frac{2}{w_l} \cdot \left(\rho_l - f_{\mathrm{BRDF},l}\right) \cdot \left(\frac{\partial \rho_l}{\partial f_j} - \frac{\partial f_{\mathrm{BRDF},l}}{\partial f_j} \right) = 0. \tag{5.30}$$

The first partial derivative of the observations ρ_l with respect to f_j is zero, whereas

$$\frac{\partial f_{\mathrm{BRDF},l}}{\partial f_j} = \frac{\partial}{\partial f_j} \left(\sum_{k=1}^{3} f_k \cdot K_{kl} \right) = \sum_{k=1}^{3} \left(\frac{\partial f_k}{\partial f_j} \cdot K_{kl} + f_k \cdot \frac{\partial K_{kl}}{\partial f_j} \right) = \sum_{k=1}^{3} \delta_{kj} \cdot K_{kl} = K_{jl}. \tag{5.31}$$

δ_{kj} denotes the Kronecker symbol and it holds $\delta_{kj} = 1$ (if $k = j$, 0 otherwise). Inserting Eq. 5.31 into Eq. 5.30, it follows

$$\frac{\partial \mathcal{E}^2}{\partial f_j} = \frac{1}{d} \sum_{l=1}^{N} \frac{2}{w_l} \left(\rho_l - f_{\mathrm{BRDF},l}\right) \cdot K_{jl} = 0, \tag{5.32}$$

which is equivalent to

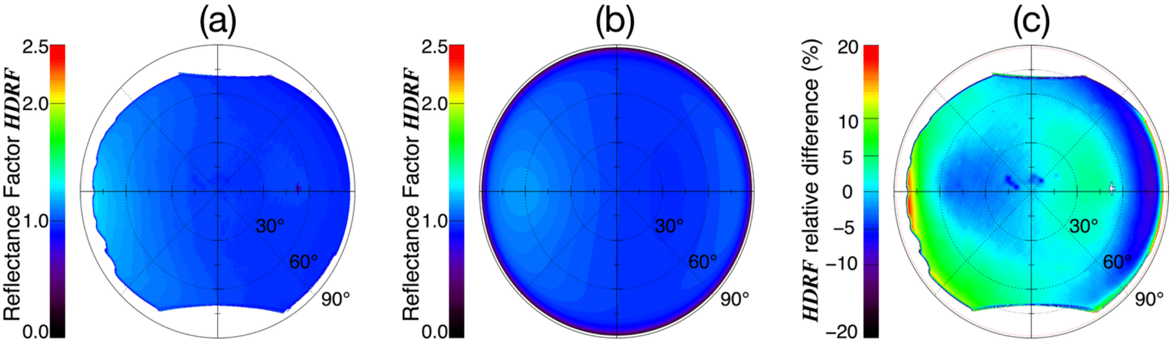

Figure 5.7: Exemplary retrieval of model parameters for HDRF measurement on 28 December 2013 ($\theta_0 = 51.6°$). **(a)** Observed snow HDRF ρ_l. **(b)** Modeled snow HDRF $f_{\mathrm{HDRF},l}$. **(c)** Relative difference $\left(\rho_l - f_{\mathrm{HDRF},l}\right)/f_{\mathrm{HDRF},l}$.

$$\sum_{l=1}^{N} \frac{\rho_l \cdot K_{jl}}{w_l} = \sum_{l=1}^{N} \frac{f_{\mathrm{BRDF},l} \cdot K_{jl}}{w_l} = \sum_{l=1}^{N} \sum_{k=1}^{N} \frac{f_k \cdot K_{kl} \cdot K_{jl}}{w_l}. \tag{5.33}$$

The second step in Eq. 5.33 follows from inserting Eq. 5.28 into Eq. 5.32. In defining the elements of the vector $\vec{\boldsymbol{V}}$ and the (3×3) matrix $\boldsymbol{M}$,

$$V_j = \sum_{l=1}^{N} \frac{\rho_l \cdot f_{jl}}{w_l} \quad \text{and} \tag{5.34}$$

$$M_{jk} = \sum_{l=1}^{N} \frac{K_{jl} \cdot K_{kl}}{w_l}, \tag{5.35}$$

such that

$$V_j = \sum_{k=1}^{3} M_{jk} \cdot f_k, \tag{5.36}$$

the model parameters f_k that minimize the error function $\mathcal{E}^2$ are given as

$$f_k = \sum_{j=1}^{3} M_{jk}^{-1} \cdot V_j. \tag{5.37}$$

Lewis (1995) showed that $\mathcal{E}^2$ has a global minimum in f_k. The analytical inversion of the BRDF model as presented above follows Strahler et al. (1996).

An exemplary inversion is performed on a snow HDRF measurement from 28 December 2013 ($\theta_0 = 51.6°$). Figure 5.7a shows the observations that are used as input for the algorithm. The inversion leads to the retrieved model parameters of 1.03 (f_{iso}), 0.24

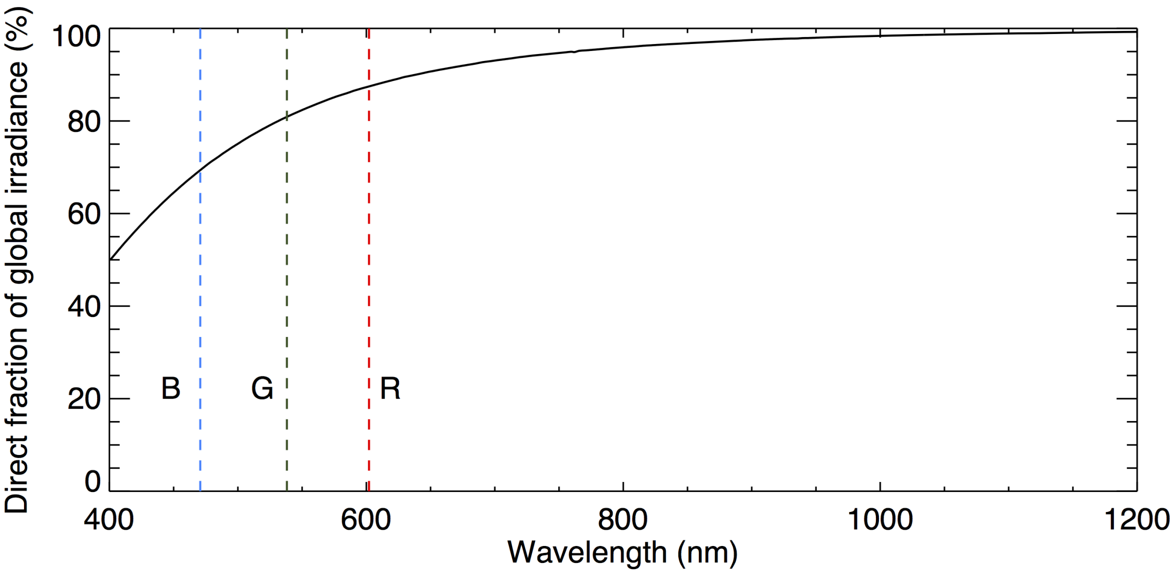

Figure 5.8: Simulated mean direct fraction of global irradiance (in %) in dependence of wavelength. Simulations were done with libRadtran using DISORT. In addition, the central wavelengths of the three camera channels are marked.

(f_{vol}), and 0.03 (f_{geo}). With the calculated kernels K_{kl}, the modeled HDRF is obtained (see Fig. 5.7b). The shapes of modeled and measured HDRF are similar; their relative difference is mostly within the range of ± 5% (see Fig. 5.7c). The largest deviations occur in the forward scattering direction (up to 20 %) because the location of maximum is not mimicked perfectly by the modeled HDRF. However, up to viewing zenith angles of around 75°, the relative difference is below 10 %.

The root-mean-square error (RMSE),

$$\sigma_{\mathrm{RMSE}} = \mathcal{E} = \sqrt{\frac{1}{N-3} \cdot \sum_{l=1}^{N} \frac{(\rho_l - f_{\mathrm{HDRF},l})^2}{w_l}}\,, \tag{5.38}$$

serves as a criterion for the quality of the inversion. For the example shown in Fig. 5.7, it is 5.4 %. σ_{RMSE} strongly depends on the anisotropy of the observed HDRF. On 28 December 2013, it was calculated for five different cases with increasing AI (from 0.3 to 0.84). As the largest deviations occur in angular domains with high reflectance values, σ_{RMSE} increases from 5.4 % to 9.8 %. Hence, the uncertainty of the inversion is in the range of 10 %.

Note that, this way, the parameters of a BRDF model are derived for a HDRF measurement as the BRDF is not measurable under atmospheric conditions. It is assumed that the atmospheric influence is negligible due to the high surface elevation and the dry, aerosol-free atmosphere on the Antarctic plateau. This is supported by simulations of the mean direct fraction of the global irradiance f_{dir} at Kohnen station between 10 December 2013 and 31 January 2014. The spectral dependence of the simulated direct fraction is shown in Fig. 5.8. For the central wavelengths of the three camera channels, the mean direct fraction is 87 % (for 602 nm wavelength, channel R), 81 % (538 nm, G), and 69 % (470 nm, B). The direct fraction strongly increases with wavelength as expected from the λ^{-4}-dependence of the Rayleigh scattering cross section. Thus, in order to minimize the differences between measured HDRF and intrinsic BRDF of the surface, longer wavelengths are favorable. Schaepman-Strub et al. (2006) simulated the difference between HDRF and BRF for snow surfaces using DISORT for different fractions f_{dir} at 550 nm wavelength. They found that with an increasing diffuse fraction of the incident irradiance, the shape of the HDRF is smoothed in comparison to the BRF ($f_{\mathrm{dir}} = 1$). For $f_{\mathrm{dir}} = 0.8$ at $\theta_0 = 30°$, the shape of the HDRF is still close to that of the BRF. Hence, the green camera channel used for the analysis within this thesis yields measured HDRF shapes that can serve as approximations for the intrinsic BRDF of the underlying snow surface.

6 Temporal and spatial variability of specific surface area

6.1 Temporal evolution of specific surface area at Kohnen station

Figure 6.1 shows the time series of SSA and respective optical snow grain size derived from satellite (MODIS, red), ground-based (CORAS, blue), and airborne (SMART, green) observations at Kohnen station between 10 December 2013 and 31 January 2014. For comparison, the in situ data are shown in black. The respective mean value and standard deviation of SSA for the different instruments are shown in Table 6.1.

6.1.1 Results obtained from ground-based measurements

SSA retrieved from CORAS measurements (blue circles in Fig. 6.1) varied between 29 and 96 $\mathrm{m^2\,kg^{-1}}$ throughout the campaign. The evolution of the time series revealed four pronounced relative maxima (minima in R_{opt}) on 18 December 2013, 3, 17, and 22 January 2014, which are related to snowfall of about 1 mm depth at Kohnen (visual estimation). The freshly fallen snow consists of smaller grains which increases SSA of the uppermost snow layer. The average snowfall-induced increase in SSA is 29 $\mathrm{m^2\,kg^{-1}}$. These highest SSA values are followed by a gradual decrease in SSA. From 18 to 30 December 2013, the SSA decreased daily by approximately 4 $\mathrm{m^2\,kg^{-1}\,day^{-1}}$ from 72 to 30 $\mathrm{m^2\,kg^{-1}}$. This corresponds to an increase in optical snow grain size by 5 $\mathrm{\mu m\,day^{-1}}$. This decrease in SSA is slightly slower than measured by Libois et al. (2015) at Dome C, Antarctica. They observed a drop in SSA from 90 to 30 $\mathrm{m^2\,kg^{-1}}$ within 10 days due to snow metamorphism. However, some abrupt decreases in SSA such as from 3 to 4 January 2014 cannot be explained by metamorphism alone, especially under the cold conditions on the Antarctic plateau. Instead, this strong increase in optical snow grain size within one day is supposedly caused by strong wind, which removes the small, freshly fallen snow grains and exposes deeper layers of larger grains. With

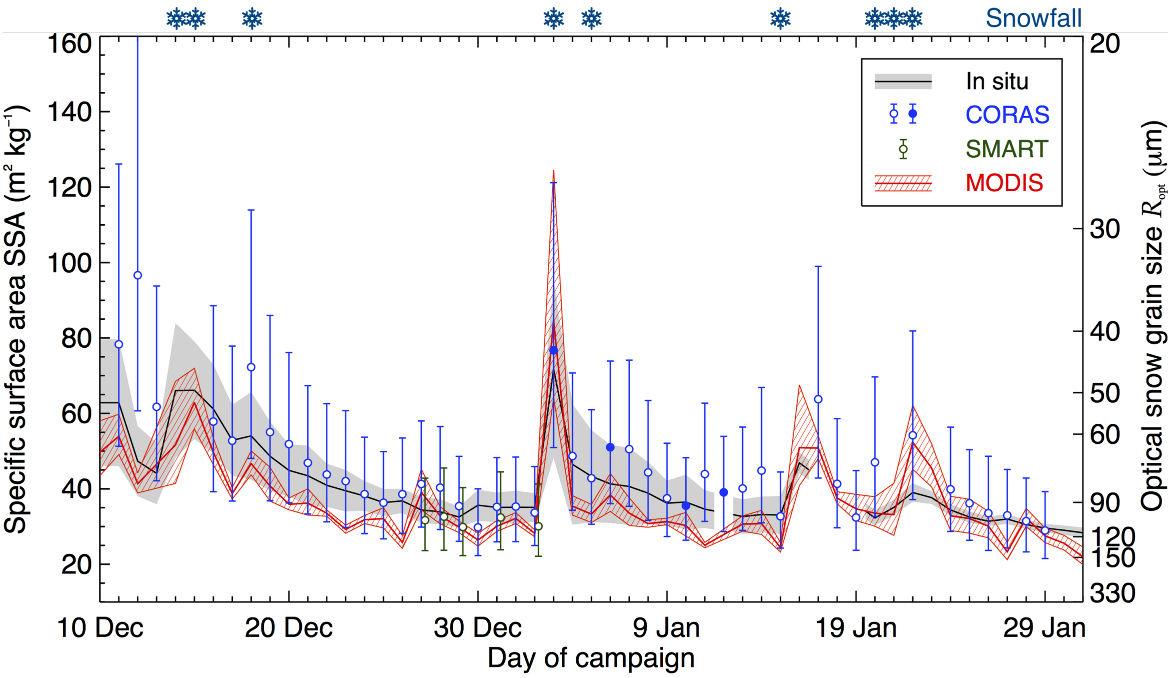

Figure 6.1: Time series of measured SSA and R_{opt} for the entire campaign at Kohnen station. Black: mean (solid line) and standard deviation (shaded gray) for in situ measurements; red: MODIS retrieval; blue: CORAS retrieval in cloudless (open circles) and overcast (filled circles) conditions; green: SMART retrieval in cloudless (open circles) conditions. For better visibility, the SMART data points are slightly shifted to the right on the respective dates. Top right: mean and standard deviation of the SSA retrieved by the different instruments. Snowflake symbols denote snowfall events.

mean horizontal wind speeds of $4\,\mathrm{m\,s^{-1}}$ and maximum wind gusts reaching $11\,\mathrm{m\,s^{-1}}$ at Kohnen station (from AWS measurements), drifting snow occurred mainly due to creeping or saltation of the ice crystals. This wind-induced transportation of freshly fallen snow grains is superimposed on the signal of snow metamorphism in the temporal evolution of SSA retrieved from CORAS.

The mean SSA is $46 \pm 14\,\mathrm{m^2\,kg^{-1}}$. The SSA retrieved from CORAS measurements reproduces the in situ probing (solid black line in Fig. 6.1) within the measurement uncertainties and range within the shaded gray area, which indicates the standard deviation of the mean SSA value along the 100 m transect where SSA was probed. The standard deviation is a measure of the small-scale variability in SSA mainly caused by wind-induced roughness structures of the snow surface. Nevertheless, the temporal signal in SSA is significant for all sample positions. Only the first and the last two snowfall-induced relative maxima in SSA are overestimated by CORAS. The agreement between the SSA retrieved by CORAS and the in situ data is reflected in the linear correlation coefficient of 0.79 (95 % confidence interval: 0.64–0.88).

Table 6.1: Mean and standard deviation of SSA measured by different instruments during the campaign at Kohnen station.

Instrument	Mean SSA ($\mathrm{m^2\,kg^{-1}}$)	Standard deviation ($\mathrm{m^2\,kg^{-1}}$)
In situ	40.9	10.9
CORAS	45.6	14.2
SMART	31.3	1.3
MODIS	36.7	11.4

On eight days throughout the campaign, no retrieval of SSA using CORAS data was possible due to broken clouds. For that reason, the first relative maximum of the in situ measured SSA (15 December 2013) could not be reproduced by CORAS data. Overcast retrieval conditions were used on four days (filled circles: 3, 6, 10, and 12 January 2014). The retrieved SSA values on overcast days agree well with the in situ measurements and are in coherence with the retrieved SSA under cloudless conditions. This illustrates the potential of extending the retrieval method by applying the spherical albedo. In addition, it highlights the benefit of ground-based observations that, in comparison to satellite observations, provide continuous time series and are not restricted to cloudless time periods only.

6.1.2 Airborne measurements

On five days between 27 December 2013 and 2 January 2014, SSA and R_{opt} were retrieved from airborne spectral albedo measurements by SMART (green circles in Fig. 6.1). With a mean value of $31 \pm 1\,\mathrm{m^2\,kg^{-1}}$, SMART seems to slightly underestimate in situ SSA by a factor of 1.3. Using the same calibration reference and the identical retrieval algorithm for both CORAS and SMART, the differences are likely related to the different sizes of the sampling areas covered by both instruments. While CORAS measurements represent a spot of about $2 \times 2\,\mathrm{m^2}$, SMART data stem from a larger footprint and were averaged over an area of $5 \times 5\,\mathrm{km^2}$ surrounding Kohnen station. Furthermore, the area over which the airborne data are averaged is largely determined by the flight track. On such scales, the local, small-scale variability of SSA as indicated by the in situ measurements can lead to significant differences in SSA. Already along the 100 m transect, in situ SSA varied by up to 34 % (4 January 2014). On larger scales, this variability is likely to increase. In addition, unidentified systematical errors in the airborne SMART measurements are a possible reason for the underestimation of SSA.

6.1.3 Satellite measurements

A smaller bias is present in the SSA retrieved from MODIS data ($37 \pm 11\,\mathrm{m^2\,kg^{-1}}$, red line in Fig. 6.1), which integrates over an area of $50 \times 50\,\mathrm{km^2}$ surrounding Kohnen station. The uncertainty in Fig. 6.1 is given as the standard deviation of SSA over the $50 \times 50\,\mathrm{km^2}$. The SSA derived from MODIS observations could reproduce the SSA signal from in situ measurements, the linear correlation coefficient is in the range of 0.86 (95 % confidence interval: 0.75–0.92); it is slightly higher than for the CORAS measurements. Furthermore, it was possible to resolve abrupt changes in SSA due to precipitation or wind-induced transportation of snow grains. For high solar zenith angles, the SGSP algorithm is known to underestimate the actual optical snow grain size (Zege et al., 2011). During the entire observation period, the solar zenith angle varied between 52 and 87° and in 48 % of the time was higher than 70°. However, the optical snow grain size retrieved from the MODIS data mostly showed a slight overestimation compared to the in situ measurements. The comparison of the ground-based (CORAS) and spaceborne (MODIS) remote sensing methods to retrieve SSA yields a linear correlation coefficient of 0.74 (95 % confidence interval: 0.56–0.85) which lies in the same range as the correlation coefficient between CORAS and the in situ measurements.

The three time series of SSA retrieved from ground-based CORAS, airborne SMART, and spaceborne MODIS measurements as shown in Fig. 6.1 were published in the Publishing Network for Geoscientific & Environmental Data (PANGAEA). The data set is available under: `https://doi.pangaea.de/10.1594/PANGAEA.880815` (Carlsen et al., 2017b).

6.2 Spatial variability of specific surface area in Dronning Maud Land

Figure 6.2 shows the time series for the SSA retrieved from SMART along the flight track of the research flight on 27 December 2013. Additionally, the time series of the MODIS SSA is plotted for comparison. Note that technically, the MODIS SSA is no time series. It is derived along the flight track from a single satellite image close to the time of flight (9:45 UTC). The right panel of Fig. 6.2 shows the corresponding spatial domain. From Kohnen station (P3), a triangular flight pattern was flown via the way

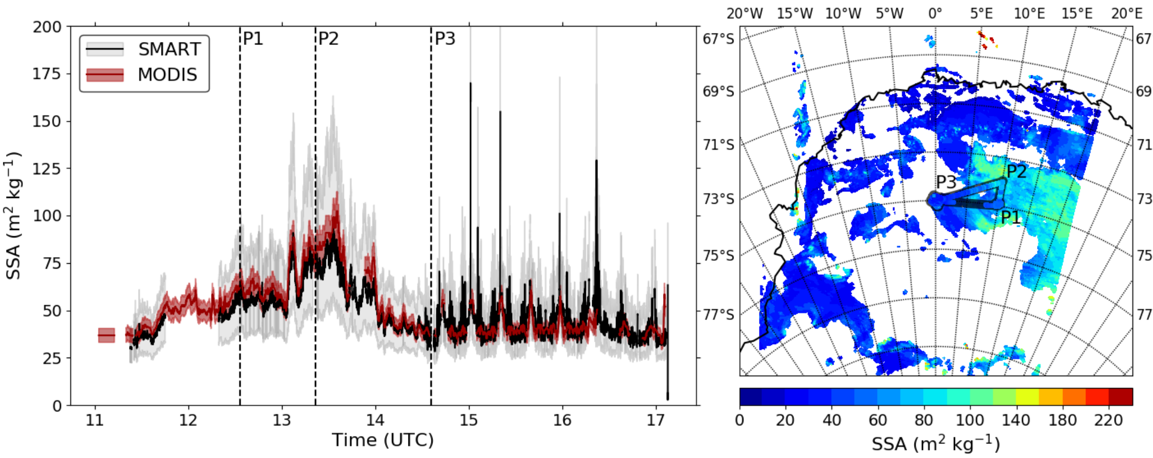

Figure 6.2: Comparison between SSA retrieved from SMART and MODIS for the research flight on 27 December 2013. P1, P2, and P3: way points during the flight. **(a)** Time series for SMART (black, uncertainty in shaded gray) and MODIS (red, uncertainty in shaded red). **(b)** Map of observation area. Colored contour: MODIS SSA on 9:45 UTC. Colored flight track: SMART SSA.

points P1 and P2. The flight track color corresponds to the SMART SSA, the colored contour in the background denotes the MODIS SSA as retrieved from the satellite image.

Between 11:45 UTC and 12:19 UTC, no SMART measurements exist due to a failure in the horizontal stabilization of SMART. Data gaps in the MODIS time series correspond to clouds (white areas in the right panel of Fig. 6.2. The SSA values mainly range between 30–100 m^2 kg^{-1}. Both SMART and MODIS agree within the ranges given by the measurement uncertainties; however, a slight underestimation is again visible for the SMART measurements. As can be seen from the satellite image, around waypoint P2, the aircraft entered an area with higher SSA values, possibly due to recent snowfall.This increase in SSA could be reproduced with the SMAT measurements. After waypoint P3 was passed, a rectangular grid pattern was flown dedicated to geophyical observations within the CoFi project. During this time, an almost constant SSA is retrieved as the grid was flown in the vicinity of Kohnen research station. The spikes in the SSA data correspond to aircraft turns. Still, the time series is interesting for comparison as the pattern was flown under overcast conditions. Nevertheless, SMART reproduces the MODIS SSA values well. Also for the SMART instrument, an extension to overcast conditions applying the spherical albedo yields reasonable values and extends the retrieval coverage. The underestimation between SMART and MODIS seems to be smaller after waypoint P3 was passed. Note that the corresponding satellite image dates back to 9:45 UTC. As can be seen from Fig. 6.1, the SSA retrieved by CORAS (at around 11:00 UTC) already shows a slight increase compared to the

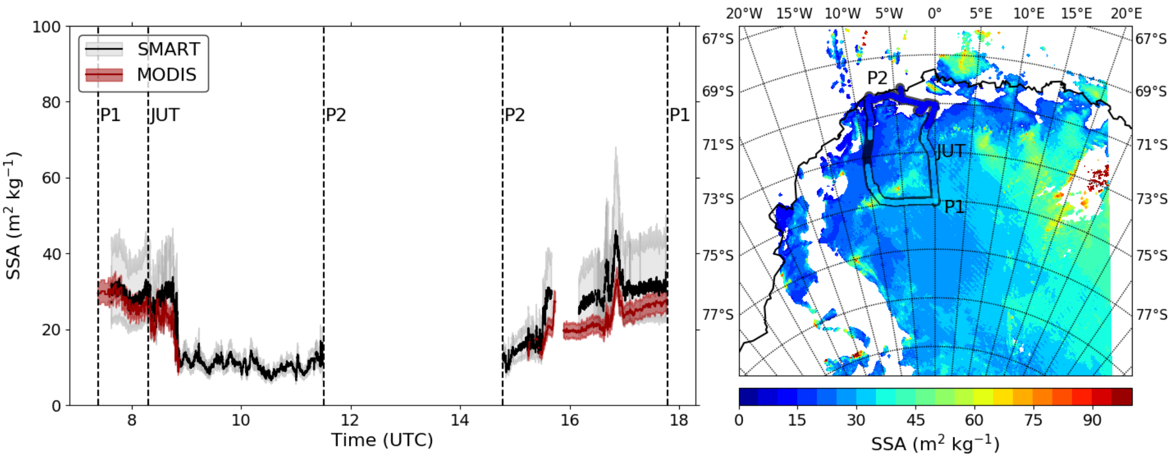

Figure 6.3: Comparison between SSA retrieved from SMART and MODIS for two research flights on 2 January 2014. P1: Kohnen research station. P2: Neumayer III station. JUT: Entrance to Jutelstraumen glacier. **(a)** Time series for SMART (black, uncertainty in shaded gray) and MODIS (red, uncertainty in shaded red). **(b)** Map of observation area. Colored contour: MODIS SSA on 7:30 UTC. Colored flight track: SMART SSA.

day before. Whereas the MODIS time series shows a constant SSA value at Kohnen station for the entire time period, this small increase in SSA could be observed by SMART, thereby decreasing the apparent offset.

On 2 January 2014, two research flights (Kohnen–Neumayer III–Kohnen) covered an area northwest of Kohnen research station. The comparison of the SSA between SMART and MODIS is shown in Fig. 6.3. The MODIS image in the right panel of Fig. 6.3 is from 7:30 UTC. However, for the comparison of the time series of the second flight, the MODIS image from 14:40 UTC was used as it was closer to the measurement times. In the first part of the flight, SMART and MODIS agree within the measurement uncertainties. However, starting at around 8:18 UTC, the differences increase. Subsequently, a strong decrease in SSA from around 30 m^2 kg^{-1} down to 10 m^2 kg^{-1}was observed. This corresponds to a three-fold increase in optical snow grain size from 110 µm to 327 µm. At 8:18 UTC, the aircraft passed the entrance of the Jutelstraumen glacier (JUT). From this point, the altitude a.s.l. decreased from approximately 2500 m to 250 m. At the same time, the near-surface air temperature increased significantly. Whereas the near-surface air temperature at Kohnen station was constantly below -20 °C on that day, the KT19 infrared thermometer onboard Polar 6 measured a surface temperature of -1.3 °C at around 10:00 UTC. This corresponds to an increase in near-surface air temperature by about 20 K due to the lower surface elevation, giving rise to stronger metamorphism processes that result in larger snow grains (lower SSA). This feature typical for coastal areas could be reproduced by the SMART measurements. At the same time, MODIS could not retrieve the SSA

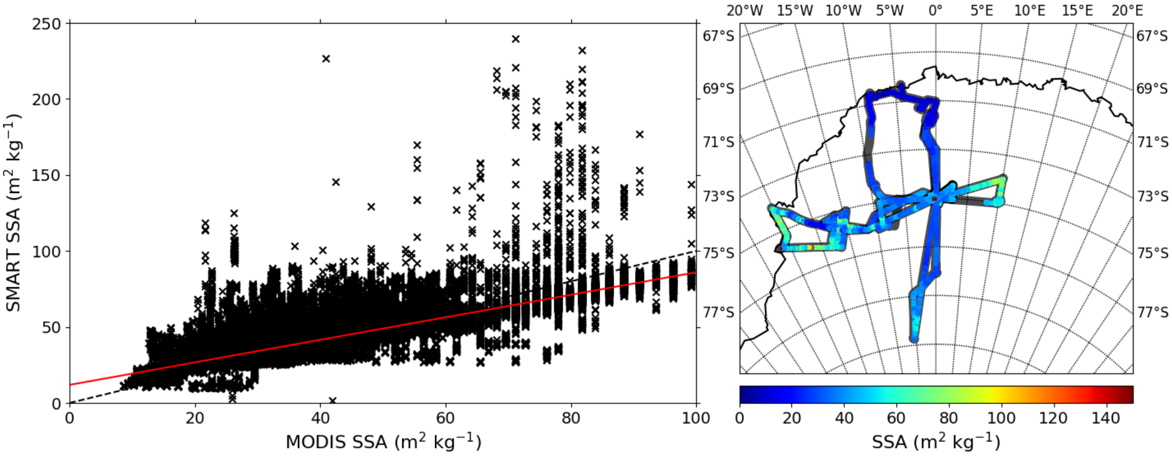

Figure 6.4: Comparison between SSA retrieved from SMART and MODIS for all research flights between 27 December 2013 and 5 January 2014. **(a)** Regression plot: $\text{SSA}_{\text{SMART}}$ in dependence of $\text{SSA}_{\text{MODIS}}$. Dashed line: 1:1-line. Red solid line: linear fit. **(b)** Map of observation area with tracks of the analyzed research flights. The colored flight tracks correspond to the SSA value as measured by SMART.

due to cloud cover. A similar increase in SSA was found on the return flight with increasing surface elevation. Only between 15:40–16:10 UTC, no SSA values could be retrieved from SMART measurements due to a stratus cloud between the aircraft and the surface.

The analyzed research flights are representative for the SSA features measured by SMART. A map covering all flight tracks and corresponding SSA as retrieved from SMART is shown in Fig. 6.4. Both coastal areas and regions in the interior of the plateau were covered by the measurements. In areas with supposedly recent snowfall, higher SSA values were measured (e.g., flight to the west of Kohnen to Halley station on 4 January 2014). In general, SMART retrieved slightly lower SSA values compared to MODIS. A similar trend has already been found for the temporal SSA measurements at Kohnen station. The linear fit in the regression plot (see left panel in Fig. 6.4) yields:

$$\text{SSA}_{\text{SMART}} = 0.74\,(\text{m}^2\,\text{kg}^{-1})^{-1} \cdot \text{SSA}_{\text{MODIS}} + 11.9\,\text{m}^2\,\text{kg}^{-1} \tag{6.1}$$

The linear correlation coefficient is 0.74. Hence, for the spatial measurements, the SSA measured by SMART agrees with MODIS within the ranges given by the measurement uncertainties. The spatial variability of SSA in the areas covered by the airborne observations lies in the same range as the temporal variability of SSA at Kohnen station.

7 Parameterization of hemispherical-directional reflectance of snow – Case studies

The HDRF of a snow surface varies, amongst others, with the position of the Sun, the surface roughness and the snow grain size. In the following, two case studies are presented to show the influence of the solar zenith angle and the surface roughness. In this regard, the anisotropy index is used as a diagnostic tool, whereas the retrieved HDRF model parameters allow for a parameterization of the HDRF. Eventually, the dependence of the model parameters from θ_0, l_{rough}, and R_{opt} is analyzed with respect to the footprint area over which the HDRF measurements are averaged.

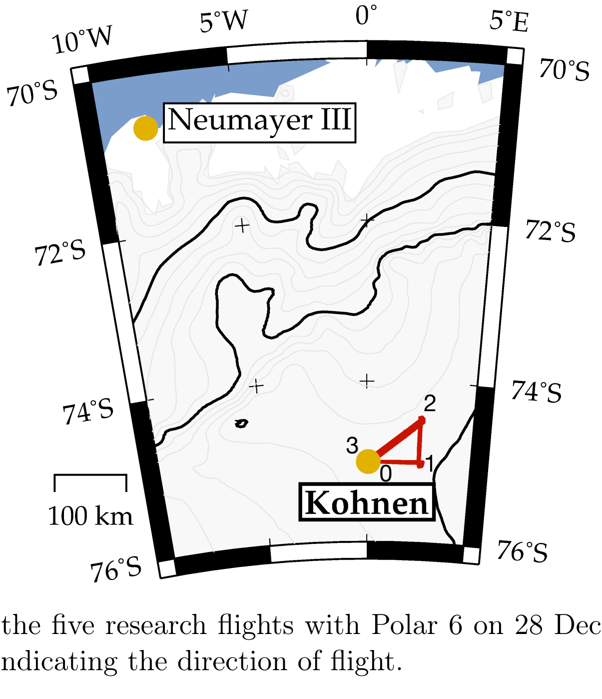

Figure 7.1: Track of the five research flights with Polar 6 on 28 December 2013. The way points are numbered, indicating the direction of flight.

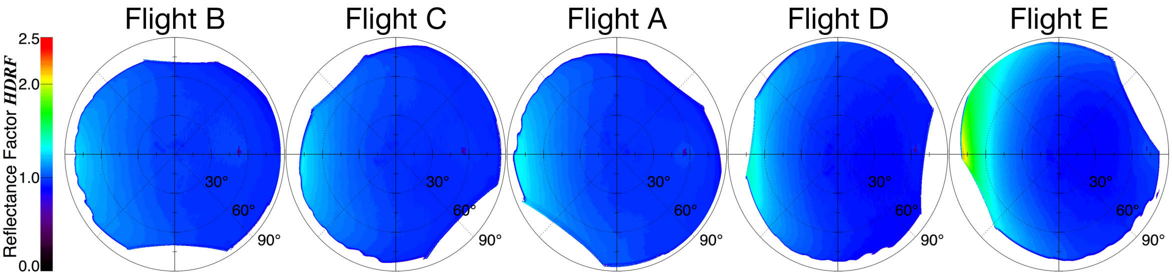

Figure 7.2: Averaged snow HDRF between WP1 and 2 for the five consecutive research flights on 28 December 2013.

7.1 28 December 2013: solar zenith angle

The research flights with Polar 6 on 28 December 2013 were dedicated to study the influence of θ_0 on the snow HDRF. For this purpose, five consecutive flights were conducted in an area northeast of Kohnen. The flight track and the way points (WP) are illustrated in Fig. 7.1.

For each flight (A-E), the snow HDRF was averaged between WP1 and WP2; the results are shown in Fig. 7.2. The solar zenith angle varied between 51.6 and 71.8°. As Polar 6 took identical routes throughout the flight, the flight leg between WP1 and WP2 always covered the same area. Therefore, the surface roughness (retrieved from the laser scanner) of approximately 0.039 m remained constant. Within the retrieval uncertainties, the same holds true for the optical snow grain size. R_{opt} varied between 79 and 94 µm. This minimizes a possible influence of R_{opt} or l_{rough} on the snow HDRF that would be superimposed on the signal of θ_0. Cloudless conditions prevailed during the flights. Table 7.1 lists all relevant parameters of the five HDRF measurements.

Table 7.1: Measured and retrieved parameters given as averages between WP 1 and 2 for the five consecutive research flights on 28 December 2013. The flights are ordered with increasing solar zenith angle.

	θ_0(°)	R_{opt} (µm)	l_{rough} (m)	AI	f_{iso}	f_{vol}	f_{geo}
Flight B	51.6	92	0.039	0.30	1.031	0.236	0.031
Flight C	54.3	94	0.039	0.33	1.015	0.235	0.029
Flight A	55.4	87	0.040	0.37	1.012	0.252	0.027
Flight D	62.5	86	0.039	0.52	0.968	0.370	0.031
Flight E	71.8	79	0.038	0.84	0.974	0.566	0.038

With increasing θ_0, the maximum of the HDRF in the forward scattering direction

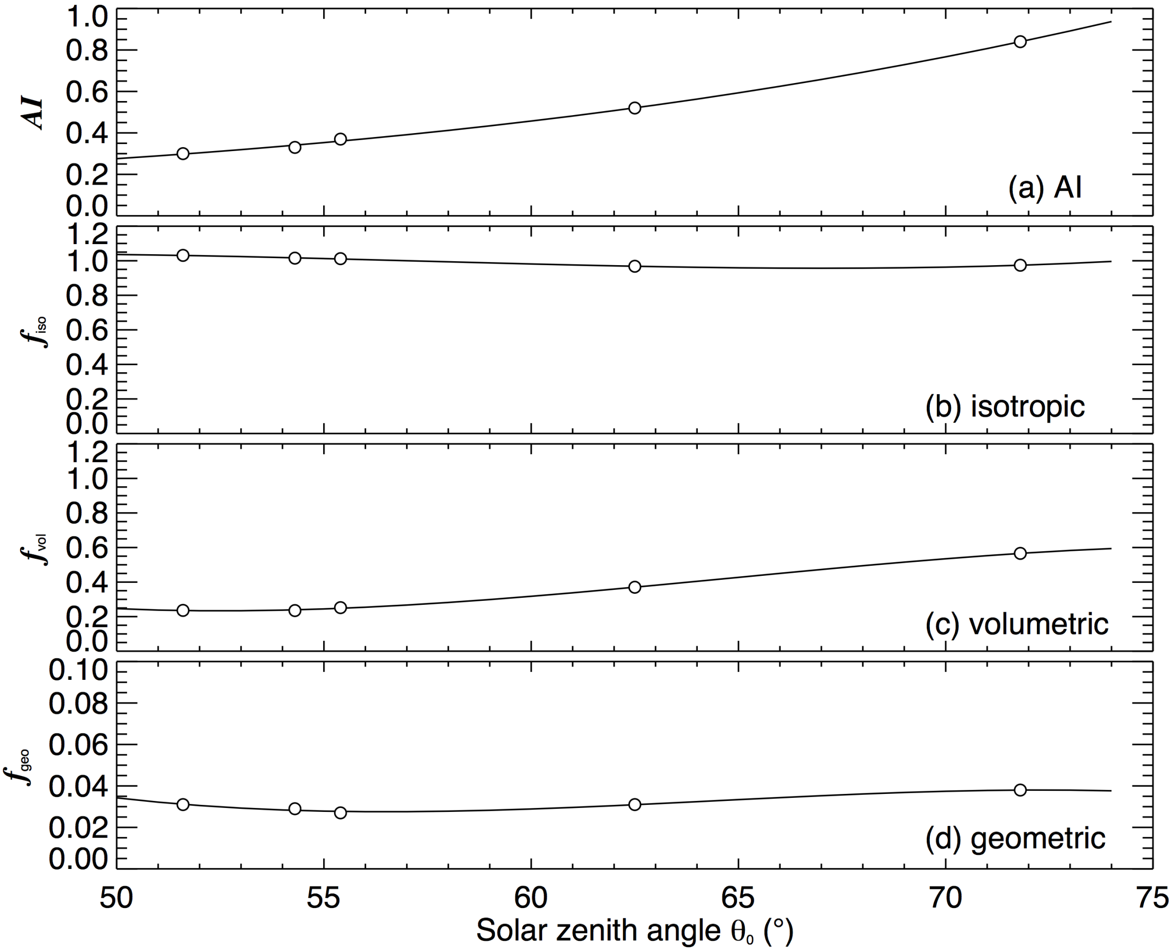

Figure 7.3: Dependence of the retrieved parameters from the solar zenith angle θ_0 for the five research flights on 28 December 2013. The solid lines represent third-degree polynomial fits of the parameters with respect to θ_0. **(a)** The anisotropy index AI. **(b)** The isotropic weight f_{iso}. **(c)** The volumetric weight f_{vol}. **(d)** The geometric weight f_{geo}.

becomes even more pronounced (see Fig.7.2). Correspondingly, the anisotropy gets larger which is demonstrated by an increase of AI from 0.3 to 0.84. The values of AI are listed in Table 7.1 together with the retrieved HDRF model parameters f_{iso}, f_{vol}, and f_{geo}. Furthermore, Fig. 7.3 shows the dependence of AI and the f_k from θ_0.

The increasing AI can be parameterized using a third degree polynomial fit such that

$$AI = 7.6 \cdot 10^{-6} \cdot \theta_0^3 - 7.3 \cdot 10^{-4} \cdot \theta_0^2 + 0.03 \cdot \theta_0 - 0.3. \tag{7.1}$$

f_{iso} slightly decreases with θ_0 from 1.031 to 0.974. f_{vol} shows a clear dependence of θ_0, increasing from 0.236 at $\theta_0 = 51.6°$ to 0.566 at 71.8°. During the first three research flights, θ_0 did vary only slightly. Therefore, the strongest trends are visible between Flight A and Flight E. The increase in f_{geo} is not as pronounced as for f_{vol} but still

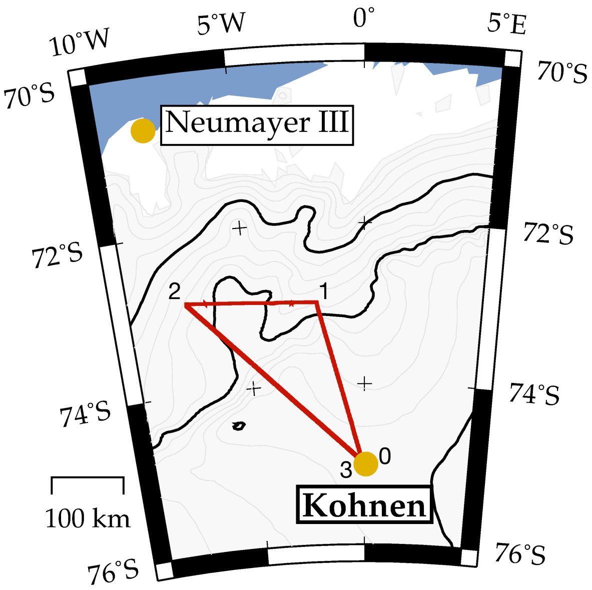

Figure 7.4: Flight track of Polar 6 on 25 December 2013. The way points are numbered, indicating the direction of flight.

visible.

The probability for photons entering the snowpack to leave it after just a few scattering events increases for lower Sun elevation. With increasing θ_0, the reflection properties of the snow layer converge to the single-scattering properties of ice crystals. In addition, longer shadows are cast by surface roughness structures at grazing angles of incidence. This expected increase in the anisotropy of the snow HDRF is obvious in the increasing AI and changing model parameters f_k.

The model parameters f_k can be parameterized with respect to θ_0 using a third degree polynomial fit such that

$$f_{\mathrm{iso}} = 2.3 \cdot 10^{-5} \cdot \theta_0^3 - 3.9 \cdot 10^{-3} \cdot \theta_0^2 + 0.22 \cdot \theta_0 - 2.9\,, \tag{7.2}$$

$$f_{\mathrm{vol}} = -5.1 \cdot 10^{-5} \cdot \theta_0^3 - 9.9 \cdot 10^{-3} \cdot \theta_0^2 - 0.62 \cdot \theta_0 + 12.8\,, \tag{7.3}$$

$$f_{\mathrm{geo}} = -5.3 \cdot 10^{-6} \cdot \theta_0^3 + 1.0 \cdot 10^{-3} \cdot \theta_0^2 - 0.06 \cdot \theta_0 + 1.4\,. \tag{7.4}$$

7.2 25 December 2013: surface roughness

The research flight on 25 December 2013 targeted an area northwest of Kohnen in the direction of the coastline. As can be seen from Fig. 7.4, the surface elevation changed drastically during the flight, decreasing until WP2 before increasing again on the flight back to Kohnen station. This fosters larger variations in the surface roughness.

Between WP1 and WP2, no roughness structure could be recognized from the pho-

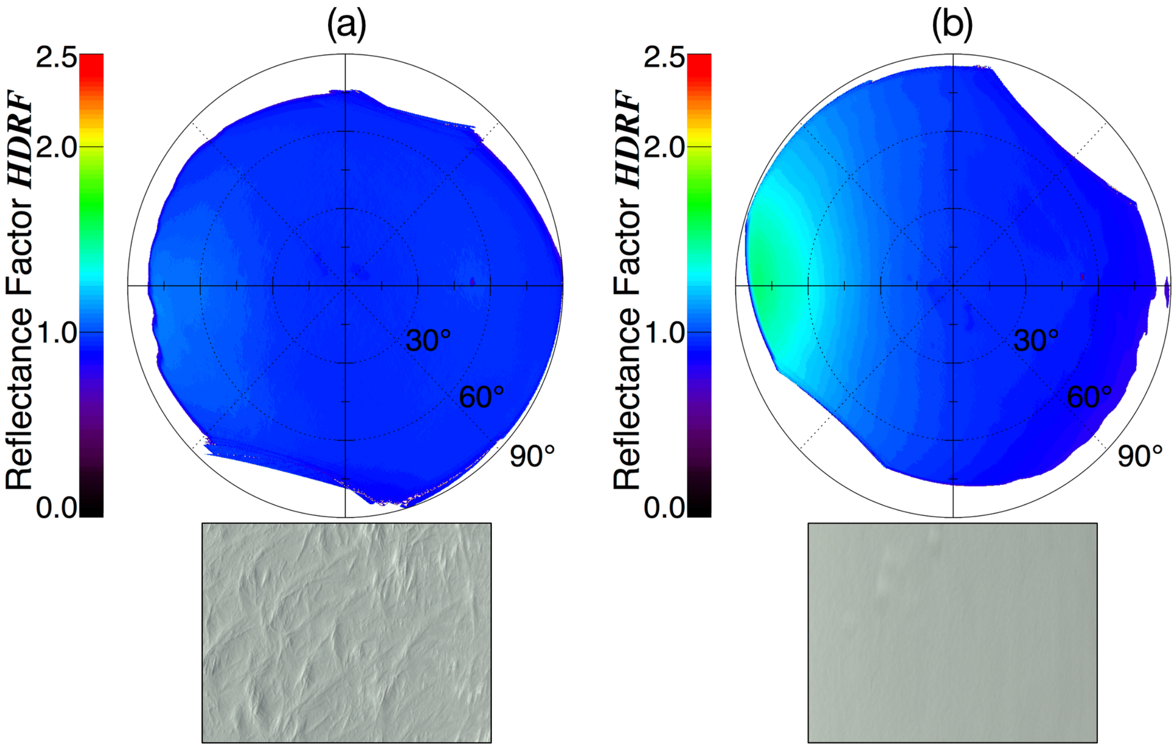

Figure 7.5: Averaged snow HDRF and corresponding photograph of the underlying snow surface during the research flight on 25 December 2013. **(a)** Surface with distinguishable roughness structures. **(b)** Smooth surface.

tograph in Fig. 7.5b. Contrarily, shortly after WP2, the surface roughness became distinguishable at least by visual inspection (see Fig. 7.5). The corresponding snow HDRF measurements were averaged over a flight time of about five minutes. During the two flight segments, ρ_0 changed between 51.6 and 53.6°. For these values, only little variation of the snow HDRF with ρ_0 was found (compare Fig. 7.3).
AI was in the range of 0.18 for the rough surface and 0.52 for the smooth surface HDRF where the maximum in forward scattering direction is more pronounced. This is in accordance with Warren et al. (1998) who observed a reduction of the forward peak due to sastrugi during tower measurements at South Pole Station. Roughness structures enhance the backscatter by changing the effective angle of incidence. In addition, they cast shadows that reduce the forward scatter.

8 Summary, conclusions, and perspectives

The significance of the polar regions for the Earth's climate system and their observed amplified response to climate change indicate the necessity for high temporal and spatial coverage for the monitoring of the reflective properties of snow surfaces. Even though polar regions exhibit partly low values of incoming solar radiation, the high snow surface albedo may facilitate substantial changes in the local surface energy budget. Hence, the cryosphere plays a fundamental role in determining the Earth's surface radiative energy budget. The surface albedo of snow is highly variable both on a temporal and spatial scale and depends mainly on the snow grain size and, amongst others, the solar zenith angle, and wavelength. Continuous observations of global coverage are provided by satellite instruments. However, the core step in the processing of satellite products involves the conversion of the measured bi-conical reflectance into albedo. This is not a simple and straightforward procedure, especially for the anisotropic reflection at snow surfaces.

Thus, the optical-equivalent snow grain size (R_{opt}) and the hemispherical-directional reflectance factor (HDRF) of snow were measured in Antarctica during austral summer 2013/14. Long-term observations at Kohnen station (75°0′ S, 0°4′ E; 2892 m above sea level) at the outer part of the East Antarctic Plateau were combined with airborne measurements (60 flight hours) over Dronning Maud Land covering different surface roughness and areas with higher (coastal areas) and lower (inner Antarctica) precipitation frequencies. With a mean aerosol optical depth (AOD) at 500 nm of 0.016 as determined by a sun photometer and a mean integrated atmospheric water vapor of 1.1 kg m^{-2}, the atmosphere at Kohnen station is both clean and dry. The near-surface air temperature ranged from -40 to -15 °C. The total cloud cover was dominated by cirrus, it was highly variable. Only five completely overcast days were reported; the mean total cloud amount over the entire observation period was less than 4 octa.

The ground-based data collected between 4 December 2013 and 31 January 2014 comprised (a) solar broadband and spectral radiation measurements of snow surface albedo,

(b) meteorological observations, and (c) daily measurements of R_{opt} and snow density.

Airborne surveys to characterize the representativeness of the local ground-based measurements were conducted using the Polar 6 research aircraft operated by the Alfred Wegener Institute, Helmholtz Centre for Polar and Marine Research (AWI) between 24 December and 5 January 2014. The airborne observations covered an area of about $1000 \times 1500\,\mathrm{km}^2$ in the vicinity of Kohnen station. Beside meteorological measurements, the airborne observations included measurements of solar broadband and spectral radiation, snow HDRF by means of digital camera, and surface roughness using a laser scanner.

The spectral surface albedo was derived from upward and downward spectral irradiances collected by the COmpact RAdiation measurement System (CORAS, ground-based) and the Spectral Modular Airborne Radiation measurement sysTem (SMART, airborne). The spectral resolution is 2 to 3 nm between 0.3 and 1.0 µm and 15 nm up to 2.2 µm wavelength. The uncertainties of albedo measurements with CORAS range between 4 and 8 % combining different sources of instrumental errors (signal-to-noise ratio, dark current and stray light, wavelength calibration, cross-calibration of the two optical inlets, non-ideal cosine characteristics of the irradiance optical inlets). The spectral albedo measurements with SMART have an estimated uncertainty between 4 and 8 %, also taking into consideration uncertainties due to the active horizontal stabilization of the optical inlets.

For the retrievals of R_{opt} and respective specific surface area (SSA) from spectral surface albedo measurements, the snow grain size and pollution amount (SGSP) algorithm (Zege et al., 2011) was extended to spectral ratios of surface albedo at 1280 and 1100 nm wavelength. Being independent of systematic measurement uncertainties (e.g., cross-calibration of the optical inlets), this approach decreases the uncertainty of the retrieved SSA compared to the single-wavelength approach. Furthermore, the retrieval was successfully applied to measurements in overcast conditions by using the spherical instead of the plane albedo. Satellite retrievals of surface albedo and SSA are restricted to cloudfree scenes. During the two months of observations at Kohnen station, cloudless conditions were present only 264 h out of 1272 h total observation time (21 %). However, many time periods with broken clouds were observed (62 % of total observation time). In this case, the concept of spherical albedo cannot be applied and SSA retrievals might fail. Therefore, only overcast conditions were included in the analysis. The retrieved SSA (ground-based and airborne) were validated against SSA measurements utilizing MODIS reflectance measurements and optical in situ measurements with an IceCube device. All retrievals considered within this thesis neglect snow layer stratification.

SSA retrieved from CORAS measurements varied between 29 and 96 $\mathrm{m^2\,kg^{-1}}$ and revealed distinct relative maxima related to light snowfall at Kohnen station. The average increase in SSA due to snowfall was 29 $\mathrm{m^2\,kg^{-1}}$. The relative maxima were followed by a gradual decrease in SSA, which was partly caused by snow metamorphism and by wind-induced transport of the freshly fallen ice crystals. During the longest dry period (18 until 30 December 2013), SSA decreased on average by 4 $\mathrm{m^2\,kg^{-1}\,day^{-1}}$. This corresponded to a daily increase of R_{opt} by 5 µm.

The temporal evolution of SSA retrieved from the ground-based CORAS measurements reproduced the in situ measurements (linear correlation coefficient: 0.79) within bars given by measurement and retrieval uncertainties. The same holds true for the spaceborne retrieval with the MODerate Resolution Imaging Spectroradiometer (MODIS, 0.86). Despite the biases in SSA retrieved from the different instruments, the agreement especially between SSA retrieved from CORAS and in situ measurements emphasizes the potential of the retrieval algorithms. SSA derived from airborne SMART measurements underestimated in situ SSA by a factor of 1.3. This might be caused by spatial averaging.

The spatial variability of SSA in Dronning Maud Land covers the same range as the temporal variability at Kohnen station. Higher values of SSA were retrieved in areas with supposedly recent snowfall, whereas coastal areas yielded lower SSA due to higher near-surface air temperature and stronger metamorphism processes. The SSA retrieved from SMART measurements is slightly lower than the SSA from MODIS measurements. However, they agree well within the ranges given by the measurement uncertainties (linear correlation coefficient: 0.74).

The validation presented in this study provided an unique test bed for retrievals of optical snow grain size from satellite reflectance and spectral surface albedo measurements under Antarctic conditions where in situ data are scarce and can be used for testing prognostic snowpack models in Antarctic conditions. The corresponding time series of ground-based, airborne, and spaceborne SSA values at Kohnen station is available in PANGAEA (Carlsen et al., 2017b). The validation study was published in The Cryosphere (Carlsen et al., 2017a).

The reflection of solar radiation at snow surfaces is particularly anisotropic in polar regions due to low Sun elevations and the anisotropic phase function of ice crystals. A 180° digital camera provides airborne radiance measurements with high angular resolution utilizing detailed radiometric and geometric calibrations. The camera was installed on the bottom fuselage of the Polar 6 research aircraft and took images with a temporal resolution of about 8 s. The characterization of the sensor characteristics revealed high linearity as well as negligible dark current and read-out noise. The radiometric calibration was performed using a certified radiance standard. The geometric calibration utilized images of a night sky and stellar positions of 66 fixed stars. The HDRF is calculated from the angular radiance measurements applying simulations of the global irradiance with the library for radiative transfer libRadtran using the discrete ordinate radiative transfer solver DISORT. The relative uncertainty of the HDRF measurements is estimated with 4.5 %. The potential of the camera measurements is demonstrated by a comparison with the upward irradiance measured by SMART. The shape of the HDRF depends on the size of the area, for which it is representative. The footprint of the snow HDRF measurements analyzed within this study varies between 1 to 6 km.

Two approaches to characterized the snow HDRF measurements were applied. Firstly, an anisotropy index AI is defined following the framework of an empirical model for the bidirectional reflectance distribution function (BRDF). The comparison between smooth ($AI = 0.52$) and rough surfaces (sastrugi, $AI = 0.18$) showed significant differences in the AI of the HDRF. Therefore, roughness structures enhance the backscatter by changing the effective angle of incidence and by casting shadows. With increasing solar zenith angle, the maximum in the forward scattering direction becomes more pronounced. Secondly, by inverting a semi-empirical kernel-driven BRDF model, the snow HDRF was parameterized with respect to the solar zenith angle. The uncertainty of the inversion is estimated with 10 %.

The influence of the camera channel and the weights w_l on the retrieved model parameters needs further attention in future studies. Furthermore, the parameterizations found within this study allow for direct comparison of the HDRF measurements with BRDF products from satellite remote sensing. To yield stronger dependence on the optical snow grain size, a camera sensitive to radiation in the NIR part of the EM spectrum needs to be employed. The analysis of the snow HDRF measurements can be readily applied to other airborne campaigns. For example, the same digital camera with a similar setup of the Polar 6 research aircraft (a) was used during the Arctic CLoud Observations Using airborne measurements during polar Day (ACLOUD) between 22 May and 28 June 2017 based at Longyearbyen, Svalbard, and (b) will be employed during the Polar Airborne Measurements and Arctic Regional Climate Model Simulation Project (PAMARCMiP) between 12 March and 6 April 2018 at Station North, Greenland. Thereby, the database of the parameterizations could be extended to wider ranges of R_{opt}, the surface roughness, and the solar zenith angle.

A Right ascension and declination of stars for geometric calibration

Table A.1: Right ascension and declination of stars used for the geometric calibration of the digital camera. The star numbers correspond to the numbers given in Fig. 4.21.

No.	Name	Right ascension (°)	Declination (°)
1	Beteigeuze	88.79291667	7.406944444
2	Bellatrix	81.28291667	6.349722222
3	Mintaka	83.00166667	-0.299166666
4	Alnilam	84.05333333	-1.201944444
5	Alnitak	85.18958333	-1.942777777
6	Saiph	86.93916667	-9.669722222
7	Rigel	78.63458333	-8.201666666
8	Dubhe	165.9320833	61.75083333
9	Merak	165.4604167	56.3825
10	Phekda	178.4575	53.69472222
11	Megrez	183.8566667	57.0325
12	Alioth	193.5070833	55.95972222
13	Mizar	200.98125	54.92527778
14	Benetnasch	206.885	49.31333333
15	Segin	28.59875	63.67
16	Ksora	21.45416667	60.23527778
17	Tsih	14.17708333	60.71666667
18	Schedar	10.12708333	56.53722222
19	Caph	2.294583333	59.14972222
20	Castor	113.65	31.88861111

Table A.2: Right ascension and declination of stars used for the geometric calibration of the digital camera. The star numbers correspond to the numbers given in Fig. 4.21 (continuation).

No.	Name	Right ascension (°)	Declination (°)
21	Pollux	116.32875	28.02611111
22	κ-Geminorum	116.1116667	24.39805556
23	Wasat	110.0308333	21.98222222
24	Mekbuda	106.0270833	20.57027778
25	Alhena	99.42791667	16.39916667
26	ν-Geminorum	97.24083333	20.21222222
27	Tejat Posterior	95.74	22.51361111
28	Tejat Prior	93.71916667	22.50666667
29	Mebsuta	100.9829167	25.13111111
30	τ-Geminorum	107.785	30.24527778
31	Procyon	114.8254167	5.225
32	Gomeise	111.7875	8.289444444
33	Subra	145.2875	9.892222222
34	Regulus	152.0929167	11.96722222
35	η-Leonis	151.8333333	16.76277778
36	Algieba	154.9929167	19.84166667
37	Adhafera	154.1725	23.41722222
38	Rasalas	148.1908333	26.00694444
39	Ras Elased Australis	146.4629167	23.77416667
40	Zosma	168.5270833	20.52361111
41	Tania Australis	155.5820833	41.49944444
42	Tania Borealis	154.2741667	42.91444444
43	ψ Ursae Maioris	167.4158333	44.49861111
44	Sirius	101.2870833	-16.71611111
45	Murzim	95.675	-17.95583333
46	Menkalinan	89.88208333	44.9475
47	θ-Aurigae	89.93041667	37.2125
48	Almach	30.975	42.32972222
49	Mirach	17.43291667	35.62055556
50	μ-Andromedae	14.18833333	38.49944444

Table A.3: Right ascension and declination of stars used for the geometric calibration of the digital camera. The star numbers correspond to the numbers given in Fig. 4.21 (continuation).

No.	**Name**	**Right ascension (°)**	**Declination (°)**
51	δ-Andromedae	9.832083333	30.86083333
52	Alpheratz	2.097083333	29.09055556
53	Mothallah	28.27041667	29.57888889
54	β-Trianguli	32.38583333	34.98722222
55	γ-Trianguli	34.32875	33.84722222
56	Hamal	31.79333333	23.4625
57	Sheratan	28.66	20.80805556
58	Mesarthim	28.3825	19.29361111
59	Mirfak	51.08083333	49.86111111

List of Figures

List of Tables

Bibliography

Aoki, T., Aoki, T., Fukabori, M., Hachikubo, A., Tachibana, Y., and Nishio, F.: Effects of snow physical parameters on spectral albedo and bidirectional reflectance of snow surface, J. Geophys. Res., 105, 10.219–10.236, 2000.

Arnaud, L., Lipenkov, V., Barnola, J., Gay, M., and Duval, P.: Modelling of the densification of polar firn: characterization of the snow–firn transition, Ann. Glaciol., 26, 39–44, doi:10.3189/1998AoG26-1-39-44, 1998.

Arrhenius, S.: On the influence of carbonic acid in the air upon the temperature of the grou, Lond. Edinb. Dubl. Phil. Mag., 41, 237–276, 1896.

Bannehr, L. and Schwiesow, R.: A technique to account for the misalignment of pyranometers installed on aircraft, J. Atmos. Oceanic Technol., 10, 774–777, 1993.

Barry, R. G., Jania, J., and Birkenmajer, K.: A. B. Dobrowolski - the first cryospheric scientist - and the subsequent development of cryospheric science, Hist. Geo-Space Sci., 2, 75–79, doi:10.5194/hgss-2-75-2011, 2011.

Bierwirth, E.: Airborne measurements of the spectral surface albedo over morocco and its influence on the radiative forcing of saharan dust, Ph.D. thesis, Johannes Gutenberg University Mainz, Germany, 2008.

Birnbaum, G., Brauner, R., and Ries, H.: Synoptic situations causing high precipitation rates on the Antarctic plateau: observations from Kohnen Station, Dronning Maud Land, Antarct. Sci., 18, 279–288, doi:10.1017/S0954102006000320, 2006.

Birnbaum, G., Freitag, J., Brauner, R., Koenig-Langlo, G., Schulz, E., Kipfstuhl, S., Oerter, H., Reijmer, C., Schlosser, E., Faria, S., Ries, H., Loose, B., Herber, A., Duda, M., Powers, J., Manning, K., and van den Broeke, M.: Strong-wind events and their influence on the formation of snow dunes: observations from Kohnen station, Dronning Maud Land, Antarctica, J. Glaciol., 56, 891–902, doi:10.3189/002214310794457272, 2010.

Bohren, C. and Barkstrom, B.: Theory of the optical properties of snow, J. Geophys. Res., 79, 4527–4535, 1974.

Bokhorst, S., Pedersen, S., Brucker, L., Anisimov, O., Bjerke, J., Brown, R., Ehrich, D., Essery, R., Heilig, A., Ingvander, S., Johansson, C., Johansson, M., Jonsdottir, I., Inga, N., Luojus, K., Macelloni, G., Mariash, H., McLennan, D., Rosqvist, G., Sato, A., Savela, H., Schneebeli, M., Sokolov, A., Sokratov, S., Terzago, S., Vikhamar-Schuler, D., Williamson, S., Qiu, Y., and Callaghan, T.: Changing Arctic snow cover: A review of recent developments and assessment of future needs for observations, modelling, and impacts, Ambio, 45, 516–537, doi:10.1007/s13280-016-0770-0, 2016.

Bond, T. C., Doherty, S. J., Fahey, D. W., Forster, P. M., Berntsen, T., DeAngelo, B. J., Flanner, M. G., Ghan, S., Karcher, B., Koch, D., Kinne, S., Kondo, Y., Quinn, P. K., Sarofim, M. C., Schultz, M. G., Schulz, M., Venkataraman, C., Zhang, H., Zhang, S., Bellouin, N., Guttikunda, S. K., Hopke, P. K., Jacobson, M. Z., Kaiser, J. W., Klimont, Z., Lohmann, U., Schwarz, J. P., Shindell, D., Storelvmo, T., Warren, S. G., and Zender, C. S.: Bounding the role of black carbon in the climate system: A scientific assessment, J. Geophys. Res., 118, 5380–5552, doi:10.1002/jgrd.50171, 2013.

Bourgeois, C., Ohmura, A., Schroff, K., Frei, H.-J., and Calanca, P.: IAC ETH goniospectrometer: A tool for hyperspectral HDRF measurements, J. Atmospheric Ocean. Technol., 23, 573–584, doi:10.1175/JTECH1870.1, 2006a.

Bourgeois, C. S., Calanca, P., and Ohmura, A.: A field study of the hemispherical directional reflectance factor and spectral albedo of dry snow, J. Geophys. Res. Atmos., 111, doi:10.1029/2006JD007296, 2006b.

Brest, C. and Goward, S.: Deriving surface albedo measurements from narrow-band satellite data, Int. J. Remote Sens., 8, 351–367, 1987.

Brown, R. and Derksen, C.: Is Eurasian October snow cover extent increasing?, Environ. Res. Lett., 8, doi:10.1088/1748-9326/8/2/024006, 2013.

Brown, R., Derksen, C., and Wang, L.: A multi-data set analysis of variability and change in Arctic spring snow cover extent, 1967-2008, J. Geophys. Res., 115, doi:10.1029/2010JD013975, 2010.

Brückner, M., Pospichal, B., Macke, A., and Wendisch, M.: A new multispectral cloud retrieval method for ship-based solar transmissivity measurements, J. Geophys. Res., 119, 11.338–11.354, doi:10.1002/2014JD021775, 2014.

Burton-Johnson, A., Black, M., Fretwell, P. T., and Kaluza-Gilbert, J.: An automated methodology for differentiating rock from snow, clouds and sea in Antarctica from Landsat 8 imagery: a new rock outcrop map and area estimation for the entire Antarctic continent, Cryosphere, 10, 1665–1677, 2016.

Calonne, N., Flin, F., Geindreau, C., Lesaffre, B., and du Roscoat, S. R.: Study of a temperature gradient metamorphism of snow from 3-D images: time evolution of microstructures, physical properties and their associated anisotropy, The Cryosphere, 8, 2255–2274, doi:10.5194/tc-8-2255-2014, 2014.

Cantrell, W. and Heymsfield, A.: Production of ice in tropospheric clouds - A review, Bull. Am. Meteorol. Soc., 86, 795–807, doi:10.1175/BAMS-86-6-795, 2005.

Carlsen, T., Birnbaum, G., Ehrlich, A., Freitag, J., Heygster, G., Istomina, L., Kipfstuhl, S., Orsi, A., Schäfer, M., and Wendisch, M.: Comparison of different methods to retrieve optical-equivalent snow grain size in central Antarctica, Cryosphere, 11, 2727–2741, doi:10.5194/tc-11-2727-2017, 2017a.

Carlsen, T., Birnbaum, G., Ehrlich, A., Heygster, G., Istomina, L., Schäfer, M., and Wendisch, M.: Snow specific surface area (SSA) retrieved from spectral surface albedo (ground-based and airborne) and reflectance (spaceborne) measurements at Kohnen research station, Antarctica, during austral summer 2013/14, PANGAEA, doi:10.1594/PANGAEA.880815, 2017b.

Carmagnola, C., Domine, F., Dumont, M., Wright, P., Strellis, B., Bergin, M., Dibb, J., Picard, G., Libois, Q., Arnaud, L., and Morin, S.: Snow spectral albedo at Summit, Greenland: measurements and numerical simulations based on physical and chemical properties of the snowpack, Cryosphere, 7, 1139–1160, doi:10.5194/tc-7-1139-2013, 2013.

Church, J., Clark, P., Cazenave, A., Gregory, J., Jevrejeva, S., Levermann, A., Merrifield, M., Milne, G., Nerem, R., Nunn, P., Payne, A., Pfeffer, W., Stammer, D., and Unnikrishnan, A.: Sea Level Change, in: Climate Change 2013: The Physical Science Basis. Contribution of Working Group I to the Fifth Assessment Report of the Intergovernmental Panel on Climate Change, edited by Stocker, T., Qin, D., Plattner, G.-K., Tignor, M., Allen, S., Boschung, J., Nauels, A., Xia, Y., Bex, V., and Midgley, P., pp. 1137–1216, Cambridge University Press, Cambridge, United Kingdom and New York, NY, USA, doi:10.1017/CBO9781107415324.026, 2013.

Coffin, D.: Decoding raw digital photos in Linux, https://www.cybercom.net/ dcoffin/dcraw/, accessed: 15 December 2017, 2017.

Cohen, J., Screen, J., Furtado, J., Barlow, M., Whittleston, D., Coumou, D., Francis, J., Dethloff, K., Entekhabi, D., Overland, J., and Jones, J.: Recent Arctic amplification and extreme mid-latitude weather, Nat. Geosci., 7, 627–637, doi:10.1038/NGEO2234, 2014.

Colbeck, S.: A review of sintering in seasonal snow, Tech. Rep. 97-10, Cold Regions Research and Engineering Laboratory, 1997.

Colbeck, S. C.: Theory of Metamorphism of Dry Snow, J. Geophys. Res., 88, 5475–5482, doi:10.1029/JC088iC09p05475, 1983.

Collins, M., Knutti, R., Arblaster, J., Dufresne, J.-L., Fichefet, T., Friedlingstein, P., Gao, X., Gutowski, W., Johns, T., Krinner, G., Shongwe, M., Tebaldi, C., Weaver, A., and Wehner, M.: Long-term Climate Change: Projections, Commitments and Irreversibility, in: Climate Change 2013: The Physical Science Basis. Contribution of Working Group I to the Fifth Assessment Report of the Intergovernmental Panel on Climate Change, edited by Stocker, T., Qin, D., Plattner, G.-K., Tignor, M., Allen, S., Boschung, J., Nauels, A., Xia, Y., Bex, V., and Midgley, P., pp. 1029–1136, Cambridge University Press, Cambridge, United Kingdom and New York, NY, USA, doi:10.1017/CBO9781107415324.024, 2013.

Cox, C. and Munk, W.: Measurement of the roughness of the sea surface from photographs of the sun's glitter, J. Opt. Soc. Am. A, 44, 838–850, 1954.

Crowther, B.: The Design, Construction, and Calibration of a Spectral Diffuse/Global Irradiance Meter, Ph.D. thesis, University of Arizona, 1997.

Dang, C., Brandt, R. E., and Warren, S. G.: Parameterizations for narrowband and broadband albedo of pure snow and snow containing mineral dust and black carbon, J. Geophys. Res., 120, 5446–5468, doi:10.1002/2014JD022646, 2015.

Dang, C., Fu, Q., and Warren, S. G.: Effect of snow grain shape on snow albedo, J. Atmos. Sci., 73, 3573–3583, doi:10.1175/JAS-D-15-0276.1, 2016.

Dirmhirn, I. and Eaton, F.: Some characteristics of the albedo of snow, J. Appl. Meteor., 14, 375–379, doi:10.1175/1520-0450(1975)014<0375:SCOTAO>2.0.CO;2, 1975.

Domine, F., Cabanes, A., Taillandier, A. S., and Legagneux, L.: Specific surface area of snow samples determined by CH_4 adsorption at 77 K and estimated by optical microscopy and scanning electron microscopy, Environ. Sci. Technol., 35, 771–780, doi:10.1021/es001168n, 2001.

Domine, F., Salvatori, R., Legagneux, L., Salzano, R., Fily, M., and Casacchia, R.: Correlation between the specific surface area and the short wave infrared (SWIR) reflectance of snow, Cold Reg. Sci. Technol., 46, 60–68, doi:10.1016/j.coldregions.2006.06.002, 2006.

Dumont, M., Brissaud, O., Picard, G., Schmitt, B., Gallet, J. C., and Arnaud, Y.: High-accuracy measurements of snow Bidirectional Reflectance Distribution Function at visible and NIR wavelengths - comparison with modelling results, Atmos. Chem. Phys., 10, 2507–2520, doi:10.5194/acp-10-2507-2010, 2010.

Dumont, M., Arnaud, L., Picard, G., Libois, Q., Lejeune, Y., Nabat, P., Voisin, D., and Morin, S.: In situ continuous visible and near-infrared spectroscopy of an alpine snowpack, The Cryosphere, 11, 1091–1110, doi:10.5194/tc-11-1091-2017, 2017.

Eamer, J., Ahlenius, H., Prestrud, P., and United Nations Environment Programme: Global Outlook for Ice & Snow, Division of Early Warning and Assessment (DEWA), United Nations Environment Programme, Nairobi, 2007.

Ehrlich, A.: The impact of ice crystals on radiative forcing and remote sensing of Arctic boundary-layer mixed-phase clouds, Ph.D. thesis, Johannes Gutenberg University Mainz, Germany, 2009.

Ehrlich, A., Bierwirth, E., Wendisch, M., Gayet, J.-F., Mioche, G., Lampert, A., and Heintzenberg, J.: Cloud phase identification of Arctic boundary-layer clouds from airborne spectral reflection measurements: Test of three approaches, Atmos. Chem. Phys., 8, 7493–7505, doi:10.5194/acp-8-7493-2008, 2008.

Ehrlich, A., Bierwirth, E., Wendisch, M., Herber, A., and Gayet, J. F.: Airborne hyperspectral observations of surface and cloud directional reflectivity using a commercial digital camera, Atmos. Chem. Phys., 12, 3493–3510, doi:10.5194/acp-12-3493-2012, 2012.

Ehrlich, A., Bierwirth, E., Istomina, L., and Wendisch, M.: Combined retrieval of Arctic liquid water cloud and surface snow properties using airborne spectral solar remote sensing, Atmos. Meas. Tech., 10, 3215–3230, doi:10.5194/amt-10-3215-2017, 2017.

Etheridge, D., Steele, L., Langenfelds, R., Francey, R., Barnola, J., and Morgan, V.: Natural and anthropogenic changes in atmospheric CO2 over the last 1000 years from air in Antarctic ice and firn, J. Geophys. Res., 101, 4115–4128, doi:10.1029/95JD03410, 1996.

Fierz, C., Armstrong, R. L., Durand, Y., Etchevers, P., Greene, E., McClung, D. M., Nishimura, K., Satyawali, P. K., and Sokratov, S. A.: The International Classification for Seasonal Snow on the Ground, IHP-VII Technical Documents in Hydrology N°83, IACS Contribution N°1, UNESCO-IHP, Paris, 2009.

Filhol, S. and Sturm, M.: Snow bedforms: A review, new data, and a formation model, J. Geophys. Res. Earth Surf., 120, 1645–1669, doi:10.1002/2015JF003529, 2015.

Flin, F. and Brzoska, J.-B.: The temperature-gradient metamorphism of snow: vapour diffusion model and application to tomographic images, Annals of Glaciology, 49, 17–21, doi:10.3189/172756408787814834, 2008.

Flin, F., Brzoska, J. B., Coeurjolly, D., Pieritz, R. A., Lesaffre, B., Coleou, C., Lamboley, P., Teytaud, O., Vignoles, G. L., and Delesse, J. F.: Adaptive estimation of normals and surface area for discrete 3-D objects: Application to snow binary data from X-ray tomography, IEEE Trans. Image Process., 14, 585–596, doi:10.1109/TIP.2005.846021, 2005.

Francis, J. and Hunter, E.: New insight into the disappearing Arctic sea ice, Eos, 87, doi:10.1029/2006EO460001, 2006.

Gallet, J. C., Domine, F., Zender, C. S., and Picard, G.: Measurement of the specific surface area of snow using infrared reflectance in an integrating sphere at 1310 and 1550 nm, Cryosphere, 3, 167–182, 2009.

Gallet, J. C., Domine, F., and Dumont, M.: Measuring the specific surface area of wet snow using 1310 nm reflectance, Cryosphere, 8, 1139–1148, doi:10.5194/tc-8-1139-2014, 2014a.

Gallet, J. C., Domine, F., Savarino, J., Dumont, M., and Brun, E.: The growth of sublimation crystals and surface hoar on the Antarctic plateau, The Cryosphere, 8, 1205–1215, doi:10.5194/tc-8-1205-2014, 2014b.

Gatebe, C. K. and King, M. D.: Airborne spectral BRDF of various surface types (ocean, vegetation, snow, desert, wetlands, cloud decks, smoke layers) for remote sensing applications, Remote Sens. Environ., 179, 131–148, doi:10.1016/j.rse.2016.03.029, 2016.

Gatebe, C. K., King, M. D., Lyapustin, A. I., Arnold, G. T., and Redemann, J.: Airborne spectral measurements of ocean directional reflectance, J. Atmos. Sci., 62, 1072–1092, 2005.

Germogenova, T.: On the properties of the transport equation for a plane-parallel layer, J. Appl. Math. Comp. Phys., 1, 928–946, 1961.

Graversen, R. and Wang, M.: Polar amplification in a coupled climate model with locked albedo, Clim. Dyn., 33, 629–643, doi:10.1007/s00382-009-0535-6, 2009.

Grenfell, T. C. and Warren, S. G.: Representation of a nonspherical ice particle by a collection of independent spheres for scattering and absorption of radiation, J. Geophys. Res., 104, 31.697–31.709, doi:10.1029/1999JD900496, 1999.

Grenfell, T. C., Warren, S. G., and Mullen, P. C.: Reflection of solar radiation by the Antarctic snow surface at ultraviolet, visible, and near-infrared wavelengths, J. Geophys. Res., 99, 18.669–18.684, doi:10.1029/94JD01484, 1994.

Hall, A.: The role of surface albedo feedback in climate, J. Clim., 17, 1550–1568, doi:10.1175/1520-0442(2004)017<1550:TROSAF>2.0.CO;2, 2004.

Han, W.: Remote sensing of surface albedo and cloud properties in the Arctic from AVHRR measurements, D.s. thesis, University of Alaska, Fairbanks, 1996.

Hansen, J. and Nazarenko, L.: Soot climate forcing via snow and ice albedos, Proc. Natl. Acad. Sci. U. S. A., 101, 423–428, doi:10.1073/pnas.2237157100, 2004.

Hartmann, D., Klein Tank, A., Rusticucci, M., Alexander, L., Brönnimann, S., Charabi, Y., Dentener, F., Dlugokencky, E., Easterling, D., Kaplan, A., Soden, B., Thorne, P., Wild, M., and Zhai, P.: Observations: Atmosphere and Surface, in: Climate Change 2013: The Physical Science Basis. Contribution of Working

Group I to the Fifth Assessment Report of the Intergovernmental Panel on Climate Change, edited by Stocker, T., Qin, D., Plattner, G.-K., Tignor, M., Allen, S., Boschung, J., Nauels, A., Xia, Y., Bex, V., and Midgley, P., pp. 159–254, Cambridge University Press, Cambridge, United Kingdom and New York, NY, USA, doi:10.1017/CBO9781107415324.008, 2013.

Holland, M. and Bitz, C.: Polar amplification of climate change in coupled models, Clim. Dyn., 21, 221–232, doi:10.1007/s00382-003-0332-6, 2003.

Hu, B., Lucht, W., Li, X., and Strahler, A.: Validation of kernel-driven semiempirical models for the surface bidirectional reflectance distribution function of land surfaces, Remote Sens. Environ., 62, 201–214, doi:10.1016/S0034-4257(97)00082-5, 1997.

Hudson, S. R. and Warren, S. G.: An explanation for the effect of clouds over snow on the top-of-atmosphere bidirectional reflectance, J. Geophys. Res., 112, D19 202, 2007.

Hudson, S. R., Warren, S. G., Brandt, R. E., Grenfell, T. C., and Six, D.: Spectral bidirectional reflectance of Antarctic snow: Measurements and parameterization, J. Geophys. Res., 111, D18 106, doi:10.1029/2006JD007290, 2006.

Jäkel, E., Wendisch, M., Kniffka, A., and Trautmann, T.: Airborne system for fast measurements of upwelling and downwelling spectral actinic flux densities, Appl. Opt., 44, 434–444, 2005.

Jaross, G. and Warner, J.: Use of Antarctica for validating reflected solar radiation measured by satellite sensors, J. Geophys. Res., 113, doi:10.1029/2007JD008835, 2008.

Jin, Z., Charlock, T. P., Yang, P., Xie, Y., and Miller, W.: Snow optical properties for different particle shapes with application to snow grain size retrieval and MODIS/CERES radiance comparison over Antarctica, Remote Sens. Env., 112, 3563–3581, doi:10.1016/j.rse.2008.04.011, 2008.

Kaempfer, T. U. and Schneebeli, M.: Observation of isothermal metamorphism of new snow and interpretation as a sintering process, J. Geophys. Res., 112, D24 101, doi:10.1029/2007JD009047, 2007.

Kanji, Z., Ladino, L., Wex, H., Boose, Y., Burkert-Kohn, M., Cziczo, D., and Krämer, M.: Overview of Ice Nucleating Particles, Meteorological Monographs, 58, 1.1–1.33, doi:10.1175/AMSMONOGRAPHS-D-16-0006.1, 2017.

Kaufmann, K.: CMOS Technology for Scientific Imaging, Spectroscopy, 25, 20–25, 2010.

Kerr, D.: The Canon sRaw and mRaw output formats, Issue 3, http://dougkerr.net/Pumpkin/index.htm#sRaw, accessed: 15 December 2017, 2015.

Klaus, A., Bauer, J., Karner, K., Elbischger, P., Perko, R., and Bischof, H.: Camera calibration from a single night sky image, in: Proceedings of the 2004 IEEE Computer Society Conference on Computer Vision and Pattern Recognition (CVPR 2004), pp. 151–157, IEEE, 2004.

Klein, A. and Stroeve, J.: Development and validation of a snow albedo algorithm for the MODIS instrument, Ann. Glaciol., 34, 45–52, doi:10.3189/172756402781817662, 2002.

Kneizys, F. X., Abreu, L. W., Anderson, G. P., Chetwynd, J. H., Shettle, E. P., Berk, A., Bernstein, L. S., Robertson, D. C., Acharya, P. K., Rothman, L. A., Selby, J. E. A., Gallery, W. O., and Clough, S. A.: The MODTRAN 2/3 Report and LOWTRAN 7 MODEL, Phillips Laboratory Hanscom AFB, Bedford, 1996.

Kobayashi, D.: Studies of snow transport in low-level drifting snow, Contrib. Inst. Low Temp. Sci., 24, 1–58, 1972.

Kokhanovsky, A.: Asymptotic radiative transfer, in: Light Scattering Reviews: Single and multiple light scattering., edited by Kokhanovsky, A., pp. 253–289, Springer, Heidelberg, Germany, 2006.

Kokhanovsky, A. and Macke, A.: Integral light-scattering and absorption characteristics of large, nonspherical particles, Appl. Opt., 36, 8785–8790, doi:10.1364/AO.36.008785, 1997.

Kokhanovsky, A. A. and Zege, E. P.: Scattering optics of snow, Appl. Opt., 43, 1589–1602, doi:10.1364/AO.43.001589, 2004.

Kokhanovsky, A. A., Aoki, T., Hachikubo, A., Hori, M., and Zege, E. P.: Reflective properties of natural snow: approximate asymptotic theory versus in situ measurements, IEEE Trans. Geosci. Remote Sens., 43, 1529–1535, doi:10.1109/TGRS.2005.848414, 2005.

Krol, Q. and Löwe, H.: Relating optical and microwave grain metrics of snow: the relevance of grain shape, The Cryosphere, 10, 2847–2863, doi:10.5194/tc-10-2847-2016, 2016.

Kuchiki, K., Aoki, T., Niwano, M., Motoyoshi, H., and Iwabuchi, H.: Effect of sastrugi on snow bidirectional reflectance and its application to MODIS data, J. Geophys. Res., 116, doi:10.1029/2011JD016070, 2011.

Kuhn, M.: Bidirectional reflectance of polar and alpine snow surfaces, Ann. Glaciol., 6, 164–167, 1985.

Kwok, R. and Rothrock, D. A.: Decline in Arctic sea ice thickness from submarine and ICESat records: 1958–2008, Geophys. Res. Lett., 36, L15 501, doi:10.1029/2009GL039 035, 2009.

LaChapelle, E.: Field guide to snow crystals, University of Washington Press, 1969.

Lebourgeois, V., Bégué, A., Labbé, S., Mallavan, B., Prévot, L., and Roux, B.: Can commercial digital cameras be used as multispectral sensors? A crop monitoring test, Sensors, 8, 7300–7322, doi:10.3390/s8117300, 2008.

Legagneux, L., Cabanes, A., and Domine, F.: Measurement of the specific surface area of 176 snow samples using methane adsorption at 77 K, J. Geophys. Res., 107, 4335, doi:10.1029/2001JD001016, 2002.

Leppänen, L., Kontu, A., Vehvilainen, J., Lemmetyinen, J., and Pulliainen, J.: Comparison of traditional and optical grain-size field measurements with SNOWPACK simulations in a taiga snowpack, J. Glaciol., 61, 151–162, doi:10.3189/2015JoG14J026, 2015.

Leroux, C. and Fily, M.: Modeling the effect of sastrugi on snow reflectance, J. Geophys. Res., 103, 25 779–25 788, 1998.

Leroux, C., Deuze, J.-L., Goloub, P., Sergent, C., and Fily, M.: Ground measurements of the polarized bidirectional reflectance of snow in the near-infrared spectral domain: Comparisons with model results, J. Geophys. Res., 103, 19 721–19 731, 1998.

Leroux, C., Lenoble, J., Brogniez, G., Hovenier, J., and De Haan, J.: A model for the bidirectional polarized reflectance of snow, J. Quant. Spectrosc. Radiat. Transfer, 61, 273–285, 1999.

Lewis, P.: The utility of kernel-driven BRDF models in global BRDF and albedo studies, Proc. Int. Geosci. Remote Sens. Symp., pp. 1186–1187, 1995.

Li, S.: A Model for the Anisotropic Reflectance of Pure Snow, M.sc. thesis, Department of Geography, University of California, Santa Barbara, 1982.

Li, X. and Strahler, A.: Geometric-optical bidirectional reflectance modeling of the discrete crown vegetation canopy: effect of crown shape and mutual shadowing, IEEE Trans. Geosci. Remote Sens., 30, 276–292, doi:10.1109/36.134078 , 1992.

Liang, S., Shuey, C., Russ, A., Fang, H., Chen, M., Walthall, C., Daughtry, C., and Hunt, R.: Narrowband to broadband conversions of land surface albedo: II. Validation, Remote Sens. Environ., 84, 25–41, doi:10.1016/S0034-4257(02)00068-8, 2003.

Libbrecht, K. G.: The physics of snow crystals, Rep. Prog. Phys., 68, 855–895, 2005.

Libois, Q., Picard, G., France, J. L., Arnaud, L., Dumont, M., Carmagnola, C. M., and King, M. D.: Influence of grain shape on light penetration in snow, The Cryosphere, 7, 1803–1818, doi:10.5194/tc-7-1803-2013, 2013.

Libois, Q., Picard, G., Dumont, M., Arnaud, L., Sergent, C., Pougatch, E., Sudul, M., and Vial, D.: Experimental determination of the absorption enhancement parameter of snow, J. Glaciol., 60, 714–724, doi:10.3189/2014JoG14J015, 2014.

Libois, Q., Picard, G., Arnaud, L., Dumont, M., Lafaysse, M., Morin, S., and Lefebvre, E.: Summertime evolution of snow specific surface area close to the surface on the Antarctic Plateau, The Cryosphere, 9, 2383–2398, doi:10.5194/tc-9-2383-2015, 2015.

Lindsay, R. and Schweiger, A.: Arctic sea ice thickness loss determined using subsurface, aircraft, and satellite observations, The Cryosphere, 9, 269–283, doi:10.5194/tc-9-269-2015, 2015.

Lucht, W., Schaaf, C. B., and Strahler, A. H.: An algorithm for the retrieval of albedo from space using semiempirical BRDF models, IEEE Trans. Geosci. Remote Sens., 38, 977–998, 2000.

Lyapustin, A., Tedesco, M., Wang, Y., Aoki, T., Hori, M., and Kokhanovsky, A.: Retrieval of snow grain size over Greenland from MODIS, Remote Sens. Environ., 113, 1976–1987, doi:10.1016/j.rse.2009.05.008, 2009.

Lyapustin, A., Gatebe, C. K., Kahn, R., Brandt, R., Redemann, J., Russell, P., King, M. D., Pedersen, C. A., Gerland, S., Poudyal, R., Marshak, A., Wang, Y., Schaaf, C., Hall, D., and Kokhanovsky, A.: Analysis of snow bidirectional reflectance from ARCTAS Spring-2008 Campaign, Atmos. Chem. Phys., 10, 4359–4375, doi:10.5194/acp-10-4359-2010, 2010.

Manabe, S. and Stouffer, R.: Sensitivity of a global climate model to an increase of CO2 concentration in the atmosphere, J. Geophys. Res., 85, 5529–5554, doi:10.1029/JC085iC10p05529, 1980.

Marks, A., Fragiacomo, C., MacArthur, A., Zibordi, G., Fox, N., and King, M. D.: Characterisation of the HDRF (as a proxy for BRDF) of snow surfaces at Dome C, Antarctica, for the inter-calibration and inter-comparison of satellite optical data, Remote Sens. Environ., 158, 407–416, doi:10.1016/j.rse.2014.11.013, 2015.

Marshall, J., Armour, K., Scott, J., Kostov, Y., Hausmann, U., Ferreira, D., Shepherd, T., and Bitz, C.: The ocean's role in polar climate change: asymmetric Arctic and Antarctic responses to greenhouse gas and ozone forcing, Phil. Trans. R. Soc. A, 372, doi:10.1098/rsta.2013.0040, 2014.

Martonchik, J. V., Diner, D. J., Kahn, R. A., Ackerman, T. P., Verstraete, M. E., Pinty, B., and Gordon, H. R.: Techniques for the retrieval of aerosol properties over land and ocean using multiangle imaging, IEEE Trans. Geosci. Remote Sens., 36, 1212–1227, doi:10.1109/36.701027, 1998.

Masson-Delmotte, V., Schulz, M., Abe-Ouchi, A., Beer, J., Ganopolski, A., González Rouco, J., Jansen, E., Lambeck, K., Luterbacher, J., Naish, T., Osborn, T., Otto-Bliesner, B., Quinn, T., Ramesh, R., Rojas, M., Shao, X., and Timmermann, A.: Information from Paleoclimate Archives, in: Climate Change 2013: The Physical Science Basis. Contribution of Working Group I to the Fifth Assessment Report of the Intergovernmental Panel on Climate Change, edited by Stocker, T., Qin, D., Plattner, G.-K., Tignor, M., Allen, S., Boschung, J., Nauels, A., Xia, Y., Bex, V., and Midgley, P., pp. 383–464, Cambridge University Press, Cambridge, United Kingdom and New York, NY, USA, doi:10.1017/CBO9781107415324.013, 2013.

Matzl, M. and Schneebeli, M.: Stereological measurement of the specific surface area of seasonal snow types: Comparison to other methods, and implications for mm-scale vertical profiling, Cold Reg. Sci. Technol., 64, 1–8, doi:10.1016/j.coldregions.2010.06.006, 2010.

Mayer, B. and Kylling, A.: Technical note: The *libRadtran* software package for radiative transfer calculations - description and examples of use, Atmos. Chem. Phys., 5, 1855–1877, doi:10.5194/acp-5-1855-2005, 2005.

McCusker, K., Fyfe, J., and Sigmond, M.: Twenty-five winters of unexpected Eurasian cooling unlikely due to Arctic sea-ice loss, Nat. Geosci., 9, 838+, doi:10.1038/NGEO2820, 2016.

Mei, L., Xue, Y., de Leeuw, G., von Hoyningen-Huene, W., Kokhanovsky, A., Istomina, L., Guang, J., and Burrows, J.: Aerosol optical depth retrieval in the Arctic region using MODIS data over snow, Remote Sens. Environ., 128, 234–245, doi:10.1016/j.rse.2012.10.009, 2013.

Mie, G.: Beiträge zur Optik trüber Medien, speziell kolloidaler Metallösungen, Annalen der Physik, Vierte Folge, 25, 377–445, 1908.

Miller, G., Alley, R., Brigham-Grette, J., Fitzpatrick, J., Polyak, L., Serreze, M., and White, J.: Arctic amplification: can the past constrain the future?, Quat. Sci. Rev., 29, 1779–1790, doi:10.1016/j.quascirev.2010.02.008, 2010.

Mishchenko, M., Dlugach, J., Yanovitskij, E., and Zakharova, N.: Bidirectional reflectance of flat, optically thick particulate layers: an efficient radiative transfer solution and applications to snow and soil surfaces, J. Quant. Spectrosc. Radiat. Transfer, 63, 409–432, 1999.

Mori, Y., Yamashita, A., Tanaka, M., Kataoka, R., Miyoshi, Y., Kaneko, T., Okutomi, M., and Asama, H.: Calibration of fish-eye stereo camera for aurora observation, in: Proc. of the International Workshop on Advanced Image Technology (IWAIT2013), pp. 729–734, Nagoya, Japan, 2013.

Mudryk, L., Kushner, P., Derksen, C., and Thackeray, C.: Snow cover response to temperature in observational and climate model ensembles, Geophys. Res. Lett., 44, 919–926, doi:10.1002/2016GL071789, 2017.

Munneke, P. K., Reijmer, C. H., van den Broeke, M. R., Konig-Langlo, G., Stammes, P., and Knap, W. H.: Analysis of clear-sky Antarctic snow albedo using observations and radiative transfer modeling RID G-8736-2011 RID F-7867-2011, J. Geophys. Res., 113, D17118, doi:10.1029/2007JD009653, 2008.

Myhre, G., Shindell, D., Bréon, F.-M., Collins, W., Fuglestvedt, J., Huang, J., Koch, D., Lamarque, J.-F., Lee, D., Mendoza, B., Nakajima, T., Robock, A., Stephens, G., Takemura, T., and Zhang, H.: Anthropogenic and Natural Radiative Forcing, in: Climate Change 2013: The Physical Science Basis. Contribution of Working Group I to the Fifth Assessment Report of the Intergovernmental Panel on Climate Change, edited by Stocker, T., Qin, D., Plattner, G.-K., Tignor, M., Allen, S., Boschung, J., Nauels, A., Xia, Y., Bex, V., and Midgley, P., pp. 659–740, Cambridge University Press, Cambridge, United Kingdom and New York, NY, USA, doi:10.1017/CBO9781107415324.018, 2013.

Nakaya, U.: Snow crystals : natural and artificial, Harvard Univ. Press, Cambridge, 1954.

Neshyba, S. P., Grenfell, T. C., and Warren, S. G.: Representation of a nonspherical ice particle by a collection of independent spheres for scattering and absorption of radiation: 2. Hexagonal columns and plates, J. Geophys. Res., 108, Art. No. 4448, doi:10.1029/2002JD003302, 2003.

Nolin, A., Fetterer, F., and Scambos, T.: Surface roughness characterizations of sea ice and ice sheets: Case studies with MISR data, IEEE Trans. Geosci. Remote Sens., 40, 1605–1615, doi:10.1109/TGRS.2002.801581, 2002.

Notz, D. and Stroeve, J.: Observed Arctic sea-ice loss directly follows anthropogenic CO_2 emission, Science, 354, 747–750, doi:10.1126/science.aag2345, 2016.

Oerter, H., Wilhelms, F., Jung-Rothenhausler, F., Goktas, F., Miller, H., Graf, W., and Sommer, S.: Accumulation rates in Dronning Maud Land, Antarctica, as revealed by dielectric-profiling measurements of shallow firn cores, Ann. Glaciol., 30, 27–34, doi:10.3189/172756400781820705, 2000.

Ogi, M., Yamazaki, K., and Wallace, J. M.: Influence of winter and summer surface wind anomalies on summer Arctic sea ice extent, Geophys. Res. Lett., 37, L07 701, 2010.

Overland, J., Hanna, E., Hanssen-Bauer, I., Kim, S.-J., Walsh, J., Wang, M., Bhatt, U., and Thoman, R.: Surface Air Temperature, in: Arctic Report Card 2016, edited by Richter-Menge, J., Overland, J., and Mathis, J., http://www.arctic.noaa.gov/Report-Card, 2016.

Overland, J., Dethloff, K., Francis, J., Hall, R., Hanna, E., Kim, S.-J., Screen, J., Shepherd, T., and Vihma, T.: Nonlinear response of mid-latitude weather to the changing Arctic, Nat. Clim. Chang., 6, 992–999, doi:10.1038/NCLIMATE3121, 2016.

Painter, T. and Dozier, J.: Measurements of the hemispherical-directional reflectance of snow at fine spectral and angular resolution, J. Geophys. Res., 109, doi:10.1029/2003JD004458, 2004a.

Painter, T. and Dozier, J.: The effect of anisotropic reflectance on imaging spectroscopy of snow properties, Remote Sens. Environ., 89, 409–422, doi:10.1016/j.rse.2003.09.007, 2004b.

Painter, T., Paden, B., and Dozier, J.: Automated spectro-goniometer: A spherical robot for the field measurement of the directional reflectance of snow, Rev. Sci. Instrum., 74, 5179–5188, doi:10.1063/1.1626011, 2003.

Palerme, C., Kay, J., Genthon, C., L'Ecuyer, T., Wood, N. B., and Claud, C.: How much snow falls on the Antarctic ice sheet?, The Cryosphere, 8, 1577–1587, doi:10.5194/tc-8-1577-2014, 2014.

Parkinson, C. and DiGirolamo, N.: New visualizations highlight new information on the contrasting Arctic and Antarctic sea-ice trends since the late 1970s, Remote Sens. Environ., 183, 198–204, doi:10.1016/j.rse.2016.05.020, 2016.

Pedersen, C. A., Gallet, J. C., Strom, J., Gerland, S., Hudson, S. R., Forsstrom, S., Isaksson, E., and Berntsen, T. K.: In situ observations of black carbon in snow and the corresponding spectral surface albedo reduction, J. Geophys. Res. Atmos., 120, 1476–1489, doi:10.1002/2014JD022407, 2015.

Pegrum, H., Fox, N., Chapman, M., and Milton, E.: Design and Testing a New Instrument to Measure the Angular Reflectance of Terrestrial Surfaces, in: IEEE International Geoscience & Remote Sensing Symposium, IGARSS 2006, July 31 - August 4, 2006, Denver, Colorado, USA, Proceedings, pp. 1119–1122, doi:10.1109/IGARSS.2006.289, URL `https://doi.org/10.1109/IGARSS.2006.289`, 2006.

Picard, G., Libois, Q., Arnaud, L., Verin, G., and Dumont, M.: Development and calibration of an automatic spectral albedometer to estimate near-surface snow SSA time series, The Cryosphere, 10, 1297–1316, doi:10.5194/tc-10-1297-2016, 2016.

Picard, G., Arnaud, L., Domine, F., and Fily, M.: Determining snow specific surface area from near-infrared reflectance measurements: Numerical study of the influence of grain shape, Cold Reg. Sci. Technol., 56, 10–17, doi:10.1016/j.coldregions.2008.10.001, 2009.

Picard, G., Domine, F., Krinner, G., Arnaud, L., and Lefebvre, E.: Inhibition of the positive snow-albedo feedback by precipitation in interior Antarctica, Nat. Clim. Chang., 2, 795–798, doi:10.1038/NCLIMATE1590, 2012.

Qu, Y., Liang, S., Liu, Q., He, T., Liu, S., and Li, X.: Mapping Surface Broadband Albedo from Satellite Observations: A Review of Literatures on Algorithms and Products, Remote Sens., 7, 990–1020, doi:10.3390/rs70100990, 2015.

Räisänen, J.: Warmer climate: less or more snow?, Clim. Dyn., 30, 307–319, doi:10.1007/s00382-007-0289-y, 2008.

Ross, J.: The radiation regime and architecture of plant stands, Tasks for vegetation sciences 3, Dr. W. Junk Publishers, The Hague, The Netherlands, 1981.

Roujean, J.-L., Leroy, M., and Deschamps, P.-Y.: A bidirectional reflectance model of the Earth's surface for the correction of remote sensing data, J. Geophys. Res., 97, 20 455–20 468, doi:10.1029/92JD01411, 1992.

Rozenberg, G.: Light characteristics of thick layers of a weakly absorbing scattering medium, Doklady, Acad. Sci. USSR, 145, 775–777, 1962.

Salzmann, M.: The polar amplification asymmetry: role of Antarctic surface height, Earth Syst. Dynam., 8, 323–336, doi:10.5194/esd-8-323-2017, 2017.

Schaaf, C. B., Gao, F., Strahler, A. H., Lucht, W., Li, X. W., Tsang, T., Strugnell, N. C., Zhang, X. Y., Jin, Y. F., Muller, J. P., Lewis, P., Barnsley, M., Hobson, P., Disney, M., Roberts, G., Dunderdale, M., Doll, C., d'Entremont, R. P., Hu, B. X., Liang, S. L., Privette, J. L., and Roy, D.: First operational BRDF, albedo nadir reflectance products from MODIS, Remote Sens. Environ., 83, 135–148, 2002.

Schaepman-Strub, G., Schaepman, M. E., Painter, T. H., Dangel, S., and Martonchik, J. V.: Reflectance quantities in optical remote sensing-definitions and case studies, Remote Sens. Environ., 103, 27–42, doi:10.1016/j.rse.2006.03.002, 2006.

Schmid, H.: Stellar calibration of the orbigon lens, Photogramm. Eng., 40, 101–115, 1974.

Screen, J. A. and Simmonds, I.: The central role of diminishing sea ice in recent Arctic temperature amplification, Nature, 464, 1334–1337, doi:10.1038/nature09051, 2010.

Serreze, M. C. and Barry, R. G.: Processes and impacts of Arctic amplification: A research synthesis, Global Planet. Change, 77, 85–96, doi:10.1016/j.gloplacha.2011.03.004, 2011.

Shindell, D. and Faluvegi, G.: Climate response to regional radiative forcing during the twentieth century, Nat. Geosci., 2, 294–300, doi:10.1038/NGEO473, 2009.

Sigmond, M. and Fyfe, J.: Has the ozone hole contributed to increased Antarctic sea ice extent?, Geophys. Res. Lett., 37, doi:10.1029/2010GL044301, 2010.

Simmonds, I.: Comparing and contrasting the behaviour of Arctic and Antarctic sea ice over the 35 year period 1979-2013, Ann. Glaciol., 56, 18–28, doi:10.3189/2015AoG69A909, 2015.

Sobolev, V.: Light Scattering in Planetary Atmospheres, Pergamon Press, Oxford, New York, Toronto, Sydney, Braunschweig, 1975.

Stamnes, K., Tsay, S., Wiscombe, W., and Jayaweera, K.: A numerically stable algorithm for discrete-ordinate-method radiative transfer in multiple scattering and emitting layered media, Appl. Opt., 27, 2502–2509, doi:10.1364/AO.27.002502, 1988.

Stanton, B., Miller, D., Adams, E., and Shaw, J. A.: Bidirectional-reflectance measurements for various snow crystal morphologies, Cold Reg. Sci. Technol., 124, 110–117, doi:10.1016/j.coldregions.2015.12.011, 2016.

Steig, E., Schneider, D., Rutherford, S., Mann, M., Comiso, J., and Shindell, D.: Warming of the Antarctic ice-sheet surface since the 1957 International Geophysical Year (vol 457, pg 459, 2009), Nature, 460, 766, doi:10.1038/nature08286, 2009.

Strahler, A., Wanner, W., Schaaf, C., Li, X., Hu, B., Muller, J., Lewis, P., and Barnsley, M.: MODIS BRDF/Albedo product: Algorithm Theoretical Basis Document Version 4.0, 1996.

Stroeve, J., Box, J., Gao, F., Liang, S., Nolin, A., and Schaaf, C.: Accuracy assessment of the MODIS 16-day albedo product for snow: comparisons with Greenland in situ measurements, Remote Sens. Environ., 94, 46–60, doi:10.1016/j.rse.2004.09.011, 2005.

Stroeve, J., Box, J., Wang, Z., Schaaf, C., and Barrett, A.: Re-evaluation of MODIS MCD43 Greenland albedo accuracy and trends, Remote Sens. Environ., 138, 199–214, doi:10.1016/j.rse.2013.07.023, 2013.

Tomasi, C., Vitale, V., Lupi, A., Di Carmine, C., Campanelli, M., Herber, A., Treffeisen, R., Stone, R. S., Andrews, E., Sharma, S., Radionov, V., von Hoyningen-Huene, W., Stebel, K., Hansen, G. H., Myhre, C. L., Wehrli, C., Aaltonen, V., Lihavainen, H., Virkkula, A., Hillamo, R., Strom, J., Toledano, C., Cachorro, V. E., Ortiz, P., de Frutos, A. M., Blindheim, S., Frioud, M., Gausa, M., Zielinski, T., Petelski, T., and Yamanouchi, T.: Aerosols in polar regions: A historical overview based on optical depth and in situ observations, J. Geophys. Res., 112, D16 205, doi:10.1029/2007JD008432, 2007.

Tomasi, C., Kokhanovsky, A., Lupi, A., Ritter, C., Smirnov, A., O'Neill, N., Stone, R., Holben, B., Nyeki, S., Wehrli, C., Stohl, A., Mazzola, M., Lanconelli, C., Vitale, V., Stebel, K., Aaltonen, V., de Leeuw, G., Rodriguez, E., Herber, A., Radionov, V., Zielinski, T., Petelski, T., Sakerin, S., Kabanov, D., Xue, Y., Mei, L., Istomina, L., Wagener, R., McArthur, B., Sobolewski, P., Kivi, R., Courcoux, Y., Larouche, P., Broccardo, S., and Piketh, S.: Aerosol remote sensing in polar regions, Earth-Sci. Rev., 140, 108–157, doi:10.1016/j.earscirev.2014.11.001, 2015.

Tsai, R.: A versatile camera calibration technique for high-accuracy 3D machine vision metrology using off-the-shelf TV cameras and lenses, IEEE J. Robot. Autom., 3, 323–344, doi:10.1109/JRA.1987.1087109, 1987.

Turner, J., Lu, H., White, I., King, J., Phillips, T., Hosking, J., Bracegirdle, T., Marshall, G., Mulvaney, R., and Deb, P.: Absence of 21st century warming on Antarctic Peninsula consistent with natural variability, Nature, 535, 411–415, doi:10.1038/nature18645, 2016.

Turner, J., Phillips, T., Marshall, G., Hosking, J. S., Pope, J., Bracegirdle, T., and Deb, P.: Unprecedented springtime retreat of Antarctic sea ice in 2016, Geophys. Res. Lett., 44, 6868–6875, doi:10.1002/2017GL073656, 2017.

Tynes, H., Kattawar, G., Zege, E., Katsev, I., Prikhach, A., and Chaikovskaya, L.: Monte Carlo and multicomponent approximation methods for vector radiative transfer by use of effective Mueller matrix calculations, Appl. Opt., 40, 400–412, doi:10.1364/AO.40.000400, 2001.

Urquhart, B., Kurtz, B., and Kleissl, J.: Sky camera geometric calibration using solar observations, Atmos. Meas. Tech., 9, 4279–4294, doi:10.5194/amt-9-4279-2016, 2016.

van de Hulst, H.: Radiative transfer in thick atmospheres with an arbitrary scattering function, Bull Astron. Inst. Netherlands, 20, 77–86, 1968.

van de Hulst, H.: Radiation and Cloud Processes in the Atmosphere. Theory, Observation and Modeling, Multiple Light Scattering, Volume 2, Academic Press, New York, London, Sydney, Toronto, San Francisco, 1980.

Vaughan, D., Comiso, J., Allison, I., Carrasco, J., Kaser, G., Kwok, R., Mote, P., Murray, T., Paul, F., Ren, J., Rignot, E., Solomina, O., Steffen, K., and Zhang, T.: Observations: Cryosphere, in: Climate Change 2013: The Physical Science Basis. Contribution of Working Group I to the Fifth Assessment Report of the Intergovernmental Panel on Climate Change, edited by Stocker, T., Qin, D., Plattner, G.-K., Tignor, M., Allen, S., Boschung, J., Nauels, A., Xia, Y., Bex, V., and Midgley, P., pp. 317–382, Cambridge University Press, Cambridge, United Kingdom and New York, NY, USA, doi:10.1017/CBO9781107415324.012, 2013.

Vaughan, D., Marshall, G., Connolley, W., Parkinson, C., Mulvaney, R., Hodgson, D., King, J., Pudsey, C., and Turner, J.: Recent rapid regional climate warming on the Antarctic Peninsula, Clim. Chang., 60, 243–274, doi:10.1023/A:1026021217991, 2003.

Vavrus, S.: The impact of cloud feedbacks on Arctic climate under greenhouse forcing, J. Clim., 17, 603–615, doi:10.1175/1520-0442(2004)017<0603:TIOCFO>2.0.CO;2, 2004.

Vermote, E. and Kotchenova, S.: Atmospheric correction for the monitoring of land surfaces, J. Geophys. Res., 113, doi:10.1029/2007JD009662, 2008.

Wallace, J. and Hobbs, P.: Atmospheric science : an introductory survey, International geophysics series, Academic Press, 2. ed. edn., 2006.

Warren, S., Brandt, R., and O'Rawe Hinton, P.: Effect of surface roughness on bidirectional reflectance of Antarctic snow, J. Geophys. Res., 103, 25 789–25 807, doi:10.1029/98JE01898, 1998.

Warren, S. G. and Brandt, R. E.: Optical constants of ice from the ultraviolet to the microwave: A revised compilation, J. Geophys. Res., 113, Art. No. D14 220, doi:10.1029/2007JD009744, 2008.

Wendisch, M.: Absorption of Solar Radiation in the Cloudless and Cloudy Atmosphere, Habilitation thesis, 174 pp., Univ. of Leipzig, Leipzig, Germany, 2002.

Wendisch, M. and Mayer, B.: Vertical distribution of spectral solar irradiance in the cloudless sky: A case study, Geophysical Research Letters, 30, 1183–1186, doi:10.1029/2002GL016529, URL `http://dx.doi.org/10.1029/2002GL016529`, 2003.

Wendisch, M. and Yang, P.: Theory of Atmospheric Radiative Transfer - A Comprehensive Introduction, Wiley-VCH Verlag GmbH & Co. KGaA, Weinheim, Germany, ISBN: 978-3-527-40836-8, 2012.

Wendisch, M., Müller, D., Schell, D., and Heintzenberg, J.: An airborne spectral albedometer with active horizontal stabilization, J. Atmos. Oceanic Technol., 18, 1856–1866, doi:10.1175/1520-0426(2001)018<1856:AASAWA>2.0.CO;2, 2001.

Wendisch, M., Pilewskie, P., Jäkel, E., Schmidt, S., Pommier, J., Howard, S., Jonsson, H. H., Guan, H., Schröder, M., and Mayer, B.: Airborne measurements of areal spectral surface albedo over different sea and land surfaces, J. Geophys. Res., 109, Art. No. D08 203, doi:10.1029/2003JD004392, 2004.

Wendisch, M., Yang, P., and Ehrlich, A.: Amplified climate changes in the Arctic: Role of clouds and atmospheric radiation, Sitzungsberichte der Sächsischen Akademie der Wissenschaften zu Leipzig, Mathematisch-Naturwissenschaftliche Klasse, 132(3), S. Hirzel Verlag, Stuttgart/Leipzig, ISBN: 978-3-7776-2386-3, 2013.

Wendisch, M., Brückner, M., Burrows, J. P., Crewell, S., Dethloff, K., Ebell, K., Lüpkes, C., Macke, A., Notholt, J., Quaas, J., Rinke, A., and Tegen, I.: Understanding causes and effects of rapid warming in the Arctic, Eos, **98**, doi:10.1029/2017EO064803, 2017.

Werner, F., Siebert, H., Pilewskie, P., Schmeissner, T., Shaw, R. A., and Wendisch, M.: New airborne retrieval approach for trade wind cumulus properties under overlying cirrus, J. Geophys. Res., 118, 3634–3649, doi:10.1002/jgrd.50334, 2013.

Wiebe, H., Heygster, G., Zege, E., Aoki, T., and Hori, M.: Snow grain size retrieval SGSP from optical satellite data: Validation with ground measurements and detection of snow fall events, Remote Sens. Environ., 128, 11–20, doi:10.1016/j.rse.2012.09.007, 2013.

Winton, M.: Amplified Arctic climate change: What does surface albedo feedback have to do with it?, Geophys. Res. Lett., 33, 2006.

Wiscombe, W. and Warren, S.: A model for the spectral albedo of snow I. Pure snow, J. Atmos. Sci., 37, 2712–2733, doi:10.1175/1520-0469(1980)037<2712:AMFTSA>2.0.CO;2, 1980.

Wuttke, S., Seckmeyer, G., and König-Langlo, G.: Measurements of spectral snow albedo at Neumayer, Antarctica, Ann. Geophys., 24, 7–21, doi:10.5194/angeo-24-7-2006, 2006.

Xie, Y., Yang, P., Gao, B. C., Kattawar, G. W., and Mishchenko, M. I.: Effect of ice crystal shape and effective size on snow bidirectional reflectance, J. Quant. Spectrosc. Radiat. Transfer, 100, 457–469, doi:10.1016/j.jqsrt.2005.11.056, 2006.

Yang, F., Ovchinnikov, M., and Shaw, R. A.: Microphysical consequences of the spatial distribution of ice nucleation in mixed-phase stratiform clouds, Geophys. Res. Lett., 41, 5280–5287, doi:10.1002/2014GL060657, 2014.

Yang, P. and Liou, K. N.: Geometric-optics-integral-equation method for light scattering by nonspherical ice crystals, Appl. Opt., 35, 6.568–6.584, 1996.

Yosida, Z., Oura, H., Kuroiwa, D., Huzioka, T., Kojima, K., Aoki, S., and Kinosita, S.: Physical studies on deposited snow: I Thermal properties, Tech. Rep. 7, Institute of Low Temperature Science, Hokkaido University, Sapporo, Japan, 1955.

Zege, E., Ivanov, A., and Katsev, I.: Image Transfer Through a Scattering Medium, Springer-Verlag, Heidelberg, 1991.

Zege, E. P., Katsev, I. L., Malinka, A. V., Prikhach, A. S., Heygster, G., and Wiebe, H.: Algorithm for retrieval of the effective snow grain size and pollution amount from satellite measurements, Remote Sens. Environ., 115, 2674–2685, doi:10.1016/j.rse.2011.06.001, 2011.

Zhuravleva, T. B. and Kokhanovsky, A. A.: Influence of surface roughness on the reflective properties of snow, J. Quant. Spectrosc. Ra., 112, 1353–1368, doi:10.1016/j.jqsrt.2011.01.004, 2011.

Nomenclature

Abbreviations

Abbr.	**Description**
AERONET	Aerosol Robotic Network
AIMMS20	Aircraft-Integrated Meteorological Measurement System
APS-H	Advanced Photo System format
ARTT	Asymptotic radiative transfer theory
ASG	Automated Spectro-Goniometer
AWI	Alfred Wegener Institut, Helmholtz Centre for Polar and Marine Research
AWS	Automatic weather station
CAR	Cloud Absorption Radiometer
CCD	Charge coupled device
CERES	The clouds and the Earth's radiant energy system
CFA	Color filter array
CMIP5	Coupled Model Intercomparison Project phase 5
CMOS	Complementary metal oxide semiconductor
CoFi	Coldest Firn
CORAS	COmpact RAdiation measurement System
CR2	Canon Raw version 2
DEM	Digital elevation model
DISORT	Discrete ordinate radiative transfer solver
DN	Digital numbers
DOME C	Dome Concordia
DUFISSS	DUal Frequency Integrating Sphere for Snow SSA measurements
EM	Electromagnetic
FOV	Field of view
FWHM	Full width at half maximum
GPS	Global positioning system
GRASS	Gonio Radiometric Spectrometer System
IAC-ETH	Institute for Atmospheric and Climate Science of the Swiss Federal Institute of Technology
INP	Ice nucleating particle
INS	Internal navigation system

libRadtran	Library for radiative transfer
LIM	Leipzig Institute for Meteorology
MCS	Multi-channel spectrometer
MISR	Multi-angle imaging spectroradiometer
MODIS	MODerate Resolution Imaging Spectroradiometer
MRPV	Modified Rahman-Pinty-Verstraete
NASA	National Aeronautics and Space Administration
NH	Northern hemisphere
NIR	Near-infrared (part of the EM spectrum)
NIST	National Institute of Standards and Technology
NOAA	National Oceanic and Atmospheric Administration
PANGAEA	Publishing Network for Geoscientific & Environmental Data
PDA	Single-line photodiode array
PGS	Plane grating spectrometer
PRNU	Photo response non-uniformity
RACEPAC	Radiation-Aerosol-Cloud Experiment in the Arctic Circle
RGB	Red, green, and blue camera channel
RTLS	Ross-Thick Li-sparse
SGSP	Snow grain size and pollution amount
SH	Southern Hemisphere
SMART	Spectral Modular Airborne Radiation measurement sysTem
SWIR	Shortwave-infrared wavelength region
TOA	Top of the atmosphere
UTC	Universal Time Code
VIS	Visible (part of the EM spectrum)
VNIR	Visible to near-infrared wavelength region

Acronym

Symbol	**Description**	**Units**
AI	Anisotropy index	–
AOD	Aerosol optical depth	–
BC	Mean black carbon concentration	ppbw
BHR, f_{BHR}	Bihemispherical reflectance	–
BRDF, f_{BRDF}	Bidirectional reflectance distribution function	–

BRF, f_{BRF}	Bidirectional reflectance factor	–
HCRF	Hemispherical-conical reflectance factor	–
HDRF, f_{HDRF}	Hemispherical-directional reflectance factor	–
LHA	Local hour angle	°
LST	Local siderial time	°
LWC	Liquid water content	$\mathrm{kg\,m^{-3}}$
RA	Right ascension	°
RSR(λ)	Relative spectral response function	$\mathrm{m^{-1}}$
SSA	Specific surface area	$\mathrm{m^{2}\,kg^{-1}}$

Constants

Symbol	**Description**	**Value**	**Units**
i	Imaginary unit	$\sqrt{-1}$	–
ρ_{ice}	Density of ice	917	$\mathrm{kg\,m^{-3}}$

Greek Symbols

Symbol	**Description**		**Units**
$\alpha(\lambda)$	Spectral surface albedo	–	1
α_{BB}	Broadband albedo	–	1
α_{p}	Plane surface albedo	–	1
α_{s}	Spherical surface albedo	–	1
δ	Declination	–	°
$\epsilon(\lambda)$	Spectral e-folding penetration depth		m
λ	Wavelength	–	m
λ_{c}	Central wavelength of camera channel	–	m
φ	Geographical latitude	–	°
Λ	Geographical longitude	–	°
μ_{s}	Mean signal	–	DN
$\mathit{\Omega}$	Solid angle	–	sr
$\tilde{\omega}$	Single-scattering albedo	–	–
$\mathit{\Phi}_{\lambda}$	Spectral radiant energy flux	–	$\mathrm{W\,m^{-1}}$
φ_{0}	Solar azimuth angle	–	°
φ_{i}	Incident azimuth angle	–	°

φ_r	Reflection azimuth angle	–	°
$\varPhi$	Roll angle	–	°
φ_v	Viewing azimuth angle	–	°
$\varPhi_\mathrm{abs}$	Radiant energy flux subject to absorption	–	$\mathrm{W\,m^{-1}}$
$\varPhi_\mathrm{ext}$	Radiant energy flux subject to extinction	–	$\mathrm{W\,m^{-1}}$
$\varPhi_\mathrm{sca}$	Radiant energy flux subject to scattering	–	$\mathrm{W\,m^{-1}}$
ψ	Yaw angle	–	°
ρ	Density	–	$\mathrm{kg\,m^{-3}}$
ρ_l	Angular observations	–	–
σ_s	Standard deviation of signal	–	DN
σ_RMSE	Root-mean-square error	–	%
τ	Optical thickness of scattering layer	–	–
θ	Scattering angle	–	°
θ_0	Solar zenith angle	–	°
θ_i	Incident zenith angle	–	°
Θ	Pitch angle	–	°
θ_r	Reflection zenith angle	–	°
θ_v	Viewing zenith angle	–	°
ξ	Relative measurement uncertainty		%

Roman Symbols

Symbol	**Description**	**Dimensions**	**Units**
A	Form factor	–	–
A_L	Global land surface area	–	$\mathrm{m^2}$
A_O	Global ocean area	–	$\mathrm{m^2}$
A_tot	Total surface area	–	$\mathrm{m^2}$
$B(\xi)$	Absorption enhancement parameter	–	–
b_abs	Volumetric absorption coefficient	–	$\mathrm{m^{-1}}$
$b_\mathrm{abs,ice}$	Absorption coefficient of pure ice	–	$\mathrm{m^{-1}}$
b_ext	Volumetric extinction coefficient	–	$\mathrm{m^{-1}}$
$b_\mathrm{sca}(\varOmega, \varOmega')$	Differential scattering coefficient	–	$\mathrm{m^{-1}}$

C_{abs}	Absorption cross section	–	m^2
$C_{\mathrm{abs}}(\lambda)$	Absolute calibration factor	–	–
$C_{\mathrm{cc}}(\lambda)$	Cross-calibration factor	–	–
$C_{\mathrm{cos,diff}}$	Diffuse cosine correction factor	–	–
$C_{\mathrm{cos,dir}}$	Direct cosine correction factor	–	–
C_{ext}	Extinction cross section	–	m^2
C_{sca}	Scattering cross section	–	m^2
C_{v}	Volumetric concentration of snow grains	–	–
D	Particle diameter	–	m
d	Degree of freedom	–	–
ΔD	Particle diameter interval	–	m
d_{J2000}	Days since standard epoch J2000		
$\mathrm{d}N$	Number of particles per volume element	–	m^{-3}
E	Geometric snow grain size	–	m
E_{rad}	Radiant energy	–	J
$\mathcal{E}^2$	Error function		
f_{diff}	Diffuse fraction of global irradiance	–	–
f_{dir}	Direct fraction of global irradiance	–	–
f_{iso}, f_{vol}, f_{geo}	Non-negative weighting functions for kernels	–	–
$F^{\downarrow}(\lambda)$	Spectral downward irradiance	–	$\mathrm{W\,m^{-2}\,m^{-1}}$
F_{i}	Incident spectral irradiance	–	$\mathrm{W\,m^{-2}\,m^{-1}}$
F_{inc}	Irradiance at top of scattering layer	–	$\mathrm{W\,m^{-2}\,m^{-1}}$
F_{λ}	Spectral irradiance	–	$\mathrm{W\,m^{-2}\,m^{-1}}$
F_{net}	Net irradiance	–	$\mathrm{W\,m^{-2}}$
$F^{\uparrow}(\lambda)$	Spectral upward irradiance	–	$\mathrm{W\,m^{-2}\,m^{-1}}$
g	Asymmetry parameter	–	–
h_0	Solar altitude angle	–	°
$\mathcal{I}$	Optometer current	–	A
$I_{\lambda}^{\downarrow}$	Downward spectral radiance	–	$\mathrm{W\,m^{-2}\,m^{-1}\,sr^{-1}}$
I_{λ}	Spectral radiance	–	$\mathrm{W\,m^{-2}\,m^{-1}\,sr^{-1}}$
I_{r}	Reflected spectral radiance	–	$\mathrm{W\,m^{-2}\,m^{-1}\,sr^{-1}}$

$I_\lambda^\uparrow$	Upward spectral radiance	–	$\mathrm{W\,m^{-2}\,m^{-1}\,sr^{-1}}$
k	Modified wavenumber	–	$\mathrm{m^{-1}}$
$k_{\mathrm{c}(\lambda)}$	Calibration factor for camera	–	$\mathrm{W\,m^{-2}\,m^{-1}\,sr^{-1}\,(DN/s)^{-1}}$
K_{iso}, K_{vol}, K_{geo}	Kernels for isotropic, volumetric, and geometric scattering	–	–
$K_0(\mu_0)$	Escape function	–	–
$K_{\mathrm{emp}}(\mu_0)$	Empirically adjusted escape function	–	–
l_{rough}	Surface roughness	–	m
m	Mass	–	kg
$\boldsymbol{\hat{n}}$	Normal unit vector	3	–
$\tilde{n}$	Complex index of refraction	–	–
$\tilde{n}_{\mathrm{im}}$	Imaginary part of $\tilde{n}$	–	–
$\tilde{n}_{\mathrm{re}}$	Real part of $\tilde{n}$	–	–
$\mathcal{P}(\theta)$	Phase function	–	–
q_{s}	Saltation flux	–	$\mathrm{kg\,m^{-1}\,s^{-1}}$
$\boldsymbol{\hat{r}}$	Direction vector	3	–
$\boldsymbol{R}_{\mathbf{pitch}}$	Rotation matrix for pitch direction	3×3	–
$\boldsymbol{R}_{\mathbf{roll}}$	Rotation matrix for roll direction	3×3	–
$\boldsymbol{R}_{\mathbf{yaw}}$	Rotation matrix for yaw direction	3×3	–
R^2	Coefficient of correlation	–	–
$\mathcal{R}$	Spectral ratio of surface albedo	–	–
R_{opt}	Optical-equivalent snow grain size	–	m
$R_{\mathrm{opt,eff}}$	Effective optical-equivalent snow grain size	–	m
$\boldsymbol{\hat{s}}$	Incident direction vector	3	–
s	Measured camera signal	–	DN
$s_{\mathrm{dark}}(\lambda)$	Scaled dark spectrum	–	DN
$s(\lambda)$	Measured raw spectrum	–	DN
$\boldsymbol{\hat{s}'}$	Reflection direction vector	3	–
T	Near-surface air temperature	–	°C
t	Time	–	s
u	Average horizontal wind speed	–	$\mathrm{m\,s^{-1}}$
u_{th}	Average threshold horizontal wind velocity	–	$\mathrm{m\,s^{-1}}$

V	Volume	–	m^3
V_{tot}	Total volume	–	m^3
w_l	Weights assigned to observations		
z	Flight altitude	–	m

Acknowledgements

This work was supported by the Deutsche Forschungsgemeinschaft (DFG) in the framework of the priority programme “Antarctic Research with comparative investigations in Arctic ice areas” (SPP 1158) by the grants WE1900/29-1 and BI 816/4-1. The support by the SFB/TR 172 “ArctiC Amplification: Climate Relevant Atmospheric and SurfaCe Processes, and Feedback Mechanisms (AC)^3” funded by the DFG is gratefully acknowledged. I am grateful to the Alfred Wegener Institute, Helmholtz Centre for Polar and Marine Research, Bremerhaven, Germany, for supporting the campaign with logistics, the aircraft and manpower in Antarctica. In addition, I would like to thank Kenn Borek Air Ltd., Calgary, Canada for the great pilots who made the complicated measurements possible.

I would particularly like to thank Michael Schäfer for his readiness to participate in the campaign at Kohnen station. I have greatly benefited from all the work you did dedicated to the measurements at the cost of regular sleeping times. Your reports and experience during the time in Antarctica definitely helped me with the interpretation of the datasets. Your input on the issues with the instruments were highly valuable. In this regard, I also want to thank Gerit Birnbaum for her efforts at Kohnen station, the fruitful discussions during the data analysis, and all the great photographs of the campaign work she provided. Of course, I want to thank all the others who are not mentioned here but were involved in the measurements in Antarctica.

I would like to thank Andreas Herber for the analysis of the sun photometer data; Anaïs Orsi, Sepp Kipfstuhl, and Johannes Freitag for the in situ snow sampling and analysis of the IceCube data; Georg Heygster and Larysa Istomina for providing the snow grain size data from MODIS measurements; and Veit Helm for analyzing and distributing the roughness data from the airborne laser scanner. For his insights into the mysterious proprietary sRaw format of the digital camera, I would like to express my gratitude to Douglas Kerr.

I am deeply grateful to my supervisor Prof. Manfred Wendisch and to André Ehrlich for their patient guidance and help throughout the last years. Thank you for the possibility to participate in the measurement campaigns at Inuvik, Canada, and Keflavik,

Iceland, which have been extraordinary experiences. I also want to express my appreciation for all the work you invested in revising the manuscript of this thesis, which definitely benefited from your input.
Special thanks to Nicola and Martin Leslie for their continuous help with the English language and for revising the manuscript at short notice.
I also want to thank the entire radiation group (and Andreas) at the Leipzig Institute for Meteorology for creating such a nice working environment and for all the activities we did together outside the office rooms. Many thanks to the colleagues sharing an office with me: Michael, Vasileios, André, Tobias, Trismono, and Kátia.

Zu guter Letzt gilt ein riesiger Dank meinen Eltern und Großeltern, meinem Bruder Franz und meiner Freundin Isabella. Ihr habt mich immer toll unterstützt, euch meine täglichen Statusberichte geduldig angehört und mir dabei geholfen, auf andere Gedanken zu kommen. Bei Isabella möchte ich mich zusätzlich für ihre Hilfe bei der Erstellung der Abbildungen 2.2 und 2.3 bedanken.